UNIVERSITY OF SOUTHAMPTON

FACULTY OF SCIENCE

DEPARTMENT OF OCEANOGRAPHY

THE ASSESSMENT OF A TOWED LASER SLOPEMETER FOR MEASURING SHORT SCALE SEA SURFACE WAVE SLOPES

by

Barrie John Willoughby

A thesis submitted for the degree of Doctor of Philosophy

April 1998

UNIVERSITY OF SOUTHAMPTON

ABSTRACT

FACULTY OF SCIENCE
OCEANOGRAPHY

Doctor of Philosophy

THE ASSESSMENT OF A TOWED LASER SLOPEMETER FOR MEASURING SHORT SCALE SEA SURFACE WAVE SLOPES

by Barrie John Willoughby

The advent of satellite -borne Synthetic Aperture Radar (SAR) has generated much interest in sea surface waves of less than a metre in wavelength. Many oceanographic processes can be identified within SAR images of the world's oceans. The limited understanding of the interactions between these phenomena and the wind-wave field and the scatter mechanisms leading to the returned radar signal has restricted the full quantitative application of this important remote sensing tool. In an effort to address this gap in our understanding there is a need for in-situ measurements.

A Towed Laser Slopemeter has been designed and developed at the University of Southampton. This is capable of measuring two orthogonal components of surface slope of between ±35° over a wavelength range of 1m to 0.007m at a rate of 250 Hz. Values of slope are determined using a laser beam and an optical detection system without the need to measure surface wave height. The instrument is towed parallel to a larger vessel to ensure that an undisturbed surface profile is sampled. It has been established that the effect of towing the slopemeter leads to a hybrid wavenumber-frequency spectrum. Studies conducted in this thesis are concerned with the characterisation of the TLS and the verification of its ability to measure sea surface wave slope. To investigate the effect of vehicle velocity on the observed spectrum a new numerical model was developed. The model was capable of providing true wavenumber, true wave frequency and wavenumber-frequency spectra. A factor of five decrease in the computational time of the model was provided by reducing the number of calculations in the Fourier transform employed. The direction between the true and observed wavenumbers was found to be a minimum at small angles to the direction of travel of the wave and at high tow speeds. Using the numerical model methods for providing a true wavenumber spectrum from the wavenumber-frequency spectrum were investigated. A new method which did not require the assumptions of the previous methods was proposed.

Data from the first deployment of the slopemeter was thoroughly investigated to assess its oceanographic content. Wave profiles, spectra and slope distributions were found to agree with accepted forms. The wave profile was noisier than expected. From an analysis of this noise, sources were identified and this led directly to a refit of the TLS. Slicks evident on the sea surface were sampled by the slopemeter during the trial. The time at which these features were intercepted by the TLS was logged. The logged time agreed with a decrease in the recorded wave slopes. The ability of the TLS to provide a sensitive and precise measurement of sea surface roughness was reinforced with an extensive comparison of the TLS and video records from the second deployment. Waves seen within the video could be seen within the TLS record. General agreement between the wavelengths causing the roughness changes estimated from the video and the TLS spectrum was found. The TLS proved to be more sensitive to changes in wave slope for a larger range of sea states than the video record. A variety of signal processing tools were found to be useful in the analysis of the TLS data sets. Confidence was gained in the ability of the TLS as a device capable of providing sensitive in-situ measurements of the interaction of ocean processes with the sea surface wave profile.

Contents

Symbols and Abbreviations

A	spectral amplitude per unit wavenumber
c_f	compression factor
c_g	group velocity
c_p	phase velocity
d	depth
F	wave height power spectrum
G	wave slope power spectrum
g	gravitational acceleration at earth's surface
h_w	height of generic slopemeter above mean sea surface level
i	imaginary number $\sqrt{-1}$
k	wavenumber
K	swell wave wavenumber
k_e	wavenumber of encounter
k_x	wavenumber in x direction
k_y	wavenumber in y direction
l	height at which wind speed measured
l_o	roughness length
n_a	refractive index of water
n_w	refractive index of air
N	action spectral density
Q	source term
P	phase term
Re	real part
S	wave slope
S_E	wave slope in east-west direction
S_N	wave slope in north-south direction
S_x	wave slope in x direction
S_y	wave slope in y direction
t	time
u	vessel speed

u_*	wind frictional velocity
U	surface current velocity
U_o	surface current velocity associated with swell wave
V_a	output signal voltage from photodiode A
V_b	output signal voltage from photodiode B
W	wind speed at 10m
x_b	spot position on generic laser slopemeter (bottom screen of TLS)
x_b	spot position on top screen of TLS
X	wave height skewness spectrum
Y	covariance of wave slope
Z	covariance of wave height
β	Spectral constant
γ	ratio of group velocity to phase velocity
ϕ	angular wave slope elevation from the horizontal
ϕ_e	angle of wave slope measured by generic slopemeter
ϕ_i	angle of incidence of laser beam at waters surface
ϕ_p	angle between vertical and refracted laser beam at waters surface
ϕ_r	angle of refraction of laser beam at waters surface
φ	surface tension
κ	von Karman's constant
μ	relaxation rate
μ_a	angular component of relaxation rate
μ_r	radial component of relaxation rate
ν	beam width parameter
θ	direction of wave propagation relative to the TLS
θ_b	direction of vessel relative to true north
θ_N	direction of wave propagation relative to true north
ρ	water density
σ	variance
σ_3	skewness
σ_4	kurtosis
ω	wave frequency
ω_e	wave frequency of encounter
ω_o	intrinsic wave frequency
Ω	Swell wave frequency
ξ	wave height

ADC	Analogue to Digital Converter
CPU	Central Processing Unit
CSTAR	Coastal and sediment transport assessment using SAR
DFT	Discrete Fourier Transform
DRA	Defence Research Agency
DSM	Digital Slopemeter
FFT	Fast Fourier Transform
IMU	Inertial Measurement Unit
NF	Nqyuist Frequency
PC	Personal Computer
PDF	Probability Density Function
PLL	Phase Lock Loop
PCB	Printed Circuit Board
RV	Research Vessel
SAR	Synthetic Aperture Radar
SNR	Signal-to-Noise Ratio
TLS	Towed Laser Slopemeter

Acknowledgements

Mum, Dad and Kate thank you very much for your support, understanding and love which has not faltered during the course of this work. If it had not been for you I would not be writing this page.

I would like to thank Dr Ian Robinson, my supervisor, for his guidance and support throughout the course of this research. I would also like to thank Dr David Ramsden who, although not officially my supervisor, never the less has provided much support and guidance. A big thank you must also go to the other members of the TLS team; Dr Harbie Ghataure, Dr Chris Lee and Grant Crossingham whose ideas, points of view and friendship have proved invaluable.

Thank you to all the project staff at DRA Farnborough for their input and prompt response to my questions. I acknowledge the DRA for their permission to use all the TLS data published in this thesis which is the property of the Crown. I acknowledge the DRA for funding my research and the project under DRA research agreements CSM2/2040/109UA and 2040/509/RAE.

I would like to thank my friends and colleagues in the Department of Physics in particular all my friends within the Detector Physics Group, led by Dr David Ramsden, and especially Dr Ian Jupp and Dr Max Palmer for their ideas on signal processing. Thank you to Graham Chadwick for CPU hardware and software support. Similarly, thank you to my friends and colleagues in the Department of Oceanography in particularly within the Remote Sensing Group, led by Dr Ian Robinson, and especially Dr Christine Gommenginger and Val Taylor.

Thank you to; the members of the Southampton University Canoe Club for fun and adventure, Joe Lo, Helen Dale, Mark Hyde, Dr Andy Neville and Saj Raza for many things including cups of tea, the lads and lasses of 70 Northcote Road, Karen Dawson and Jane Flatman.

Finally, it should be said that I consider myself very fortunate to have made such a large number of friends, not only in the Departments of Physics and of Oceanography, but throughout the University during my years in Southampton.

Chapter 1

Introduction

1.1 Background and Context

The earliest scientific observations of the sea surface were motivated by the impact of waves on coastal regions and the activities of the human race at sea. Consequently, studies were focused on long waves with wavelengths greater than a metre as these present a hazard to shipping and can alter coastlines. Initial studies of larger waves were limited solely to observations but emerged as a science in the last century as detailed studies of their dynamics and generation mechanisms were made. A consequence of these studies was the realisation that small wavelength waves of a few centimetres are generated by the action of wind on the sea surface. As the wind persists these ripples increase in wavelength eventually leading to the larger waves that fuelled the initial desire for a deeper understanding of the sea surface. Studies began to focus on these short scale waves as precursors to swell waves. However, the main interest in the short scale sea surface waves arose after the advent of high frequency radar and in particular Synthetic Aperture Radar, or SAR, in the latter half of this century.

High frequency radio waves generated by the radar system are reflected by the sea surface and used to generate an image of the wave field. From a basic knowledge of electromagnetic theory, it is understood that ocean waves with wavelengths of the order of the electromagnetic radiation scatter the radar signal. For SAR systems these waves are a few centimetres to decimetres in wavelength. It became apparent from SAR imagery that a variety of ocean processes including internal waves, swell waves, natural and man made chemical slicks and bathymetrically modulated tidal flows interact with these short scale sea surface waves. The interactions alter the wave profile in such a manner as to modulate the returned radar signal. These ocean processes have an impact on activities at sea. The monitoring of surface active films may provide an indication of the presence of fisheries and other marine organisms, help predict the impact of oil

slicks and aid any clean-up operations. Swell and internal waves affect surface and sub-surface operations. The interactions of bathymetry-influenced tidal flows on the sea surface may help to provide maps of sub-surface features, aid shipping and dredging and studies of sediment transport.

Imaging radar and in particular satellite-borne SAR systems offer the prospect of studying and monitoring such phenomena on a truly global scale. However, to be of any use, SAR imagery must be able to provide a quantitative measure of the sea surface wave profile. To permit this a detailed understanding not only of the interactions of these ocean processes with the sea surface but also the mechanisms leading to the modulation of the scattered radar signal is required. Consequently, the interest in short scale sea surface waves expanded. Numerical models to explain the interaction processes were developed.

To provide observational data for these studies, in-situ instruments capable of providing a precise measure of the short scale sea surface wave profile are required. To aid studies being pursued within the Department of Oceanography at the University of Southampton an interdepartmental project was initiated with the Department of Physics to design and develop such an instrument. The instrument design was influenced by the need to quantify the models describing the sea surface interactions. It was envisaged that the system would need to be easily deployed, provide a non-destructive measurement of the sea surface and have a wavelength resolution of a centimetre. To meet these design requirements, and with reference to previous instrument designs, it was decided to measure the sea surface wave slope by the detection of a laser beam refracted by the sea surface. Such devices are referred to as Laser Slopemeters. To avoid disturbing the wave field under investigation the Southampton Slopemeter is towed, parallel to a tow vessel, across the sea surface and consequently is referred to as the Towed Laser Slopemeter, or TLS. To determine the wave slope, a measure of the height from the sea surface to the plane in which the laser spot position is determined, is required. Previous slopemeters have either assumed a constant wave height, or have measured wave height some distance from the point of refraction. Both methods introduce an error into the slope measurement. The TLS avoids this problem by using two detection planes to determine beam slope, and therefore the wave slope, without the need to measure wave height. It is hoped that this step will give a more precise measurement of wave slope.

To develop and deploy the Towed Laser Slopemeter external funding was sought. This was provided by the Defence Research Agency, or DRA, under research agreements CSM2/2040/109UA and 2040/509/RAE. The author joined the small inter-disciplinary team, comprising of Dr H. S. Ghataure (PDRA) and C. G-Y. Lee (research student), at the point at which the design concept of the Towed Laser Slopemeter was being implemented. It was envisaged that the author's work would be to analyse the oceanographic data from the TLS and to

apply these data sets to the study of radar backscatter from the sea surface. However, as the project evolved, the focus of the work changed from the application of the data from the TLS, in an effort to further our understanding of sea surface oceanography, to the physical interpretation of the data from the Slopemeter. The reason for this was two fold. Firstly, the towing of the TLS introduces a Doppler shift into the observed wavenumber spectrum and it became apparent that this needed to be investigated before the TLS could be used for oceanographic applications. Secondly, following the analysis of the data from the first trial of the TLS it became apparent that further development of the instrument was required to reduce sources of noise in the signal. However, with no independent alternative measure of sea surface wave slope at these scales there is no simple way of evaluating the TLS performance. It therefore emerged as a challenging task to characterise the TLS record and to verify, or otherwise, that this signal was representative of the sea surface wave slope. These issues form the focus for the work presented in this thesis.

The objectives of this work therefore became:-

- To assess the effect of the Doppler shift on the recorded wavenumber spectrum induced by towing slope measuring instruments.

- To meet the first objective, it became necessary to develop a numerical model for the simulation of the ocean surface over the length scale range measured by the Towed Laser Slopemeter.

- To assess the performance of the slopemeter in relatively sheltered conditions by identifying the components in the data record, distinguishing between system noise, signals relating to the sea surface wave slope and other surface features.

- To determine whether the slopemeter can be considered to give a reliable measure of sea surface roughness variability encountered in the open sea.

In addition, the author provided both mechanical and technical support and played a major role in the development of the instrument. During deployments the author was particularly responsible for recording written logs detailing oceanographic and meteorological conditions. Throughout the course of the project the author provided feedback to the development team, reporting on the results of data analyses and influencing improvements in the design and method of deploying the instrument. The slopemeter was returned to the DRA in November 1996 together with the majority of support instrumentation. Activity on the contract was wound down and work conducted by the author on the North Sea data as part of CSTAR (Coastal and sediment transport assessment using SAR) project was funded under an EC contract from April 1997.

1.2 Thesis Overview

A basic review of the main features of the models developed to account for the interaction of bathymetry-influenced tidal flow, internal waves, swell waves and oil slicks with the sea surface is given in chapter 2. To verify these models in-situ measurements of the sea surface wave profile are required. The sea surface profile is parameterised in terms of wave height and wave slope and this is outlined in chapter 2 together with forms for the short wave scale dispersion relation. Statistical and spectral techniques for the analysis of these observables are presented together with suggested forms for the wavenumber spectrum. The review of the literature is focused on providing the context for understanding the role of the TLS, rather than as a precursor to a detailed application of the data from the TLS to furthering our understanding and knowledge of the sea surface.

A review of previous instrumentation used to measure sea surface wave height, or wave slope, is given in chapter 3. The suitability of the range of approaches for measuring these sea surface parameters is discussed. The advantages and disadvantages of the particular instruments are cited and the case for developing the Towed Laser Slopemeter is made. A detailed outline of all aspects of the Towed Laser Slopemeter is given. This includes the method used to determine the sea surface wave slope, an overview of the instrument's electronic and optic systems, the method of its deployment and proposed methods for analysing the wave slope data.

To investigate the effect of towing the TLS across the sea surface wave profile on the observed wavenumber and wavenumber spectrum a new numerical model was developed. The model was required to generate wave heights and wave slopes at different positions and times. These values could then be used to generate true wavenumber, true wave frequency and more importantly wavenumber spectra as observed by the Slopemeter. The model which uses Fourier transforms to generate the surface wave profile is outlined in chapter 4. The reduction in the number of calculations used in the specially modified form of a Fourier transform decreased the time of execution of the model by a factor of five.

Having tested the new model for numerical precision and for the correct implementation of the oceanographic parameters used as inputs, chapter 5 extends the characterisation of the TLS with an investigation of the effects of towing the Slopemeter across the wave profile. Variations in the wave incidence and vessel speed will lead to differences between the observed and true wavenumber spectra. These changes are investigated in detail. Relationships between the true and observed wavenumber and wavenumber spectra are developed. Methods for estimating the true

wavenumber spectrum from spectra gained whilst a vessel is underway were proposed by Cartwright (1963) and Hughes (1978). These methods are assessed for their suitability in providing a true wavenumber spectrum from the TLS wave slope record. A new approach which avoids the assumptions required by the previous two methods is suggested. The research conducted in chapters 4 and 5 has not only provided a better understanding of the effect of the sampling methodology employed by the TLS on the analysis of the wave profile but also a greater understanding of spectral techniques. Both will be required for the analysis of the TLS record gained during in-situ measurements.

The Towed Laser Slopemeter was first deployed in Loch Linnhe, Scotland in 1994 and the characterisation of the TLS continues in chapter 6 with an analysis of the data from this trial. The motivation for the campaign together with an overview of the trial and the role of the TLS and its crew is given. The focus of the chapter is to verify, or otherwise, that the TLS is capable of measuring the sea surface wave slope and to propose ways of increasing the precision of such measurements. The results from the analysis of the TLS data set are compared against known sea surface wave slope characteristics. The data sets exhibited a wave like profile, the slope distributions were near-Gaussian and the wave spectrum and its power index were in agreement with suggested values. It was concluded that the TLS was capable of giving a measure of the sea surface wave slope. However, a greater than expected level of noise was apparent in this signal, and this is analysed in the thesis. Possible sources are suggested and the investigation led to a substantial review and refit of the optic and electronic systems of the Towed Laser Slopemeter following the trial. The analysis of the Loch Linnhe data concludes with a comparison between the TLS data set and the trial log in relation to its ability to detect surface slicks.

The investigation of the TLS as an instrument for providing a quantitative measure of changes in the sea surface roughness is extended in chapter 7. A detailed comparison between a video and TLS record is made. Both data sets were recorded during the second deployment of the Slopemeter as part of a CSTAR (Coastal and sediment transport assessment using SAR) campaign in the North Sea during April 1996. Corresponding roughness changes can be seen in both the TLS record and video footage. This analysis has enabled the behaviour of the TLS to be fully explored and its unique sampling capabilities to be identified. The conclusions reached in this chapter will provide the foundation for subsequent applications of the data to the study of oceanographic processes occurring at the sea surface. The experience gained over the course of the TLS project and work conducted in this thesis has led to a design for a new Digital Slopemeter, or DSM, being proposed. This is discussed in chapter 8 together with the conclusions following from the research presented in this thesis.

1.3 Statement on Originality of the Research Conducted

Whilst chapters 2 and 3 provide the motivation and the scientific background to the research work presented in this thesis, the original research which forms chapters 4, 5, 6 and 7 is entirely the author's own work. The concept for a new Digital Slopemeter, discussed in chapter 8 and outlined in detail in appendix C, was conducted in collaboration with Dr. D. Ramsden, Dr I.S. Robinson and Mr G. J. Crossingham.

Chapter 2

Sea Surface Roughness; A Scientific Account

2.1 Introduction

The first oceanography studies of sea surface roughness were focused at large wave scales because of their significant impact on man for reasons of marine safety and coastal defences. Interest in shorter waves increased as it became apparent that they were a precursor to swell waves. The advent of radar, especially satellite radar and synthetic aperture radar (SAR), increased the oceanographic interest in small scale waves. Imagery from satellite-borne SAR systems was found to contain surface roughness features generated by ocean processes such as internal waves, bottom topography, surface films and wave modulation. Attention was then focused on small scale waves because SAR radars operate at microwave wavelengths below a metre. From Bragg theory surface waves of a similar scale are responsible for the scattering of electromagnetic waves (Holliday et al (1986)). The natural phenomena apparent in the radar imagery must therefore be perturbing the sea surface at scales less than a metre and hence the importance of measuring at such short length scales.

Observing the ocean surface at short wavelength scales will lead to a better understanding of the marine environment in which man operates. The use of satellite technologies will allow this to be done on a truly global scale at a high repeat rate. The mechanisms responsible for the interaction of ocean surface processes, microwaves and short surface waves are not fully understood and theoretical models (Alpers and Hennings (1984), Vogelzang (1997)) need experimental

verification. This provides the motivation for the design and deployment of instruments capable of providing a measure of sea surface roughness in terms of wave height or wave slope.

If we intend to measure sea surface roughness, it is important to parameterise the surface in terms of observable parameters. These parameters will influence the design of instrumentation required to measure the sea surface profile. Therefore in this chapter, expressions for the wave height and wave slope are given together with suggested forms for the dispersion relation which relates wavenumber and wave frequency. Statistical and spectral tools for the analysis of wave profiles are reviewed and suggestions describing the shape of the wavenumber spectrum presented.

Ocean processes will modulate the sea surface wavenumber spectrum, changing wave height and wave slope and lead to a visible variation in the sea surface roughness. As will be described in later chapters, the Towed Laser Slopemeter was deployed to investigate the modulation of the sea surface wave slope by bottom influenced tidal flow, internal waves, swell waves and surface active films. The need for a greater understanding of these interactions is discussed and models to account for the modulation of the sea surface by these ocean processes are presented. The effect of such ocean processes is to perturb the wave spectrum. Energy exchange will occur as the perturbed spectrum relaxes towards its equilibrium level. This energy exchange is parameterised by a source term and the rate at which the wave spectrum relaxes back to its equilibrium value is referred to as the relaxation rate. Proposed forms for the source term and the relaxation rate are therefore also discussed.

2.2 Basic Sea Surface Characteristics

As the wind blows gently across the water surface waves are formed by the interaction. Referred to as capillary waves, with scales of millimetres to a few centimetres, these propagate short distances before dissipative processes restore the medium to the unperturbed mean sea level. If the wind persists the wave size increases. Capillary-gravity waves with wavelengths of a few centimetres to decimetres in scale, gravity waves with wavelengths of decimetres to metres and long gravity, or swell, waves are formed given sufficient time and wind strength. Gravity waves are restored by the action of gravity assuming there is no further energy input. All these wave scales are responsible for the visible sea surface roughness. Surface waves can be considered to be sinusoidal in form which is the first order, or Stokes approximation, to the hydrodynamic equations describing the surface profile. Referring to the basic theory (Kinsman (1965), Phillips (1958)) wave height, ξ, is given by:

$$\xi = A(k)\cos(\underline{k}.\underline{r} - \omega(k)t) \tag{2.1}$$

and the components of slope $\underline{S}$ are

$$\underline{S} = \frac{d\xi}{d\underline{k}} = -A(k)\underline{k}\sin(\underline{k}.\underline{r} - \omega(k)t) \tag{2.2}$$

where, ω is wave frequency, $\underline{k}$ is wavenumber and *A(k)* is wave amplitude (Kinsman (1965)). The surface wave height and surface wave slope can be described as a superposition of sinusoidal infinitesimal waves of the forms given in equations 2.1 and 2.2 To a first order, measurements made of the long waves agree with this sinusoidal approximation. In the lower limit of the capillary-gravity wave range and the capillary wave range the application of the linear superposition of sinusoidal waves to describe the true ocean surface is uncertain.

The wavenumber and frequency of a wave are related by the dispersion relation. The forms of the dispersion relation for different wave ranges are now presented. A more detailed discussion including their derivation can be found in Phillips (1958) and Kinsman (1965). For deep water waves where the dominant restoring force is gravity, *g*, the dispersion relation is:

$$\omega^2 = gk \tag{2.3}$$

Similarly, at higher frequencies where surface tension is the main force in the restoration of the surface to its mean level, the dispersion relation is of the form;

$$\omega^2 = \frac{\varphi}{\rho}k^3 \tag{2.4}$$

where, φ is the surface tension and ρ is the water density, which for the studies presented in this thesis are taken to be 0.074 Nm^{-1} and 1000 Kgm^{-3} (Robinson (1991)) respectively.

For the capillary-gravity wave range, in which both restoring forces are important, the combined dispersion relation is of the form;

$$\omega^2 = gk + \frac{\varphi}{\rho}k^3 \tag{2.5}$$

and is used throughout this thesis unless otherwise stated. If shallow water is to be considered then equation 2.5 takes the form;

$$\omega^2 = \left(gk + \frac{\varphi}{\rho} k^3 \right) \tanh kh \qquad (2.6)$$

where h is the water depth. This takes account of the way the seabed controls the fluid motion beneath the surface, but the presence of the seabed can be ignored when the depth of the sea is greater than half the surface wavelength.

2.3 Methods for the Analysis of Wave Profiles

To a first order, the sea surface can be composed of a continuous summation of sinusoidal waves with a near random distribution. This randomness limits the information that can be gained from a single wave profile. Instead, general properties of the sea surface are determined over a number of such wave profiles. To aid the characterisation of the sea surface, statistical and spectral techniques are used to analyse the wave profile.

2.3.1 Statistical Techniques

It is apparent that in the ocean waves vary irregularly in both space and time. Statistical techniques are commonly used to analyse oceanographic data sets. Such tools will smooth out the randomness and enhance the underlying trends. The probability density function, or PDF, is a simple descriptor of the wave profile. Samples of height, or slope, can be grouped as a function of their size providing a distribution of probability, or frequency of occurrence. The distribution of wave height and each component of wave slope are considered to be approximately Gaussian with the greatest number of values at the mean. The distribution decreases about this with increasing height, or slope component, magnitude. The mean, or first order moment of the PDF, together with higher order moments of variance, skewness and kurtosis give a statistical description of the surface profile. The total slope has a radial distribution given by the angular integration of a two dimensional Gaussian distribution.

The statistics of the profile will be dominated by slowly varying surface waves on which faster variations will be present. These large waves are not central to this study but provide a useful means of describing prevailing surface conditions and can be removed through filtering of the

data. The mean of wave height and slope should be constant over large data sets and consequently wave height and wave slope are referenced to a zero mean. The variance, or mean square, and the standard deviation, or root mean square, are second order moments and are the principal descriptors of the sea state giving a direct measure of roughness. The variance is equivalent to the width of the PDF at $e^{-0.5}$ of the height. The rougher the surface the greater number of waves with a particular value of wave height, or slope. This gives an increase in the variance and a broader PDF. The reverse is true for smooth surfaces. The skewness, or third moment, characterises the degree of asymmetry of the PDF about the mean, a positive value of skewness indicating that the tail of the PDF will extend to higher positive values of wave height and slope. The reverse is true for negative skewness. The fourth moment, or kurtosis, is an indicator of the peakedness, or flatness, of the PDF relative to a Gaussian distribution.

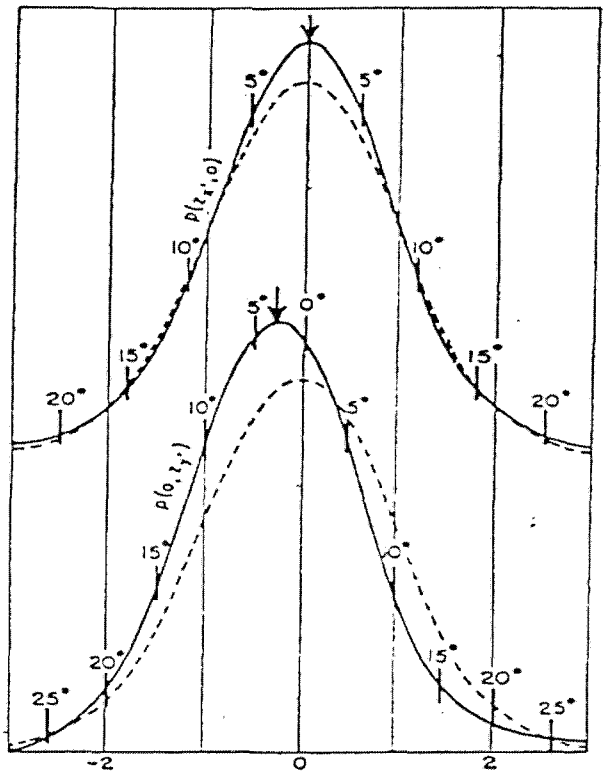

Figure 2.1 Cox and Munk's (1954) PDFs of surface slope for cross-wind (upper curve) and downwind (lower curve). The solid curves are the observed distribution and the dashed curves are Gaussian distributions with the same variance. The vertical lines show the scale for standardised slope components.

A comprehensive application of the above statistical descriptors was applied to the analysis of sea surface slopes by Cox and Munk (1954). The PDF was approximately Gaussian, but had a higher peak and greater extreme values than a Gaussian distribution with the same variance. The PDF was skewed, the most probable slope being in a positive downwind direction (see figure 2.1). The skewness increased with wind speed. Kinsman (1965) presumed that the skewness was associated with a distortion of the sea surface by the wind field being characteristic of incipient and actual breaking waves. The variance of slope increased linearly with wind speed. The variance indicated

a broad directional wave field with cross-wind variance being at least half that of along-wind variance. A peakedness, barely above the limit of observational error, indicated that the probability of very large slopes and very small slopes was greater than the equivalent for a Gaussian surface. Cox and Munk also measured the surface slope distribution for surfaces perturbed by oil slicks. Slope variances were reduced by a factor two to three times that of an unaffected surface, the skewness was eliminated and peakedness remained unchanged. Kinsman (1965) suggested that this value of mean square slope can be attributed to the portion of the mean squared slope associated with long waves in the case of a clean surface at the same wind speed. The study conducted by Cox and Munk remains to this day the authoritative guide to sea surface slope statistics, although it was based on data collected by sun glitter measurements which are restricted by their inability to provide a near continuous record of the ocean surface. This and other techniques for providing in situ measurements of the ocean surface are discussed in more detail in the next chapter.

Statistical techniques can be applied to data sets in order to quantify variations in roughness and indeed infer information on the wave shape and gain an idea of the predominant direction of travel. However, this method of analysis does not offer information on the energy associated with a particular wavenumber, or wave frequency, and consequently falls short of giving a complete picture of the surface profile. An account of spectral approaches which will enable wave energies to be determined is now given.

2.3.2 Spectral Analysis

The statistical description of the sea surface provides quantitative information on the occurrence of certain slopes and heights and can be used to infer a form of the wave profile. Going beyond this basic statistical description, the surface can be described in terms of its component sinusoidal waves with an application of the Fourier transform. The Fourier transform of the covariance of wave height $Z(\underline{x},\underline{r};\tau,t)$ gives the power spectrum, (Phillips (1958));

$$F(\underline{k},\omega) = (2\pi)^{-3} \iint Z(\underline{x},\underline{r};\tau,t) e^{-i(\underline{k}.\underline{r}-\omega t)} d\underline{r}dt \tag{2.7}$$

where,

$$Z(\underline{x},\underline{r};\tau,t) = \langle \xi(\underline{x},t)\xi(\underline{x}+\underline{r},\tau+t) \rangle \tag{2.8}$$

where <> donates the covaraince.

and wave height is taken at two points separated in space by $\underline{r}$ and in time by τ. The power spectrum $F(\underline{k},\omega)$ is equal to the square of the amplitude, or intensity, of the wave at a particular wavenumber, k and frequency, ω. Similarly, the slope spectrum can be obtained by Fourier transforming the slope covariance:

$$Y(\underline{x},\underline{r};\tau,t) = \langle S(\underline{x},t)S(\underline{x}+\underline{r},\tau+t)\rangle \tag{2.9}$$

The wavenumber spectrum in the y-direction $G_{yy}(\underline{k},\omega)$ is given by:

$$G_{yy}(\underline{k},\omega) = (2\pi)^{-3}\iint < \frac{\partial\xi(\underline{x},t)}{\partial y}\frac{\partial\xi(\underline{x}+\underline{r},t+\tau)}{\partial y} > e^{-i(\underline{k}.\underline{r}+\omega t)}d\underline{r}dt \tag{2.10}$$

and as $\dfrac{\partial\xi(\underline{x},t)}{\partial y} = k_y\xi(\underline{x},t)$ then

$$G_{yy}(\underline{k},\omega) = k_y{}^2F(\underline{k},\omega) \tag{2.11}$$

and similarly for $G_{xx}(\underline{k},\omega)$. Following from this the total slope wavenumber spectrum is given by;

$$G(\underline{k},\omega) = G_{xx}(\underline{k},\omega) + G_{yy}(\underline{k},\omega) = k^2F(\underline{k},\omega) \tag{2.12}$$

and is equivalent to the multiplication of the wave height spectrum by a k^2 term. This multiplicand implies a greater sensitivity of slope at high wavenumbers and presents a practical advantage for the measurement of wave slope instead of wave height.

The calculation of the above power spectrum requires the surface to be measured instantaneously in both spatial dimensions and temporally. This is impractical from an instrumentation point of view. Significant information can be calculated from a limited data set and measurements of the surface can be made either spatially i.e. time fixed giving a spatial covariance and hence wavenumber power spectrum, or temporally i.e. at a single point giving temporal covariance and a frequency power spectrum. Given enough data storage it is possible to build a temporal picture by taking a set of spatial realisations at different intervals. It is possible to extend the transformation of data to higher order moments, a skewness spectrum can be obtained by the calculation of a third order covariance using (Phillips (1958)):

$$X(\underline{x},\underline{r};\tau,t) = \langle \xi^2(\underline{x},t)\xi(\underline{x}+\underline{r},\tau+t)\rangle \tag{2.13}$$

The power spectrum $F(\underline{k}, \omega)$ and its purely wavenumber and purely frequency equivalents are of great importance as an aid to characterising the wave field and understanding the hydrodynamics at play. Most of the energy of sea surface waves is in long wavelength waves about a peak frequency and wavenumber, both of which are generally lower at high wind speeds and high fetches. At high frequencies and wavenumbers there is evidence that most wave spectra obtained both through laboratory and in-situ measurements show a degree of similarity. It should be of no surprise that there has been a great deal of effort to find a theoretical underpinning to this similarity and to characterise both the shape and amplitude of the wave spectra in a variety of surface conditions.

One of the earliest and most respected theories of this kind was advanced by Phillips (1958) which supposes the similarity arises from the saturation of waves in a given wavenumber range. This implies that amplitudes of the waves are such that if the energy at a given wavenumber were increased the waves with this wavenumber would break, dissipating the energy acquired and returning the spectrum to equilibrium. A dimensional argument is used to propose an equilibrium spectrum of the form;

$$F(k) = \beta k^{-4} \tag{2.14}$$

where β is a constant.

This early theory of Phillips' was very successful, but does not explain the wind dependence of surface roughness, or accurately give an estimate of the slope of many wave spectra. This led to new theories for the form of the wave spectrum. Phillips (1985) proposed a new spectral formulation which investigated the possibility of a local equilibrium between wind input, non linear wave-wave interactions and dissipation including wave breaking, of the form;

$$F(k,\theta_w) = \beta \cos^{\nu} \theta_w u_* g^{-\frac{1}{2}} k^{-\frac{7}{2}} \tag{2.15}$$

where ν is the beam width, or spreading parameter, u_* is the wind frictional velocity, g is gravity at the earth's surface and θ_w is the direction of wave propagation relative to the wind. The $cos^{\nu}\theta$ introduces directionality into the power spectrum and u_* introduces wind dependence.

Although in-situ measurements have been made, disagreement concerning the exact shape of the wave spectrum remains. This is especially true at high wavenumbers where the modulation of the

sea surface wave profile by a variety of ocean processes occurs. These ocean processes act to change the wavenumber spectrum, leading to a change in the surface wave height and wave slope. A basic understanding of these ocean processes and the method by which they are believed to interact with the sea surface influenced the design of the Towed Laser Slopemeter. Ocean going trials involving the TLS were motivated by the need to investigate the effects of bathymetry influenced tidal flow, internal waves, surface active films and swell waves on the sea surface wave profile.

2.4 Ocean Processes

2.4.1 Effects of Bottom Topography

The study of the distribution and the dynamic behaviour of shallow water seabed features and sediment transport is of vital importance to the construction of effective coastal defences, to the safe operation of shipping traffic in shallow seas and to the understanding of the eco-system in these regions. Currently, information on the behaviour of bottom topographies such as sand waves and sand banks is collected from echo sounder measurements. Such features have been successfully imaged with SAR radar which as a consequence might be used to routinely observe the seabed profile. To correctly interpret bottom topographic signatures in radar data sets, not only will a deeper understanding of the mechanisms involved in the backscatter of microwaves from the ocean surface be required, but theories to explain the tidal current-seabed feature interaction and the hydrodynamic modulation of the wind-wave field by this current will be needed. The development of these theories is currently hampered by the lack of knowledge of the underlying physical processes although steps have been taken to rectify this (Hennings et al (1994)). Hence we offer a short synopsis of the main components of recent models developed to explain the interactions of seabed features and tidal currents and the resulting hydrodynamic modulation of the wind-wave field.

2.4.1.1 Interactions between Bottom Topography - Tidal Currents

Alpers and Hennings (1984) assumed that the current flow above the bathymetry was laminar, free of any vertical current gradients, only weakly time dependant and that the tidal velocity component U_x parallel to the sand wave obeyed the continuity equation:

$$U_x(x)d(x) = const = c \tag{2.16}$$

where *d(x)* is the depth parallel to the sand waves, or perpendicular to their crests, and *const* refers to a constant value, *c*. The tidal velocity component U_y perpendicular to the sand waves, or parallel to their crests, is assumed constant

$$U_y = const \tag{2.17}$$

Venn and D'Olier (1983) found these two equations acceptable as a first order approximation to the tidal current flows across the South Falls sand bank in the Southern Bight of the North Sea. Deviations from these relationships were noted although a more refined theory was not presented.

The next step is to develop a model for the hydrodynamic modulation of the wind wave field by the surface current.

2.4.1.2 Wave-Current Interactions

The interaction between surface wind waves and the surface current can be described by weak hydrodynamic theory. As the motivation behind such studies is to relate observed ocean phenomena to radar imagery the surface waves of interest are of the Bragg wavelength scale occurring at wavelength bands in both the decimetre and the centimetre range. The current variation is assumed to vary slowly spatially and temporally when compared to the space time scales of these small gravity and capillary-gravity waves on which it acts. The radiation balance equation is used to describe the variation in action spectral density (Longuet-Higgins and Stewart (1964), Keller and Wright (1975), Alpers and Hasselmann (1978) and Alpers and Hennings (1984));

$$\frac{dN(\underline{k},\underline{x},t)}{dt} = \left(\frac{\partial}{\partial t} + \frac{d\underline{x}}{dt}\frac{\partial}{\partial \underline{x}} + \frac{d\underline{k}}{dt}\frac{\partial}{\partial \underline{k}}\right) N(\underline{k},\underline{x},t) = Q(\underline{k},\underline{x},t) \tag{2.18}$$

where $N(\underline{k},\underline{x},t)$ is the action spectral density of the wave packet, $Q(\underline{k},\underline{x},t)$ is a source function which models the effect of wind input, non-linear energy transfer between wavenumbers and dissipation process such as wave breaking on the spectrum. The spatial position and wavenumber of the wave packet are given by $\underline{x}$ and $\underline{k}$ respectively. The relationship between the action spectrum $N(\underline{k},\underline{x},t)$, the energy spectrum $E(\underline{k},\underline{x},t)$, and the wave height spectrum $F(\underline{k},\underline{x},t)$ is given by:

$$N(\underline{k},\underline{x},t) = \frac{E(\underline{k},\underline{x},t)}{\omega_0(k)} = F(\underline{k},\underline{x},t)\frac{\rho\omega_0(k)}{k} \tag{2.19}$$

Spatial variations in the action spectrum need to be determined if the radar return is to be modelled. These are given by the integration of equation 2.18 along the paths given by the ray equations;

$$\frac{d\underline{x}}{dt} = \frac{\partial\omega}{\partial\underline{k}} = \underline{c}_g(\underline{k}) + \underline{U}(\underline{x}) \tag{2.20}$$

$$\frac{d\underline{k}}{dt} = -\frac{\partial\omega}{\partial\underline{x}} = -\left(\underline{k}\frac{\partial}{\partial\underline{x}}\right)\underline{U}(\underline{x}) \tag{2.21}$$

along which the waves propagate in phase space and couple spatial and wavenumber variations to conserve apparent frequency ω;

$$\omega = \omega_0 + \underline{k}.\underline{U}(\underline{x}) \tag{2.22}$$

$\underline{c}_g=\partial\omega_0/\partial\underline{k}$ denotes the group velocity of the wave packet. The intrinsic frequency, ω_o, is defined with respect to a stationary co-ordinate system.

The action spectrum N will be modulated by tidal current interactions and will formalise the effects of tidal flow on the wind wave field. It is provided by a solution to the radiation balance equation. Alpers and Hennings (1984) assumed that the change in action $\delta N(\underline{k},\underline{x},t)$ from the non perturbed equilibrium value $N_o(\underline{k})$ was small such that:

$$N(\underline{k},\underline{x},t) = N_o(\underline{k}) + \delta N(\underline{k},\underline{x},t) \tag{2.23}$$

$N_o(\underline{k})$ is known from an assumption on the form of the wavenumber spectrum and $\delta N(\underline{k},\underline{x},t)$ can be gained analytically which was found by Alpers and Hennings (1984) to be:

$$\delta N(\underline{x},k_x) = -\frac{4+\gamma}{\mu}N_o(k_x)\frac{dU_x(\underline{x})}{dx} \tag{2.24}$$

where k_x and U_x are the wavenumber and current flow in the x direction, respectively. The ratio of group to phase velocity is γ and μ is the relaxation rate. The steps between equation 2.18 and equation 2.24 are given explicitly by Alpers and Hennings (1984). Before spatial variations in the

action spectrum can be determined a form for $Q(\underline{k},\underline{x},t)$, the source term, has to be gained. The form of the source term, $Q(N)$, which is dependent on the action density is not well known and is formulated from theoretical considerations. It is discussed further in section 2.4.5.

To date the majority of experimental data pertaining to surface features has been gained from remotely sensed data sets (Alpers and Hennings (1984), Alpers and Hasselman (1978) and Shuchman et al (1985)). Alpers and Hennings (1984) combining the models of bathymetry-current interaction and hydrodynamic modulation of Bragg waves related their model with SAR imagery and found it to be capable of explaining basic features within the radar data sets. The model is incapable of being fully tested against radar measurements when the precise nature of the radar backscatter is not known. Steps have recently been taken to provide in-situ data sets using wire probes (Hennings et al (1994)). The experiment described in chapter 7 seeks to add to such observations although it is not within the scope of this thesis to contribute to them. However the purpose of this thesis is to evaluate the role which the slopemeter can play in the observation of such phenomena.

2.4.2 Internal Waves

Internal waves propagate along horizontal and near horizontal boundaries marking a sudden vertical change in ocean density and are normally formed as the result of fluctuations in pressure about this stratification. They are important mechanisms for the transportation of energy and can have an associated mass flux. If the wave breaks, vertical mixing will be induced. Moreover, the strong currents symptomatic of internal waves can cause problems for shipping and offshore drilling operations. The current near the surface induced by the presence of the internal wave modulates the surface wind-wave field. Two mechanisms have been proposed to explain this change in the surface spectrum. The first is the hydrodynamic interaction between the surface currents and the wave field and the second is a result of the redistribution of surfactants by these currents.

The hydrodynamic interaction is explained with reference to figure 2.2. The surface current is convergent above the descending part of the wave leading to a concentration of wind waves, or a rip, and an associated increase in surface wave energy. Corresponding to the rising column of water associated with the internal wave, the divergent surface current leads to a dilution of surface waves and wave energy forming a visible slick on the surface. For a convergent surface current field:

$$\frac{\partial U}{\partial x} < 0 \tag{2.25}$$

For a divergent surface current field;

$$\frac{\partial U}{\partial x} > 0 \tag{2.26}$$

where U is the surface current velocity and x a measure of distance in the same direction. The position of these surface features relative to the internal wave, as for bottom topography, will depend on the direction, energy and relaxation rates of the surface waves being affected.

A second method involving the redistribution of surfactants through the action of the surface current has been proposed (Scott, 1979 and 1986). A high concentration of surfactant material gathers in regions of convergence, the associated increase in surface tension leads to the destruction of capillary waves present in that area and a smoother rather than rougher surface results in the convergent zones. The first method is likely to be the dominant mechanism for surface modulation due to the presence of internal waves (Watson (1989)).

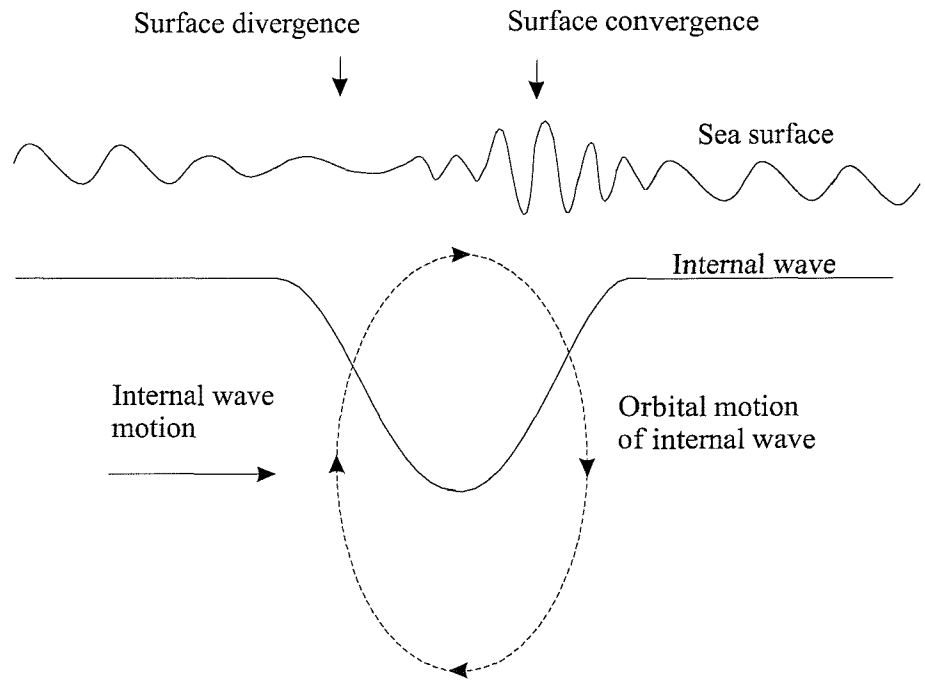

Figure 2.2 Internal wave modulation of the wind wave field

The hydrodynamic process responsible for the interaction of the surface current is similar to that presented in section 2.4.1.2. Hughes (1978) applied this specifically to the case of internal wave interaction. In-situ measurements of internal-wave surface-wave interactions have been made by Hughes and Grant (1978) using a laser slopemeter gauge fixed to the bow of a research vessel. The motivation for the deployment of the TLS in Loch Linnhe, Scotland in 1994 was to investigate such interactions. Detailed work has been conducted in relating the presence of internal waves to SAR and other radar imagery (Apel and Gonzalez (1983) and Watson (1989)).

2.4.3 Modulation of Short Waves by Swell Waves

There is evidence from radar imagery that swell waves modulate short surface waves leading to high backscatter near crests and a corresponding reduction of ripples at the troughs (Robinson (1991)). Referring to figure 2.3, the mechanism is similar to that of internal waves; a divergent surface at the descending orbital motion leading to a reduction in short wave concentration and a convergent surface arising from a upward orbital motion leading to a higher short surface wave concentration.

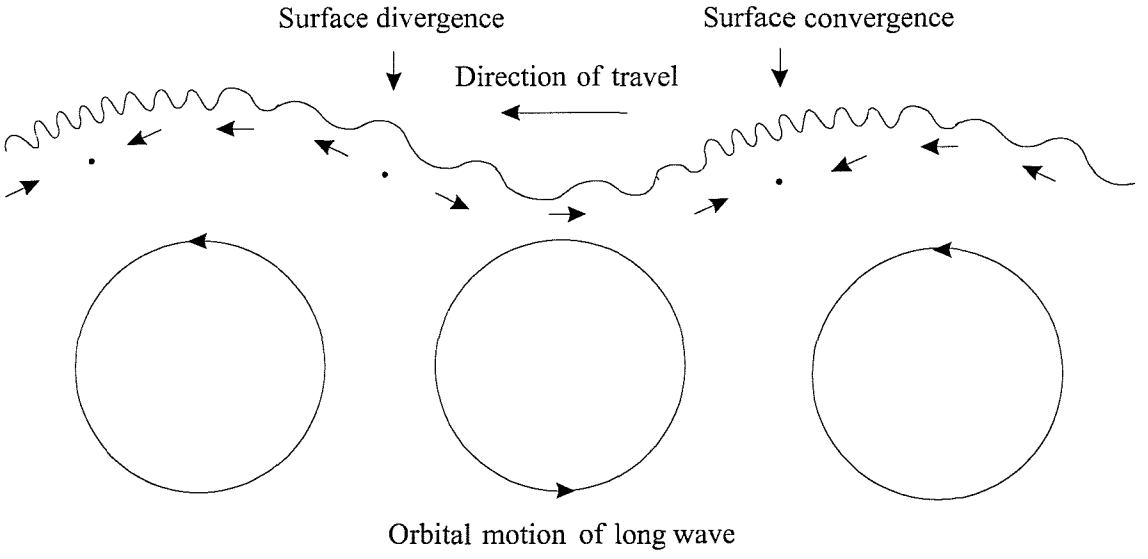

Figure 2.3 Long wave modulation of the wind wave field

The long surface wave current is assumed to be of the form (Keller and Wright (1975));

$$U = U_o e^{i(\underline{K}.\underline{r}-\Omega t)} \tag{2.27}$$

where $\underline{K}$, Ω and U_o are respectively the wavenumber, frequency and magnitude of the current of large wave. Keller and Wright (1975) presented a theory for the interaction of this current with short surface waves. The Longuet-Higgins and Stewart (1964) radiation transfer function is transformed to the frame of the long wave and the short spectra expanded as a perturbation series. The theory applies to low magnitude wave heights, and as for internal waves and bottom topographic effects, to weak interactions with short decimetre rather than capillary waves.

In-situ observations have been made by Evans and Shemdin(1980) using a laser slopemeter probe on a wave rider to image short scale waves and a pressure sounder to measure the long wave profile. They found that the position of the short waves on the long waves was in agreement with that found from radar imagery. Evans and Shemdin used a laser probe similar to that developed by Tober et al (1973).

2.4.4 Effect of Surfactants on the Sea Surface

The term surfactants covers a wide range of organic materials present on the ocean's surface that can lead to a change in surface roughness. Surfactants, or surface active agents, are molecules having either a hydrophobic or hydrophilic chemical property. Sources of these agents are marine organisms, terrestrial sources supplied to the ocean through water run off, atmospheric transport and oil seeps and spills. Interest in surfactants has grown from their role in modulating the surface roughness, generated by wind stress, wave-current interaction and internal waves. These produce areas of local convergence that favour the presence of more hydrophilic species producing a band of hydrophobic species at the boundary to this zone (Bock and Frew (1993)).

The currently accepted mechanism presumes that the presence of the surfactant leads to small changes in surface tension in response to changes in surface area, caused by convergence and divergence as capillary and capillary gravity waves propagate through the local surface. This affects the dispersion relation and hydrodynamic boundary conditions. Bock and Frew (1993) conducted field experiments in the presence of surface active agents using a laser slopemeter. They found that in regions in which surface convergence was absent damping was enhanced over a broad range of surface wave frequencies. This was consistent with the presence of hydrophobic species, and in the presence of convergent zones, damping enhancements were consistent with the presence of hydrophilic species.

2.4.5 The Source Term and the Relaxation Rate

Ocean processes which lead to observed changes in sea surface roughness perturb the wavenumber spectrum. Energy exchange arising from wind input, non-linear energy transfer between wavenumbers and dissipation processes such as wave breaking will act on the spectrum. This is modelled by the source term. The source term Q will tend to relax the shape of the spectrum to that associated with equilibrium. The rate at which the perturbed spectrum relaxes back to its equilibrium value is parameterised by the relaxation rate. If Q is large, there is a strong trend for current induced changes in the action spectrum to tend back to equilibrium. Weak hydrodynamic theory assumes that the action spectrum for a perturbed region of the sea surface remains close to its equilibrium value. Provided this assumption holds, $Q(N)$ is expanded as a Taylor series around $N=N_o$ and the order to which this expansion is taken leads to a number of forms for the source term.

The simplest source function is the linear one which was used, for example, by Alpers and Hasselmann (1978) and by Alpers and Hennings (1984):

$$Q(N) = -\mu \partial N_0 \qquad \text{or} \qquad Q(\mathrm{N}) = -\mu(N - N_0) \tag{2.28}$$

where, μ is the relaxation rate and its inverse is the relaxation time, τ_r the time that the surface takes to respond to current variations and can be determined experimentally. Hughes (1978) and Shuchman et al (1985) have used a form which included terms to the second order. Relative to the first order solution above this is stronger for positive deviations from equilibrium and is given by:

$$Q(\mathrm{N}) = -\mu\left((N - N_0) + \frac{(N - N_0)^2}{N_0}\right) = \mu N\left(1 - \frac{N}{N_0}\right) \tag{2.29}$$

Caponi et al (1988) and Trulsen et al (1990) considered cubic terms in the action spectrum:

$$Q(\mathrm{N}) = \frac{\mu N}{2}\left(1 - \frac{N^2}{N_0{}^2}\right) \tag{2.30}$$

The relaxation rate, as for the source term, is not well known. It is a crucial parameter determining the time of the perturbed action spectrum to relax back to its equilibrium value. A number of suggestions for its formalization have been made and were based on theoretical considerations and

experimental data. Alpers and Hennings (1984) considered μ to be an adjustable parameter. Hughes (1978) derived a form for the relaxation rate from experimental data;

$$\mu = \frac{\omega(k)u_*}{c_p}\left(0.01+0.016\frac{u_*}{c_p}\right)\left\{1-\exp\left[-8.9\left(\frac{u_*}{c_p}-0.03\right)^{\frac{1}{2}}\right]\right\} \tag{2.31}$$

where c_p is the phase speed of the waves. Hsiao and Shemdin (1983) derive a parameterisation for μ again by fitting to experimental data;

$$\mu = 0.0003\sqrt{gk}\left(0.85\frac{W}{c_p}-1\right)^2 \tag{2.32}$$

where W is the wind speed at 10m above mean sea level. Plant and Wright (1977) based their formalization of the relaxation rate on laboratory measurements and theoretical considerations:

$$\mu = 0.04\omega(k)\left(\frac{u_*}{c_p}\right)^2 \tag{2.33}$$

The one dimensional relaxation rates given above can be extended into two dimensions by allowing $\mu=\mu_r$, where μ_r is the radial form of the relaxation rate, and developing a form for the angular part of the relaxation rate μ_a. Little is known about μ_a. Plant (1982) suggested;

$$\mu_a = \left|\cos\theta_w\right| \tag{2.34}$$

where θ_w is the angle between the wind and the wave direction. Lyzenga (1991) proposed:

$$\mu_a = \left|\cos^2\frac{\theta_w}{2}\right| \tag{2.35}$$

The wind speed can be expressed in terms of the wind frictional velocity;

$$\underline{W}(l) = \frac{\underline{u}}{\kappa}\ln\left(\frac{l}{l_o}\right) \tag{2.36}$$

where $\kappa \approx 0.4$ is von Karman's constant, l is the height at which the wind speed was measured and l_o the roughness length parameterised by Charnock (1955):

$$l_o = \frac{0.0144}{g} u_*^2 \tag{2.37}$$

It is apparent from the last two sections that a number of forms for the source term and the relaxation rate exist, limiting the confidence of the application of these parameters to the modelling of sea surface modulation. The characterisation of the source term Q and the relaxation rate μ form important tasks for in situ measurements which will help test the above theories.

2.5 Discussion

The study of the ocean surface processes discussed so far in this chapter and their interaction with radar forms the context in which the Towed Laser Slopemeter was developed and is to be used. Radar waves are scattered by the sea surface. SAR imagery has provided evidence of the modulation of the sea surface by a variety of ocean processes. The limits of our knowledge of these processes and the mechanisms of radar scatter from the sea surface restrict us to a qualitative analysis of SAR imagery. However, it is established from Bragg theory that these processes are occurring at high wavenumbers.

Before SAR imagery can be routinely used for the quantitative monitoring of ocean processes our understanding of mechanisms of radar interaction with the sea surface and the modulation of the sea surface wave profile by these ocean processes must be extended. In-situ measurements of the sea surface are required to eliminate the uncertainty associated with radar backscatter and to permit the study of the effects of a particular ocean process in great detail. The mathematical characterisation of the sea surface provides two observables, wave height and wave slope, which permit the definition of the sea surface through in-situ measurements. The most interesting interactions between the sea surface wave profile and the ocean processes occur at small wavelengths between millimetres and metres. Such short wavelength waves are easily perturbed if the surface is physically disturbed. This restricts the method of measuring wave heights, or wave slopes, at such scales to instruments which do not perturb the surface under study.

Chapter 3

Review of Previous Surface Measuring Instrumentation and the Towed Laser Slopemeter

3.1 Introduction

We have already noted that the variety of ocean processes identified in radar imagery has led to an increase of scientific interest in short wavelength sea surface waves and the development of theories for the modulation of short surface waves. Parameters within these theories need quantifying but little is known about roughness profiles and wavenumber spectra at the short gravity, gravity-capillary and capillary wave ranges. The range of wave frequencies over which such wave modulating interactions occur needs to be established. The requirement for in-situ data and as a consequence the need to design and deploy instrumentation capable of providing such information is strong.

A critical review of in-situ instrumentation which might be capable of measuring short scale surface roughness is now given. The systems to be described can be divided into two groups; mechanical and optical. Mechanical systems include pressure gauges, accelerometers and wire probes and these normally only sample the time series at a single point. Optical techniques can be divided into two categories; which rely either on the reflection or the refraction of light at the surface boundary. Reflective systems include measurements of sun glitter, and Stilwell and stereo photography giving spatial coverage. Refractive techniques use either non laser, or laser, light sources. Laser slopemeters which can measure wave profiles as a time series at a fixed point or along a transect of the sea surface, are outlined before a review of scanning laser slopemeters. Scanning laser slopemeters measure wave profiles over a given area extending single point measurements. This leads into a systems review of the Southampton Towed Laser Slopemeter

which describes the theoretical principles, systems design and deployment methodology. The ability to interpret and successfully apply data resulting from deployments of the Towed Laser Slopemeter is the focus for this thesis.

3.2 Mechanical and Electrical Measurements of the Water Surface

Accelerometers, pressure gauges and wire probes which include resistance, capacitance and resistance-capacitance hybrid probes are all examples of how mechanical and electrical devices can be used to give information on the surface profile. Data is gained through the interaction of the device with the water surface at a fixed point.

3.2.1 Accelerometers and Pressure Gauges

Traditionally accelerometers and pressure gauges have been used for the analysis of gravity waves, of lengths greater than a few metres, and are not sensitive enough for the wavelengths discussed above. However, they are included for completeness. To measure surface waves accelerometers need to be deployed on a floating platform capable of riding the waves of interest. Tucker (1952) deployed an accelerometer on board a research vessel to measure the period of long waves responsible for ship heave. Ship motions are not responsive to high frequency, short wavelength waves and these disturbances must be measured in additional ways.

The addition of another two accelerometers will enable the device to analyse pitch and roll, as well as heave. This was demonstrated by Longuet-Higgins et al (1963), who deployed a set of accelerometers in a wave riding buoy. Such observations were used to find the mean direction and angular spread of the wave energy, and to give an indication of the wave energy for varying wind speeds. The accuracy of the latter is reduced by the inertia and float size as well as frictional effects. The output signal from each accelerometer is integrated twice to give a value equivalent to wave displacement. Floats lend themselves to studies of swell and gravity waves. Surface displacements with a period greater than twenty five seconds cannot be accurately measured and such probes do not respond to very high frequency, short wavelength waves.

A second method suggested by Tucker (1956) which would allow the measurement of shorter wavelengths, was the use of a pressure gauge attached to the side of the ship beneath the sea surface. Pressure gauges work by sensing pressure fluctuations which result from changing wave height. There is a pressure perturbation associated with the wave. This change in pressure extends

to a depth with a length scale comparable to half the wavelength. Swell waves produce changes in pressure which can be sensed several metres below the sea surface. Typically the higher the frequency of the wave the shallower the pressure change and the closer the detector has to be to the surface. To enable sensible readings to be taken, the detector must be kept beneath the surface at all times and the ship must remain stationary. Waves with a period greater than several seconds can be observed in this manner. Shorter periods increase the probability of uncovering the detector and producing erroneous results. To correct for ship roll and the reflection of waves off the hull, two sets of sensors, a pressure gauge and an accelerometer were placed on opposite sides of the vessel and the mean wave displacement taken.

3.2.2 Wire Probes

Two classes of wire probe exist; resistance and capacitance probes. A sketch of three types of wire probes is given in figure 3.1. Resistance wire probes shown in figure 3.1 (a) consist of a length of conducting, typically tungsten, wire which is held taught within a frame work and is partly submerged within the water. A current is applied to the wire, changes in water height will produce a change in the resistance of the wire and hence a varying current. To avoid electrolysis of the wire, an oscillating current rather than a constant DC current must be applied. A further drawback is that the device is dependant on the conductive properties of water which can vary with temperature and salinity, and lead to possible spurious results in the wave height measured.

The second type sketched in figure 3.1 (b) works as a capacitor formed by surrounding a central wire in a dielectric, the wire forms one of the electrodes and the second is provided by the surrounding water. The water height determines the length of the capacitor and hence the capacitance of this instrument will be proportional to the water height. The dielectric must be uniform throughout its length and chemically stable in, and impervious to, the surrounding water. Generally, capacitance probes are thicker than their resistance counterparts and as a result have a poorer wavelength resolution. Lobemeier, (1981) developed a hybrid version of the two systems given in figure 3.1 (c). The fully immersed end of a resistance probe was connected to a conducting plate via a portion of dielectric. The impedance of the system is calibrated for different wave heights. This has the advantage of being insensitive to variations in water salinity and temperature whilst retaining the resolution attained using resistance probes.

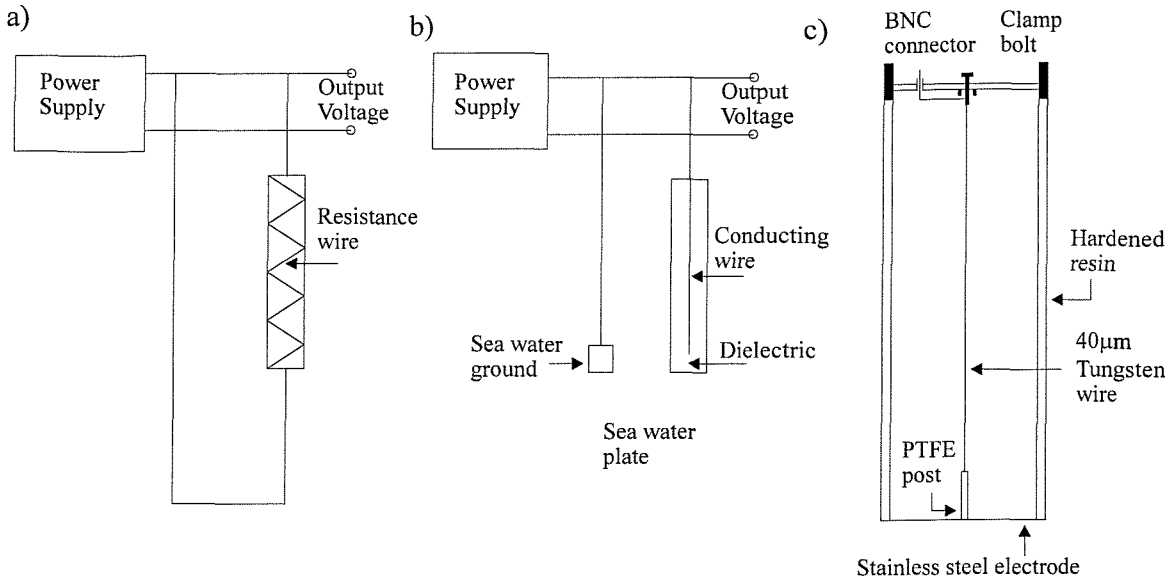

Figure 3.1 Schematics of a) a resistance wire probe b) a capacitance wire probe and c) a resistance-capacitance hybrid wire probe.

The output signal can be corrupted if the wire probe is excessively wetted by spray or splashing. Additional problems may arise through the distortion of the sea surface through interference of the surrounding probe structure and the formation of a meniscus about the wire. These distortions can lead to an error in the measurement of small wavelength wave profiles. The latter has been corrected empirically by Liu (1982) who compared the wire output with that of a laser. Liu used a resistance wire probe with a diameter of 0.13mm to measure waves with frequencies up to 7Hz.

Wire probes can be deployed in a fixed position which requires shallow water and a well defined range of wave heights to prevent waves of large amplitude either completely submerging, or uncovering, the probes. Short wavelength waves in large seas can be analysed by the deployment of wire probes on wave riders and wave buoys. An idea of wave direction and hence a directionality within the wave spectra may be gained by using an array of wire probes. In such a configuration, the problems above are further complicated and probe spacing will restrict measurements to waves of comparable wavelengths (Panicker (1975)). Stolte (1994) used three resistance wire probes, each with a diameter of 0.35 mm, on a wave buoy to provide information on the directionality of the sea surface. Wave frequencies up to 8 Hz were measured. This wave buoy was also deployed during the 1996 CSTAR trial.

The instrumentation outlined in this section are examples of mechanical devices. Their main disadvantage is that they interact with the surface they measure, perturbing the wave field and corrupting the data. This limits the frequency resolution of these devices. The surface is sampled as a time series and can be used to generate frequency information. Spatial coverage can be gained by the deployment of a number of such instruments over an area. The coverage is incomplete and

such methods impractical. The main advantage of these system is that the technology behind such devices is uncomplicated, readily available and relatively cheap

3.3 Optical Measurements of the Water Surface

Optical techniques are well suited to providing spatial information on sea surface roughness. A review of optical instrumentation is now given. We start with reflection methods which include stereo and Stilwell photography and sun glitter measurements. An account of the working principles of these systems together with their main advantages and disadvantages is presented.

3.3.1 Sun Glitter Measurements

The use of sun glitter is perhaps the simplest method of measuring the physical properties of the sea surface. Sun glitter arises from the specular reflection of the sun's rays towards an observer. Only certain wave tilts will render the observer with an image, the information gathered being dependant on the viewing angle and position of the light source. The method has been used by Hulbert (1934) and most extensively by Cox and Munk (1954) to interpret photographs of sun glitter on the ocean surface. Cox and Munk photographed the areas of interest and made a comprehensive statistical analysis of the ocean's surface for a range of differing wind speeds and wind directions. The effect of oil on the surface was also investigated. The main restriction of the method is its inability to provide a near continuous measurement of the ocean surface, limiting the ability of the data analysis to give a spectral account of the surface slope. However, at present the measurements of Cox and Munk (1954) still provide the most reliable statistical data set for ocean surface slope.

3.3.2 Stilwell Photography

The inability of sun glitter measurements to provide a continuous representation of the wave field and as a result being of little use in determining a wave spectrum, was addressed by Stilwell (1969). The technique which is now referred to as Stilwell photography replaced the point image of the sun with a continuous sky luminance. Photographs of the ocean surface were taken with a camera under uniform sky conditions. Optical analysis resolved variations in the density of a photographic emulsion into components of a two dimensional Fourier spectrum of the surface.

The camera altitude and field of view of the lens dictated the longest wavelength and the resolution restricts the shortest wavelength detectable by this method.

Although the results reported by Stilwell were encouraging, the technique has a number of serious limitations. Jähne et al (1992) found that the reflection coefficient of the sea varied non-linearly with reflection angle and therefore surface slope. The brightness difference was fifty times higher for positive slopes than negative slopes with a camera incidence angle of 45°. Increasing the incident angle has little effect. This effect is especially troublesome for the study of smaller waves on the backs of larger waves. In addition up-welling light, resulting from the backscatter of light having already penetrated the ocean, will add to the reflected intensity. The effect can be minimised in the near infra-red where light is absorbed relatively quickly by the ocean. The next problem with this method is the need for the surface illumination to be uniformly bright, or uniformly overcast, to ensure a homogenous radiance. These sky conditions are rare. The use of an artificial source to overcome this problem is impractical due to the associated need for the light source to be extended. The observation of oil slicks is also problematic due to alteration of the reflectivity of the surface in a discontinuous manner.

3.3.3 Stereo Photography

If two images of the ocean surface are taken at the same time and over the same area, but from different incidence angles, it is possible to determine the true surface height from the difference in position of features within each image. This technique is known as stereo photography and relies on the correct positioning of two imaging devices above the wave field. Referring to figure 3.2 which gives a typical schematic of the set-up,

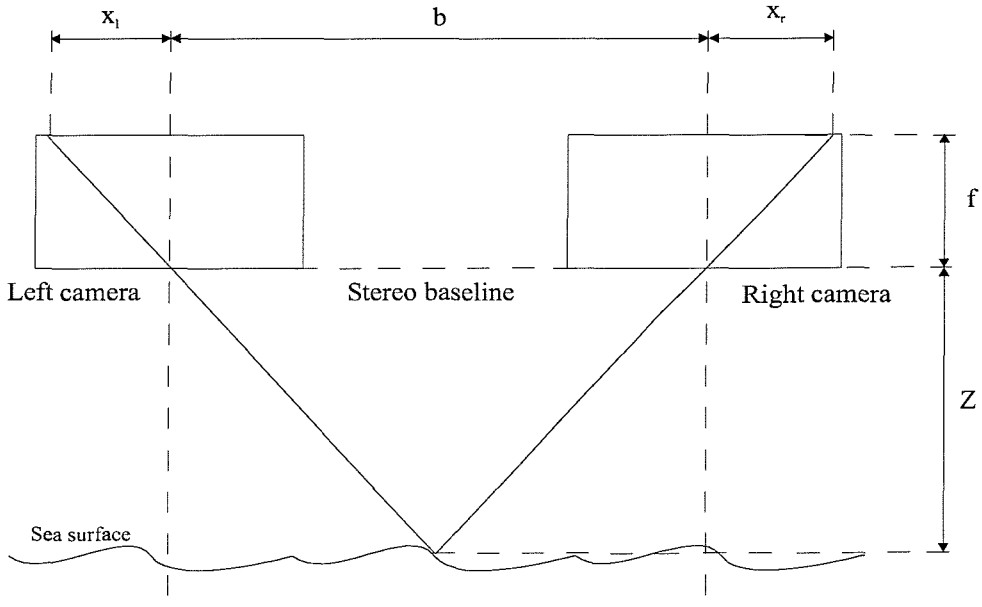

Figure 3.2 Schematic of typical stereo photographic set up.

the distance from the feature, Z, and hence the wave height is related to the difference of the position of the feature within each image, x_l and x_r, and is dependant the separation, b, and the focal length, f, of each imaging device:

$$x_l - x_r = \frac{bf}{Z} \tag{3.1}$$

The use of stereo photography to measure sea surface topography was applied by Cote et al (1960) for ocean waves with wavelengths of 15m to 300m. To cover such areas it was necessary to deploy two aircraft, flying parallel, at heights of around 800 feet above the ocean surface. Each aircraft had an on-board camera mounted such that overlapping areas of the surface could be imaged. Higher wavelengths have been measured using this technique by Shemdin et al (1988) and by Banner et al (1989). Shemdin deployed cameras from a tower in order to obtain stereo photographs with a 0.85cm resolution in the horizontal over a 250cm area. From the images which were taken over a range of wind speeds from 1.5 to 5.0 ms^{-1}, the surface elevation and direction were determined. High pass filtering of the images was necessary in order to obtain useful information on the shorter waves.

Omnidirectional wavenumber spectra were computed and had a Nyquist length of 3.2cm. A power law index of 3.6 was found for wavelengths greater than 30cm, and 2.4 for wavelengths less than 30cm. A noise deck was present for wavelengths shorter than 8.0cm. The Nyquist length was changed to 1.7cm and the power law index of 3.6 was found to extend to wavelengths of 10cm. The 2.4 power index extended from 10cm to 5.0cm at which point the noise floor was reached. This change in the extent of the power index probably occurred from the transition of the 3.6 region to the noise floor as a result of the method used.

Shemdin et al (1988) used their measurements to investigate the modulation of short waves by long waves. Short wavelength spectral intensities where found to be largest in the troughs of the long waves, as opposed to the crests where the lowest intensities appeared. Directional modulation was also examined and once again, the troughs showed higher spectral wavenumber densities than those at other phase locations along the long wave. The centimetre waves were found to have a highly directional distribution being aligned in the same direction as the wind. Digital images can be produced by using a charge couple device, CCD, camera (Jähne and Waas (1992)), allowing images to be recorded and processed faster. However, images recorded on photographic film have a finer resolution leading to more precise estimates of wave height.

Problems with this technique do exist. To match images corresponding features need to be identified. If natural illumination of the surface is used the specula nature of light reflection, from

the water surface, leads to the same patch of water appearing different when viewed from a different angle. When matching these features, errors will be induced giving the wrong surface elevation. This is referred to as the correspondence problem. Jähne and Waas (1992) attempted to overcome this by using two CCD cameras and illuminating the area with two sources. Each source was polarised and both cameras fitted with polaroid filters allowing reflected light from one of the two sources to be imaged by only one of the cameras. The system was set up so the surface glints appear in both images and this avoids the correspondence problem. The second problem associated with stereo photography is the need for a large baseline relative to the height above the surface. This enables wavelengths of the same order as the horizontal resolution to be measured. This is not often practical and wavelength resolution is decreased (Jähne et al (1992)). The technique is also hindered by the light reflection problems of Stilwell photography.

The main disadvantage with Stilwell and stereo photography is the requirement for a uniform sky luminescence. Stilwell photography is hindered by non-linearities which result from the reflection coefficients varying with angle and therefore wave slope. Stereo photography is affected by the correspondence problem and although this can be eliminated by the use of CCD cameras and polarised light sources, the technique is limited in wavelength resolution. Sun glitter has provided useful statistical information but cannot give a near continuous surface representation and is therefore limited in the recovery of spectral information.

3.4 Refraction Based Measurements of the Ocean Surface

The optical methods discussed previously which included sun glitter, Stilwell photography and stereo photography all rely on the reflection of light whether it is natural, or artificial, in origin. Attention is now turned to a number of techniques which rely on the refraction of light through the water surface. All the methods associated with this approach require the optical detection system to be on the opposite side of the air-water boundary to the light source. The two main advantages (Jähne et al (1992)) of using light refraction, instead of light reflection, to determine the properties of the surface are:

- From Fresnel's equations for reflection, more light is transmitted at the water surface than is reflected. Signals are therefore stronger and easier to detect.

- Incident rays at the ocean surface are deflected though smaller angles when refracted than when reflected. To measure slopes of equal size requires a larger detector for rays that are reflected than for rays that are refracted. Not only will a detector measure larger slopes

from a refracted ray but a refracting system can also cope with slopes greater than 45° which cannot be detected if reflection techniques are used.

Refraction based techniques require the illumination of the surface under observation. This has been done by the use of a laser beam either pointed in a single direction, or scanned over the surface to cover an area. Incandescent lamps have also been used as a light source for this type of instrumentation. A single incandescent lamp will give a point measurement. A number of lamps can be used to illuminate the sea surface over an area. The main difference is not the type of light source used but the method by which the refracted beam is detected. These detection systems are now reviewed. Non-laser techniques are discussed before moving onto laser slope gauges.

3.4.1 Non Laser Refraction Techniques

Cox (1958) performed an experiment to measure the slope of high frequency wind waves generated within an enclosed tank. The experimental set up is sketched in figure 3.3. The light source consisted of four cylindrical incandescent light bulbs beneath the wave tank. The emerging light beam passed through a plate glass window on the tank bottom, and through a hollow glass wedge. After refraction at the water surface the beam passes through a plate glass window, on the top of the tank, into a telescope where it is focused on to a photocell.

The wedge was filled with inky water which produced a linear variation in light intensity from zero at the thick end, to unity at the thin end. This ensured a linear change in brightness within the detector proportional to the up-down wind component of surface water slope. Rotating the wedge through 90° gave the orthogonal cross-wind slope component. The wavelength response of the system is determined by the spot size. Waves of length much less than the diameter of the spot do not cause variations in brightness and hence are not detected. A two dimensional version of Cox's original system was developed by Wright and Keller (1971) and consisted of a long fluorescent lamp along one of the sides of a large container in which was placed the scattering medium giving an exponentially varying light source. The data were recorded on a photographic film which was later replaced with a CCD camera by Keller and Gotwols (1983) to eliminate the effects of non-linearities in the photographic emulsion and in the conversion of the analogue recording to a digital format. Variations in wave height produced non-linearities in the recording which can be reduced by increasing the distance of the camera from the water surface.

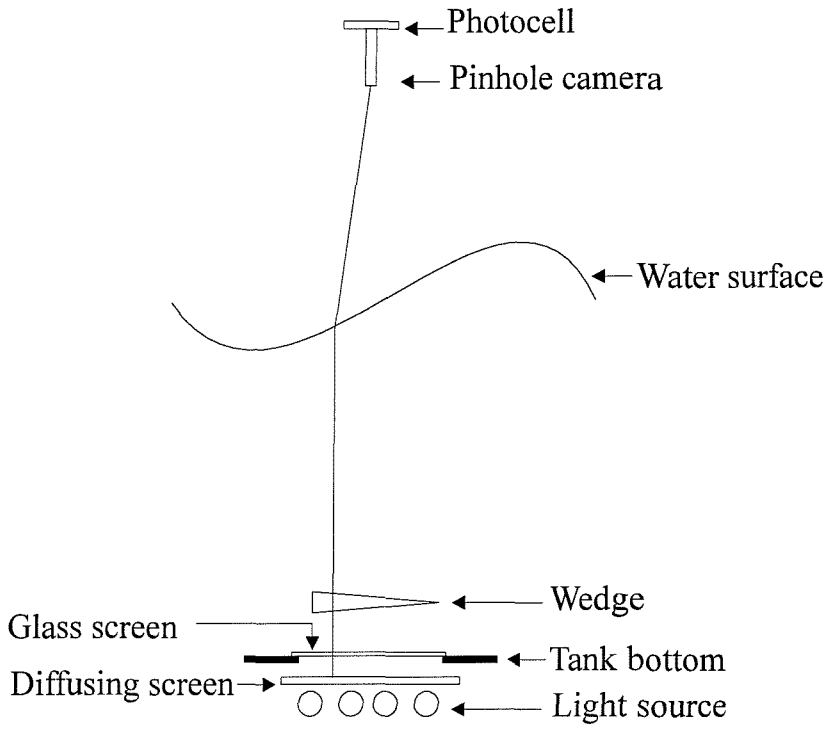

Figure 3.3 Schematic of the Cox (1958) wave slope imager

The non laser refraction techniques presented have been limited to the analysis of wave surface profiles generated in wave tanks. We are interested in making in-situ measurements and the conversion of such devices to the real ocean environment might prove difficult. We now turn our attention to laser slopemeters which have been proven in the field.

3.4.2 Laser Slopemeter Gauges

Slopemeters consist of a laser light source offering a coherent narrow beam which is refracted by, but does not perturb, the surface under investigation and a detector assembly of varying design and performance. A generic laser slopemeter system is illustrated in figure 3.4. Typically helium-neon, or HeNe, lasers, with a wavelength of 632 nm, have been used as the basis of the light source. Red light is not scattered as easily as shorter wavelengths of visible light, this reduces the intensity of the source required to give a measurable signal in the detector, reducing the power demands and size of the device required. The detector assembly can either be deployed beneath, or above, the water surface. The advantages of deploying the detector beneath the surface is an increase in slope range for a fixed detector size and elimination of the occurrence of total internal reflection (TIR). However, the advantages are outweighed by the need for a substantial waterproofing of the detector assembly and the possibility of perturbing the wave field under investigation by the introduction of a body of large volume just underneath the water surface.

From Snell's Law (equation 3.2) and assuming refractive indices, n_w and n_a, of 1.33 and 1 for water and air respectively then TIR occurs at 48.2°. It is unlikely that surface slopes will be this large and so the deployment of the detector above the surface is in general the favoured option.

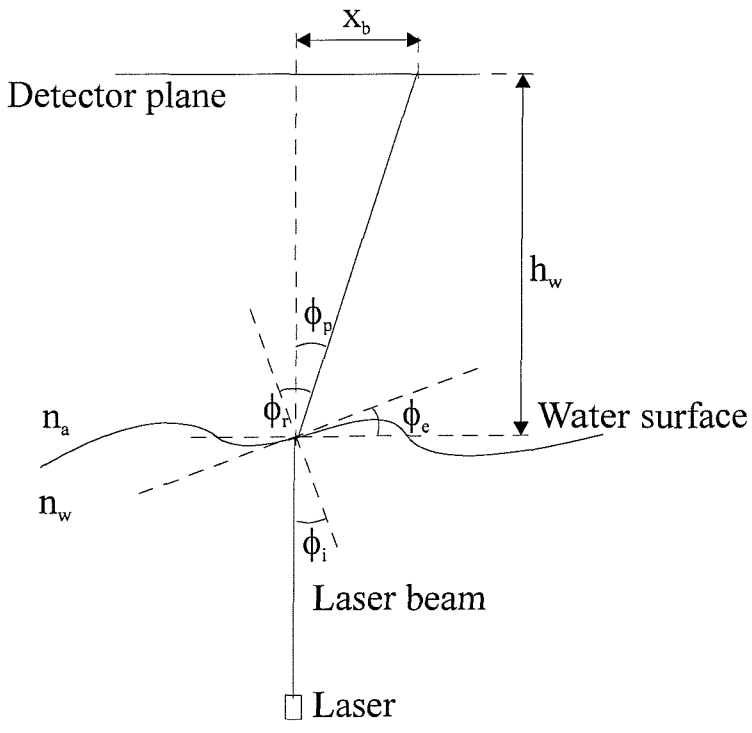

Figure 3.4 Generic laser slopemeter system

Referring to figure 3.4, the detector plane is situated above the water, the beam is refracted away from the local normal, through an angle ϕ_r, and impinges on the detector at a distance x_b from a reference point usually taken to be the centre of the detection plane. The angle of wave slope, ϕ_e, is given by Snell's Law:

$$n_r \sin\phi_r = n_i \sin\phi_i \tag{3.2}$$

Now, as;

$$\phi_i = \phi_e, \qquad \phi_r = \phi_e + \phi_p \quad \text{and} \quad \sin A\cos B + \cos A \sin B = \sin(A+B)$$

then,

$$\cos\phi_e \sin\phi_p + \sin\phi_e \cos\phi_p = \frac{n_w}{n_a}\sin\phi_e \tag{3.3}$$

and as;

$$\phi_p = \arctan\left(\frac{x_b}{h_w}\right) \tag{3.4}$$

then;

$$\phi_e = \arctan\left\{\left[\frac{n_w}{n_a}\cos ec\left(\arctan\left[\frac{x_b}{h_w}\right]\right) - \frac{h_w}{x_b}\right]^{-1}\right\} \tag{3.5}$$

where h_w, is the height of the detector above the water surface at the point of detection. This distance is either estimated from a measure of surface height taken from a different instrument, typically a wire probe or by assuming a constant surface height. A greater insight into the specific methods by which values for wave slope can be measured using laser slopemeters is gained from the following critical review.

Prettyman and Cermak (1969) developed the first laser slopemeter and used a helium-neon source. They deployed their detector system, consisting purely of a diffusing screen and video camera, underneath the water line from a fixed framework. An average surface height was assumed, this assumption resulted in a 10-20% error in the measured wave slope. A movement of 1-2° in the structure in moderate sea states and the requirement of night-time deployment to limit ambient light levels restricted its usefulness.

Tober et al (1973), used an objective lens to focus the refracted beam emerging from the water surface onto a beam splitter. This divided the beam into two components each intensity modulated using a graded transmission filter orientated to make the beam sensitive to two orthogonal slope components. Filters were positioned along the optical axis at locations selected to ensure measurements made were independent of water height within a ±6mm change in water level. Each spot, whose motion was kept to a minimum in order to reduce cathode non linearity, was spread over the face of a photomultiplier tube. Filters reduced ambient light to a level at which the tubes worked during daylight. The non-linearity and light dependency of the instrument was revealed during calibration and attributed to the graded transmission filters. Wave slopes of ±20° and waves of length 0.17m, or greater, could be measured. The system was deployed in a wave tank and later by Shemdin and Hwang (1988) on a stationary wave follower.

Sturm and Sorrell (1973) determined refracted laser position using a one dimensional photodiode with an active length of 255mm. Variations in beam intensity were compensated for, giving a signal dependent on spot position only. A cylindrical lens placed between the water surface and the photodiode kept the beam focused on the active area. The system which was deployed within a wave tank gave one component of wave slope and was limited, at the time, by the cost of the photodiode. The system was used to measure the slope of gravity-capillary waves over 6-18Hz frequency range with an error of 5% which resulted mainly from the assumption of a mean wave height.

Scott (1974) presented a system which would avoid the non-linearities associated with Tober et al's (1973) system and the expense of Sturm and Sorrell's (1973) Schottky photodiodes. The spot location system, situated above the water surface consisted of a "photentiomatic"; similar to a potentiometer with one conducting plate placed parallel but not touching a resistor, about which a voltage was applied. The intercepting beam produced a low resistance path between the two plates to give a linearly varying spot position to within 0.25%. The beam was concentrated onto the photentiomatic using a cylindrical lens placed halfway between this and the water surface. Although only one component of slope could be measured, an additional photentiomatic placed in an orthogonal direction within the same plane as the first would give a second slope component. A shield about the sensor reduced ambient light, although no effect due to laboratory lighting was detected. A beam focusing cylindrical lens placed at the laser head reduced spot diameter such that wavelengths less than 10mm could be detected. The wave height was taken to be constant which would introduce errors into the measurements caused by actual variations in water level.

Palm et al (1977), offered another variation on the now standard laser slopemeter design. A receiver consisting of an objective lens and a frosted acrylic disk scattered light from the refracted laser beam to a transfer lens which in turn produced an image on a Schottky photodiode with a 3.65 cm by 3.65 cm active area. The maximum uncertainty in calibration was about 7%. Problems associated with the output of the electronic circuits decreased as the supplied signal reached a critical lower level. This was attributed to light loss resulting either from laser attenuation or occurring within the acrylic sheet. The frequency response of the system was greater than 400Hz and measured waves of slopes up to 35°. The system was deployed on a stationary wave follower which used a wire probe to determine wave height.

Hughes et al (1977) positioned a fixed point laser slopemeter 10m ahead of the bow of a research vessel. By keeping the velocity of the ship constant Hughes was able to gain a spatial and temporal transect of the sea surface. Surface aberrations on this lens conspired to make the system weakly dependant on wave height. To correct for this a capacitance probe was placed a metre from the spot in the direction of the bow of the vessel. The recorded value of height was then used

in the subsequent data analysis. The beam passed through a translucent screen producing a spot from which the angle of slope could be determined. The spot was imaged using a video camera with a silicon diode array which replaced the usual photoconductive film. An interference filter centred about the laser wavelength sat in front of the camera lens and allowed the instrument to be deployed during daylight providing no sun glint fell within the screen's field of view. Frequency spectra gained from the analysis had to be compensated for boat motion which introduced a Doppler shift (Hughes (1978)).

Group	Measure of h_w	Main optical component	Statistics	Deployment
Prettyman and Cermak (1969)	Constant height	Video camera, diffusion screen	Slope <±40°. Error 10-20%. Sample rate 400 frames s^{-1}	Fixed ridged framework
Tober et al (1973)	Constant height	beam splitter, PM tube	Slope <±20°. λ>0.017m	Wave tank Wave follower
Strum and Sorrel (1973)	Constant height	photodiode	Waves of 6-18Hz. Error 5%	Wave tank
Scott (1974)	Constant height	photentiomatic	λ>0.01m	Wave tank
Palm et al (1977)	Wire probe	photodiode	Slope <±35°. Error 7%. Sample rate 400 Hz	Wave follower
Hughes et al (1977)	Wire probe	Video camera	Error 15%. Sample rate 110 Hz	Bow of vessel

Table 3.1 A summary of the main features of a number of laser slopemeter systems. The symbol λ is the wavelength of the wave

The main characteristics of each of the devices reviewed above are summarised in table 3.1. Fixed laser slopemeters give a time series of measurements at a point and correspondingly generate frequency spectra. Deploying more than one gauge to cover an area as is done with wire probes would prove expensive. Slopemeters can be towed giving a transect through the surface. Such a system samples the wave field at points which vary both spatially and temporally. However this does not offer a complete spatial picture. This is addressed by scanning laser slopemeters which are now discussed.

3.4.3 Scanning Laser Slopemeters Gauges

Although Hughes' adaptation of the laser slopemeter gave two components of slope this was restricted to only one spatial dimension; the direction of travel of the vessel. To gain a better representation of surface slope recent developments have been made to produce a scan of the sea surface giving slope components over two spatial dimensions.

A scanning laser slopemeter was developed by Lee et al (1992) for TRW. The detector and optical assemblies were deployed on a rigid framework which could be bolted on to the front of a suitable vessel, much like the system used by Hughes. The system fed an Argon ion laser beam via a nitrogen filled tube from the laser, situated above the water on the deployment arm of the steel frame, to a scanning unit underneath the ocean surface. The laser beam was intensity modulated using an acousto-optic modulator, the detector electronics were phased locked to this signal and this feature helped to reduce the effect of background light from the signal produced by the laser. Within the scanning unit the laser beam was focused onto a pair of mirrors which in turn were attached to a servo. This enabled the laser beam to be scanned in the horizontal plane, over the water surface. The scan covered an area of 20cm by 40cm. A scan rate of 264 lines per second was achieved.

The detector assembly consisted of an array of photodiodes, positioned above a fluorescent acrylic sheet which absorbed the green light and re-emitted it at red wavelengths. These were used to determine the horizontal displacement from the point of exit from the water. A set of three wire probes situated behind the beam were used to determine wave height at the point of refraction to give two orthogonal components of slope. The scan pattern was quite complicated and required a long processing time. The inclusion of the wire probes disturbed the water surface, introduced errors associated with such devices and was located away from the point of refraction. No results from this detector have been published.

Martinsen and Boch (1992) developed a system which could operate in both stationary and scanning modes. A 10mw HeNe laser with a spot diameter of 0.8mm was contained below the surface in a laser pod. The beam was deflected onto two moving galvo mirrors which produced a scan pattern in the horizontal plane. The scan pattern was then collimated using an aspheric lens. The detector head, positioned above the sea surface consisted of a band pass filter, a convex lens and a diffusing plate. The beam spot was located on the plate using four silicon photodiodes. Again, interference filters in front of these reduced ambient light level.

The instrument was deployed in front of a catamaran and was moved at a constant velocity of $2ms^{-1}$. The maximum slope that could be measured was 34.8° and has a frequency response up to 83Hz. The wave surface was assumed to be a constant 40cm from the detector. The detector aperture was small, limiting the measure of surface tilt and it was possible that the laser pod would have produced interference with surface waves due to its size.

3.4.4 Discussion

The use of light as a means of measuring a wave profile rather than mechanical and electronic methods permits non-evasive observations of the sea surface to be conducted. This is especially important at the short wavelengths of interest to us. Capillary and capillary-gravity waves can be easily perturbed, even destroyed, by physical contact, reducing the precision of the measurement. Refraction based measurements of the sea surface wave profile avoid non-linearities which can arise from reflection coefficients varying with the angle of incidence. They are also less prone than reflection based methods to variations in ambient light levels whilst offering a greater resolution and the ability to detect a larger range of wave slopes for a given detector size.

Lasers have been used as the light source for all in-situ refraction based instruments. They can provide a signal point at the surface or, when combined with a scanning mirror, can be used to scan over an area of the wave field. For a generic laser slopemeter the laser source and the optical detection system must be deployed on opposite sides of the water-air boundary. The favoured option is to deploy the optical detection unit above the waters surface avoiding the need for extensive waterproofing. This also reduces the chances of perturbing the observed wave profile which could occur if a large detector is placed just beneath the sea surface. These features are included in the design of the Southampton Towed Laser Slopemeter (TLS). An overview of the TLS system is given in the next section. The need to know the distance between the detector plane and the point of refraction on the sea surface limits the precision in the wave slope measurement if this distance is assumed to be constant or is imprecisely measured. To offer greater performance the TLS design does not require a value for surface height greatly increasing the precision to which the wave slope can be measured.

Scanning slopemeters can be used to determine the wave slope over a given area. However, their design is more complex than single point instruments. The size of data sets and limits on data storage capacity and telemetry bandwidths restricts the sample rate to frequencies below those of a single point slope gauge. The scanning unit tends to be large and although below the sea surface may perturb the wave profile being observed. Because of these limitations it was decided to develop the TLS as a single point device. Finally, a decision was taken to tow the TLS. This avoids the Doppler shift in the power spectrum associated with the advection of short waves by swell and large waves. It permits the effective measurement of dynamic ocean processes and prevents the observed wave profile from being disturbed by the surrounding structure of the instrument.

3.5 The Southampton Towed Laser Slopemeter

A Towed Laser Slopemeter (TLS) instrument has been designed and developed by the Departments of Physics and Oceanography at the University of Southampton. The instrument comprises of an optical detector, signal processing electronics, computer rack, and an inertial motion unit (IMU) mounted on a modified catamaran. The craft is towed by a larger vessel at a speed of approximately $1ms^{-1}$. Two tow cables together with an RF controlled rudder system ensure that during data acquisition the front of the TLS is sampling the undisturbed ambient wave field. This gives an uncoupled measurement of the surface gradient. The instrument is sensitive to wave slopes, relative to the catamaran, of $\pm 35°$ and a wavelength range of 7mm to 1m. Figure 3.5 shows a plan view of the configuration during operation. In this section an overview of the laser and optical detection system, electronic design, deployment procedure and slope reconstruction is given. A more detailed account of the system can be gained from Lee et al (1994) and Lee (1995).

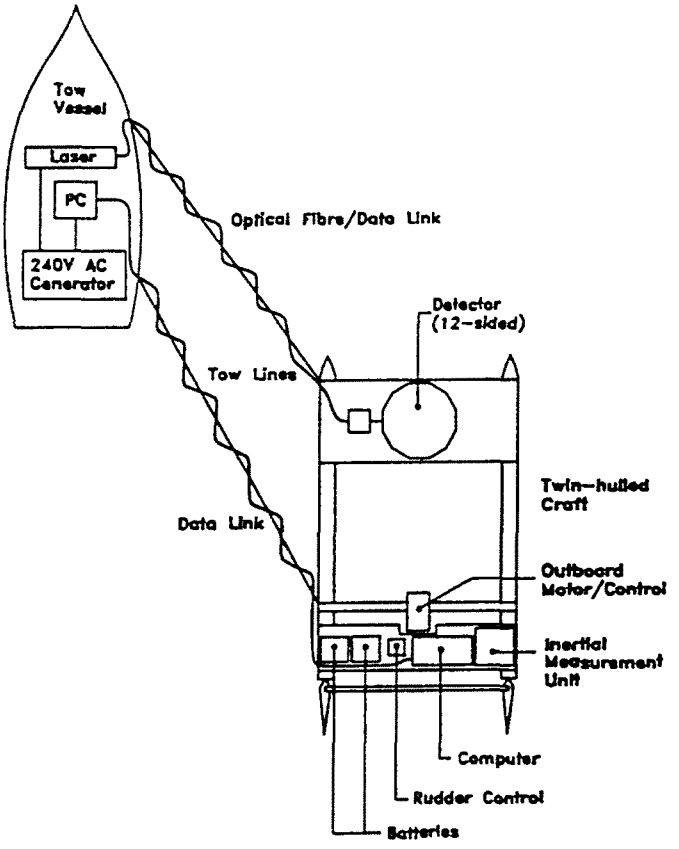

Figure 3.5 View of TLS system in operational mode (not to scale).

3.5.1 The Laser and Optical Detection System

The surface gradient measuring system comprises of a laser beam source, a collimator and associated mount, and an optical detector as sketched in figure 3.6. The optical detector is mounted above the water surface to reduce drag and minimise the disturbance of the wave field. The laser beam is produced by a single-mode helium-cadmium (HeCd) laser at a wavelength of 442 nm with a power of 90 mW continuous wave which, for reasons of power demand, resides on the tow vessel. The laser head is attached to an acousto-optical modulator with a 50% duty cycle at 9600 Hz. Beam modulation is required to decouple ambient light from the laser spot within the optical detection system and also to control laser power delivered to the system. The light is then injected into a fibre optic cable which is passed along the forward tow rope to the catamaran where the end of the optical link is attached to a collimator. The collimator sits in a receptacle and focuses the diverging beam, as well as channelling some of the laser light into a second optical fibre for use as a phase reference for the electronics system. The receptacle is mounted directly underneath the optical detector assembly, at a depth of 300 to 400mm below the mean sea level on a tripod. The tripod is designed to minimise surface interference. The beam, when not refracted by the surface, passes vertically through the centre of the optical detection system producing a low divergence spot with a diameter of 2 mm. 50% of the beam is lost along the 30m fibre link.

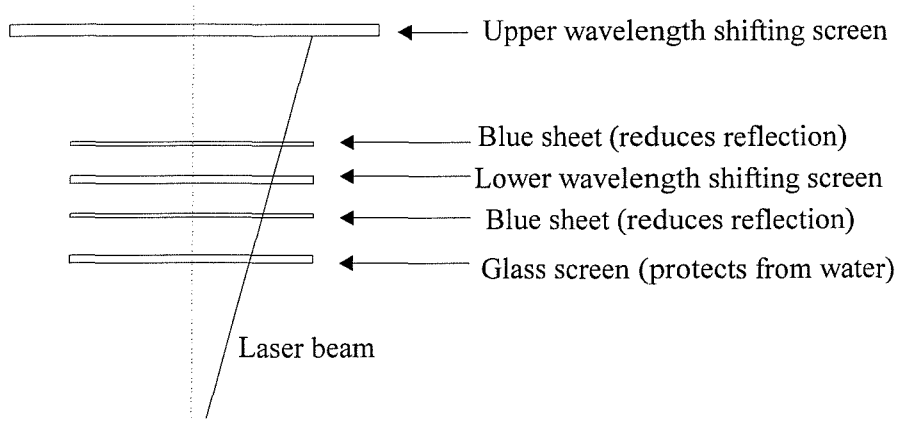

Figure 3.6 Side on view of optical detection system.

The gradient measuring assembly which includes the optical detector and collimator mount, sits between the bows of the catamaran and as far forward as possible to minimise surface disturbances. The beam emerges from, and is refracted by, the water surface and enters the detector through a glass window which sits above the sea surface at a mean height of 300mm. The glass window has a blue filter attached on the inside to minimise the ambient light level. When the laser beam strikes the lower wavelength shifting screen 50% of the power is converted to a spot of green light within it. The remaining 50% of the power is transmitted through to strike the upper screen, producing a second green spot. Light from the spot within each of the screens propagates

away, totally internally reflected within the sheet, towards the edge of the screen where it is detected by the photodiodes placed around the edges. A second blue filter is placed directly above the lower screen to reduce the possibility of back reflection from the upper screen. The edges of each screen are polished and coated in black ink to minimise reflection of light from the screen edge.

The relative signal strengths from the photodiodes allow the spot position to be determined and, knowing the distance between the two screens, the beam gradient to be calculated. By using a differential measurement achieved by having two screens, the wave height does not need to be monitored, indeed it can be calculated by extrapolation from the beam gradient. The number of photodiodes about each screen is governed by a trade off between location accuracy and electronic complexity. A minimum of three photodiodes, an equidistance apart about the screen edge, are required to locate the spot position unambiguously. Photodiode resolution drops with distance from the spot and increasing the number of photodiodes will increase accuracy in spot location. Six photodiodes were used about each screen (figure 3.7). Green filters were mounted to the photodiodes and the photodiode-filter combination mounted to the screen using optical glue. As the positional error is greatest between diodes, each screen was rotated prior to permanent fixing so when viewed from above, the twelve photodiodes lay 30° apart.

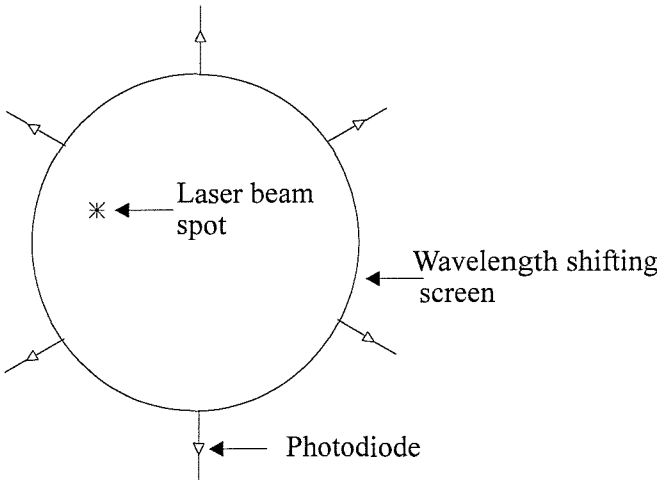

Figure 3.7 Photodiode configuration about wave guide screen

The relative strengths from the photodiodes which allow the spot position to be calculated are expressed in terms of a difference over sum ratio. The ratio for opposing diodes A and B is;

$$\frac{V_a - V_b}{V_a + V_b} \tag{3.6}$$

where V_a and V_b are the voltages of the opposing photodiodes A and B, respectively. The ratio is scaled by 2048.

3.5.2 Electronic Design

Each photodiode is connected to a preamplifier circuit to amplify the low level current output. A block diagram of the on-board electronics system for the acquisition of the light spot on the detector screens is given in figure 3.8. A separate photodiode and preamplifier circuit are also connected to the phase reference signal. A phase lock loop, or PLL, circuit is used to lock onto the main frequency component in the input signal. Due to scattering and attenuation within the optical fibre, the signal output from the photodiodes is of low quality, the phase sensitive detector, or PSD, combines this signal with that from the PLL to enhance the fundamental frequency contained within the photodiode signal. The output from the PSD is passed to the Analogue to Digital converter, or ADC, circuit which as its name suggests converts the analogue photodiode output to a digital equivalent, allowing the signal to be handled by the on-board computer. A sample and hold circuit is included prior to the ADC. This ensures that the ADC receives the signals from each photodiode relating to a particular spot position. When a "hold" signal from the CPU is received the sample and hold circuit samples each photodiode value.

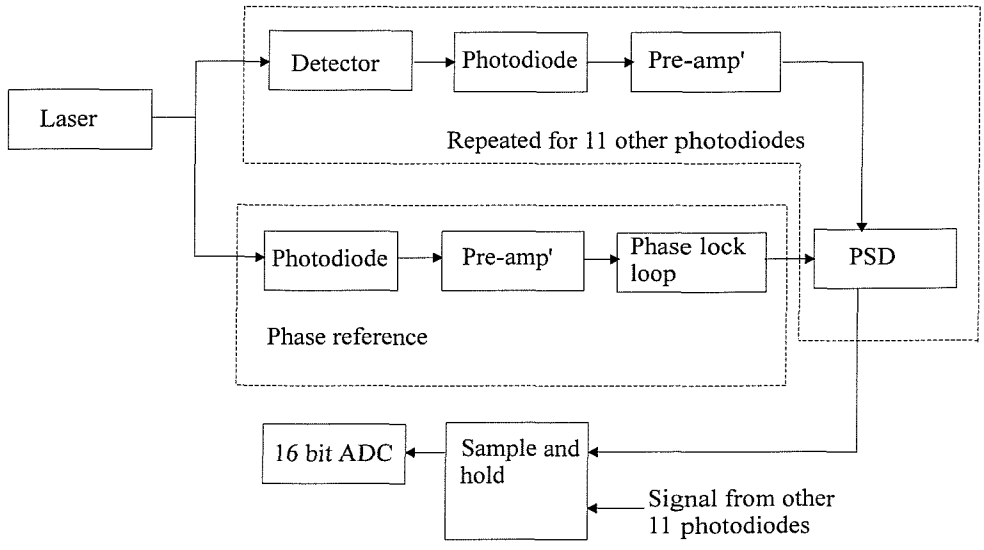

Figure 3.8 Electronic system for acquisition of light spot on detector screens

3.5.3 Deployment Procedure

The IMU is mounted along with the on-board computer and associated power supply (two standard 12v car batteries), and rudder control and associated power supply (one 6v battery), at the aft section of the catamaran to counter balance the forward sitting detection system. The IMU provides measurements of yaw, pitch, and roll motions and along track, cross track and upward acceleration vectors which can be used to determine vehicle movement and hence decouple it from laser beam measurements to gain the water slope relative to the horizontal. The onboard computer, a 68040 VME processor supporting an OS9 operating system, is mounted together with the system electronics, excluding the preamplifiers, within a card rack located in a water tight box. The preamplifiers are mounted in the optical detector assembly. The data obtained from the optical detector and the IMU, together with the system environmental variables (temperature within the rack and battery level), are passed to the on-board computer where they are formatted into data packets before being transferred to the tow vessel via a ship-to-ship RS232 link. In addition, the computer receives commands from the tow vessel also via the RS232 link.

3.5.4 Data Processing

Profiles of photodiode outputs for both of the screens were produced using two rotary tables to slowly sweep the laser beam across the optical detector aperture, during which time the on-board computer records the photodiode outputs. Contour plots of these data sets, which were later used as calibration tables, were found to be surprisingly noisy. The appearance of lobes either side of the main photodiode signal were attributed to the characteristics of the filters used between the photodiodes and the screens. Irregularities were evident in the contour lines and were probably caused by the contamination of both screens and a greater than expected system noise. This meant that real-time processing of the data could not be achieved. Instead, post processing using look-up tables obtained from the calibration scans would have to be implemented.

The CPU and telemetry specifications had been designed with the constraint that the slope data would be transmitted to the tow vessel. As real time processing was no longer possible, the raw photodiode ratios would have to be included in the telemetry. However, the bandwidth required to do this was too great. Instead of passing all twelve photodiode values, prior to the difference over sum being calculated which was needed for determining spot position, the ratio was calculated within the telemetry software. As a second step in decreasing the bandwidth the resolution of the transmitted photodiode ratio values was reduced from 16 bits to 12 bits which accounts for the scale factor of 2048. The sample frequencies for the photodiode ratios was 250Hz and that for the

IMU data was 50Hz. To avoid data drop out during recording two personal computers (PC's), rather than one, received the telemetry data on-board the tow vessel.

The data reduction procedure which is conducted on a Sun Sparc 5 processor under Solaris 2.3, comprises of four phases; data collation, data processing, slope reconstruction and removal of vehicle motion. First the data which is stored initially on the two PC's is combined to enable the data not contained within one file to be properly restored from the second file. The data processing software then takes this combined file, removes the packet structure, and gives a listing of photodiode ratios, navigational and CPU environmental variables in order of their correct time stamp. The photodiode values are then ready to undergo reconstruction to yield the true surface slope in two orthogonal components.

The data quality is first checked. Samples which have low photodiode signals, or where the laser signal has not been locked onto by the PLL, are declared "null" before reconstruction of the entire data set begins. Various parameters within the software used for reconstruction determine the level, and precision, to which the slope is reconstructed. For example, the accuracy to which the photodiode values are matched to the calibrated screen voltages is controlled by a tolerance level. If the data are valid, the tolerance values are set to their initial states and the position of the spot on the upper screen is determined first. The photodiode value is matched to a similar value in the lookup table. Precision is further increased by interpolation between the matching point and its neighbours, for each photodiode pair, and by calculating a position estimate which minimises the error from each interpolation. A similar process is conducted on the lower screen. The positions on each sheet are finally matched together from an understanding of the instrument geometry. All possible solutions are assessed for quality by looking at individual errors and by matching them to a predicted solution from the previous samples. Finally, either the best solution is selected, or the search is abandoned and a "null" solution is used, or the search is continued by increasing the search parameters. The wave slope is then calculated from the spot positions and recorded in an output file. Referring to figure 3.9, the wave slope is determined from the spot positions in a similar manner to the calculation of the wave slope from the generic slopemeter of section 3.4.2, except this time, h_w, is replaced by the known distance between the two screens, h_s. From equation 3.3 and as

$$\phi_p = \arctan\left(\frac{x_t - x_b}{h_s}\right) \tag{3.7}$$

then the wave slope, ϕ_e, can be calculated without a measure of the variable surface height h_w:

$$\phi_e = \arctan\left\{\left[\frac{n_w}{n_a}\cos ec\left(\arctan\left[\frac{x_t - x_b}{h_s}\right]\right) - \frac{h_s}{x_t - x_b}\right]^{-1}\right\} \tag{3.8}$$

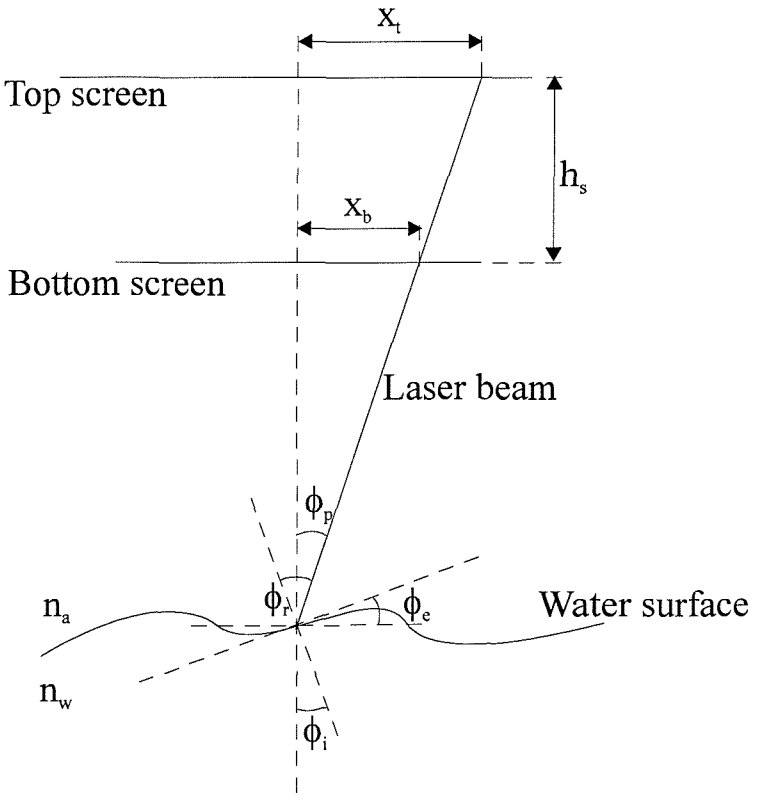

Figure 3.9 Reconstruction of surface slope from spot position

3.5.5 Signal to Noise Files

To provide a check on the basic performance of the whole laser, detector, electronic and telemetry systems of the Southampton Laser Slopemeter, a set of data files are recorded without the presence of a perturbing water surface. The tests are regularly carried out during a trial on dry land. The laser beam is fired vertically through the geometric centre of the screens for a period of usually one to two minutes. The subsequent analysis of the photodiode ratios obtained in this manner will give a value of any noise within the system. The files are referred to as signal to noise ratio, or SNR, files.

3.5.6 TLS Data Analysis Methodology

3.5.6.1 Calculation of Slope Data Products

The Towed Laser Slopemeter measures two orthogonal components of slope. The processing of the photodiode ratios corrects for the pitch and roll motions of the catamaran and produces values of slope, for a given point on the sea surface, in terms of the angular slope elevation from the horizontal, ϕ and the direction of the elevation from the bow-stern axis of the catamaran, θ. The bearing of the instrument with respect to magnetic north was removed at a later date. Two slope components, one parallel to the bow-stern axis of the TLS, S_x and the other perpendicular to this direction, S_y can be calculated:

$$S_x = \phi \cos\theta \tag{3.9}$$

$$S_y = \phi \sin\theta \tag{3.10}$$

To a first order, the two sea surface slope components are Gaussian distributions with mean values of zero. As the slopemeter cannot distinguish between waves travelling towards or away from it, the distribution of θ will be double peaked with a peak centred parallel and anti-parallel to the angular direction of travel of the main wave slope relative to the yaw of the TLS vehicle.

3.5.6.2 Numerical Tools for the Analysis of Slope data

A number of statistical and spectral methods appropriate for the analysis of wave height and wave slope data were presented in section 2.3 and their physical interpretations discussed. If the TLS data set is to be interpreted physically these numerical tools will have to be applied to the slope record. Slope variance, skewness and kurtosis all higher order statistical moments can be calculated using the following equations (Press et al (1988)):

Variance: $$\frac{1}{M-1}\sum_{j=1}^{M}\left(S_j - \bar{S}\right)^2 \tag{3.11}$$

Skewness: $$\frac{1}{M-1}\sum_{j=1}^{M}\left(\frac{S_j - \bar{S}}{\sigma}\right)^3 \tag{3.12}$$

Kurtosis: $$\frac{1}{M-1}\sum_{j=1}^{M}\left(\frac{S_j-\bar{S}}{\sigma}\right)^4 \qquad (3.13)$$

where σ is the standard deviation which is the square root of the variance, M is the number of data points over which the value is calculated and the over bar denotes the mean value of the variable. The total slope, S, is used as an example variable but it can be replaced by S_x, or S_y. Slope data can also be investigated using the power spectrum. There are a number of methods that can be applied to a data set to yield power spectra (Press et al (1988)). For reasons of comparison, the method used by Phillips (1985) which is widely applied in the field of sea surface analysis, is used in this text;

$$F(\underline{k}) = (2\pi)^{-2}\int\overline{S(\underline{x})S(\underline{x}+\underline{r})}e^{-i\underline{k}.\underline{r}}d\underline{r} \qquad (3.14)$$

where x and r are different position vectors and $F(k)$ is a power spectrum. Again, S, the total slope can be replaced by S_x, or S_y.

3.5.6.3 Implications of Surface Variability on Data Length

The analysis and studies applied to real data sets, obtained from the TLS, within the body of this thesis will be concerned with;

- the assessment of the TLS data record from an oceanographic prospective
- the investigation of a number of ocean processes occurring at the sea surface

Each of these aims will require a differing approach to the data. The first aim will require that results from the ensuing data analysis are reconciled with our knowledge of the sea surface and any deviations that exist adequately explained. Tests to be applied to the TLS slope data are:

a) Is the slope profile believable?
b) Is the distribution of slopes what we expect?
c) Does the spectrum exhibit a shape and power law consistent with previous studies and theory?
d) Is the TLS data set reconcilable with surface conditions, i.e. is wind direction and capillary wave direction aligned?

Points b) to d) are concerned with general rather than specific surface conditions and consequently, variations in distributions and sporadic fluctuations in the wave spectrum should be kept to a minimum. This can be achieved by assuming a homogeneous and stationary surface and proceeding to average over a large set of data points.

Ocean processes were discussed in chapter 2, and it is apparent from this that these influence the ocean surface over shorter scales and their effects will occupy a shorter section of the data set. During the Loch Linnhe campaign, long thin strips of surfactant material were evident on the waters surface. These filaments were a few metres in width and had sharp boundaries dividing them from the surrounding ambient water. Analysis of the these slicked regions must be performed on the data recorded within the boundary to ensure that the results are not contaminated by ambient conditions. If the slicked region is too small for a comprehensive analysis to be applied, the data from similar slicked regions can be combined and analysed as a whole. This must be done with care as changes in surface conditions both temporally and spatially will affect the outcome of the analysis and conclusions drawn from it. A search of the slope profile will be used to identify portions of the data in which slopes affected by ocean processes were sampled.

Power spectra are generated through the Fourier transformation of data. Fourier analysis requires that data are divided into sample sets which are a power of two in length. Sporadic fluctuations are reduced by averaging over a number of such transformed sample sets. For a fixed data rate, increasing the sample length will increase the resolution of the Fourier transformed data set. The power law relationship of sea surface spectra sets leads to a rapid change in spectral density at low wavenumbers. If we are interested in examining the general shape of the power spectrum, increasing the size of the sample set will help to define a spectral shape at low frequencies. Regions modulated by ocean processes will occupy relatively brief periods in the TLS data set. When applying power spectral analysis it will be necessary to use a smaller sample set to maximise the number of averages that can be applied. The reduction in size of the sample set leads to a corresponding decrease in resolution of the spectrum but this is not too serious as the modulations tend to occur at higher frequencies.

3.5.6.4 Error Analysis

Where possible error analysis will be applied. Statistical error analyses are easily implemented. A more difficult application of error analysis is the propagation of the errors in the slope data through to the Fourier transformed data. The Fourier transformed data will no longer have a Gaussian distribution and because of the transforming process are no longer independent.

Techniques do exist from which an error estimate of this type can be gained. The most straightforward, is to generate a number of surface realisations and transform each to give a spread in spectral intensity at a particular frequency from which the standard deviation can be estimated. The surface realisations are constructed from random values distributed between the maximum and minimum error for each value of slope. This method allows the effect of instrumental error on the spectrum to be considered. However in some cases, for example when comparing spectra from surfaces exhibiting different roughness scales, it may be more appropriate to consider the scatter about the mean value. This is done by calculating the standard deviation in the spectral intensity at a particular frequency which then forms the error in the mean value.

3.5.6.5 Implication of Sampling Method for the Analysis of the Data

Data are recorded along a transect and consequently vary both spatially and temporally. The waves measured are moving at speeds comparable to that of the TLS. The instrument cannot be assumed to be at rest with respect to the wave nor can the wave be assumed to be stationary with respect to the instrument. The true wavelengths and frequencies of the waves suffer from essentially a Doppler shift and the resultant spectrum has both wavenumber and frequency components. This confused spectrum is not directly comparable to purely wavenumber, or purely frequency spectra. The importance of the wave spectrum, as apparent from the previous chapter, gives impetus to efforts to resolve true spectra from this wavenumber-frequency spectrum. These ideas are developed further in the next chapter.

3.6 Summary

The need to develop in-situ instruments capable of observing sea surface roughness has been motivated by our need to fully understand the mechanisms governing the interaction of ocean processes and microwaves with the sea surface. Extending our knowledge in such areas is important if we are to fully exploit the information on the oceans that is contained within satellite-borne radar imagery. The design of the Towed Laser Slopemeter has been influenced by the strengths and weaknesses associated with previous instruments developed to give a measure of the sea surface wave height or wave slope.

A refraction based approach was decided upon. This offers a non-invasive measure of the sea surface wave profile whilst avoiding the problems associated with reflection based devices. Slopemeters are ideally suited for providing a measure of the sea surface wave slope at the

wavelengths of interest to us. However, this relatively new approach has been limited in precision. To determine the wave slope, the angle of the refracted beam from the normal to the sea surface must be found. This has tended to require a knowledge of the instantaneous distance of the detection plane of the instrument from the sea surface and therefore a knowledge of the wave height. The wave height can either be assumed to be constant or it can be measured. The wave height cannot be measured with the laser gauge and a different device, typically a wire probe, must be used. These probes are limited in precision through wetting or the generation of a meniscus which perturbs the local sea surface profile. If the probe is not to disturb the surface wave slope being measured by the laser gauge it must be placed away from the point of refraction. Away from the point at which the beam emerges from the sea surface it is not capable of giving a precise measure of the local wave height and this limits the precision in the wave slope especially at high wavenumbers. The Towed Laser Slopemeter design removes the need to determine the sea surface wave height. This is achieved by using two detection planes parallel to the undisturbed sea surface.

The TLS is towed across the wave field to be able to sample in both space and time across the surface features. This ensures that the surrounding structure does not interfere with the wave slope being observed. A mobile device permits a more effective investigation of the dynamic effects of ocean processes on the sea surface wave profile. The theoretical principles, systems design and method of deploying the TLS have been presented. This has an important bearing on how the data from the instrument are analysed and interpreted. Using the statistical and spectral techniques outlined in chapter 2 we are now in a position to take a quantitative look at the data from recent TLS deployments to assess the response of the TLS to a variety of sea surface conditions. This will be done in chapters 6 and 7. Before we can proceed with this we need to establish a theoretical basis for understanding how the towing of the instrument along a transect will effect the data and how to interpret the resulting spectra. Our attention is now focused on this task

Chapter 4

The Development of a Sea Surface Model

4.1 Introduction

A review of the instrumentation used to measure sea surface wave height and wave slope has shown that data can be recorded either at a fixed point or over an area at a fixed time. From such observations either purely wave frequency, or purely wavenumber, power spectra can be calculated. The information contained in these type of spectra is easily interpreted. In order to provide a true measurement of the wave slope the TLS is moved at a constant velocity to avoid perturbing the surface under investigation which would lead to the loss of high frequency detail. This provides information on the surface slope at different locations and times. The effect of this approach of sampling the wave field on the standard methods for the spectral analysis of sea surface characteristics must be examined.

A numerical model to simulate a representative TLS data set is required to aid with the investigation of this problem. Such a model is described in this chapter. Known sea surface parameters may be used as inputs to this model and lead to the generation of a realistic wave field. A spatially and temporally varying transect may then be made through the resultant data set and used to generate a set of corresponding surface parameters as an output. The simulation inputs and outputs may be compared and conclusions drawn about the effectiveness of this method for sampling the surface.

4.2 Methods for Modelling Rough Surfaces

Typically, the modelling of rough surfaces has not been specific to the case of modelling sea surface roughness. Such models have been developed to investigate acoustic and electromagnetic backscatter. The emphasis has been on understanding the general processes of the scattering occurring at the rough boundary rather than specific characteristics of the medium which would require a more realistic surface model to have been developed. Work in this area has been reported by Ogilvy (1988) and Fung and Chen (1985). Both groups generated a rough surface model using uncorrelated normally distributed random numbers with a zero mean and a pre-defined root mean square to give a measure of the surface height. In practice, such surface height values will not be independent and will exhibit a degree of correlation. Height values can be correlated by applying a moving average on the uncorrelated values. A weighting factor is applied during this averaging, the form of the weighting factor determining the form of the correlation of the surface height. A Gaussian correlation function was used in the two sets of work cited, but the model could be extended to give a representation of the sea surface by using an appropriate correlation function. Both studies were limited to a one dimensional model and the extension of the model to two dimensions would require a two dimensional weighting factor. The complexity of such an approach increases when we try to implement a time evolving surface which could be realised by the use of a temporal weighting factor. However, the increasing difficulty of adopting this approach to representing the sea surface is discouraging and it has not been pursued further.

In order to investigate the mechanisms for the electromagnetic backscatter of radar waves from the sea surface Holliday et al (1986), developed a sea surface model. The model was simple and relied on the Fourier transform of the wavenumber power spectrum. Holliday believed that the power of the scattered electromagnetic waves was related to the sea surface solely through the power spectrum and therefore his model did not include other sea surface properties. A new model applicable to our studies was developed. Although, the final solution was to use a Fourier approach this new model did not evolve directly from Holliday's model but rather from a consideration of the problem of simulating a representative TLS data set.

4.3 Formalization of the Problem

As discussed previously, the Towed Laser Slopemeter moves across the sea surface measuring wave slopes as a function of time. The speed of the vessel determines the position between each sample point and is not fast enough to prevent the waves moving between each measurement.

Therefore, when simulating the effect of this measuring technique on the observed values of wave slope, it is necessary to develop a model which is not only two dimensional in the horizontal plane but can also evolve in time. These considerations will have an impact on the complexity to which the sea surface must be modelled.

The sea surface, to a first order, can be assumed to consist of the superposition of cosine wave trains, as was discussed in section 2.2. Each sinusoidal wave will have an amplitude $A(k_x,k_y)$, frequency ω, two components of wavenumber, k_x and k_y, and a wave direction θ. For a continuous surface the wave height $\xi(x,y,t)$ is of the form;

$$\xi(x,y,t) = \iint A(k_x,k_y)\cos(k_x x + k_y y - \omega(k_x,k_y)t + \varepsilon)dk_x dk_y \qquad (4.1)$$

where, ε is a random phase term. The resultant wave-height varies in two orthogonal spatial co-ordinates x, y and with time, t. The wavenumber and frequency of each wave component is related through the dispersion relation. The TLS instrument is sensitive to capillary-gravity waves which in deep water obey a dispersion relation of the form;

$$\omega^2 = gk + \frac{\varphi}{\rho}k^3 \qquad \text{where} \qquad k = \sqrt{k_x^{\,2} + k_y^{\,2}} \qquad (4.2)$$

φ is the surface tension and ρ is the water density, Kinsman(1965).

The wave height wavenumber spectrum, F($\underline{k}$), is defined as the Fourier transform of the covariance as shown by Phillips (1958);

$$F(\underline{k}) = \beta k^{-4} \qquad (4.3)$$

where β is a constant of value 0.008. For simplicity, Phillips' (1958) spectrum has been used in the development of this model, although other spectral forms could easily be substituted.

Two methods for implementing a sea surface model were identified. The first would generate the surface through the summation of cosine components at each position in the wave-field space. The second would use the Fourier transform of the wavenumber spectrum to generate the surface amplitude as a function of wavenumber. The second method was chosen. It not only allows the efficient introduction of features at particular wavenumbers but also provides an easy method for the complexity of the entire input spectrum to be varied rapidly. This is especially attractive since

the wavenumber spectrum is not fully defined and its exact form is still open to debate as indicated in section 2.3.2. Data obtained during a deployment of the TLS in the field will be Fourier transformed to provide wave slope power spectra and the above approach is consistent with this.

Returning to equation 4.1 and expressing the integral as the real part, *Re*, of a complex function then:

$$\xi(x,y,t) = \mathrm{Re} \iint \left\{ A(k_x,k_y) e^{i(-\omega(k_x,k_y)t+\varepsilon)} \right\} e^{i(k_x x + k_y y)} dk_x dk_y \tag{4.4}$$

This is equivalent to the two dimensional Fourier transform of the bracketed term $I(k_x,k_y)$, within the integral which is;

$$I(k_x,k_y) = A(k_x,k_y)\cos\{P(k,t)\} + iA(k_x,k_y)\sin\{P(k,t)\} \tag{4.5}$$

where $P(k,t)$ is a phase term, allowing the model to vary temporally:

$$\underline{P}(k,t) = \varepsilon - \left(\sqrt{kg + \frac{\varphi}{\rho} k^3} \right) t \tag{4.6}$$

The amplitude $A(k_x,k_y)$ is given by the wavenumber spectrum and on transformation will provide a spatial description of the surface. The dispersion relation is included in the phase term. The dispersion relation is important as it will be used to relate the wavenumber of a particular wave to its frequency. As time is allowed to vary, the waves will propagate through the model at a frequency dependent on their wavenumber. A random term is also included in the phase term. The random term determines the relative distribution of the sinusoidal components in the Fourier transformed image. Without it, the waves would be distributed in a manner unrepresentative of a real sea surface. Little is known about the true form of this random phase term. This is a consequence of the investigation on electromagnetic backscatter from the sea surface focusing studies towards providing information on the amplitude rather than the phase relationship of the sea surface. The random phase term will influence the distribution of wave heights and wave slopes. As these tend to be Gaussian it is reasonable to assume for this model that the random phase term is Gaussian in distribution. The term is also cyclic and consequently is assumed to be distributed between 0 and 2π.

$A(k_x,k_y)$ and $P(k,t)$ provide the inputs to the simulation and $\xi(x,y,t)$ the output. The numerical Fourier transformation of $I(k_x,k_y)$ calculated discretely is:

$$\xi(x,y,t) = \mathrm{Re}\,\Delta k_x \Delta k_y \sum_{k_x}\sum_{k_y} I\left(k_x,k_y\right)e^{i(k_x x+k_y y)} \tag{4.7}$$

where Δk is the wavenumber sample interval.

The matrix $I(k_x,k_y)$ may be calculated from equations 4.3, 4.5 and 4.6 for discrete intervals of k_x and k_y. For each value of k, a random term ε is included. This allows the effective simulation of the randomness associated with the sea surface. For a single Fourier transform, t is kept constant. To allow the surface to evolve temporally, the value of t is varied within the phase term $P(k,t)$ and the Fourier transform of $I(k_x,k_y)$ is repeated.

4.4 Implications of a Limited Computing Run-Time on the Model

The TLS instrument is sensitive to a wavenumber range of 6 m^{-1} to 897 m^{-1} which is equivalent to 1 m to 7 mm in wavelength. The fast Fourier transform (FFT) requires the matrix size to be a power of two. The wavenumber resolution is determined by the sample size. If we set the wavenumber resolution to 1m^{-1} which is a reasonable value, then the minimum matrix size which can be employed without compromising this wavenumber range and resolution is therefore 1024. Reducing the resolution will reduce the size of this matrix. However, any reduction in resolution will be felt strongly at lower wavenumbers where the spectrum varies more rapidly. The longer wavelength waves will not be properly defined, limiting the applicability of the model. The Towed Laser Slopemeter was towed at a speed of 1ms^{-1}. If a one dimensional time varying sea surface is to be modelled over say 1024 time steps, then 1024 FFT's of a 1024 number array are needed. Similarly, for a two dimensional time varying wave field 1024 FFT operations of a 1024 by 1024 matrix are required.

The size and duration of the numerical operations required to generate the model presented problems relating to the capacity of the computer memory and its speed. Two methods were explored in an effort to reduce the run-time. The first used a logarithmic scale on which the amplitude and phase matrices were constructed. This curtailed the slowly varying high frequency components without loss of the low wavenumbers. However, the mathematical complexity in interpreting the resultant wave field restricted its effectiveness. The second approach exploited the sampling method employed by the TLS instrument. The TLS samples the surface along a transect, the position in the transect varying as a time series. The model generates a set of sea surface

realisations which are incremented in time. Each realisation provides a value of wave slope at a single position without attempting to generate slopes at any other locations in the model field at that instant. The next value of wave slope occurs at the adjacent position along the transect. This is taken from the next realisation of the sea surface. Therefore, each realisation provides a single sample of the wave field, its position being defined by the transect described by the TLS. If the Fourier transform employed could be altered to provide a single output at the required position then the run-time could be minimised. This required a knowledge of the internal operation of the fast Fourier transform. Appendix A contains a mathematical exposition of the FFT used as the basis of the model. In the next section, a pictorial representation of the process is introduced to provide a better understanding of the fast Fourier transform.

4.4.1 The Fast Fourier Transform and the Signal Flow Diagram

The fast Fourier transform was developed by Cooley and Tukey (1963) as a technique for reducing the number of arithmetic operations associated with the computation of discrete signals using the then conventional discrete Fourier transform (DFT). Consider the discrete one dimensional Fourier transform;

$$X(n) = \sum_{m=0}^{M-1} x_0(m) e^{-i2\pi nm/M} \tag{4.8}$$

where; M is the matrix size, the number of values to be Fourier transformed; x_0 is the studied observable dependant upon m; and X is the Fourier component of x dependent on n. The Fourier component of m is n. The summation of the real and imaginary sinusoidal terms of amplitude $x_0(m)$ over all m gives $X(n)$.

Let $W = e^{-i2\pi/M}$ therefore $X(n) = \sum_{m=0}^{M-1} x_0(m) W^{nm}$ (4.9)

Expanding equation 4.9 for M=4 then;

$$\begin{aligned}
X(0) &= x_0(0)W^0 + x_0(1)W^0 + x_0(2)W^0 + x_0(3)W^0 \\
X(1) &= x_0(0)W^0 + x_0(1)W^1 + x_0(2)W^2 + x_0(3)W^3 \\
X(2) &= x_0(0)W^0 + x_0(1)W^2 + x_0(2)W^4 + x_0(3)W^6 \\
X(3) &= x_0(0)W^0 + x_0(1)W^3 + x_0(2)W^6 + x_0(3)W^9
\end{aligned} \tag{4.10}$$

The FFT permits equations 4.10 to be given by

$$\begin{aligned} x_1(0) &= x_0(0) + x_0(2)W^0 \\ x_1(1) &= x_0(1) + x_0(3)W^0 \\ x_1(2) &= x_0(0) + x_0(2)W^2 \\ x_1(3) &= x_0(1) + x_0(3)W^2 \end{aligned} \quad \text{and} \quad \begin{aligned} X(0) &= x_1(0) + x_1(1)W^0 \\ X(1) &= x_1(0) + x_1(1)W^2 \\ X(2) &= x_1(2) + x_1(3)W^1 \\ X(3) &= x_1(2) + x_1(3)W^3 \end{aligned} \tag{4.11}$$

The steps between equations 4.10 and 4.11 are given in appendix A or they can be found in Brigham (1988). Comparing both sets of equations, it is apparent that the number of multiplications has been reduced from 16 to 8. The number of multiplications, which is proportional to computation time can be further reduced, by capitalising on the relationship between pairs of equations. The value of $x_1(0)$ maybe computed by one addition and one multiplication;

$$x_1(0) = x_0(0) + W^0 x_0(2) \tag{4.12}$$

as is $x_1(2)$. However, since $W^0 = -W^2$ and as $W^0 x_0(2)$ has been calculated for $x_1(0)$ then only one addition is required to compute $x_1(2)$:

$$\begin{aligned} x_1(2) &= x_0(0) + W^2 x_0(2) \\ &= x_0(0) - W^0 x_0(2) \end{aligned} \tag{4.13}$$

This reduces the one multiplication and one addition required to calculate $x_1(2)$ to a single addition. There is an equivalent reduction in the number of computations required to determine $X(n)$. Pairs of numbers exhibiting this relationship are referred to as dual-node pairs i.e. $x_1(1)$ and $x_1(3)$ are dual-node pairs. Since the computation of a dual-node pair is independent of other calculations it is possible to perform in-place computation and thus greatly reduce storage requirements by returning values computed to the original array. Equation 4.11 is simplified to:

$$\begin{aligned} x_1(0) &= x_0(0) + x_0(2)W^0 \\ x_1(1) &= x_0(1) + x_0(3)W^0 \\ x_1(2) &= x_0(0) - x_0(2)W^0 \\ x_1(3) &= x_0(1) - x_0(3)W^0 \end{aligned} \quad \text{and} \quad \begin{aligned} X(0) &= x_1(0) + x_1(1)W^0 \\ X(1) &= x_1(1) - x_1(1)W^0 \\ X(2) &= x_1(0) + x_1(3)W^1 \\ X(3) &= x_1(1) - x_1(3)W^1 \end{aligned} \tag{4.14}$$

The main requirement on the fast Fourier transform is that M, the matrix size has to be a factor of 2, i.e. $M=2^{\gamma}$, where γ is a positive integer. This requirement is outweighed by the reduction in computation time of the FFT when compared to the DFT. The number of multiplications required to calculate $X(n)$ is reduced from M^2 to $M\gamma/2$ and the number of additions is reduced from M^2 to $M\gamma$.

The signal flow diagram of figure 4.1 is a pictorial representation of steps in the calculation of $X(n)$ given by the set of equations 4.14. The input data, or data array, $x_0(m)$ is represented by a vertical column of nodes on the left hand side of the flow diagram. The array $x_1(m)$ forms the next column which is referred to as the first computational array. The nodes $x_2(m)$ which for $M=4$ is equivalent to $X(n)$ forms the next column and the second, and in this case the final, computational array. There are γ computational arrays in the signal flow diagram. The nodes $x_3(m)$ are scrambled and a final column represents the unscrambled output data array. The two solid lines entering a node are referred to as transmission paths. Each path brings a quantity from a previous node, multiplies it by W^p where $p=0,1..M-1$, and provides the input to the node in the next array. Absence of W^p from a transmission path within the diagram implies that $W^p=1$. Results entering a node from two transmission paths are combined additively. The signal flow diagram exhibits a degree of symmetry and it is this that is to be utilised in channelling the M inputs to a single output value in order to reduce computational time.

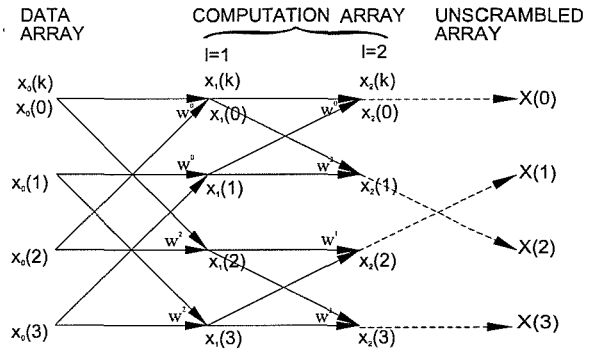

Figure 4.1 A N=4 radix 2 signal flow diagram with input data naturally ordered

4.4.2 Reduction of the FFT Computation Time

The TLS samples the surface along a space-time trajectory. For each surface realisation only one sample point is required. To reduce the number of computations and hence the run-time of the simulation an effort was made to identify a method which would give a single output from the

FFT of $I(k_x,k_y)$. To generate this single output not all the computations within the FFT will be required. By stepping back through the signal flow diagram from a specific output position to the initial input array the computational steps can be investigated and a procedure in reducing run-time identified. Figure 4.2 gives an example of a signal flow diagram for an M=8 matrix. Referring to this figure, a single output requires that the second computational array will contribute values from two nodes, the first computational array will contribute values from four nodes and initial data array contributes values from all nodes. Each column can be numbered to reflect the number of nodes it uses in the calculation of a single output. This quantity is α. The nodes in the signal diagram that contribute to the calculation of the value at a given single output position can be identified using α. An example is now given.

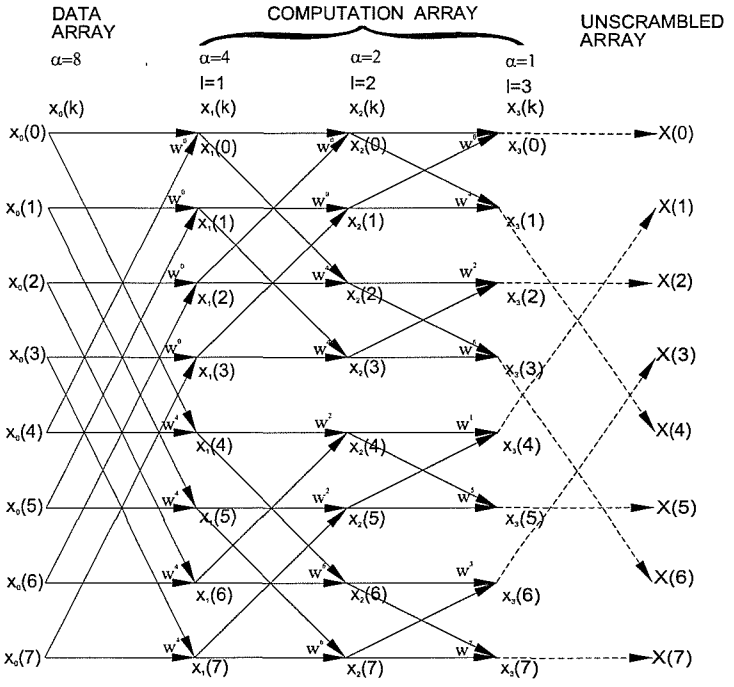

Figure 4.2 A signal flow diagram with computational arrays assigned values for the number of nodes that contribute to the final output.

Suppose we require the value of the node $x_3(2)$ in the output array. All the values in the data array are needed. For the first computational array with α=4 nodes $x_0(0)$ to $x_0(3)$ will contribute to the calculation of the final output. This is because m=2 in $x_3(2)$ falls in the range 0 to α-1. If m in $x_3(m)$ had been greater than α then nodes $x_0(\alpha)$ to $x_0(2\alpha-1)$ would have been need in the calculation. For the second computational array α=2 and nodes $x_1(\alpha)$ to $x_1(2\alpha-1)$ contribute to the output value at $x_3(2)$. If the output value at m=5 in $x_3(m)$ was required then nodes $x_1(2\alpha)$ to $x_1(3\alpha-1)$ would have been used in the calculation. It is apparent that the nodes which contribute to the

calculation of a single output value at $x_3(m)$ can be found by determining the range, in multiples of α, in which m falls. This method reduces the number of steps required to find the output value at a single point in the matrix. A problem exists with this method. If an output is produced at a position which needs to be unscrambled, the value at this point will correspond to a position in the output array which is not required. After further consideration of this problem a second method was sought utilising an FFT technique not requiring the unscrambling of the output data array.

The fast Fourier transform discussed previously, and in appendix A, described the radix-2 or Cooley-Tukey algorithm. An investigation of other FFT methods for generating Fourier data, such as the prime factor algorithm, offered slight increases in computational speed but sacrificed the simplicity of implementation. In addition the symmetry of the radix-2 method, apparent from its signal flow diagram, was also compromised. A method which scrambled the data prior to its input into the FFT was found. This eliminated the need to unscramble the data in the output array. The method is referred to as an inverse data order radix-2 FFT, as opposed to the input data being in a natural order. The corresponding signal flow diagram is shown in figure 4.3.

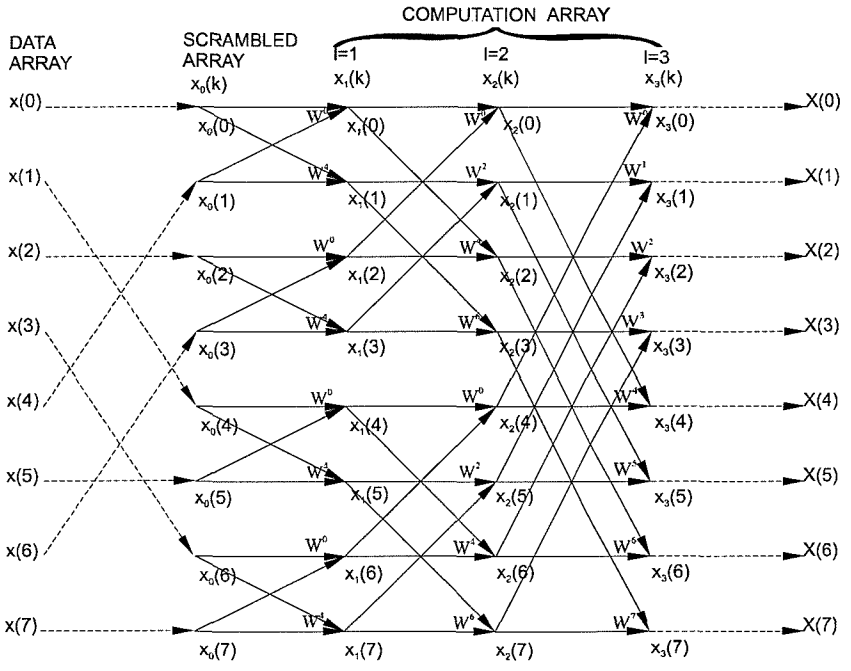

Figure 4.3 A N=8 radix 2 signal flow diagram with input data in inverse order.

The symmetry associated with the inverse data ordered method is not as simple as in the previous, naturally ordered case but the scrambling of the data at the input removes any additional complication in trying to find the correct position of a value at the end of the calculation. Again, a method for reducing the number of computations needed to generate a single output was sought.

Both m and n in x(m) and X(n) can be expressed in their equivalent binary form. This is shown in figure 4.4.

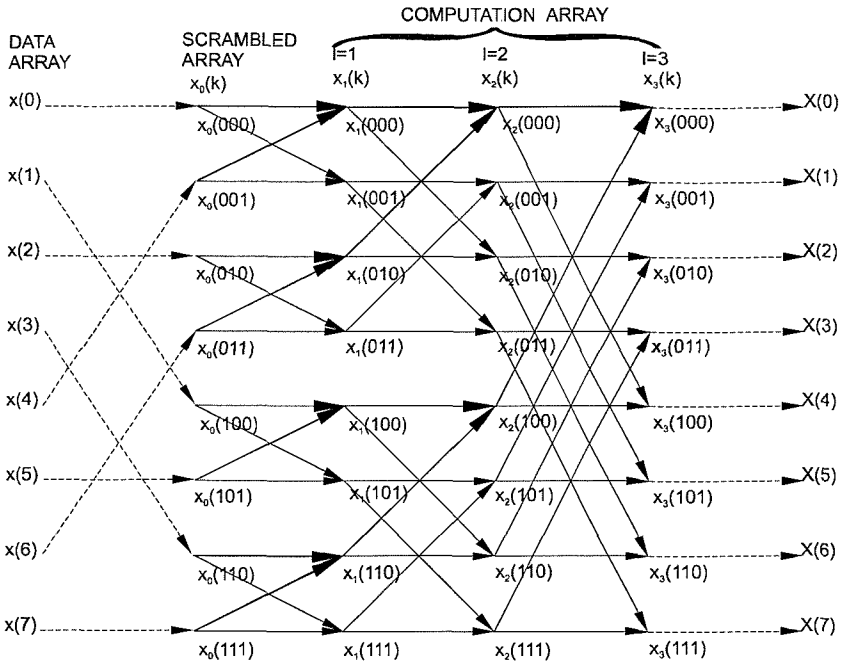

Figure 4.4 A signal flow diagram with nodes expressed in their equivalent binary form.

The new method is illustrated for a M=8 FFT array where $M=2^{\gamma}$ and γ=3, and an output node *X(0)*. All input values are required. The contributing nodes in the first computational array are found by comparing the first, or the right hand side, γ-2, bit of the binary number m in $x_1(m)$ with the equivalent bit in the binary value of n in the required output node *X(n)*. Nodes in the second computational array required in the computation of the final output are found in a similar fashion but this time the first and second, or the two further most right, γ-1, bits are compared. Finally, $x_3(m)$ contributes to the output of *X(m)* if the binary values of m and n agree. This provides a method for determining the nodes and hence the calculations needed to find the Fourier transform value at a single output position. The technique bit-shifts node numbers to the left and compares them to the equivalent bit-shifted number of the final output node. If agreement is reached, then the node is needed in the calculation of the output value. The number of bits to be shifted is determined from the value of γ-l where l is the column number of the computational array. By shifting m and n within *x(m)* and *X(n)* by the required number of bits to the left, a method for identifying the components needed to generate a value at the required output position was found. This reduced the number of computations and, applying the same calculation as Nussbaumer (1981), represents a 5 to 1 reduction in processing time for a radix-2 M=1024 FFT.

This method speeds up the calculation of the slope at a particular point on a transect. The algorithm needed to calculate the amplitude, $A(k_x,k_y)$, and phase, $P(k,t)$, have been given in equations 4.3 to 4.6. These are used to determine the real and imaginary components in the Fourier domain and on transformation will give a simulated sea surface. As noted in section 4.3 the sea surface is purely real. To enable the model to generate a purely real surface the amplitude and phase input matrices must be constructed in the correct manner.

4.5 Generation of a Purely Real Surface

The sea surface is a real function with no imaginary components. To ensure that the output of the Fourier transform employed was purely real, certain properties had to be met by the amplitude and phase inputs. For the one dimensional case the first parameter of each array is the D.C. component which represents the average of the values contained in the matrix. The $M/2$ position within the array contains the Nyquist frequency, or NF, which is the highest frequency present in the array. The input data are contained in the array positions 2 to $M/2$. The negative array positions follow the Nyquist frequency and must, in the case of the amplitude matrix, be symmetric about the Nyquist frequency. The phase components are anti-symmetric about the Nyquist frequency which is zero, as is the corresponding D.C. component. The final amplitude and phase constructions are shown in figure 4.5. The phase was varied from 0 to 2π and not $-\pi$ to π which was found to give a higher concentration of waves at the origin of the simulated surface.

$$\begin{bmatrix} DC & A_{02} & A_{03} & A_{04} & NF & A_{04} & A_{03} & A_{02} \end{bmatrix} \quad \text{Amplitude}$$

$$\begin{bmatrix} DC & P_{02} & P_{03} & P_{04} & NF & -P_{04} & -P_{03} & -P_{02} \end{bmatrix} \quad \text{Phase}$$

Figure 4.5 One-dimensional amplitude and phase array construction. Letters represent numbers and the negative sign indicates anti-symmetry.

A true sea surface has two rather than one spatial dimension. The two dimensional fast Fourier-transform applies one dimensional FFTs to the rows of the matrix and then to its columns. Consequently, the methods for saving computing run-time could be incorporated within the two-dimensional case without need of revision. However, the construction of amplitude and phase symmetries for the two-dimensional case was more complex than their one-dimensional counterparts. A purely real arbitrary random matrix was Fourier transformed into the frequency domain. The structure of the real and imaginary matrices produced on transformation were used to determine the method of construction of the amplitude and phase matrices in our model.

The phase matrix must be constructed in the following manner: Assuming that the top row which contains the values P_{1j}, j=1 to M, the far most left-hand column containing values P_{i1}, i=1 to M, and the diagonal of the matrix containing values P_{ij}, j=i=1 to M, are one dimensional arrays in their own right, then each must be anti-symmetric about its Nyquist position. The Nyquist frequency and the D.C. component are zero for all three arrays. The region above the diagonal but below the top row of the matrix is filled with a set of numbers which have anti-symmetry with the numbers below the diagonal but outside the far left-hand column. This anti-symmetry is about the diagonal such that the value at position P_{ij} corresponds with the value at position $P_{M+2-i\ M+2-j}$. The amplitude matrix is symmetric in the same manner as the phase matrix is anti-symmetric. The final amplitude and phase constructions are displayed in figure 4.6.

$$\begin{bmatrix} DC & A_{12} & A_{13} & A_{14} & NF & A_{14} & A_{13} & A_{12} \\ A_{21} & A_{22} & A_{23} & A_{24} & A_{25} & A_{26} & A_{27} & A_{28} \\ A_{31} & A_{78} & A_{33} & A_{34} & A_{35} & A_{36} & A_{37} & A_{38} \\ A_{41} & A_{68} & A_{67} & A_{44} & A_{45} & A_{46} & A_{47} & A_{48} \\ NF & A_{58} & A_{57} & A_{56} & NF & A_{56} & A_{57} & A_{58} \\ A_{41} & A_{48} & A_{47} & A_{46} & A_{45} & A_{44} & A_{67} & A_{68} \\ A_{31} & A_{38} & A_{37} & A_{36} & A_{35} & A_{34} & A_{33} & A_{78} \\ A_{21} & A_{28} & A_{27} & A_{26} & A_{25} & A_{24} & A_{23} & A_{22} \end{bmatrix}$$

Amplitude

$$\begin{bmatrix} DC & P_{12} & P_{13} & P_{14} & NF & -P_{14} & -P_{13} & -P_{12} \\ P_{21} & P_{22} & P_{23} & P_{24} & P_{25} & P_{26} & P_{27} & P_{28} \\ P_{31} & -P_{78} & P_{33} & P_{34} & P_{35} & P_{36} & P_{37} & P_{38} \\ P_{41} & -P_{68} & -P_{67} & P_{44} & P_{45} & P_{46} & P_{47} & P_{48} \\ NF & -P_{58} & -P_{57} & -P_{56} & NF & P_{56} & P_{57} & P_{58} \\ -P_{41} & -P_{48} & -P_{47} & -P_{46} & -P_{45} & -P_{44} & P_{67} & P_{68} \\ -P_{31} & -P_{38} & -P_{37} & -P_{36} & -P_{35} & -P_{34} & -P_{33} & P_{78} \\ -P_{21} & -P_{28} & -P_{27} & -P_{26} & -P_{25} & -P_{24} & -P_{23} & -P_{22} \end{bmatrix}$$

Phase

Figure 4.6 Two-dimensional amplitude and phase array construction. Letters represent numbers and the negative sign indicates anti-symmetry.

4.6 Wave Slope Model

So far, the Fourier transforms of amplitude and phase have only been used to generate values of sea surface wave height. The TLS instrument gives a direct measure of surface gradient and this needs to be incorporated into the model. Numerical differentiation of surface wave heights is imprecise; the simulated wave height is essentially a discrete signal and because it is not continuous cannot be differentiated accurately to give wave slope. In addition numerical differentiation would require that more than one output component be produced, thus reducing program speed. A better approach is to use the Fourier relationship;

$$\frac{dx(m)}{dn} \Leftrightarrow -inX(n) \tag{4.15}$$

where $\Leftrightarrow$ is used to represent a Fourier relationship, to give the differential of $x(m)$ on transformation. Applying this relationship to the wave height, $\xi(x,y)$, two orthogonal components of wave slope S_x and S_y can be calculated;

$$S_x = \frac{d\xi(x,y)}{dx} \Leftrightarrow -ik_x A(k_x,k_y) \tag{4.16}$$

and

$$S_y = \frac{d\xi(x,y)}{dy} \Leftrightarrow -ik_y A(k_x,k_y) \tag{4.17}$$

where x and y are orthogonal positions, k_x and k_y are orthogonal components of wavenumber and $A(k_x,k_y)$ is the wave amplitude. The amplitude matrix is multiplied by respective wavenumber values to form a matrix that can be used to give wave slope. The wave slope matrix is constructed in a similar manner to that of the phase matrix.

4.7 Wave Directionality

The model was developed using the Phillips 1958 wavenumber spectrum (equation (2.14)). Although, initially used to limit the complexity of the model, this relationship falls short of describing an explicit directionality in waves on the sea surface. Consequently when this spectral relationship is used within the sea surface model it describes an isotropic surface. Phillips recognising the limitations of this relationship developed a second formulation for the

wavenumber spectrum (Phillips (1985)). This relationship explicitly includes a directionality within the spectrum and is given by:

$$F(k,\theta_w) = \beta \cos^{\nu} \theta_w u_* g^{-\frac{1}{2}} k^{-\frac{7}{2}} \tag{4.18}$$

where ν is the beam width, or spreading parameter, u_* is the wind frictional velocity, g is gravity at the earth's surface and θ_w is the direction of wave propagation relative to the wind. The $\cos^{\nu}\theta_w$ term introduces directionality into the spectrum. Varying the beam width parameter varies the level of anisotropy in the spectrum. Typically values of 0 to 3 for the beam width parameter were used in the numerical model. For the numerical model the direction of wave propagation was taken relative to the direction of travel of the TLS and calculated using the relation:

$$\arctan\frac{k_y}{k_x} \tag{4.19}$$

4.8 Summary of the Development of the Sea Surface Model

The main features of the new sea surface roughness model are as follows:

- A purely real spatial sea surface realisation is provided by the Fourier transform of complex components of wave amplitude and phase.
- The wave amplitude as a function of wavenumber is determined from the square root of the power spectrum.
- A random phase term is included to give the surface a degree of randomness.
- The spatial wave field can evolve temporally by the inclusion of a frequency-time term. This is added to the random phase term.
- The frequency is related to the correct wavenumber through the dispersion relation.
- For each time increment the frequency-time term has to be re-calculated and the Fourier transform of complex components of wave amplitude and phase repeated.

To ensure that the wave field is purely real, amplitude and phase matrices have to be constructed as follows:

- For a one dimensional surface profile the amplitude must be symmetric and the phase anti-symmetric about the Nyquist frequency. The D.C. and Nyquist frequency components are zero.

- For a two dimensional surface profile, the top row, the far left hand column and the diagonal arrays of the phase matrix are anti-symmetric about their Nyquist frequencies whilst for the amplitude matrix they are symmetric. The remaining region within the phase matrix is anti-symmetric about the diagonal array. This region is symmetric about the diagonal for the amplitude matrix. Again, the D.C. and Nyquist frequency components are zero. This will give the surface wave profile in terms of wave height.
- If wave slope is required, the amplitude matrix is multiplied through by respective components of wavenumber and constructed in a similar manner to the phase matrix.

Three types of sea surface model can be produced;

- a spatial wave field at a given time as described by an instantaneous measurement of the sea surface,
- a time series of measurements at a fixed position as sampled by a fixed probe,
- a set of single point measurements along a position-time trajectory as described by the TLS instrument moving over the sea surface.

For the last two models temporal information is required. However, only one spatial position is needed reducing computing run-time. The number of calculations needed in the FFT is reduced using a bit reversal technique.

Before the models can be applied to the task of investigating the effects on the wavenumber spectrum as a result of the Towed Laser Slopemeter following a transect across the surface, they need to be tested to ensure that they are numerically and oceanographically valid. An example of a surface wave field generated by the new numerical model is given in figure 4.7.

4.9 Testing and System Checks

It is crucial that the model be tested firstly for accuracy in the implementation of the Fourier transformations used and secondly by verifying that it produces credible ocean surface spectra. The successful Fourier transformation of the input data, in both amplitude and phase, was confirmed by comparing the results from the FFT used in the simulation with those obtained using a commercially available FFT package; MATLAB 4.1. Both programs were supplied with matching input matrices and any discrepancies in the resulting data sets were corrected through the identification of, and alterations to, the part of the program responsible. This procedure was used to develop and test the Fourier transforms within the three types of sea surface model.

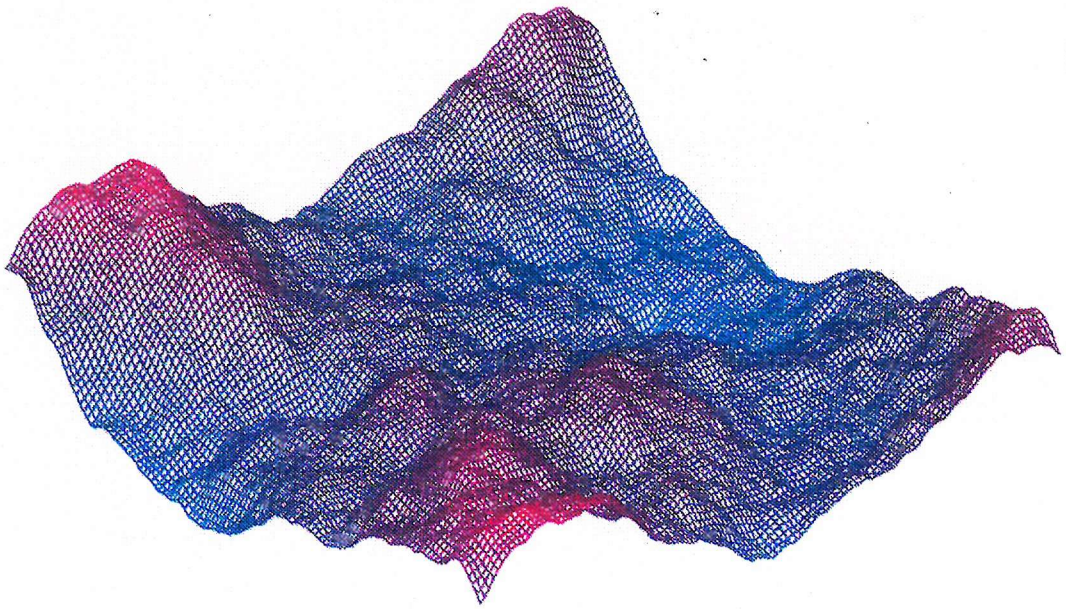

Figure 4.7 An example of a surface wave field generated by the sea surface model

The second series of checks centred on determining whether the results were oceanographically credible. This involved comparing the spectral results obtained from the simulated wave field with that used as an input in the software. For spatial wave field simulations, a transect was taken through a single surface model to find the power spectrum. This was repeated for a number of different surface realisations having identical properties but different random phase components. The derived spectra were averaged to reduce random fluctuations and to enhance the signal as would be done with real oceanographic data sets. The results were then compared with the expected forms. The wave height and wave slope wavenumber spectra produced from the spatial wave field model are compared with the initial input spectrum in figure 4.8. A two dimensional wave height spectrum proportional to k^{-4} and a two dimensional wave slope spectrum proportional to k^{-2} were used as inputs to the simulation which, in one dimension, will give wave height and wave slope spectra proportional to k^{-3} and k^{-1} respectively (Phillips (1958)). Good agreement between the expected one dimensional spectra and the power spectra calculated from the output of this simulation is seen from figure 4.8.

Analysis of frequency spectra from the model provided a second check. A time series of single point measurements of the wave height and wave slope components were made. From the data, power spectra were calculated and averaged over different surface realisations. Unlike the spatial case, an explicit frequency spectrum does not provide an input to the simulation. The output frequency spectra of the wave height and wave slope are plotted against the equivalent spectra derived from the input wavenumber spectra in figure 4.9. To aid the comparison of these plots a gravity, rather than gravity-capillary, dispersion relation was used for this case. A two dimensional wave height spectrum proportional to k^{-4} and a two dimensional wave slope spectrum proportional to k^{-2} will give wave height and wave slope frequency spectra proportional to ω^{-5} and ω^{-1} respectively (Kinsman (1965)). Good agreement between the input and output curves for both the wave height and wave slope spectra is seen in figure 4.9.

These series of checks helped in the development and final testing of the model, before the analysis of spatial-temporal wave measurements, an example of which is given in figure 4.10. For all the graphs, the maximum wavenumber was 897 m^{-1} and the maximum sample frequency was 250Hz. A Fourier matrix of 1024 x 1024 was used. An average of one hundred output power spectra was made. A gravity dispersion relation was used for the purely temporal simulation to simplify the comparison of input and output spectra. Both the spatial and spatial temporal models used the capillary-gravity dispersion relation which is the default relation throughout the thesis. The simulations were written in the ANSI standard C programming language.

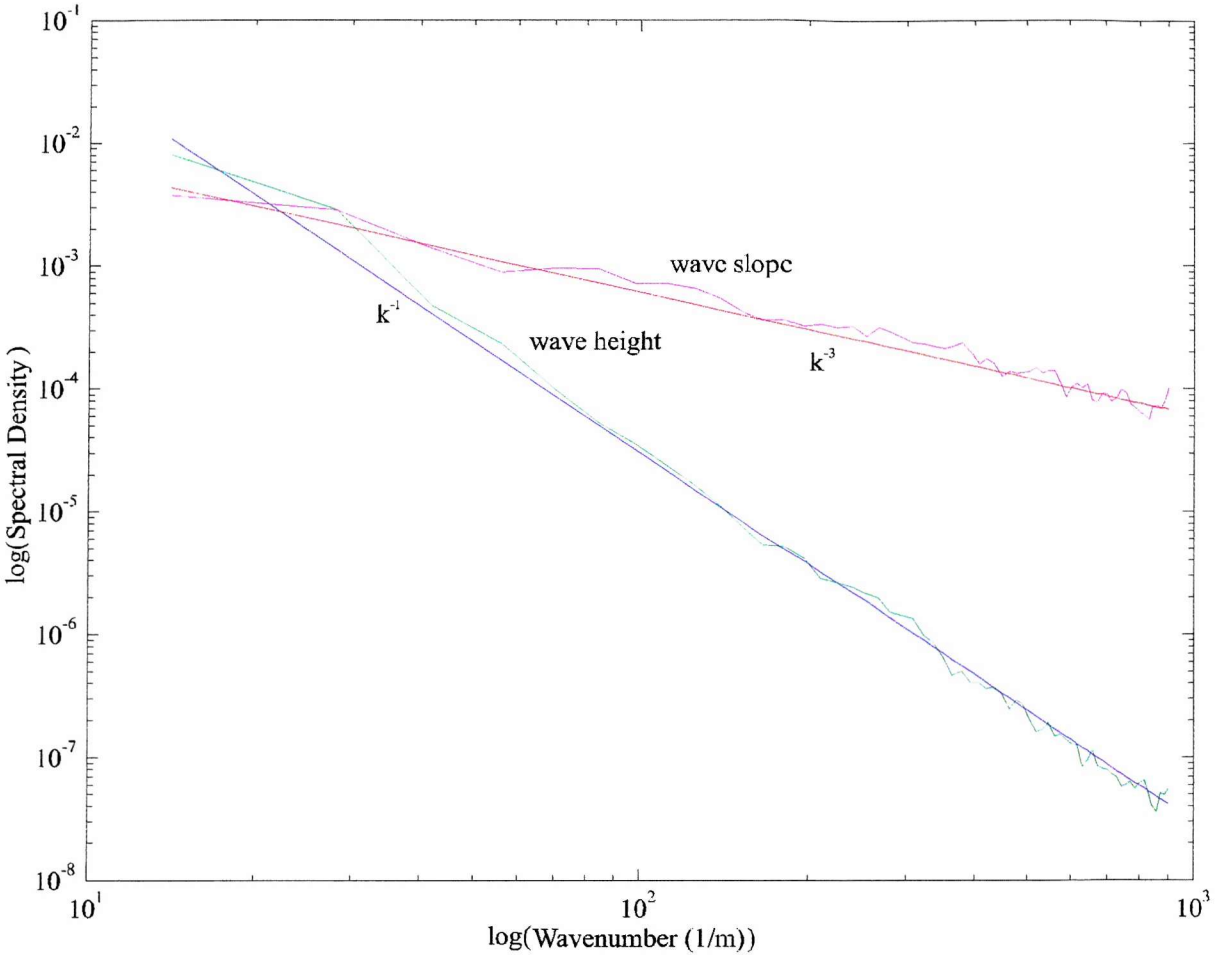

Figure 4.8 Wave height and wave slope wavenumber spectra (curved) produced by the spatial wave field model together with corresponding spectral inputs (straight lines) k^{-3} and k^{-1}, respectively.

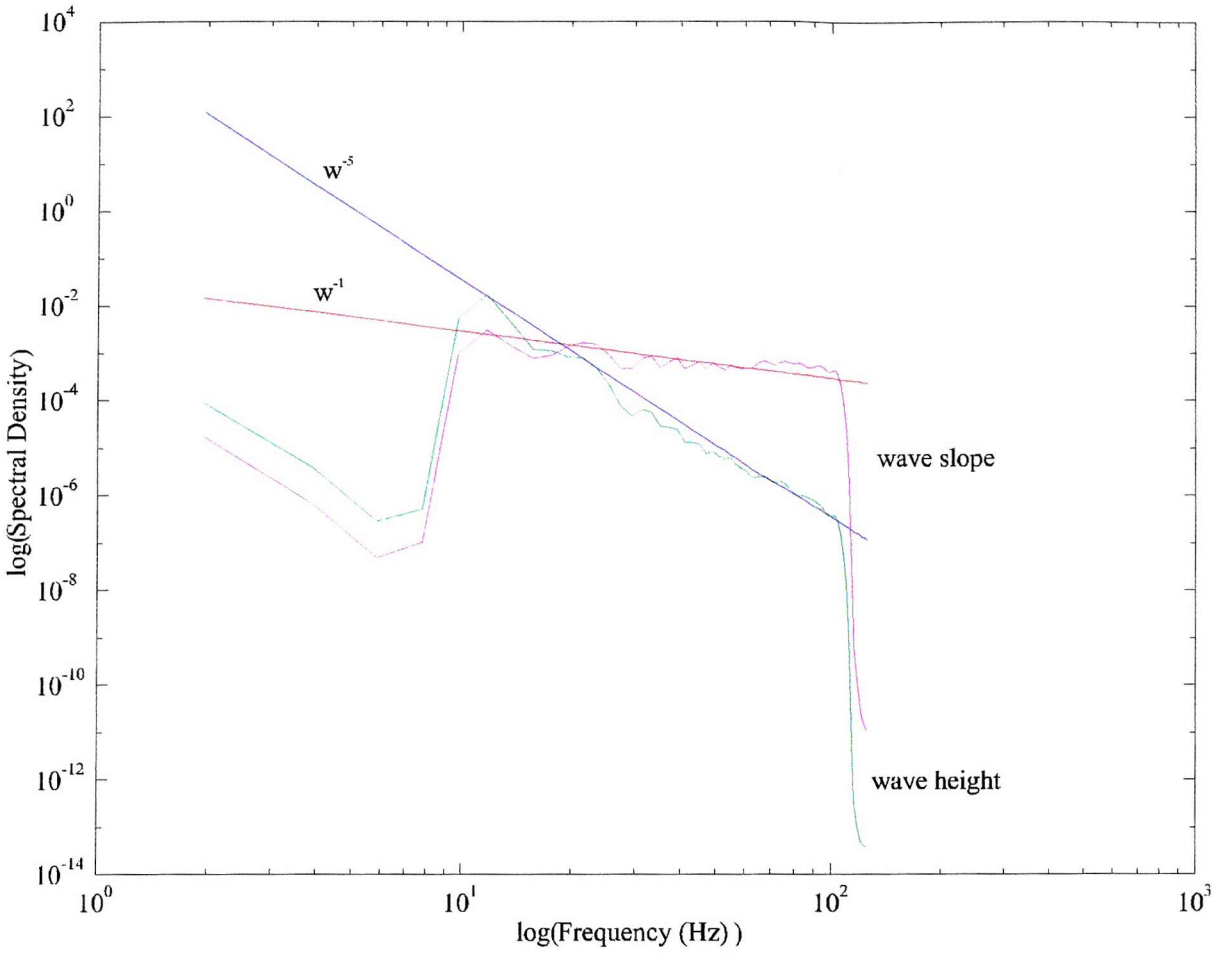

Figure 4.9 Wave height and wave slope frequency spectra (curved) produced by the temporal wave field model together with corresponding spectral inputs (straight lines) ω^{-5} and ω^{-1}, respectively.

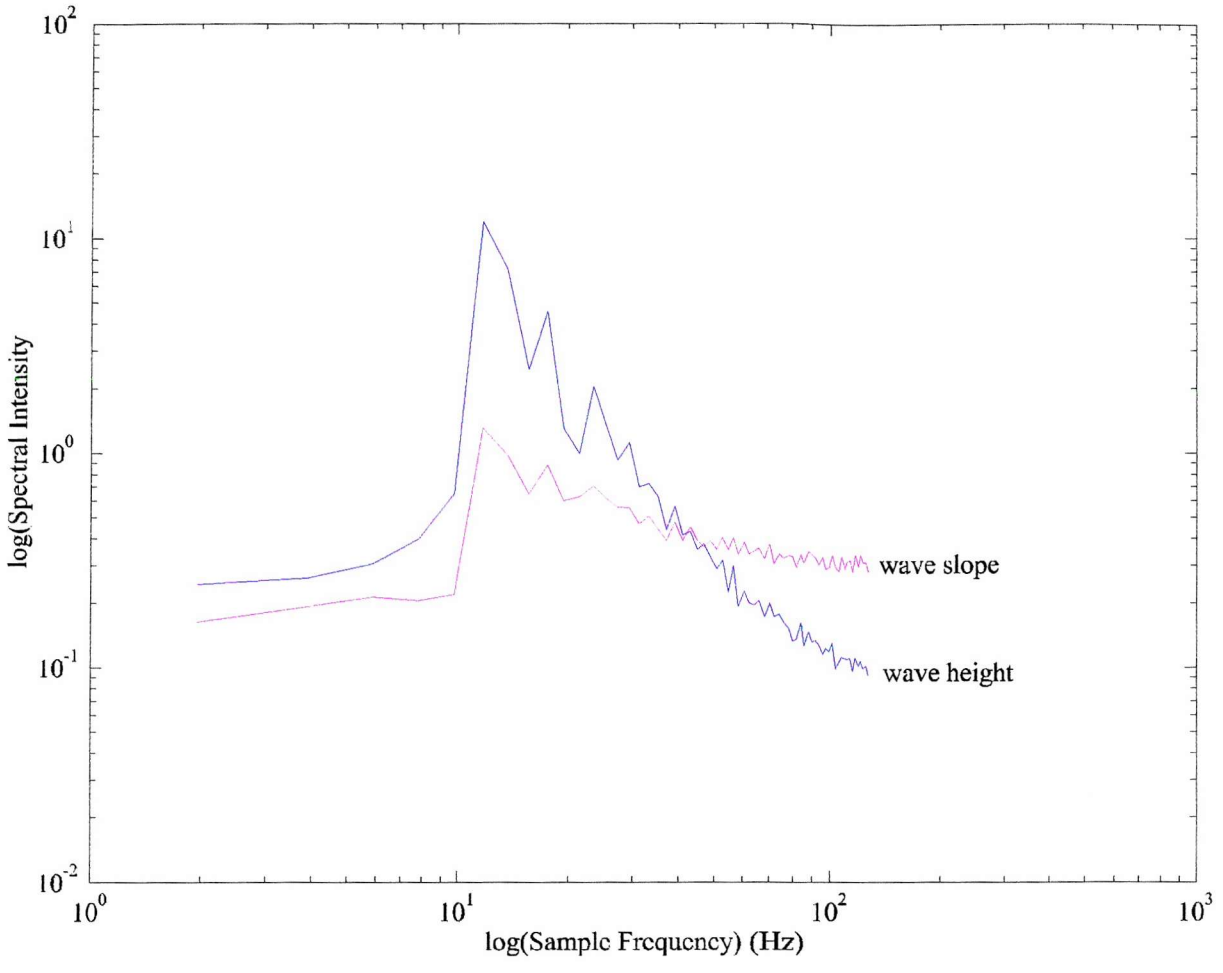

Figure 4.10 Wave height and total wave slope wavenumber-frequency hybrid spectra produced by the spatial-temporal wave field model.

4.10 Discussion

A set of models capable of simulating the sea surface from the perspective of instantaneous and stationary measurements and a time series of observations made along a transect through the wave-field have been developed. These models will be used to investigate the effect of the sampling strategy employed by the TLS instrument on the observed wave slope power spectrum. The models are spectrally correct. However, little is known about the phase relationship of sea surface waves. The phase is responsible for the wave shape and the relationship between waves of differing wavenumber. Our inability to correctly define the phase term of the model limits the extent to which the statistical values of the sea surface wave height and wave slope profiles can be said to represent those of a natural wave field. The impact of this is limited as the motivation for the development of the model was to investigate the effect of towing the TLS on the true wavenumber wave slope power spectrum. A cyclic random phase term with a normal distribution was used. This ensured a random rather than an unrealistically ordered wave profile which would have been obtained if no phase term had been included. The data from the model, unlike true sea surface data, will be correlated over all spatial and temporal scales. A degree of uncorrelation could have been simulated if Olgivy's (Olgivy (1988)) method had been adopted.

The model may also be combined with models of the physical interactions between the sea surface wave profile and ocean processes. Such a step would permit a greater understanding of the change to the observed TLS wave slope power spectrum within these modulated regions. It may be desirable to extended the model of a time evolving transect of the sea surface to a complete two dimensional time evolving sea surface model. The reduction in the number of computational steps within the FFT used to reduce the computing run-time would be inappropriate if such a model were to be implemented successfully. Instead, it may be necessary to develop the technique of gridding the phase matrices on a logarithmic scale, as discussed in section 4.4, to reduce the computing time needed to implement such a model.

The aims of this chapter have been achieved. A numerical model of the sea surface has been designed, developed and shown to work. We now turn to investigate the effects on the wavenumber spectrum of the TLS following a transect across a spatially and temporally varying wave field. The above simulation has been used extensively in this task.

Chapter 5

Towed Laser Slopemeter Spectral Reconstruction

5.1 Introduction

As emphasised in chapter 4 the Towed Laser Slopemeter makes a slow transect across the sea surface. The towing velocity which is approximately $1ms^{-1}$, is of the order of the phase velocity of the waves which it samples. This sampling therefore cannot be considered to be either purely spatial or purely temporal. This leads to the observed wave slope spectrum containing both frequency and wavenumber components. The effect of vehicle motion on this observed spectrum will be investigated and compared with the true wavenumber and wave frequency spectra.

Work has been done by Cartwright (1963) and Hughes (1978) to reconstruct true wavenumber spectra from observed spectra gained from data recorded by instrumentation describing a transect across the ocean surface. Cartwright's solution was to take the non-perturbed spectra from a wave buoy in a fixed location and, assuming that the wave field was unaltered, compare it to that of the Doppler shifted spectrum taken whilst the vessel was underway. From this data, a set of algorithms were obtained which allowed the conversion of the Doppler shifted spectrum to the true frequency spectrum. The technique was applied to swell waves and ignored the high frequency end of the wave spectrum. The problem at smaller wavelengths was addressed by Hughes (1978). Hughes assumed a form for the dispersion relation and made assumptions regarding the detector speed and the wave direction relative to the vessel to provide a numerical solution for the problem. In this chapter a new method is developed for deriving the true wavenumber spectrum in a way that does not rely on the assumption of a particular dispersion

relation, vehicle velocity or on any other instrumentation. This new method is compared with Hughes' approach.

5.2 Discussion and Formalization of the Doppler Shift Problem

To a first order, the sea surface wave height ξ(x,y,t) can be assumed to consist of a continuous superposition of cosine wave trains such that;

$$\xi(x,y,t) = \int_{-\infty}^{\infty} \int_{-\pi}^{\pi} A(k,\theta)\cos(k\cos\theta x + k\sin\theta y - \omega(k)t + \varepsilon)dkd\theta \qquad (5.1)$$

where x and y are Cartesian co-ordinates, and θ is the wave direction. The Towed Laser Slopemeter moves on a path at a speed u. If we define the x direction to be parallel to the direction of travel and the y direction orthogonal to this, then the position of the instrument will vary with time in the x direction;

$$x = x_o + ut \qquad \text{and} \qquad y = y_o \qquad (5.2)$$

where x_o and y_o are the initial position in the x and y direction respectively.

Substituting the relationships in equations 5.2 into equation 5.1 and defining x_o=0 and y_o=0 gives:

$$\xi(x,t) = \int_{-\infty}^{\infty} \int_{-\pi}^{\pi} A(k,\theta)\cos\left(-[\omega(k) - ku\cos\theta]t + \varepsilon\right)dkd\theta \qquad (5.3)$$

The term in the square brackets has been defined by St. Denis and Pierson (1953) as the *frequency of encounter* ω_e:

$$\omega_e = \omega(k) - ku\cos\theta \qquad (5.4)$$

An expression for the *wavenumber of encounter* may also be derived. It is assumed that the vessel moves with a constant speed and there is no motion in the y direction;

$$t = t_o + \frac{x}{u} \qquad \text{and} \qquad y = y_o \qquad (5.5)$$

where t_o is the time at the initial positions of x_o and y_o. This relationship is substituted into equation 5.3 and setting t_o=0 and y_o=0 then:

$$\xi(\underline{x},t) = \int_{-\infty}^{\infty}\int_{-\pi}^{\pi} A(k,\theta)\cos\left(\left[k\cos\theta - \frac{\omega(k)}{u}\right]x + \varepsilon\right)dkd\theta \tag{5.6}$$

The term in the square brackets is referred to as the *wavenumber of encounter* k_e and may be written as:

$$k_e = k\cos\theta - \frac{\omega(k)}{u} \tag{5.7}$$

Both the *wavenumber of encounter* and the *frequency of encounter* are dependent on the vessel speed and wave direction relative to the direction of travel. This dependence introduces a Doppler shift in their measurement. If we rearrange equation 5.6 to give:

$$\xi(x,t) = \int_{-\infty}^{\infty}\int_{-\pi}^{\pi} A(k,\theta)\cos\left(\left[1 - \frac{\omega(k)}{u(t)k\cos\theta}\right]k\cos\theta x + \varepsilon\right)dkd\theta \tag{5.8}$$

The term in the square brackets of equation 5.8;

$$c_f = \left(1 - \frac{\omega(k)}{uk\cos\theta}\right) \tag{5.9}$$

is defined as the *compression factor*, c_f. The *compression factor* acts on the true wavenumber to give the observed *wavenumber of encounter*. This action will lead to an increase, or a decrease, in the observed wavenumber relative to its true form. The degree of deformation is dependent on the wave direction relative to the vessel and the vessel speed. Having derived an expression for the distortion introduced in the measurement of the wave slope by the motion of the TLS instrument, we can now investigate the dependency of the compression factor on u and θ over the range of observed wavenumbers.

5.3 The Effect of Compression on Wavenumber

We now investigate the variation in the value of the compression factor for a changing vessel speed, u, whilst the value of θ, the angle between the wave direction and direction of travel of the

vessel, is kept constant. At u=0 a temporal measurement can be made. The TLS instrument will act as a stationary wave probe giving a measurement of the wave slope as a time series. The Fourier analysis of such a data set would give us information on the wave frequencies present. Deploying the TLS in this manner is impractical as the structure surrounding the instrument would interfere with the sea surface wave profile being observed. To minimise this structural interference the TLS instrument is towed.

A plot of the *compression factor* verses wavenumber for an increasing vessel speed at θ=0°, is given in figure 5.1. At slow speeds, the $\omega/k_x u$ term dominates the *compression factor*. The distortion in the observed wavenumber from its true value is at a maximum for small u. As the speed of the vessel increases, the $\omega/k_x u$ term decreases in its influence and the compression factor tends towards unity. At such high speeds, the sea surface is seen to evolve much more slowly and it can be assumed that the instrument makes an instantaneous measurement of the sea surface profile. The wave slope is measured as a series of positions and Fourier analysis will give information on the wavenumbers present. The values of observed and true wavenumbers will agree.

Limitation in the towing speed of the TLS instrument prevents it from making an instantaneous measure of the sea surface wave slope. There is a rapid change in the *compression factor* at low wavenumbers with the magnitude of the *compression factor* being largest at small values of k_x. As wavenumber increases, the *compression factor* reaches a minimum value before increasing again at high k_x values. This minimum is a result of the gravity-capillary wave dispersion relation and corresponds to the slowest propagating wavenumbers. A negative compression factor results when waves move with an apparent velocity greater than the Slopemeter.

Values of the *compression factor* for varying values of u for along-track components of wavenumber equal to $7m^{-1}$ and $897m^{-1}$ are given in table 5.1. These values correspond to the minimum, k_{min}, and maximum, k_{max}, values of wavenumber that can be measured by the TLS instrument. At low speeds, it is possible for waves to overtake the TLS and this leads to an increase in the observed wavelength of theses waves. For a towing speed of $1ms^{-1}$ the longer wavelength waves are observed to have a greater wavelength than their true value. The shorter waves can be overtaken by the TLS and their observed wavelengths will be smaller than their true value. If we were to increase the towing speed from $1ms^{-1}$ to $2ms^{-1}$ the value of the *compression factor* tends towards unity and the difference between observed and true values of wavenumber would be less. Increasing the towing speed will lead to an under-sampling of the surface and decrease the value of the highest wavenumber which can be observed by the TLS instrument. It is difficult to maintain a constant towing velocity and it must be appreciated that a change in speed from $1ms^{-1}$ to $2ms^{-1}$ leads to a four fold variation in the distortion of the wavenumber.

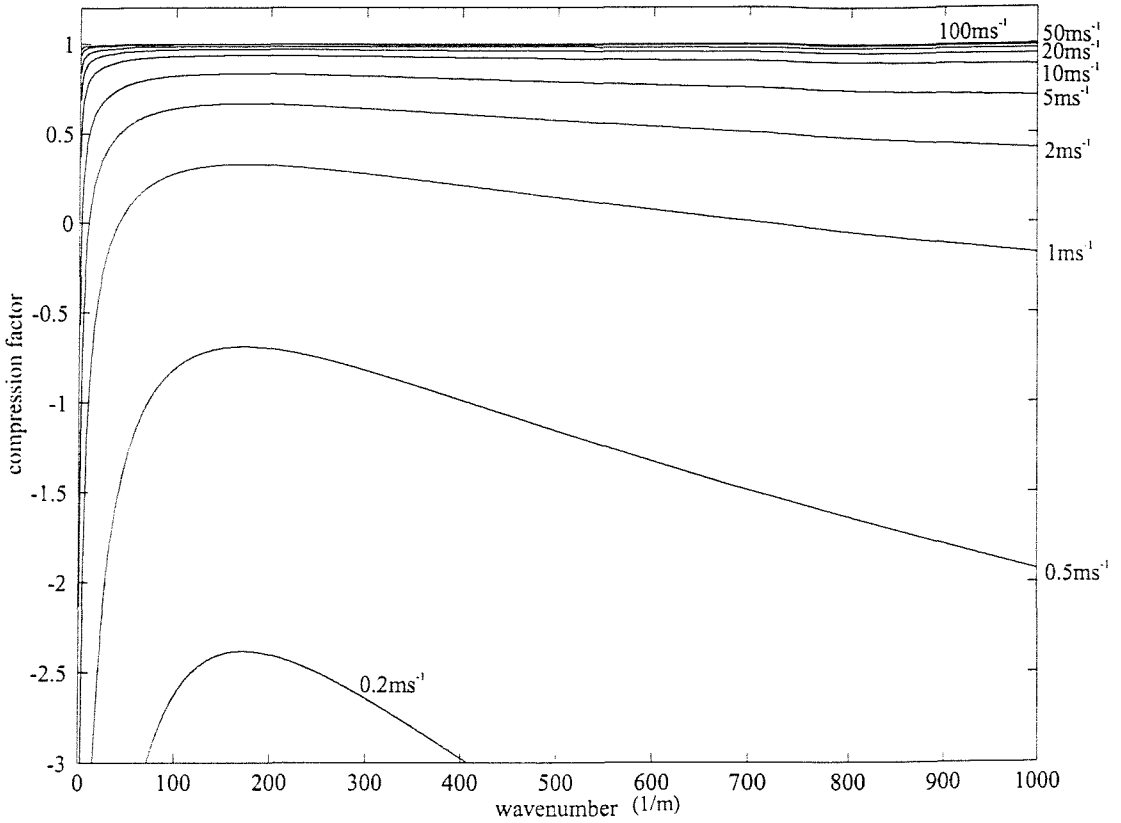

Figure 5.1 *Compression factor* verses wavenumber as a function of vessel speed for a constant wave direction of 0°.

U	Compression Factor	
[ms^{-1}]	$k=7m^{-1}$	$k=897m^{-1}$
0.1	-10.8481	-4.5713
0.2	-4.924	-1.7856
0.5	-1.3696	-0.1143
1	-0.1848	0.4429
2	0.4076	0.7214
5	0.763	0.8886
10	0.8815	0.9443
20	0.9408	0.9721
50	0.9763	0.9889
100	0.9882	0.9944

Table 5.1 *Compression factor* for $k_{max}=897m^{-1}$ and $k_{min}=7m^{-1}$ for a range of vessel speeds at a constant wave direction of 0°.

We now investigate the dependence of the *compression factor* on the wave direction relative to the direction of travel of the instrument, θ, for a constant towing speed. A plot of the compression factor verses wavenumber for a range of values of θ at a constant towing speed of $1ms^{-1}$ is given in figure 5.2. Referring to this figure, we consider the effect of θ ranging from 180° to 270° which also corresponds with the angles 180° to 90°, on the compression factor. The magnitude of the compression factor increases as θ approaches the normal and the observed wavenumber increases in value. A similar change is seen for waves with incident angles of 0° to 90° which corresponds to 360° to 270°. As the incident angle moves toward the normal the distortion in the observed wavenumber is greater. At low wavenumbers, the compression factor is large but this decreases to a minimum as wavenumber increases. The compression factor increases again at higher wavenumbers. The negative values in compression factor can again be attributed to waves catching up and overtaking the TLS.

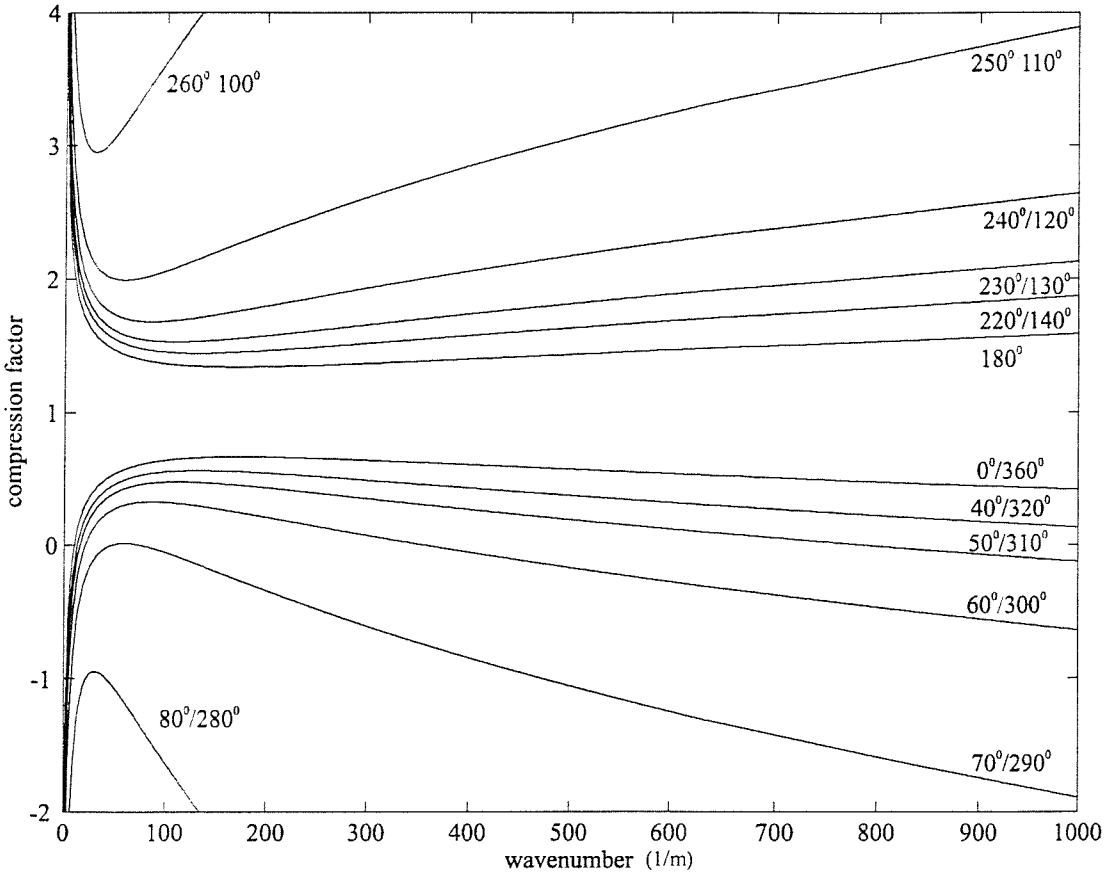

Figure 5.2 *Compression factor* verses wavenumber as a function of incident wave direction under a constant vessel speed of $1ms^{-1}$.

Values of the *compression factor* for varying values of θ at a constant vessel speed of $1ms^{-1}$ for the maximum and minimum observed wavenumber is given in table 5.2. From the table the change in the magnitude of the *compression factor* for small angles, i.e. 0° to 40° is not as rapid as for

larger angles, i.e. 70° to 80°. The *compression factor* is also closer to unity at smaller angles. From this work, a strategy of towing the TLS instrument in the opposite direction to the direction of the main wave propagation would limit the difference between the observed and true wavenumbers. In the open ocean the main wave direction is aligned to the wind direction which is easily identifiable. This strategy may be difficult to achieve in confused sea states and enclosed waters where wave interference will lead to a spread of wave directions.

Theta	Compression Factor	
[Degrees]	$k=7m^{-1}$	$k=897m^{-1}$
0	-0.1848	0.4429
40	-0.3545	0.1751
50	-0.4795	-0.0698
60	-0.6797	-0.5549
70	-1.0386	-1.7417
80	-1.9183	-6.5667
180	2.1848	1.5571
220	2.3545	1.8249
230	2.4795	2.0698
240	2.6797	2.5549
250	3.0386	3.7417
260	3.9183	8.5667

Table 5.2 *Compression factor* for $k_{max}=897m^{-1}$ and $k_{min}=7m^{-1}$ for a range of incident wave angles at a constant vessel speed of $1ms^{-1}$.

5.5 Slope Reconstruction Methods

Methods for reconstructing the observed wavenumber spectrum obtained by the TLS to retrieve a true wavenumber spectrum are now investigated. Cartwright (1963) developed a method to correct spectra obtained from ship motions using data from a wave probe. This method is not considered because of its dependence on a second measurement of the spectrum. Hughes (1978) developed a mathematical solution in order to provide a technique for obtaining the true wavenumber spectrum from moving slopemeter measurements. The solution required that the form of the true wavenumber spectrum and the dispersion relation as well as vehicle velocity were known. A further method which does not rely on these assumptions is proposed. These two techniques are investigated using simulated data sets provided by the model developed in chapter 4.

In 1978 Hughes developed a method for approximating the true wavenumber spectrum from a wavenumber-frequency spectrum gained from data taken using a moving laser slopemeter gauge (Hughes et al (1977)). The observed spectrum, $F(\omega_e)$, was found to be equal to an integral equation containing the unknown true one dimensional wavenumber spectrum, $F(k)$, and a term which could be generated through assumptions on the dispersion relation and vessel velocity, $\eta(k,\omega_e)$. The integral was of the form;

$$F(\omega_e) = \int_0^\infty F(k)\eta(k,\omega_e)dk \tag{5.10}$$

or in its discrete form:

$$F_q = \sum_{p=1}^{N} F_p \eta_{pq} \qquad q=1,2...,N \tag{5.11}$$

This is a standard linear single Fredholm integral equation of the first kind which may be inverted. The term η_{pq} is given by;

$$\eta_{pq} = \frac{a_v}{\Delta\omega_e} \int_{k_{p-1}}^{k_p} \left\{ \int_{\theta_{lp}(k)}^{\theta_{up}(k)} k\cos^v\left[0.5(\theta_\omega - \theta)\right]d\theta + \int_{\theta_{lm}(k)}^{\theta_{um}(k)} k\cos^v\left[0.5(\theta_\omega - \theta)\right]d\theta \right\} dk \tag{5.12}$$

where, v is a beam width parameter, $\Delta\omega_e$ is the difference between adjacent frequencies of encounter and:

$$a_v^{-1} = \int_0^{2\pi} \cos^v\left(\frac{\theta}{2}\right)d\theta \tag{5.13}$$

The terms a_v and $cos^v\theta$ arise from assumptions made by Hughes about the form of the true wavenumber power spectrum. Before the Fredholm integral equation is inverted η_{pq} must be determined numerically. For each value of ω_q which is the discrete argument of the *frequency of encounter* and dependent on the sample frequency, two values of k can be determined, one for each sign of ω_q. This forms two sets of k_p, the wavenumber at each value of p, which provides a set of limits for integration. For the set $+\omega_e$, the limits of integration $\theta_{up}(k)$ and $\theta_{lp}(k)$ of the angular term in equation 5.12, are given by:

$$\theta_{up}(k) = \arccos\left[\frac{\omega(k) - \omega_q}{uk}\right] \quad \text{and} \quad \theta_{lp}(k) = \arccos\left[\frac{\omega(k) - \omega_{q-1}}{uk}\right] \tag{5.14}$$

For $-\omega_e$ the limits $\theta_{um}(k)$ and $\theta_{lm}(k)$ are given by:

$$\theta_{um}(k) = \arccos\left[\frac{\omega(k) + \omega_q}{uk}\right] \quad \text{and} \quad \theta_{lm}(k) = \arccos\left[\frac{\omega(k) + \omega_{q-1}}{uk}\right] \tag{5.15}$$

The integration is evaluated numerically to give two matrices, η_{pq}^{+} and η_{pq}^{-} which are summed to give the matrix η_{pq}. The matrix is then inverted using a method for the inversion of a single Fredholm integral of the first kind developed by Phillips (1962) and improved upon by Twomey (1963). After the inversion has been performed, the result gives $F(k)$, the one dimensional wavenumber spectrum. The inversion is very sensitive to discontinuities and zero values within the η_{pq}. This sensitivity limited the technique when applied to the simulated data set. Figure 5.3 gives a comparison between the true wavenumber spectrum, the Doppler shifted spectrum and a Doppler shifted spectrum corrected using the above method. The data set was generated using a Phillips (1985) equilibrium spectrum, and applying values of u=1ms^{-1} and ν=2. No improvement on the observed spectrum could be found. Its accuracy when applied to real oceanographic data sets is reduced by its assumption on the form of the dispersion relation, the true wavenumber spectrum and the velocity of the vessel.

During the design of the instrument it was envisaged that the TLS would be capable of giving a precise measure of the wave height. Hence it was hoped that a wave height spectrum could be obtained such as the wave slope spectrum. Both spectra would be subject to the spectral distortions introduced by sampling from a moving vehicle. These distortions will be the same for both types of spectra. The Fourier transform of wave slope is equivalent to the product of the wavenumber and the Fourier transformation of the wave height. This continues to be true for the distorted spectra assuming they do not suffer from aliasing or spectral folding. This allows approximate reconstruction of the measured slope and height spectra as a function of wavenumber. However, due to system noise, credible values of wave height could not be obtained from the TLS so the proposed technique could not be fully investigated.

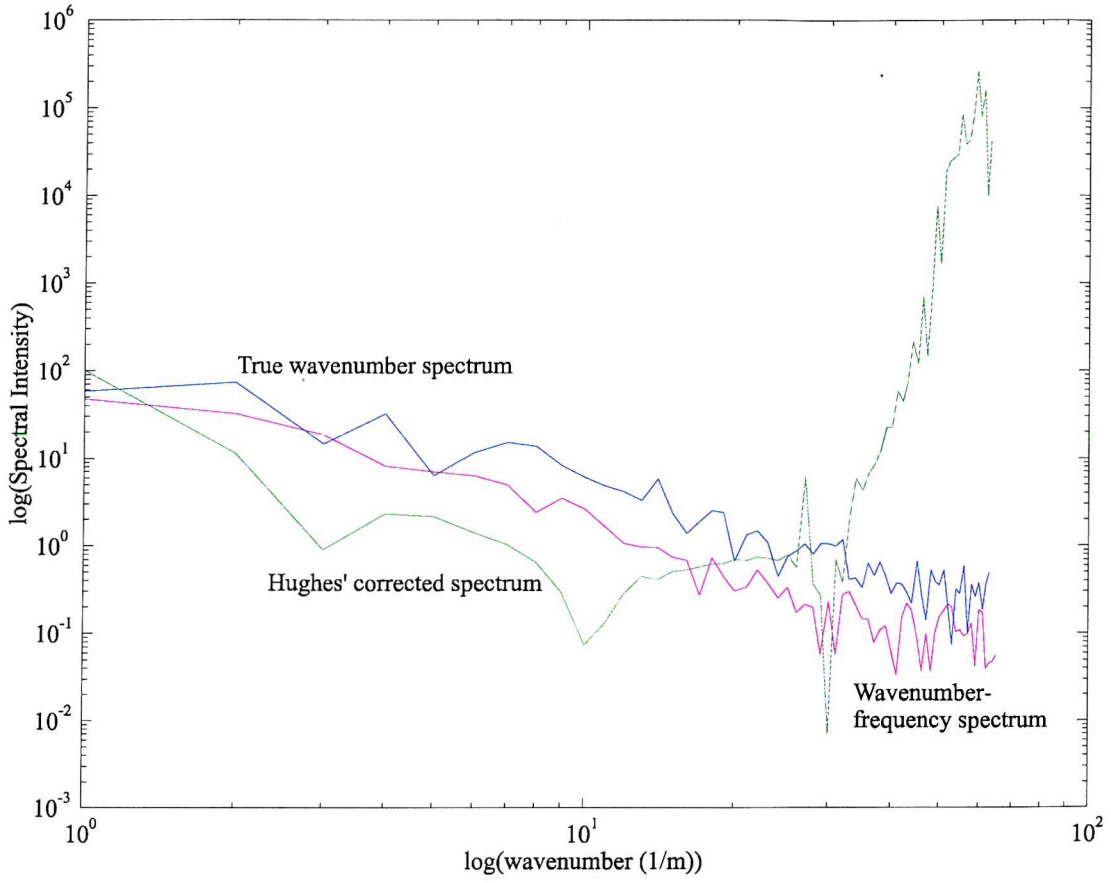

Figure 5.3 Comparison of true wavenumber (red curve), wavenumber-frequency (blue curve) and Hughes' corrected wavenumber (green curve)-frequency Phillips (1985) spectra.

5.6 Discussion

From the work conducted in this chapter, it is evident that the observed wavenumber and therefore the observed wavenumber spectrum will undergo distortion due to vehicle velocity. A frequency spectrum can be obtained if the TLS instrument remains stationary but this is impractical as the surrounding structure will interfere with the wave slope profile being examined. Instead, the vehicle is towed through the wave field and it is this towing that leads to the Doppler shift in the observed spectrum. The observed spectrum is dependant not only on the wavenumber but the wave frequency, the vehicle speed and the angle between the direction of travel of the instrument and the wave direction. This distortion is minimal at high vessel speeds where the vessel speed is much greater than the wave speed and a near instantaneous profile of the sea surface will be gained. This leads to an agreement between the observed and true wavenumber spectra. The speeds needed to do this cannot be attained by towing the TLS instrument.

A $1ms^{-1}$ towing speed for the TLS was decided upon. Increasing the towing speed decreases the effect of the distortion but will lead to an under-sampling of the sea surface profile and reduces the value of the highest wavenumber that can be measured by the instrument. It will be difficult to maintain a constant tow velocity leading to variations in the amount of distortion that the observed spectrum suffers. Towing the vessel into the direction of main wave propagation reduces the effect of changes in the angle of wave incidence. Methods exist for calculating the true wavenumber spectrum for the observed spectrum. Hughes (1978) suggested such a technique but this relied on a prior knowledge of the form of the true wavenumber spectrum, the form of the dispersion relation and a value for the vessel velocity. The method was found to be unstable. Another technique was suggested which did not need to apply the assumptions made by Hughes. It was necessary to be able to measure both the wave slope and wave height and to smooth the observed spectra.

The difficulty in determining a precise form for the true wavenumber spectrum led the Southampton team to propose a second instrument capable of resolving this. This is discussed in more detail in chapter 8 and appendix C. The theoretical investigation presented in this chapter has led to an increased understanding of the effects of TLS motion on the wavenumbers of individual waves and wavenumber spectrum. An appreciation of these effects will be important for the analysis and evaluation of data from the Towed Laser Slopemeter which is presented in the next two chapters.

Chapter 6

The Oceanographic Analysis of TLS Data from Loch Linnhe 1994

6.1 Introduction

The Towed Laser Slopemeter was deployed in Loch Linnhe, Scotland in September 1994 and constituted the first in-situ deployment of the complete TLS system. The trial therefore provided a chance to test all aspects of the instrument as well as the deployment strategy. In keeping with the theme of this thesis, this chapter is concerned with developing methods which will be needed for the scientific exploitation of the TLS and will add experimental and data analysis techniques to the theoretical investigations previously presented. The aim of the work described was to test extensively the TLS data set for evidence of sea surface slope measurements against known wave field characteristics. The effect of the TLS system on the recorded data set is therefore assessed. As a result of these studies and the experience gained during the deployment of the instrument improvements to the TLS system, where necessary, have been recommended and these are also discussed in this chapter, such steps are contributing to the further development of the TLS.

6.2 Overview of Loch Linnhe, Scotland 1994 TLS Trial

The Towed Laser Slopemeter was deployed for the first time in Loch Linnhe between 29th August and 17th September 1994 as part of a joint UK-US project organised by the DRA. The trials area is shown in figure 6.1. The overall aim of trial was to detect interactions between artificially generated internal waves and the wind generated sea surface roughness and to investigate the relationship between the received radar signal and this modulated surface roughness. Loch Linnhe was chosen for these trials since it contains two stratified layers; an upper layer of fresh water

which runs off from the surrounding hills, and a denser layer of sea water which flows into the Loch through the Corran Narrows. The 1300 ton Research Vessel (RV) Colonel Templer was piloted through the test area. Its hull perturbed the stratified layer generating internal waves with typical maximum amplitudes of 0.5 m, periods of 600s and speeds of 0.25-0.55ms^{-1} (Taylor et al (1995)).

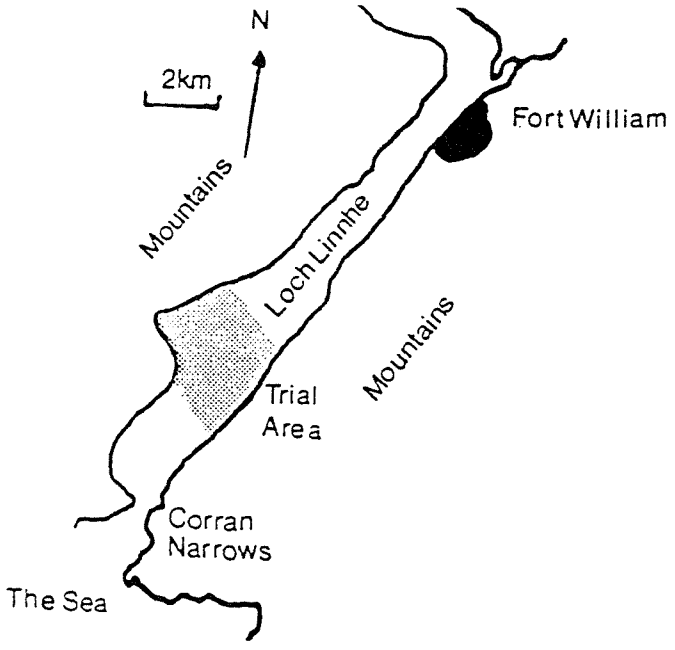

Figure 6.1 Map of Loch Linnhe showing trail area.

This thesis is concerned only with the analysis of the data from the TLS and the author was not involved directly in the wider application of the TLS data to the internal wave analysis. However, it is useful to note in this paragraph how the deployment of the TLS related to all the observations being made. Instruments were deployed in the test area to ;

- detect the internal wave within the Loch,
- detect internal-wave sea-surface interactions,
- provide truth data to be used as inputs to internal wave models.

These included satellite and hillside radar systems, current meter arrays, conductivity, temperature and depth (CTD) chains, a CTD profiler, shear spars, an echo sounder, a meteorology station and the TLS. The echo sounder, deployed from RV Calanus, was used primarily to record depth but permitted a visible profile of the internal wave to be gained. The CTD sensors measuring water stratification in terms of temperature and salinity were deployed on two chains 1m apart. Each chain was positioned from the stern of the RV Calanus and contained twelve sensors each spaced 2m apart. The data were combined to form a single data set with a sampling rate of 0.2Hz. A CTD

profiler was deployed from the RV Calanus allowing a more precise measure of water stratification at varying depths. The current meter array monitored the motion of the internal wave. The shear spars consisted of four vertical groups of current sensors which measured the average bulk current and shear in the Loch. Wind speed and direction were measured by the RV Calanus every five minutes some 500 to 800m from the TLS. ERS-1, the European Space Agency's first European Remote Sensing (ERS) satellite which incorporated a SAR system, also made a pass over the Loch during the trials period. The ground based radar was deployed on the hillside above the Loch having an incident angle of 5° and a footprint of 1000m in length. The radar systems together with the TLS were deployed to detect interactions between the internal wave and the sea surface. The general position of the TLS relative to the other instrumentation deployed in the trial area is shown in figure 6.2.

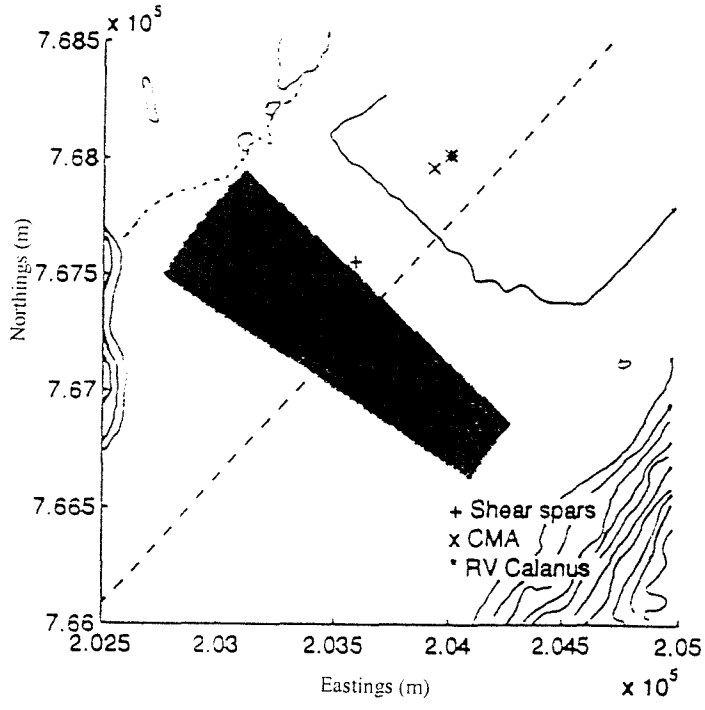

Figure 6.2 TLS course (solid) for run 4 on the 14th September 1994 relative to the course of the wake generating vessel (dashed), other instrumentation and the radar footprint (shaded).

The TLS was deployed in the configuration described in section 3.5 and sketched in figure 3.5. The tow vessel for the TLS was the Loch Shiel owned and operated by the Underwater Centre, Fort William. The vessel was approximately 8m in length and 3m in beam. A cabin below the wheel house which was situated towards the bow, provided cover for TLS support instrumentation but remained close to the two tow points of the TLS minimising cabling on the deck. The tow points were situated on the port side of the Loch Shiel, one amidships and the other towards the bow of the vessel. A hired diesel generator located amidships powered all support equipment. A GPS instrument was fitted on the catamaran next to the second tow rope and was operated by RACAL Survey allowing the position of the TLS within the Loch to be known precisely. The tow

points on the catamaran were situated on its starboard side, one amidships and the other at the bow. During each scientific run, a tow cable was connected from each tow point on the Loch Shiel to its counterpart on the catamaran.

The TLS was berthed on the quay side at the Underwater Centre which was the operations site for the DRA during the three week trial. At the start of each day of scientific study, the TLS was lowered into the water using a dockside crane. The TLS was towed behind the Loch Shiel to the test area. Once at the test area the Loch Shiel was stopped, the catamaran brought alongside and the tow ropes connected. A volunteer equipped with a dry suit was put on-board to ready the TLS for scientific deployment. The aperture to the optical detector was cleaned to remove any splashes and salt deposits resulting from the fast tow speed, typically $6ms^{-1}$, to the test area. The optical fibre and telemetry and GPS cables were passed from the Loch Shiel and connected to the TLS. The batteries were connected to the on-board electronics. The volunteer was retrieved from the catamaran.

The laser which was allowed to warm up for some thirty minutes before the test area was reached, was connected to the optical fibre. The two PCs were set to receive data from, and send commands to, the VME on-board the TLS. Once all crew members were wearing laser protection goggles the laser aperture was opened and the VME was switched on. Final checks were then made to determine whether the laser signal had been locked onto by the sample-and-hold electronics and whether telemetry data were being logged by both PCs. After the final checks had been concluded, the VME was switched off and the laser aperture closed until the order was received from the RV Colonel Templer to proceed with a scientific run. The Loch Shiel started moving and the tow ropes slowly let out until the TLS was some 30m from the Loch Shiel and parallel to its port side. Laser goggles were donned, the laser aperture opened, the VME switched on and the data logged by the two PC's.

After the RV Colonel Templer had passed, the TLS was towed through the region on a track normal to that of the internal wave generating vessel. The TLS transect was perpendicular to the sides of the Loch and generally lasted twenty minutes. During each run a detailed written log of observations of the sea surface and weather conditions was kept. At the end of each run, the laser aperture was closed, data logging stopped and the VME switched off. The TLS was then brought alongside the Loch Shiel and the screens cleaned if required. An hour's recovery time between each passage of the internal wave generating vessel was given to allow the loch conditions to return to an ambient state. After a number of runs the two batteries on-board the TLS had to be replaced with a fully charged set. It was necessary to man the tow points on-board the Loch Shiel at all times in order to keep the catamaran parallel to the Loch Shiel, during a run, and to prevent damage to the TLS whilst alongside.

From a deployment perspective the TLS behaved well in low sea states with winds typically 3-4 ms^{-1} As the sea state increased and the waves became increasingly choppy the pitch and roll of the catamaran became more violent and on occasion the laser mount would leave the water. This was exaggerated when the wind was against the tide. If the motions became too violent the run would be stopped and the TLS returned to the underwater centre to prevent damage to the instrument. The run direction was perpendicular to the tidal currents. In strong tidal currents, the TLS was seen to crab through the water. An RF controlled rudder would have limited the crabbing and reduced the need for the continued manning of the tow ropes.

Between four and six runs were made during each day of scientific study. The TLS was deployed successfully on eight days. Two runs were conducted on 10^{th} September before the TLS was returned to the Underwater Centre due to adverse weather conditions. The instrument experienced a range of wind speeds from 0.7 to 10.16 ms^{-1}, wind directions, and light conditions as well as rain and hail over the course of the campaign. A brief summary of the trial log is contained in appendix B. A more detailed account of the trial can be found in Lee (1995) and the references contained therein.

6.3 Analysis of Loch Linnhe Data

Prior to the full scientific exploitation of the instrument, confidence must be gained in the ability of the TLS to provide a true measure of the sea surface wave slope. It is understood from established theories and observations that:

- To a first order the sea surface wave profile will consist of sinusoidal shaped wave trains.
- The wavenumber slope spectrum has a power index of -0.5 (Phillips (1985)).
- Slope distributions are Gaussian, or near-Gaussian (Cox and Munk (1954)).
- Smaller gravity and gravity-capillary waves will be aligned to propagate parallel to the wind direction (Kinsman (1965)).

These sea surface characteristics provide the basis for assessing the oceanographic content of the TLS record. The experience gained in the analyses conducted was important for developing a methodology for any future analysis of data from the TLS. As well as evaluating the advantages of the measurement strategy employed by the TLS, it could highlight steps that may be taken to improve the system through its ongoing development.

6.3.1 The Wave Slope Profile

It was expected that the TLS record would exhibit a profile containing sinusoidal shaped wave trains. In addition to this, other signals may be apparent which could be caused by the TLS system. For example; an overlying spikiness might be characteristic of random noise in the system; discontinuities in the data may occur if the values of slope are misrepresented during the measurement and computer processing; and periodic and discrete features may also be apparent. By viewing the TLS record it may be possible to identify such features.

The software used to process the photodiode ratios uses IMU data to correct for the pitch and roll motions of the catamaran and produces values of slope, for a given point on the sea surface, in terms of the angular elevation from the horizontal, ϕ and the direction of the elevation from the bow-stern axis of the catamaran, θ. The bearing of the instrument with respect to magnetic north was removed at a later date. Two slope components, one parallel to the bow-stern axis of the TLS, S_x and the other perpendicular to this direction, S_y can be calculated:

$$S_x = \phi \cos\theta \tag{6.1}$$

$$S_y = \phi \sin\theta \tag{6.2}$$

The angular elevation from the horizontal, ϕ, is equivalent to the total slope, S.

A typical two second time history of the two slope components is given in figure 6.3 (a) and (b). Immediately, we are drawn by the high frequency 'spikiness' in the plots. A low pass filter was applied to the data, to smooth out this spikiness and from figure 6.3 (c) and (d) lower frequency variations in the data are apparent. From the plots, these low frequency variations are wave like rather than random fluctuations and are therefore unlikely to be noise-induced leading us to the conclusion that the slopemeter is measuring sea surface wave slope. The spikiness might be attributed to rapidly varying capillary waves on the sea surface but it also resembles random Gaussian noise which is a common cause of corruption of instrument signals. It is unclear, whether these are high frequency waves or system noise. White Gaussian noise has a characteristically flat spectrum. If the wave slope spectrum flattens off at higher frequencies this would be consistent with the presence of noise in the slope signal. The wave slope spectrum from the TLS record is now investigated to determine if noise is present in the data set and whether the spectrum is consistent, given the existence of a Doppler shift in the data, with the expected shape of oceanographic spectra.

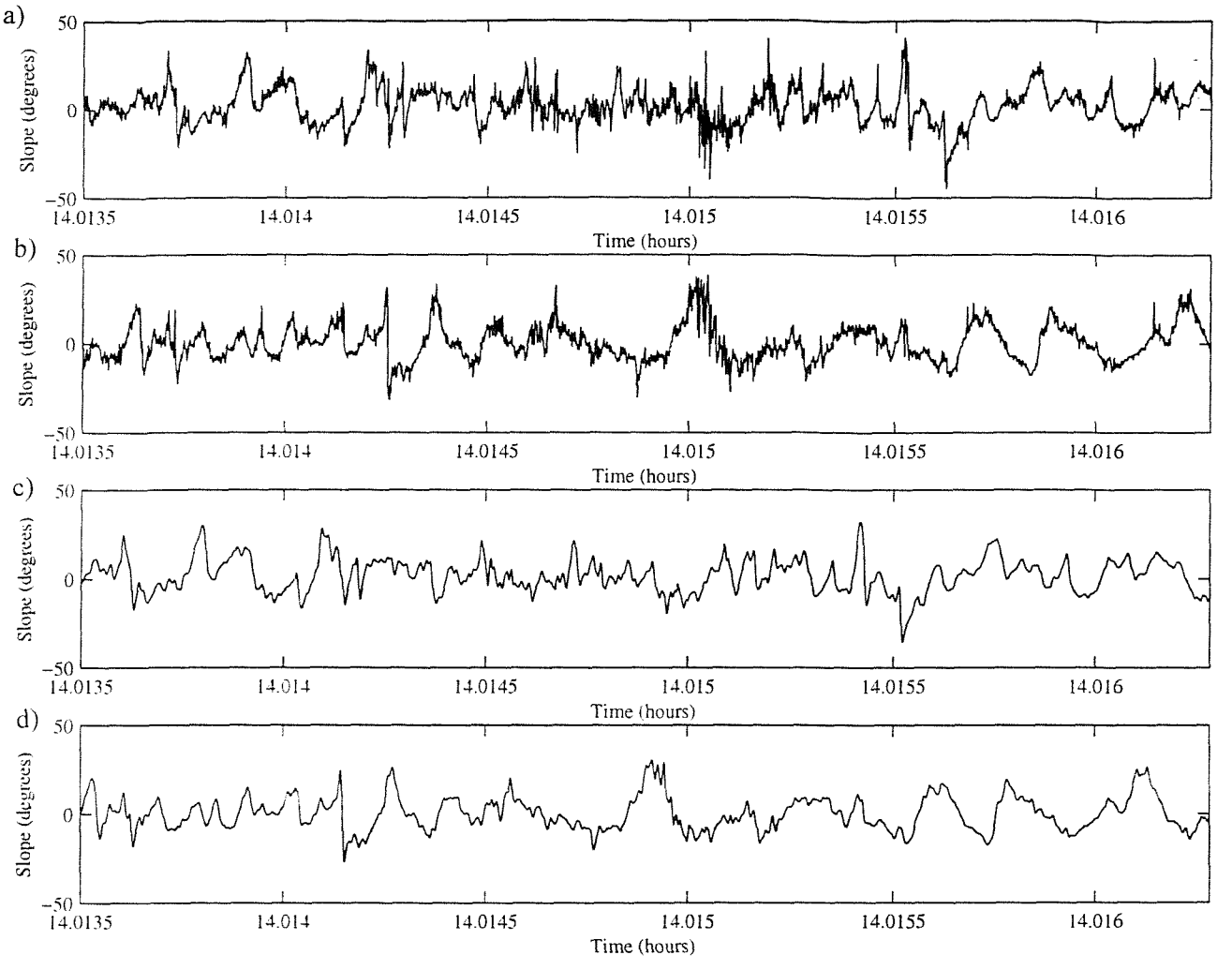

Figure 6.3 Plots of unfiltered a) along track and b) cross track slopes and low pass filtered c) along track and d) cross track slopes taken between 14:00:48 and 14:10:48 GMT on 9th September 1994.

6.3.2 Power Spectral Analysis

The intensity, or the square of the amplitude, at a particular frequency of oscillation can be investigated using power spectra. This is important for determining the wave energy and the effects on wave energy at a given frequency, or range of frequencies, caused by the influence of ocean processes and the action of wind. Power spectra are obtained through the Fourier transformation of the data set under analysis. Measurements reported in the literature have shown that the sea surface has an associated inverse power law. Higher frequencies, or higher wavenumbers, having a lower spectral intensity than at lower frequencies. The exact form of the sea surface power spectrum and its dependence on the wind which drives wave generation and

growth is unknown especially at the very high wavenumber end (0.5-50 cm waves). A number of different theoretical forms (Pierson and Moskowitz (1964), Holliday et al (1986), Phillips (1985)) based on limited measurements exist. One such form for the wave height power spectrum, *F(k)*, as a function of wavenumber which is widely used was proposed by Phillips (1985);

$$F(\underline{k}) = \beta \cos^{\nu} \theta u_* g^{-\frac{1}{2}} k^{-\frac{7}{2}} \tag{6.3}$$

where β is a constant, ν is the beam width parameter, u_* is the wind frictional velocity, g is gravity at the earth's surface and θ is the direction of wave propagation. The wave slope power spectrum $G(k,\theta)$ as a function of wavenumber is more relevant to the measurements made using the Towed Laser Slopemeter and is of the form:

$$G(k,\theta) = \beta \cos^{\nu} \theta u_* g^{-\frac{1}{2}} k^{-\frac{1}{2}} \tag{6.4}$$

Various methods and algorithms can be implemented to calculate the power spectrum (Press et al (1988)). Generally, oceanographers calculate power spectra from the mean of square of the sea surface parameter. This method was used by Phillips (1985);

$$F(\underline{k}) = (2\pi)^{-2} \int \overline{S(\underline{x})S(\underline{x}+\underline{r})} e^{-i\underline{k}\cdot\underline{r}} d\underline{r} \tag{6.5}$$

where $\underline{x}$ and $\underline{r}$ are different position vectors and the over-bar denotes a mean value. The TLS power spectrum will be a function of sample frequency containing both wavenumber and wave frequency components. Although the TLS power spectrum will suffer from a Doppler shift, investigated in detail in chapter 5, it will have a similar shape to the true power spectrum.

Having calculated the square of the total wave slope the data must undergo a Fourier transformation, the only practical means of implementing this is to use the fast Fourier transform which was discussed and applied in great depth in chapter 4. This requires the data set to be a power of two in size. It is quicker to transform a number of smaller data sets rather one large one. A typical 20 minute run will contain some 300,000 data points. It is impractical to transform this number of points in one go. Instead the data are divided into segments, each a factor of two in length, and each segment transformed individually to give a faster implementation of the power spectral analysis of the data set. Each transformed segment can then be summed to give a mean spectrum for the entire run.

This segmentation, followed by averaging, has the advantage of enhancing the underlying trend in the shape of the power spectrum by reducing spurious signals in the spectral intensity which are associated with the randomness of the wave profile. Reducing the fluctuations is important as we are interested in determining the general shape of the power spectrum of the TLS record and in obtaining a value for the power index. If the data set is contaminated with noise, as suggested in the previous section, we may obtain a flat spectrum or a flattening of the wave slope power spectrum at high wavenumbers. Therefore, it is important that all spurious fluctuations are minimised. In averaging over such a large data record we must assume that the sea surface slope profile is both homogenous and stationary. This assumption is justifiable in an effort to achieve the above aim. However, it would be foolish to make such an assumption if we were interested in examining the effect of ocean processes, or the action of wind, on the wave slope power spectrum.

Although the division of the data set into segments of smaller size is advantageous as it provides a quicker computation of the power spectrum and can reduce spurious fluctuations when averaged, it is at the expense of the resolution in sample frequency. A compromise was reached and a segment size of 1024 points was used. This gives a sample frequency resolution of 0.2 Hz. Another disadvantage is that segmentation can induce oscillations in the transformed data set. Effectively the data have been segmented by the multiplication of each section with a top hat function. The Fourier transformation of a top hat leads to a sinc function in the spectral domain. To reduce the effects of the sinc function, the data are multiplied with a Hanning window which has the property of producing less oscillations than the top hat when transformed.

A typical total wave slope power spectrum calculated from the TLS record obtained during the Loch Linnhe trials is plotted in figure 6.4. The spectral intensity is plotted on a logarithmic scale as is the sample frequency. This makes the viewing of the curve easier as its associated inverse power law leads to a rapid decrease in spectral intensity with increasing sample frequency. The gradient of this log-log curve is the index of the power spectrum. From a review of the wave slope power spectra obtained from each run, it was evident that the gradient of the curve was flatter at lower and higher sample frequencies than at mid range frequencies. It is likely that the flatting of the gradient of the curve at higher frequencies is due to the effect of system noise and led to the spikiness seen in the wave slope profile of figure 6.3. The spectral components at lower frequencies will be sensitive to some corruption by the data folding in from higher frequencies, a result of the under sampling of the surface as the vessel moves through the wave field.

To gain a greater insight into the variability of the power index with sample frequency and the extent of the corruption of the spectrum from noise and undersampling, the spectra were initially fitted without an error treatment. A least squares fit (Press et al (1988)) was applied to the log-log form of the wave slope power spectra by assuming a value of one for the error in the spectral

intensity. Lower values for the power index were obtained at low and high frequencies, with larger values in the mid sample frequencies. From this initial fitting to the wave slope power spectrum, a middle frequency range between 7Hz and 73Hz was identified. This was believed to be less influenced by the effects of noise and undersampling.

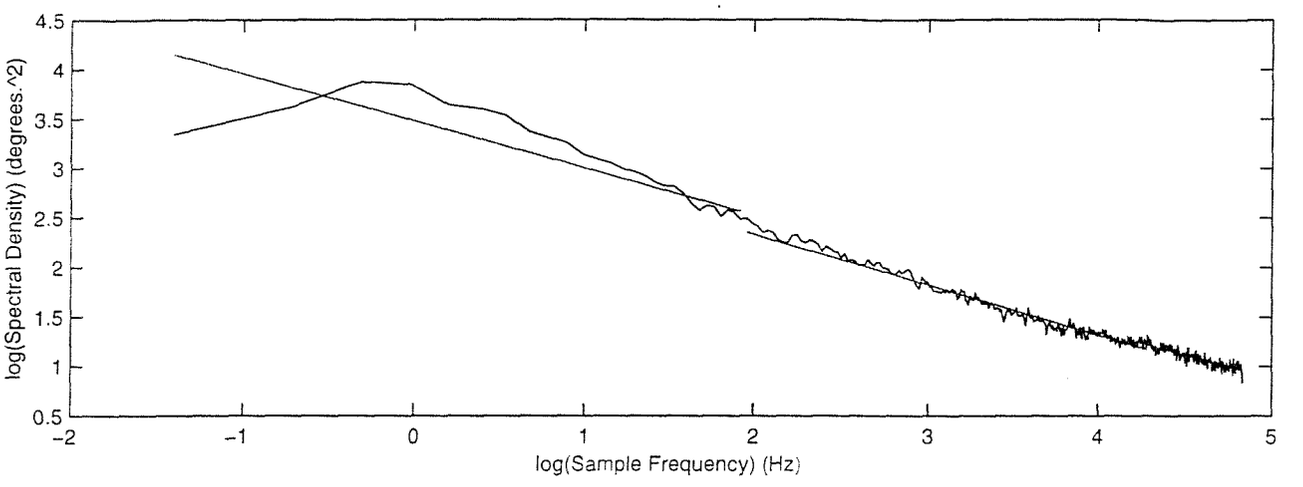

Figure 6.4 Typical power spectra of slopes taken between 14:37:01 and 14:54:00 GMT on the 8th September 1994 and least square fits (straight lines) between 0 and 7 Hz, 7 and 73 Hz and 73 and 128 Hz.

A more precise value for the power index can be obtained from the fitting of the power spectrum together with its associated instrumental error. The estimation of errors in the spectral domain is difficult as the data points are not independent of each other. Independence must be assumed when applying Gaussian statistics in standard error analysis.

A method for estimating errors in the spectra was applied. The technique relies on the generation of a number of sea surface realisations. A random number with a value determined by the errors in the wave slope is generated. These constrained random values are then used to construct the sea surface realisation. Uniform, or normal, random number distribution can be used. For each measure of wave slope a random number is generated. If the random number is uniformly distributed then it must fall between the error range in wave slope. If a normal random number distribution is used then the error in the wave slope forms the standard deviation of the distribution and the value of the wave slope is taken as the mean of the distribution. A normally distributed range of random numbers was used as this better represents the range of errors. A number of such slope realisations were generated for each value of sea surface slope. Each realisation was divided into segments containing the same number of points as the segments of

wave slope data. For each of the segments of the surface realisation a power spectrum was calculated. The mean standard deviation of each of these power spectra about the power spectrum derived from the true wave slope profile was calculated. This was used to provide an estimate of the error in spectral intensity at each sample frequency. This methods allows the instrumental error in the slope data to be propagated into the spectral domain.

The spectral intensity together with its associated error could now be fitted over the 7 to 73 Hz frequency range previously identified. A least square fit was impractical as expressing the errors on a logarithmic scale proved difficult. Instead a Levenberg-Marquadt (Press et al (1988)) method was used to provide the fitting to the power spectrum. A model of the form;

$$G(k) = \beta f_e^{\alpha} \tag{6.6}$$

where f_e is the sample frequency, α is the power index and β a multiplying factor, was provided.

Date [d.m.y]	Run Number	Power Index	Index error	Reduced χ^2
05.09.94	1	0.533	0.005	0.005
	2	0.525	0.004	0.004
	3	0.414	0.003	0.002
	4	0.576	0.005	0.005
09.09.94	1	0.372	0.005	0.005
	2	0.436	0.01	0.01
	3	0.427	0.005	0.004
	4	0.524	0.008	0.008
	5	0.484	0.005	0.006

Table 6.1 Values of the power index, error and reduced chi-squared (χ^2) over a sample frequency range of 7 to 73 Hz for power spectra taken from total wave slope data recorded during the 5th and 9th September 1994.

Values for α, its associated error and reduced chi-square over the middle range of sample frequencies calculated from the data recorded on the 9th and 17th September 1994 is given in table 6.1. The average value of the power index was 0.477 ± 0.006 which is similar, in order, to that proposed by Phillips (1985). Taylor (1996) using a visual best line fit found a similar value for the average power index. The range of values for α is attributed to the variations in the wave

slope power spectrum which occur from differing tow velocities and directions of wave propagation relative to the Slopemeter. Returning to figure 6.4 and ignoring the associated error, spectral intensity does not fluctuate significantly about the fit, this explains the low error in the value of the power law. The values of the reduced chi-square which gives a measure of the goodness of the fit are low. This indicates that the errors have been over estimated. This is evident from the figure 6.5 in which a typical power spectrum and associated error over the middle frequency range of 7 Hz to 73Hz is plotted. The error in the spectrum is calculated from the error in the slope. It is concluded that the original errors in the TLS slope record had been over estimated during the processing of the photodiode ratios.

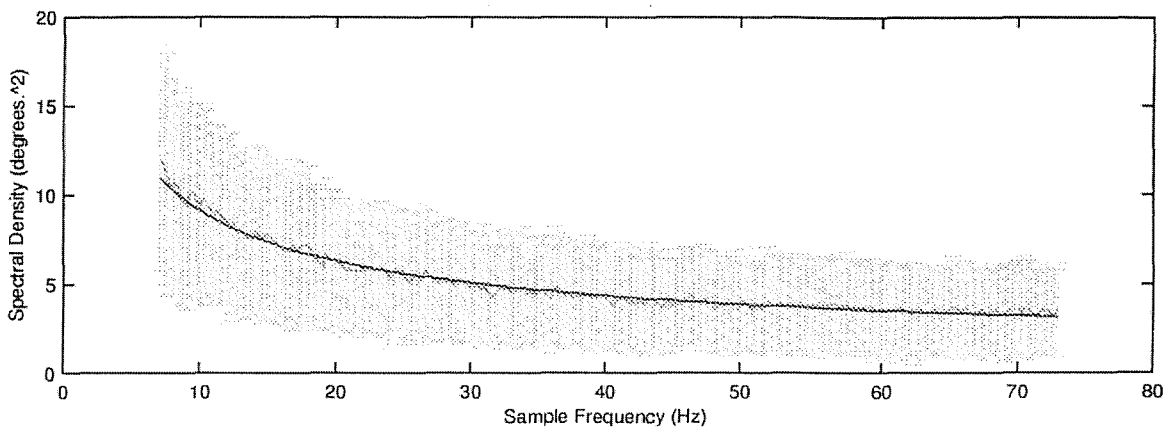

Figure 6.5 Typical total wave slope power spectrum and associated spectral error taken between 14:37:01 and 14:54:00 GMT on the 8th September 1994

From figure 6.5 we can determine the percentage error in the spectral density at a given sample frequency. For a low sample frequency at 10Hz the error is 47% and correspondingly for a high sample frequency of 70Hz the error is 74%. The errors in both cases are significant. The TLS was developed with the object of precisely measuring the effect of a variety of ocean processes on the sea surface wave slope. Such modulations are believed to occur at high frequencies and a reduction in precision at such frequencies will limit the usefulness of the instrument. The large error in the spectral density of the wave slope spectrum will restrict the information that can be gained from the shape and power law of the power spectrum and consequently any characterisation of variations in the sea surface roughness. The large error associated with the spectral density is a result of a corresponding large error in the wave slope. Small variations in wave slope due to oceanographic processes which occur predominately at these high frequencies would remain undetected due to the magnitude of the error in the data. The TLS would be incapable of giving a precise measure of the effect of ocean processes on the sea surface wave

slope. The error in spectral density at lower frequencies, although not as large in magnitude as the errors associated with higher frequencies, will give the same imprecision in the measurement of wave slope and the spectral density, as discussed above.

However, these conclusions are not as worrying as they sound. The error in the spectrum is calculated from the error in the slope. The original errors in the TLS slope record were estimated during the processing of the photodiode ratios. The very small chi-squared values given in the table 6.1 indicate that the errors in the spectrum have been over estimated. This conclusion is supported by the agreement between the power spectrum and its fit given in figure 6.5. Additional evidence for the claim that the instrumental errors in the wave slope have been over estimated comes from section 6.5 in which there is strong evidence for the detection of the effect of surface active films on the wave slope Significant differences between slick affected and non-affected regions can be seen in both the spectrogram of figure 6.10 and the power spectra of figure 6.11. The errors in the total wave slope spectrum of figure 6.11 have been estimated from the standard deviation about the mean spectrum. As it is evident that the instrumental errors in the wave slope have been over estimated one way to proceed with an investigation of this data set would be to use the standard deviation about the mean spectrum as an error estimator. This will not suffer from over estimation and should be more precise.

6.3.2.1 Total Slope Power Spectrum Reconstruction

In chapter 5, a method for determining the true wave slope power spectrum from the Doppler shifted wave slope spectrum obtained from the Towed Laser Slopemeter was proposed. The technique was successfully applied to simulated data. The technique requires that a wave height power spectrum can be obtained from the data record. A wave height profile can be gained from the TLS data set. The method connects the two spot positions on the screens with an imaginary line. This line is then traced away from the bottom screen until it intersects the vertical line which passes through the centre of the two screens. The point of intersection is taken as the wave height. The main draw back with this method is that at a wave slope of zero, the value of wave height is indeterminate and errors in the wave slope data will cause spurious values in wave height. Using this method, estimates of wave height were gained and the wave height power spectrum obtained. The wave height spectra were not believable, the power index being much lower in value than expected. The cause was attributed to noisy data. As a result the Doppler shifted total wave slope power spectrum could not be used to give a true wave slope power spectrum from the observed data set as suggested in chapter 5.

6.3.3 Slope Distributions.

As discussed in chapter 2, the surface waves can be considered to be sinusoidal in form as a result of the first order solution, or Stokes approximation, to the hydrodynamic equations describing the surface profile. If the sea surface is represented by an infinite number of such sinusoidal waves of varying wavenumber and wave frequency then, the probability of a given surface slope occurring will be described by a Gaussian distribution function. Small deviations in the wave profile from the first order solution lead to a near Gaussian probability distribution as studied by Cox and Munk (1954). They fitted a Gaussian and a Gram-Charlier function to the curves. This was later explained physically by Longuett-Higgins (1963). From such studies we expect the TLS slope record to be distributed as a Gaussian, or near Gaussian function, about a zero mean. The analysis of the TLS data set in terms of the shape of its wave slope distribution will help to provide evidence that the TLS is capable, or otherwise, of measuring sea surface slopes in-situ.

Typical plots of north-south, S_N, and east-west, S_E, slope distributions are given in figure 6.6 for run 1 on 5th September 1994. Each was calculated by the addition of the bearing of the instrument relative to true North, θ_b, to the direction of maximum wave slope, θ:

$$S_N = S\cos(\theta + \theta_b) \tag{6.7}$$

and

$$S_E = S\sin(\theta + \theta_b) \tag{6.8}$$

Using the Levenberg-Marquadt method (Press et al (1988)), Gaussian and Gram-Charlier models are fitted to the data. The Gaussian is of the form:

$$\frac{1}{\sqrt{2\pi\sigma}} e^{\left(-\frac{x^2}{2\sigma^2}\right)} \tag{6.9}$$

and the Gram-Charlier series is:

$$\frac{1}{\sqrt{2\pi\sigma}} e^{\left(-\frac{x^2}{2\sigma^2}\right)} \left\{1 - \frac{\sigma_3}{6}\left(\frac{x^3}{\sigma^3} - 3\frac{x}{\sigma}\right) + \frac{\sigma_4}{24}\left(\frac{x^4}{\sigma^4} - 6\frac{x^2}{\sigma^2} + 3\right)\cdots\cdots\right\} \tag{6.10}$$

where x is an observable, σ is the standard deviation, σ_3 is the skewness and σ_4 is the kurtosis of the distribution. The errors in the distribution are estimated from the square root of the number of counts, or the frequency of occurrence, for each bin of slope. From the Gram-Charlier fit, the

mean was found to be zero as expected. For the north-south slope component, recorded during run 1 on 5th September 1994, the standard deviation was 10.86±0.16° the skewness was 0.05±0.02 and the kurtosis was 0.93±0.12. For the east-west slope component, the standard deviation was 9.73 ± 0.08°, the skewness was 0.03±0.01 and the kurtosis was 1.00±0.06. The wind speed range was 3-8ms^{-1} for that run.

The skewness identified in Cox and Munk's wave slope distribution was attributed by Kinsman (1965) to a greater number of waves travelling in a down-wind direction as opposed to a cross-wind direction. A direct comparison between the direction of wave propagation as recorded by the TLS and the wind direction recorded on the RV Calanus was made. Both measurements are given relative to true North. The direction of maximum wave slope relative to true North, θ_N, was calculated as follows:

$$\theta_N = \theta + \theta_b \tag{6.11}$$

Although the TLS is capable of providing a measure of the direction of propagation of the recorded wave slope, there is an associated 180° ambiguity in the result. The instrument is not able to determine whether a wave is approaching, or receding, from the catamaran. We would expect a peak in the distribution of the direction of maximum wave slope corresponding to the dominant direction of wave travel which from Cox and Munk's and Kinsman's results, coincides with the dominant wind direction. However, as the TLS has an associated inability to differentiate between the direction of maximum wave slope it was expected, and subsequently found, to have a doubled peak in its distribution. One peak coinciding with the dominant direction of maximum wave slope and the other at 180° from this. An example of the distribution of the direction of maximum wave slope is given in figure 6.6 (c).

The RV Calanus was moored some 800m from the point of closest approach of the TLS. An average value of wind speed and direction was recorded every five minutes on the RV Calanus at a height of 8m above the mean water surface. The duration of a typical run was twenty minutes giving an average of four wind measurements over this period. Because of this, the average wind and wave directions were compared over the entirety of each run. This required the assumption that the surface was both homogeneous and stationary during the run. It was also necessary to assume that there was surface homogeneity between the TLS and RV Calanus positions. Such conditions were unlikely but the assumption was necessitated by the infrequent and non-localised wind measurements.

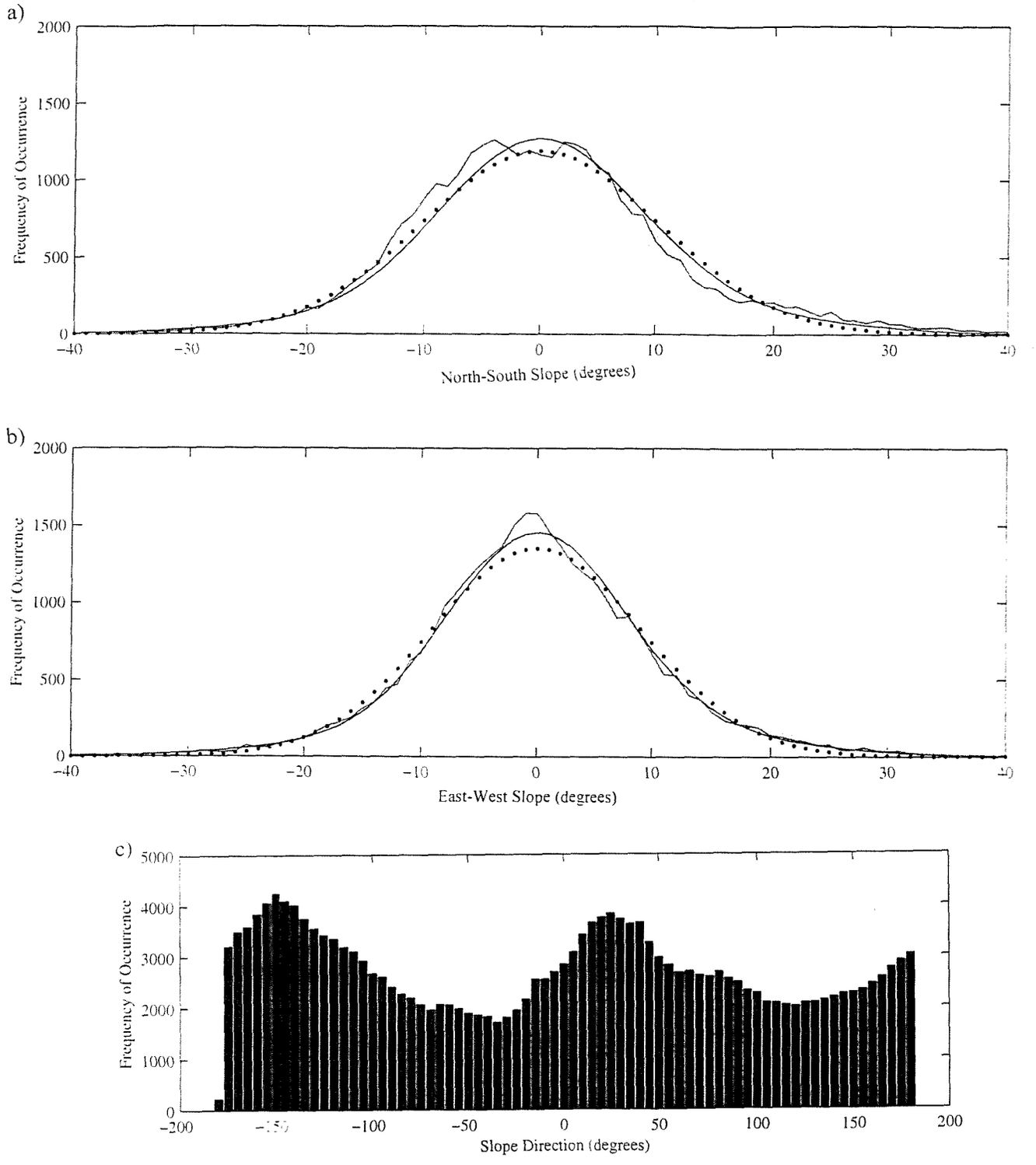

Figure 6.6 a) North-south and b) east-west slope distributions (solid curve with error bars) with Gaussian (smooth curve) and Gram-Charlier (dotted curve) fits and c) distribution of the direction of the maximum wave slope taken from run 1 on 5th September 1994.

The values for the maximum wave slope direction were grouped in 5° bins from -180 to 180°. The mean value of the peak in the distribution closest to the predominant wind direction is taken to give the predominant direction of the maximum wave slope. The error in the mean value was estimated from the square root of the variance in the distribution about the mean value. From the distributions of the direction of the maximum wave slope and the examples given in table 6.2 it was evident that there was some agreement within ±40° between the average wind and wave directions. However, there were also examples of non agreement between the two directions.

Date [d.m.y]	Run Number	wind direction range (°)	mean wave direction (°)	error (°)
05.05.94	1	288-214	188	48
	2	216-212	174	49
	3	212-206	212	49
	4	222-218	166	49
09.09.94	1	241-209	195	55
	2	na	218	41
	3	219-218	160	41
	4	221-219	218	39
	5	226-223	181	65

Table 6.2 Range of wind directions and dominant direction of wave propagation for a number of runs made during the Loch Linnhe trial. (na=not available).

It is unlikely that the direction of the maximum wave slope at low wave slopes will be representative of the mean wave direction. To reduce the signal that the low wave slopes contribute to the direction of maximum wave slope a lower threshold was set. Maximum wave slope directions above this threshold were used to generate the distribution outlined in the previous paragraph. The threshold was varied but the position of the peaks remained consistent with the value gained from the distributions calculated over all the values for the direction of maximum wave slope for each data set.

The Loch is long and narrow. Long wavelength waves will be reflected from both the Loch boundaries and lead to a confused surface. The high frequency waves will be influenced not only by the wind direction but also by the larger wavelength waves giving a direction of travel of the short gravity-capillary waves different from that of the predominant wind direction. A confused sea state will develop. Under such conditions, averaging over the entire data set may lead to an isotropic wave distribution at high frequencies. Waves occurring in the middle range of

frequencies to which the TLS is sensitive may prove to show greater alignment with the wind direction than at lower and higher frequencies. The north-south and east-west slopes were filtered over a range of different frequencies using low, band and high pass Hanning window filters and the direction of wave propagation relative to true North recalculated. From the distributions of the slope direction, the high frequency wavenumber range were found to be isotropic which could be attributed to a confused wave field or as a result of system noise. Generally, the mean value of each peak in the distributions at all other frequencies were the same as the non filtered data sets to within 5-10°.

The previous section has been concerned with reconciling the dominant wave slope direction with the direction of the wind flowing over the water surface. The results are not conclusive. The problem is exacerbated by the distance between the TLS and the meteorological station which was a minimum of 800m. The wind data were recorded every five minutes which makes comparisons difficult. In addition the flow of air over the Loch will be turbulent on account of the surrounding hills inducing rotor. This will confuse the wind direction and hence the wave direction. The Loch boundaries will reflect the large surface waves increasing the state of confusion. Considering these conditions it is not surprising that similarity between the wind and wave slope directions has not been conclusively proven. The ideal conditions for this sort of comparison would be a large expanse of water and a large fetch. The CSTAR trial, discussed in the next chapter, was conducted in the North Sea 30km from the Dutch coast. It was hoped that a similar treatment of the data from the CSTAR campaign might help to provide a more conclusive result from the comparison of the wind and wave directions.

6.4 Characterisation of the Noise in the TLS System

The contamination of the sea surface wave slope record by noise in the TLS system has been highlighted by the analysis of the wave slope profiles and power spectra. The high frequency spikiness in the wave slope profile and the flattening of the wave slope power spectrum at these frequencies suggests evidence for the presence of white Gaussian noise in the slope signal. White Gaussian noise is characterised by a flat power spectrum, a Gaussian distribution of values, an autocorrelation function which has a positive correlation at zero lag and is uncorrelated at all other times and an uncorrelated cross-correlation at all lags. Three main types of electronic noise exist (Wilmhurst (1990));

- shot noise; attributed to the flow of discrete electrons across a semiconductor junction i.e. a photodiode

- thermal noise; white Gaussian noise attributed to the random thermal agitation of charge carriers producing a noise voltage at the terminals of any resistance
- flicker noise; although not fully understood it is characterised by an inverse frequency spectrum.

The main aim of this section is to analyse data sets, recorded without the perturbing water surface, to characterise the nature and therefore the type of noise which dominates the instrument signal. This will aid any future review of the noise generated by the individual system components, an important step if a more precise measurement of sea surface slope is to be gained from any future scientific deployments of the TLS.

6.4.1 SNR File Analysis

The data sets used for the analysis presented in this section were recorded on the quay side of the Underwater Centre in Fort William during the Loch Linnhe trials. The measurements were made using the same system set-up as the scientific runs conducted in the Loch with the exception that the perturbing sea surface was not present and as a result the beam shone directly through the centre of each of the two screens. The data recorded will be dominated by system noise and will not be influenced by a changing slope profile. Five such signal-to-noise, or SNR, files were made on the 11th, 14th 15th and 17th September 1994. Two files were recorded on the 17th. Each file contains six photodiode ratios and a corresponding time stamp. The ratios are calculated from a difference over sum;

$$\frac{V_a - V_b}{V_a + V_b} \tag{6.12}$$

of the voltages V_a and V_b from opposing photodiodes A and B, respectively. The ratio is then scaled by 2048. From the six ratios available, ratios 1 to 3 are taken from the top screen and ratios 4 to 6 from the bottom screen.

Normalised probability distributions of the photodiode values were plotted. Ratios were grouped in bins of 0.1, sample sizes of 1024 data points were used. The distribution approximated that of a Gaussian (figure 6.7) and for a given ratio the position of the peak and variance remained approximately constant for the file duration. The variance increased during the campaign, with the

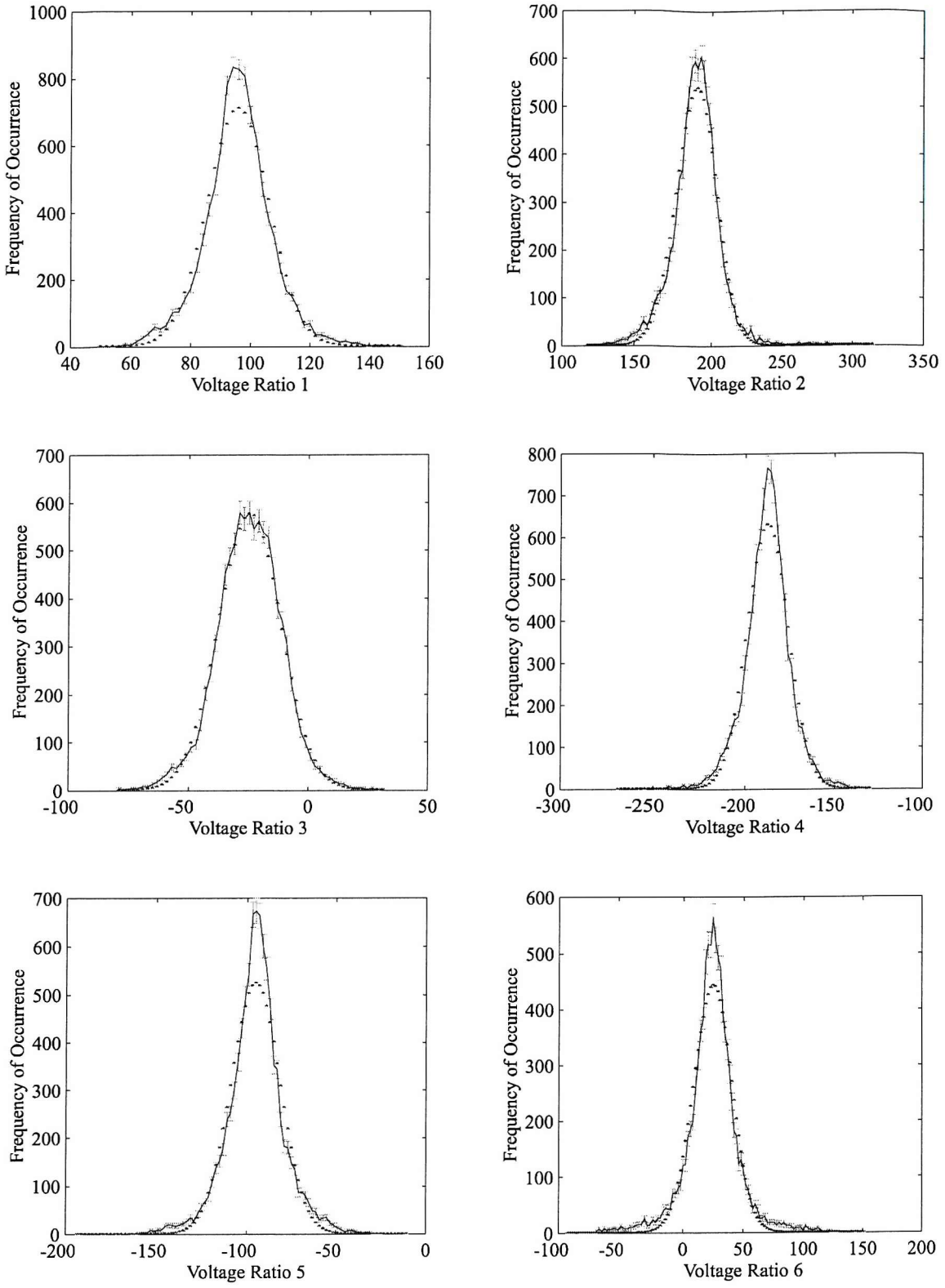

Figure 6.7 PDFs of photodiode voltage ratios (solid curve with error bars) and fitted Gaussian curves (dotted curve) taken from the SNR file recorded on the 14th September 1994.

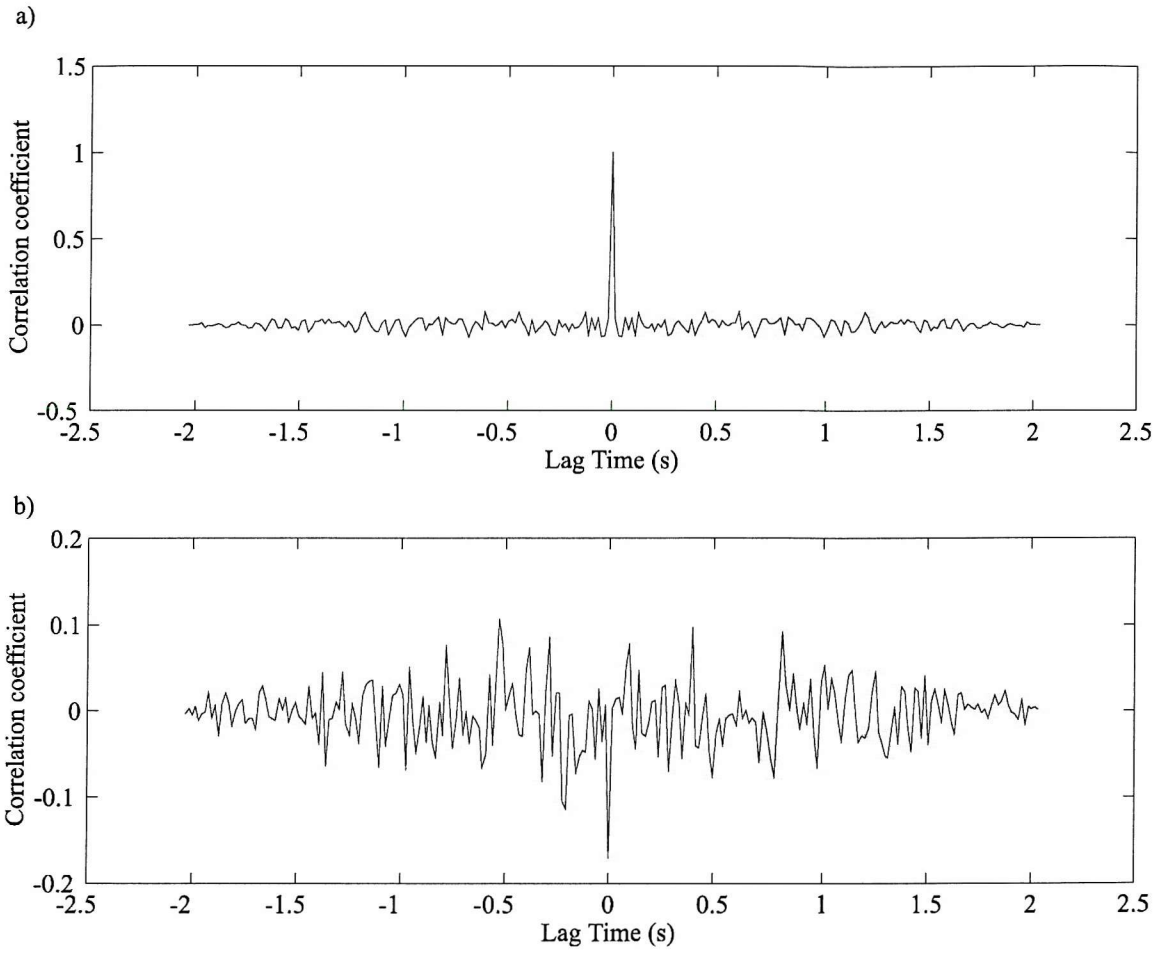

Figure 6.8 An example of a) an autocorrelation for the second photodiode voltage ratio and b) a cross correlation between the second and third photodiode voltage ratios recorded on 14th September 1994.

exception of the variance of the distribution recorded on the 17th which exhibited a significant decrease. The mean value of the distribution varied from file-to-file and between ratios, implying the existence of transitory offsets between ratios

Autocorrelations on the individual photodiode ratios were found to have a large, correlated signal at a zero lag time and were uncorrelated at all other lags. These features were seen in all ratios and over all SNR files. The size of the correlated signal increased during the campaign until the 17th September when the correlation exhibited a marked decrease in the size of the peak at a lag of zero. Corresponding cross-correlations between different photodiode ratios for each file were calculated. In all cases, the correlation was characterised by a large peak at the zero lag time but uncorrelated at all other lags. The correlated product was found to increase during the campaign for all ratios with the exception of the cross correlation of the data recorded on the 17th September which showed a decrease in magnitude. An example of an autocorrelation for the second photodiode voltage ratio and a cross correlation between the second and third photodiode voltage ratios recorded on 14th September 1994 is given in figure 6.8. Power spectra were calculated for all ratios and for all files. The resultant spectra had a flat distribution at all frequencies except at the lowest frequency where a large amplitude was found to be present. The component increased during the campaign, with the exception of the SNR power spectra of the 17th September.

6.4.2 Discussion on the Results of the Noise Analysis

The above trends, with the exception of the low frequency peak in the power spectra and the correlated signal at zero lag in the cross correlation, are characteristic of white Gaussian noise. This result confirms the conclusion, formed from the analysis of wave slope profiles and power spectra recorded during the scientific runs made in the Loch, that the slope data had been contaminated by white Gaussian noise. A large low frequency component in power spectra and correlated cross-correlations are not consistent with the characteristics of white noise. Drifts in the electronics system would lead to the above trends. Such signals could have arisen from;

- start up transients
- laser power fluctuations

The magnitude of the low frequency component in the power spectrum and the correlation at zero lag increased during the campaign. Start up transients would not vary systematically and would exhibit an unpredictable change from record-to-record. Care was taken to allow significant time for the system to warm up before the SNR files were recorded. The reduction in the low frequency

signal evident in the SNR files recorded on the 17th September 1994 followed a re-calibration of the laser.

The re-calibration was conducted in response to growing evidence that the laser beam power had become more variable during the course of the campaign. The re-calibration reduced these fluctuations in laser power and gave a better signal-to-noise. A low signal-to-noise would explain the response of the system to variations in the laser beam but the re-calibration did not completely remove the large peak in the cross-correlations and power spectra. In an ideal optical system any effect of fluctuations in spot intensity would be eliminated using the difference over sum technique to calculate the photodiode ratio. However, the response of each photodiode varies substantially and non-linearly from the ideal model. This is evident in figure 6.9. These non linearities were due to impurities in and on the screens. Such imperfections would have conspired to make the photodiode ratios susceptible to changes in the laser intensity. It is likely that the low frequency trends are caused by a variable laser power. The fluctuations increased with trial duration and were reduced through re-calibration of the laser source.

Although steps had been taken during the electronics design to reduce noise in the individual printed circuit board (PCB) components, the total noise in the fully integrated TLS system was greater than expected. The analysis and interpretation of the results presented in this section prompted a review, conducted by Lee (1995), of the noise associated with the individual and integrated system components. The result of this investigation was to attribute the main sources of white noise in the system to:

- noisy power converters used on each PCB
- cross-talk between the sample and hold circuit and the ADC

A significant refit was instigated on these findings. The power converters were replaced with counterparts that exhibited a better signal-to-noise performance. Extensive shielding throughout the electronics rack eliminated cross-talk. The helium-cadmium laser was returned to the supplier in an effort to limit power fluctuations which are common in such gas lasers. Solid state lasers do not exhibit power fluctuations. Such a laser source emitting light in the required wavelength range was not commercially available at the time. An investigation by Lee (1995) of the calibration files used to determine the spot positions in the processing of the TLS photodiode ratios were found to be noisier than expected. This noise was attributed to interference filters attached to the front of the photodiodes and contaminated screens. During the refit, the filters were removed and the screens replaced. Steps were taken to improve the water-tight housing of all on-board systems.

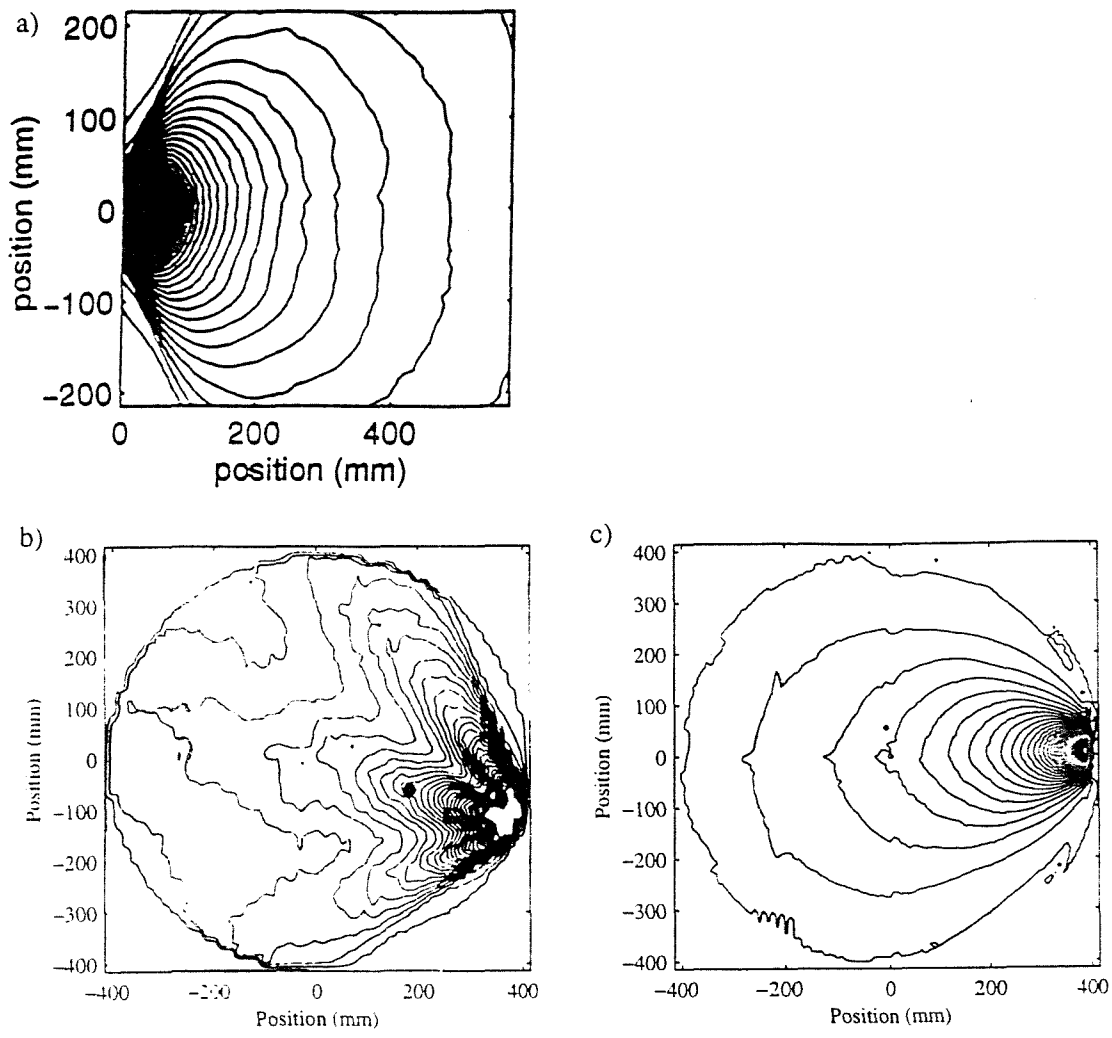

Figure 6.9 a) Ideal and b) actual photodiode response and c) photodiode response after refit.

It was not possible to include plots of SNR power spectra following the refit to compare with examples recorded during the Loch Linnhe campaign. However, the improvements in the response of the photodiodes following the refit can be seen in figure 6.9 (c). When compared with figure 6.9 (b) which was recorded prior to the Loch Linnhe trial immediately it can be seen that the interference pattern is no longer present in the photodiode response.

6.5 The Detection of Surfactants Through Their Effect on the Sea Surface

The motivation for the development of the Towed Laser Slopemeter was to design an instrument capable of giving a measure of the effects on the sea surface wave slope caused by a number of ocean processes. Such interactions lead to a modulation of the waves present on the surface and result in a visible change in the sea surface roughness. During the Loch Linnhe trial a number of regions in which the sea surface roughness was smoother than surrounding areas were noted. The

visual observations, together with the time of intersection, were noted in the trial log book. These regions may be attributed to either surfactants, such as organic materials in the run off of water from the surrounding hills, natural debris on the surface i.e. pine needles, or visible wakes, resulting from bubble entrapment, seen behind vessels moving in the Loch.

Surfactants increase the surface tension of the water. This increase attenuates wind generated waves and has the greatest effect on capillary and small capillary-gravity waves. The effect of surfactants on the waters surface should be detectable in the TLS record of sea surface slope. Through the analysis of the data recorded in areas affected by surfactants it can be established whether the TLS is sensitive to such changes in sea surface roughness. This forms the main aim of this section.

The detection from the wave slope profile of changes in the sea surface roughness induced by surfactants was difficult due to the length of the records. A better method for visualising the affected areas was identified. The technique relied on the dividing up of the data set from each scientific run into segments of equal length. Each segment of wave slope data was a factor two in length which enabled the power spectrum to be calculated through Fourier analysis. The power spectra were then placed side-by-side such that time increased along the horizontal axis and sample frequency increased along the vertical axis. The sample length was either increased to give increased frequency resolution, or decreased, to give increased temporal resolution. The spectral intensity was assigned a different colour depending on its value. This resulting image is referred to as a spectrogram. An example is given in figure 6.10.

The spectrogram technique was applied to runs identified in the trial log book as containing features of interest. Smoother water surfaces may be identified by a change in image colour. This colour change may be attributed to a decrease in the intensity of the spectrum at the affected frequencies and is related to the amplitude of the waves present on the surface. A decrease in spectral intensity was observed for all of the recorded slicks. The decrease in spectral intensity corresponded to a reduction in the wave slope and a decrease visible in the sea surface roughness of the affected region. Of particular interest were a number of features in the spectrogram relating to run 4 on the 17th September 1994. These coincided with observations of a surfactant material acting on the wave field. The surfactant was assumed to be material which made its way into the Loch in the run off of fresh water from the surrounding mountains.

The spectrogram of the two orthogonal components of north-south and east-west slope is given in Figure 6.10. Each wave-slope segment had a sample size of 1024 data points. The areas of interest corresponding to observations noted in the trial log are marked on the image. Areas B, D and E correspond to areas of sea surface slope influenced by the presence of the surfactant. Areas A, C

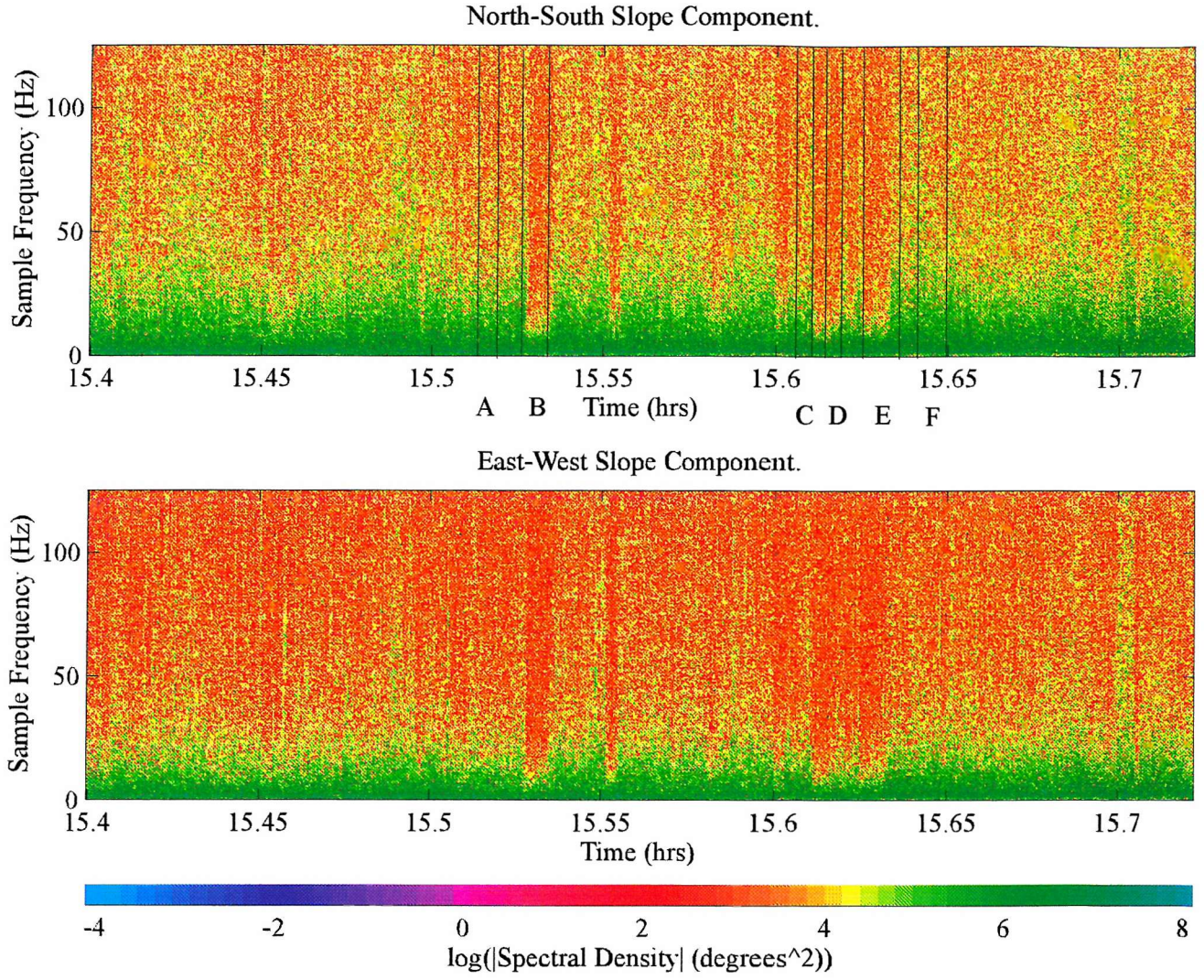

Figure 6.10 Spectrograms of north-south and east-west wave slope taken over run 2 on 17th September 1994 with areas of clean (A, C and F) and slicked (B, D and E) surfaces marked.

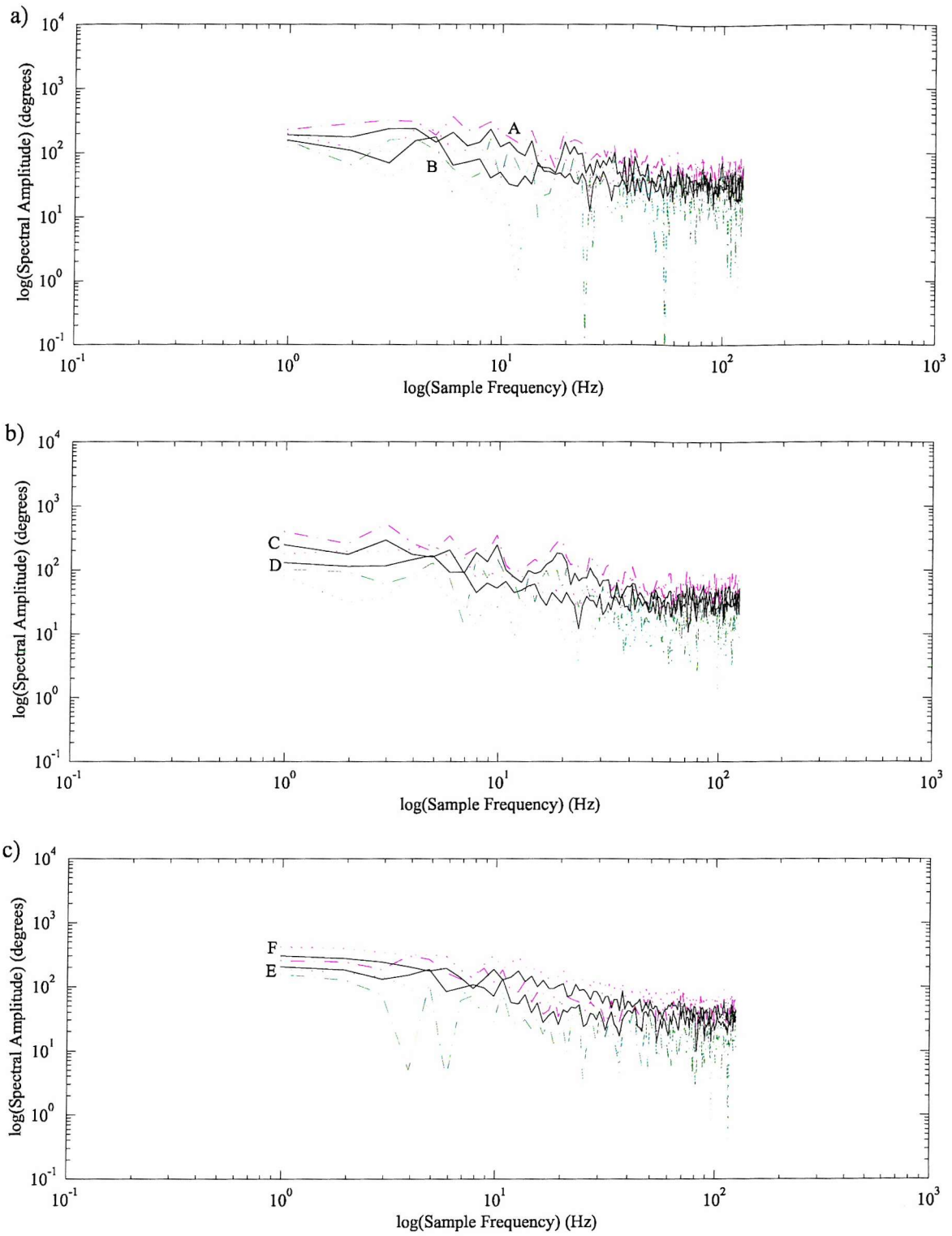

Figure 6.11 Total slope power spectra a) sections A (solid curve) with upper (red dashed curve) and lower error (green dashed curve) and B (solid curve) with upper (red dotted curve) and lower error (green dotted curve), b) sections C (solid curve) with upper (red dashed curve) and lower error (green dashed curve) and D (solid curve) with upper (red dotted curve) and lower error (green dotted curve) and c) sections E (solid curve) with upper (red dotted curve) and lower error (green dotted curve) and F (solid curve) with upper (red dashed curve) and lower error (green dashed curve).

and F are included as reference spectra and are free of any influence of the surfactant on the surface roughness. The reference spectra were derived from surfaces adjacent to the contaminated regions. This limits the influence of changes in other processes, such as the wind, in the hope that the surfactant is the only variable influencing the conditions in the slick.

The use of the spectrogram has enabled the identification of regions affected by the modulation of surfactants on the sea surface wave slope and corresponding reference areas. Individual spectra can now be analysed in more detail to gain information on the sample frequencies affected. Total wave slope power spectra for the above regions were calculated. The surfactant influenced spectra together with their reference spectra are given in figure 6.11. The error in the spectrum was estimated from the scatter, or standard deviation, about the mean value of spectral intensity at each frequency. In all cases, the wave slope spectra of regions modulated by the surfactants have a lower spectral intensity than their non contaminated counterparts in the middle frequency range. The difference in the spectra is not significant in all cases. It is likely that the wave slope values recorded in the regions affected by the surfactant are more susceptible to system noise, reducing the difference in the spectra and increasing the associated error. However, these differences confirm that the effect of the surfactant is to attenuate gravity-capillary waves in the region affected, thus giving a visibly smoother surface compared with the surrounding wave field. There is little difference between the spectral intensity at low frequencies where gravity waves dominate. The spectra then converge at higher frequencies as the slope of the graph flattens off, this is a possible result of the noise level being reached.

One way to proceed with the investigation of the effect of the surfactant on the wave slope spectrum would be to smooth in frequency reducing fluctuations in the spectrum associated with the degree of randomness in the sea surface wave profile. This may help to enhance the underlying trend and reduce the standard deviation at a given frequency providing a more significant measure of the effect of slicks on the spectrum of the wave slope profile.

Similar methods of analysing slick data have been applied to laser slopemeter measurements by Bock and Frew (1993). The results obtained agree with the general trends stated above. Bock and Frew also went onto gain some idea of the frequencies affected by the presence of different slicks. This was done by dividing the clean, rougher surface spectrum by the smoother contaminated surface spectrum and plotting the resulting ratio against frequency. Bock and Frew analysed hydrophilic and hydrophobic surfactants on the surface and found that for hydrophilic slicks the ratio was wide ranging in frequency and for hydrophobic slicks ratios are concentrated into more discrete bands of frequency. No explanation was given for this behaviour. The spectra over slicked and non slicked regions were ratioed in such a manner but was of little use as no

supporting information on the hydrochemical nature of the surfactant material was available and some of the frequencies of interest had been contaminated by system noise.

6.6 Summary of Results and Consequent Recommendations for Instrument Improvement

The aim of this chapter was to assess the ability of the Towed Laser Slopemeter as an instrument for measuring sea surface wave slope. The above analysis of the data set recorded by the TLS during the Loch Linnhe trials of September 1994 found agreement between this record and established sea surface characteristics, including;

- a low frequency slope components exhibited profiles similar to that of a sinusoidal wave train
- a total slope power spectrum comparable with the expected form
- a near Gaussian, or Gram-Charlier, slope distributions

and it was concluded that the TLS is capable of measuring sea surface wave slope.

In an effort to determine the index of the total wave slope power spectrum an estimate of the error in the spectral intensity had to be provided. This proved difficult as Gaussian statistics cannot be applied in the spectral domain. Previous measurements of sea surface power spectra did not make any attempt to estimate the associated error and fits to the spectral curves were applied without an error treatment. A technique often used in the study of astronomical spectra was used to give a value for the error in spectral intensity for each sample frequency in the wave slope power spectrum. The technique was applied successfully. Previous studies usually used a least squares method to fit to sea surface power spectra expressed on logarithmic scales. Expressing the errors in the TLS total slope power spectrum on such a logarithmic scale proved difficult. Instead, a Levenberg-Marquadt fit was successfully applied to the total slope power spectrum and used to give a value for the power index. During the application of these signal processing techniques to the oceanographic data sets it became apparent that the error in the total slope elevation and the direction of wave propagation had been over estimated during the processing of the photodiode ratios. Because of this and in an effort to speed up the processing of the voltage ratios it became clear that the processing software needed revision.

From a spikiness in the slope profile and a flattening of the power spectrum at high sample frequencies it was concluded that there was a higher than expected level of noise in the TLS system. A number of SNR files were recorded during the Loch Linnhe trials. The evidence of

noise in the slope data prompted an analysis of the SNR files. The aim of the analysis was to characterise the type of noise present, which was found to be predominantly white Gaussian noise indicating an electronic source. Imperfect screens and interference filters, placed on the photodiodes in an effort to reduced the effects of ambient light, had led to non-linearities in the response of the photodiode ratios. When combined with a fluctuating laser power this led to a low frequency noise component evident in the analysis of the SNR files. These findings motivated the Southampton team to identify the sources of electronic noise. This led to the replacement of the power converters on each printed circuit board and the implementation of extensive shielding to limit cross-talk between the electronic components. During this refit which was conducted at the clean room assembly at the Rutherford Appleton Laboratories to limit contamination of the optical system, the screens were replaced, and new photodiodes without interference filters attached. These steps were shown to have reduced the level of noise in the TLS system following the completion of the refit. In addition, an RF rudder control system was fitted to limit the crabbing of the catamaran experienced during the Loch Linnhe deployments. Action was taken to improve the waterproofing of all on-board components.

Loch Linnhe was chosen as it allows the generation of internal waves which strongly modulate sea surface waves (Gibson (1994)). The search for evidence of this modulation in the TLS data set was conducted by the DRA but proved difficult due to limitations in the knowledge of the position of the internal wave relative to the TLS. The fitting of an echo sounder, either to the catamaran or the tow vessel, would have removed some of this ambiguity. Although ideal for the generation of internal waves, the Loch with its narrow width and high sides was not an ideal environment for the analysis of wind-sea surface wave interaction. An open expanse of water would have been better suited for such a study. The location and low rate of the wind measurements taken from the RV Calanus restricted the analysis conducted in section 6.3.3. The deployment of an anemometer on-board the tow vessel would have provided a set of wind measurements more applicable to the study of wind - wave modulation using data from the TLS.

Roughness changes caused by surfactant material on the surface of the water were visible to the eye. The TLS made transects through such areas and notes on the changes to the water surface together with the associated time stamp were recorded in a log book. The combination of the written log and a video record would have provided a more comprehensive and continuos account. Changes in sea surface roughness were identified in the TLS data sets using a spectrogram method. As the time stamps between observations in these two records concurred the roughness changes could be attributed to the effects of these slicks. Although the spectral analysis gave an idea of the sample frequencies affected by the presence of surfactants, the study was limited as little was known about the physical and chemical properties of the slicks. A slick sampler would have aided in the study of the effects of various surfactants on the slope profile.

From the experience gained in deploying the TLS in Loch Linnhe and from the subsequent analysis and interpretation of the slope data, it is evident that such studies could have been extended further given appropriate support instrumentation deployed either on board the catamaran or on the tow vessel. It was recommended to the DRA that such an action should be taken prior to further scientific trials and a number of such instruments were fitted to the TLS prior to the CSTAR campaign. Care must also be taken when choosing the site for scientific study, such a choice being driven by the science that is to be conducted.

Chapter 7

Analysis of Data from the CSTAR Trial

7.1 Introduction

In this final substantive chapter of this thesis we continue with the theme of investigation of the TLS as an oceanographic tool capable of providing a measure of the sea surface roughness, by making a comparison of the TLS record with a video record. The video footage was recorded during the deployment of the TLS as part of an experiment to study the interactions between the sea surface wave profile and a bathymetry-influenced tidal flow. During the trial conditions were such that the TLS encountered a range of different wave scales of varying durations and intensities. Before the comparison and subsequent analysis of the TLS data set with the video record, the quality of the wave slope data from the trial is assessed. First, the chapter commences with a brief outline of the trial and the role the TLS played within it.

7.2 An Overview of the 1996 CSTAR Campaign

The Towed Laser Slopemeter, with the permission of the DRA, was operated during 14th and 17th April 1996 as part of the first CSTAR (Coastal Sediment Transport assessment using SAR imagery) experiment. The trial was conducted in a test area 30 km from the Dutch coast (figure 7.1) as part of a European collaboration to study the effects of bathymetry-induced changes to tidal currents on the sea surface wave field and to investigate the radar return from the perturbed surface. It is hoped that such studies will eventually allow SAR radar imagery to be used in cartographic studies of the sea bed and to further our understanding of sediment transport. To maximise the change in sea surface roughness the area chosen had a rapid and large change in

bottom topography, an example of which is given in figure 7.2, and a strong tidal flow. The bottom topography comprised of a set of large sand waves with gentle faces and sharp escarpments. The sand waves varied in depth from 25m at the trough to 19m at the crest and had a typical crest-to-crest spacing of some 400 m. The crests of the sand waves ran perpendicular to the coast. There was little variation parallel to the crests which led to the bottom topography being considered to be one dimensional in models of the area (Vogelzang (1997)). The tide flows parallel to the coast.

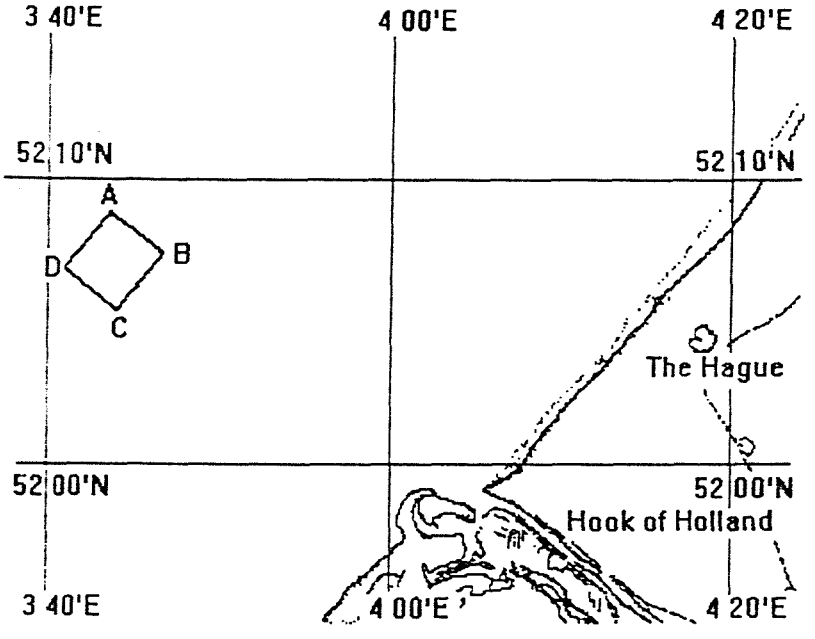

Figure 7.1 CSTAR trial area (lettered square) relative to Dutch coastline.

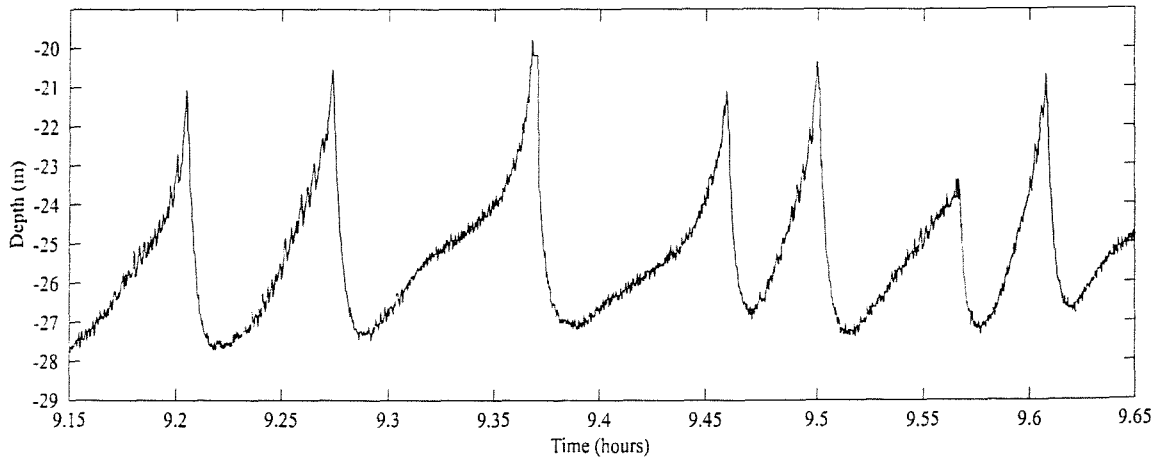

Figure 7.2 Bottom topography of a section of the CSTAR trial area recorded during run 3 on 16th April 1996.

A number of mathematical models exist to account for the changes to radar backscatter from the sea surface caused by the interaction of bottom influenced tidal currents on the sea surface wave profile. To validate, or otherwise, these models and hence gain a better understanding of the processes occurring, a variety of parameters within the models have to be quantified. To provide a complete data set a variety of instruments were deployed in the trial area over the course of the campaign. The RV Planet used an ADCP to provide current measurements and an echo sounder to profile the sea bed. The RV Planet, the main research vessel operated during the campaign, monitored meteorological and oceanographic conditions including air and sea temperature, sea height, swell height, humidity, visibility, wind speed and direction and air pressure. A drift buoy (Stolte (1994)) comprising of three wire probes was also deployed from the research vessel to measure short scale wave height. Position fixes of the buoy and the RV Planet were provided by GPS systems. An airborne SAR system was flown over the area on the 16th April 1996. This provided radar data sets in X, C, L and P-bands. A detailed bathymetric survey of the area was conducted in May 1996 using a single beam echo sounder deployed from the RV Belgica. The sand waves are known to evolve on time scales much greater than the time separating the main part of the trial and the bathymetric survey.

For the duration of the trial the TLS was deployed from, and towed by, the Albatross, a vessel owned and crewed by Rederij Vrolijk of Scheveningen. The vessel was approximately 25m in length and 5m in beam. For the purposes of towing the catamaran the vessel was somewhat large, but this was necessary to transport the TLS to the test area each day. The support equipment was housed at the front of the vessel, with a differential GPS (DGPS) and sonic anemometer placed at the bow some 4m above the mean water surface. The wheel house was situated at the stern and there was enough room amidships for the TLS to sit whilst underway to the test area. A crane aboard the Albatross was used to lift the TLS into, and out of, the water. The support equipment was powered using a hired generator positioned towards the stern.

Once at the test area the slopemeter made transects parallel to, and near, the south eastern edge of the experimental site. This position did not affect the other instruments being deployed but ensured that transects were made perpendicular to the crests of the sand waves. During each run records of the bottom profile, position fixes and wind measurements were made using an echo sounder, the DGPS, and the anemometer, respectively. In addition, video and written logs of the surface conditions were kept. A brief account of the general surface features recorded in the written log is given in appendix B. The addition of extra equipment followed from recommendations made after the Loch Linnhe trial. The echo sounder was placed underneath the amidships tow point of the catamaran. Both the echo sounder and sonic anemometer were provided by the DRA. Prior to the trial an RF system was fitted to the rudders of the catamaran so their direction within the water could be controlled from the tow vessel. The IMU was also moved

to a position next to the optical detection system to limit the possibility of inducing errors when removing vehicle motions from the slope measurements. A more detailed account of the trial is given by Wensink (1997).

7.3 TLS Data Processing and Quality

7.3.1 Data Processing

The TLS photodiode data from the CSTAR trial was initially processed with the software developed for the Loch Linnhe campaign of September 1994. Plots of the along track and cross track slope profiles, taken from a section of data recorded during run 2 on the 15th April 1996, are given in figures 7.3 (a) and (b). Both slope profiles exhibit discontinuous values. These sudden discontinuities are seen in all the wave slope data sets recorded during the CSTAR trial and were obtained in a variety of different wind and sea states. These discontinuous slope values which occur at a high frequencies were not found in the Loch Linnhe data.

To investigate the discontinuities in more detail probability distribution functions, PDFs, of along track and cross track slope profiles were plotted. Typical PDFs taken from the data recorded during run 2 on 15th April 1996 are given in figures 7.3 (c) and (d). Both the along track and the cross track slope components exhibit a highly non-Gaussian slope distribution. The non-Gaussian slope distributions were found to be caused by the discontinuities in the wave slope data. The non-Gaussian shape remained constant for different sample sizes and vessel directions taken over the course of the run. Variations in the PDF shape occurred from run-to-run but not in a manner consistent with the sea surface features being sampled from different vessel directions. In the light of this evidence it was unlikely that the discontinuities in the slope profiles were oceanographic in origin. This conclusion was reinforced after an analysis of the photodiode ratios. These did not exhibit the discontinuities apparent in the slope record. Plots of each of the six photodiode ratios recorded during run 2 on 15th April 1996 for the same period as the profiles of figure 7.3 (a) and (b) are given in figure 7.4. The profiles are typical of the photodiode ratios obtained throughout the course of the campaign.

From the above analysis it was apparent that the processing of the photodiode ratios, recorded during the CSTAR campaign, had introduced the discontinuities into the wave slope data. The processing software had been developed for the Loch Linnhe trial of 1994 at which time algorithms had to be incorporated within the processing software to compensate for the effects of

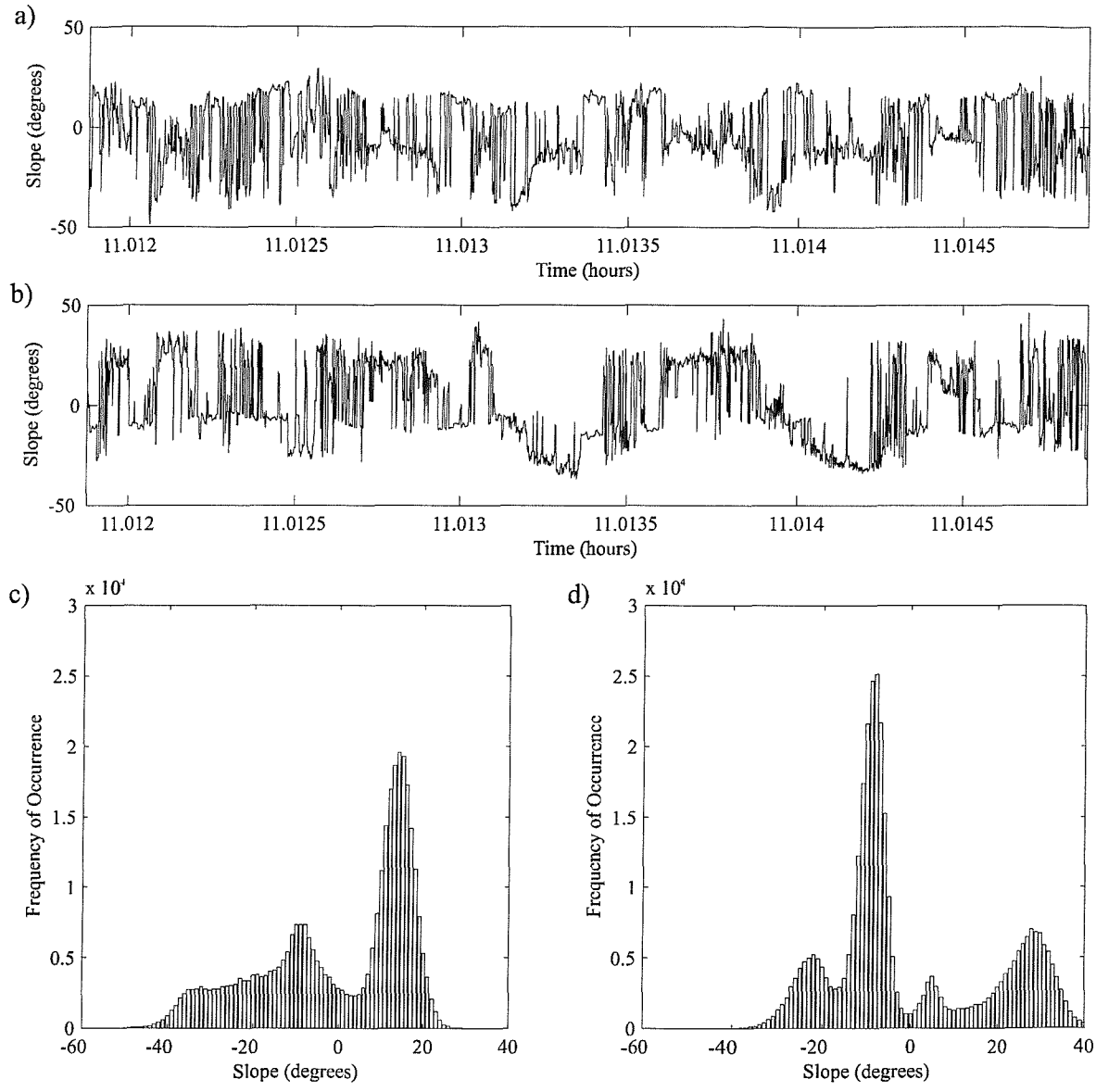

Figure 7.3 Plots of a) along track slope profile, b) cross track slope profile, c) along track slope distribution and d) cross track slope distribution recorded during run 2 on the 15th April 1996.

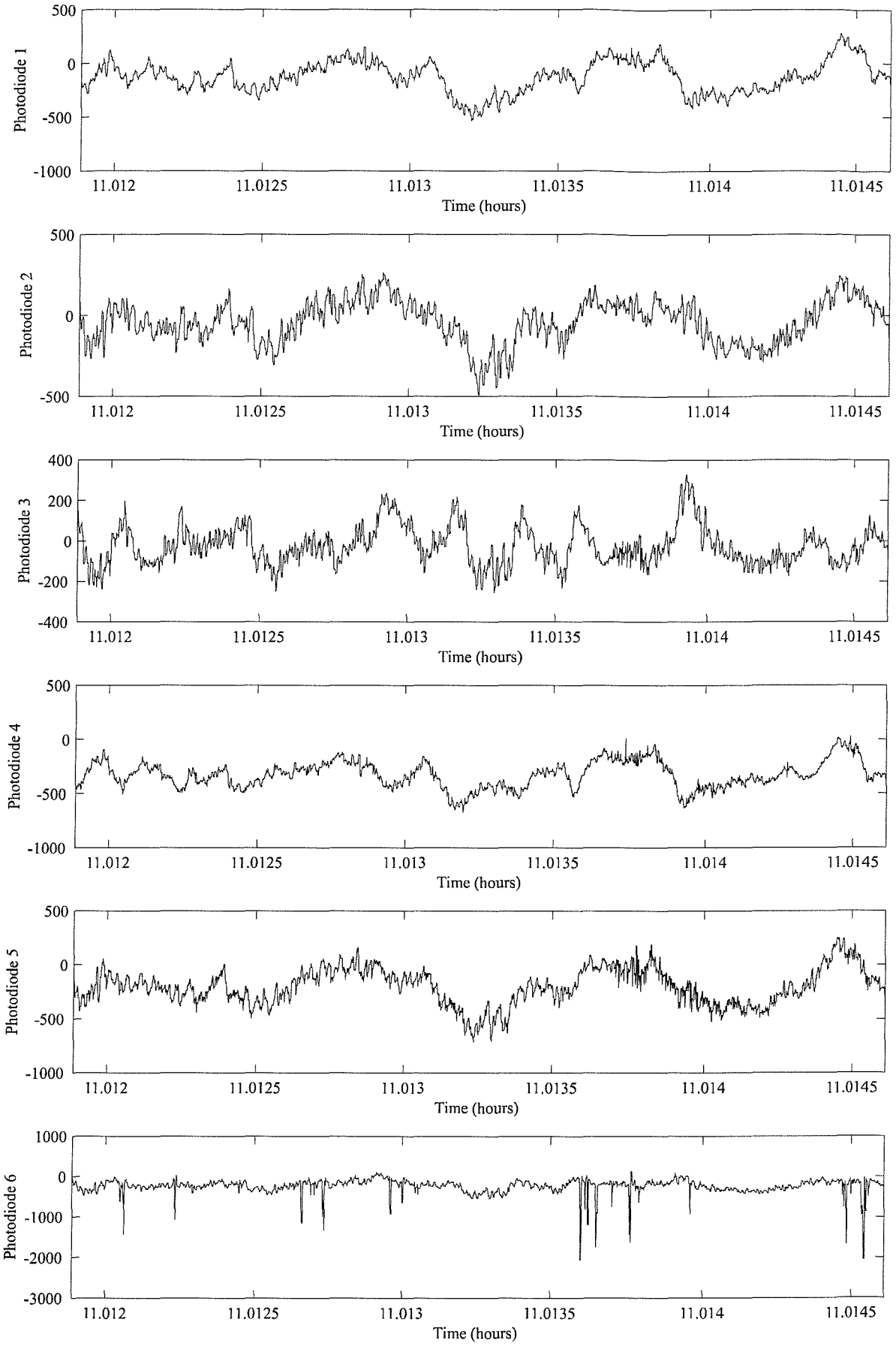

Figure 7.4 Plots of six photodiode ratios with photodiode ratios 1 to 3 on the lower screen and photodiode ratios 4 to 6 on the upper screen. Data taken from run 2 on the 15th April 1996.

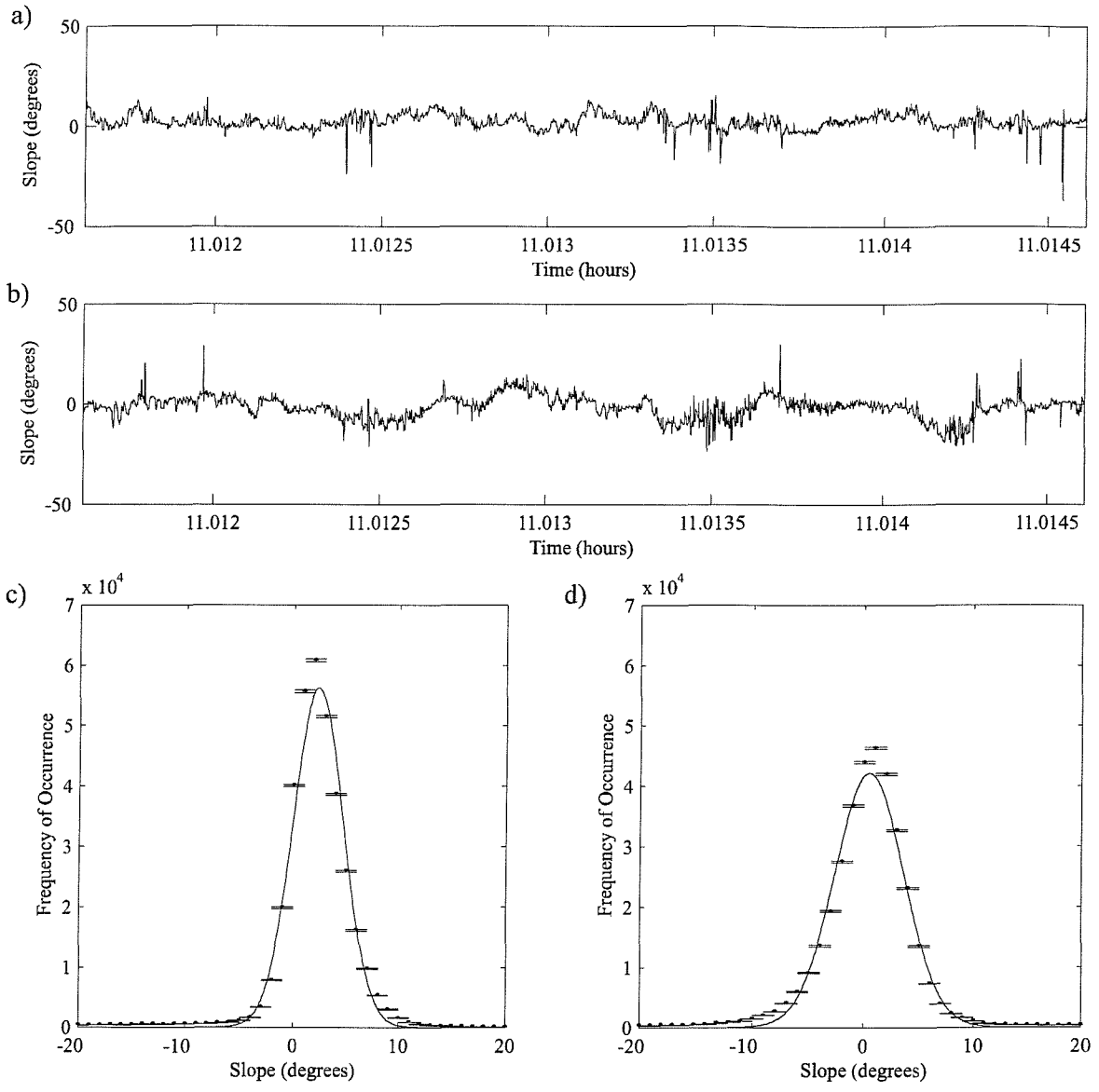

Figure 7.5 Re-processed plots of a) along track slope profile, b) cross track slope profile, c) along track slope distribution and d) cross track slope distributions recorded during run 2 on the 15th April 1996. The slope distributions are plotted with their associated error and fitted with a Gaussian curve.

the higher than expected system noise and the interference patterns within the calibration files. Prior to the CSTAR trial the system noise had been substantially reduced and the removal of the interference filters from the faces of the photodiodes ensured that the photodiodes had the desired response. Following these changes, the methods used within the processing software to compensate for the high system noise and the irregularities within the Loch Linnhe calibration files were no longer appropriate for the processing of the data obtained by the new system. This led to the inaccurate processing of the CSTAR data, introducing discontinuous values in the slope profiles. Following return of the entire TLS system to them in November 1996, the DRA re-wrote the processing software. Following the successful testing and implementation of this software, the DRA re-processed the data set recorded by the TLS during the CSTAR campaign (Taylor (1997)).

Plots of re-processed along track and cross track slope profiles, for the same period as the profiles in figures 7.3 (a) and (b), are given in figure 7.5 (a) and (b). The discontinuities are no longer present and a more representative wave slope profile is apparent. Indeed, a number of gravity waves can be seen in each profile. The slope distributions also exhibited a more believable near Gaussian shape. Typical along track and cross track slope distributions taken from run 2 on 15th April 1996 are given in figure 7.5 (c) and (d).

7.3.2 Photodiode Drop-Out

During the analysis of the photodiode ratios, in response to the discontinuities in the initial wave slope profiles, it was noted that photodiode drop-out had occurred during a number of runs made over the course of the CSTAR trial. Photodiode drop-out can occur when;

- the laser spot leaves the screen
- the phase lock loop has not detected a laser signal
- no signal is generated by a photodiode.

Runs 2 and 3 on the 15th April 1996 exhibited the greatest degree of photodiode drop-out. This was particularly worrying as a review of the video record of the sea surface conditions encountered by the TLS during these two runs contained a variety of different sea surface roughness scales. It was necessary to assess the extent of the problem in terms of its effect on the spectral analysis of the data. Spectral techniques will be used extensively to compare the video and TLS records. Photodiode drop-out is usually encountered at the beginning, or end, of each run as the recording of the photodiode values occurs before the laser aperture opens. Consequently, there is no laser beam signal for the TLS electronics to lock onto and a photodiode ratio of ±2048 is recorded. These regions do not pose any problem to the analysis of the slope data as they are

easy to identify and remove. However, during runs 2 and 3 on the 15th April 1996, intermittent photodiode drop-out occurred on the top screen, affecting photodiode ratio 6 in particular. It is possible to determine the spot position on each screen from just two photodiode ratios but this can reduce the precision to which the spot position, and therefore the slope value, can be determined.

The cause of this drop-out is not clear. Surface conditions were relatively calm so it is not thought that adverse sea conditions would have induced the problem. For these two runs it was noted that drop-out was greatest when the surface was roughest; converging short scale waves may have led to large angles of laser beam refraction resulting in large spot positions. If the response of photodiode six was lower than normal it may not have detected the laser spot at these positions. However, it is just as likely that a loose connection could have caused the drop-out.

The effect of this drop-out on the spectral analysis of the slope data was assessed. The photodiode ratios were used to flag the times at which photodiode drop-out had occurred, a flag of one indicating that one, or more, photodiode ratios had suffered from drop-out and a flag of zero indicating that no drop-out had occurred. The flagged time stamps were then incorporated within the corresponding wave slope data sets. This provided a means of identifying wave slopes that had been determined from photodiodes exhibiting drop-out.

The flagged wave slope data permitted two data sets to be produced. The first contained all the slope values from a run and in the second set photodiodes exhibiting drop-out had been replaced. A mean spectrum was generated over the entire length of each of the data sets using the method outlined in section 6.3.2. By comparing these two spectra it should be possible to determine the extent of the effect of photodiode drop-out on the wave slope spectrum. A significant difference between the two requiring that the wave slope values exhibiting photodiode drop-out are replaced before further analysis can continue. Three methods were used to replace the wave slopes experiencing photodiode drop-out; the first was to remove these data points and shift adjacent values to give a continuous data set; the second replaced these values with an adjacent value of wave slope which had not experienced photodiode drop-out and the third method used a mean value of wave slope calculated from adjacent values of wave slope not experiencing photodiode drop-out to replace the affected data points. The results are graphed in figures 7.6 (a), 7.7 (a) and 7.8 (a), respectively. The corresponding errors were generated by propagating the errors in the wave slope data into the spectral domain using the technique discussed in section 6.3.2. In all cases the errors were greater than the any difference between the two types spectra and are not plotted to aid clarity. From these plots it can be seen for all three cases that there is no significant difference between the two types of spectra. This is an encouraging result, we can conclude that

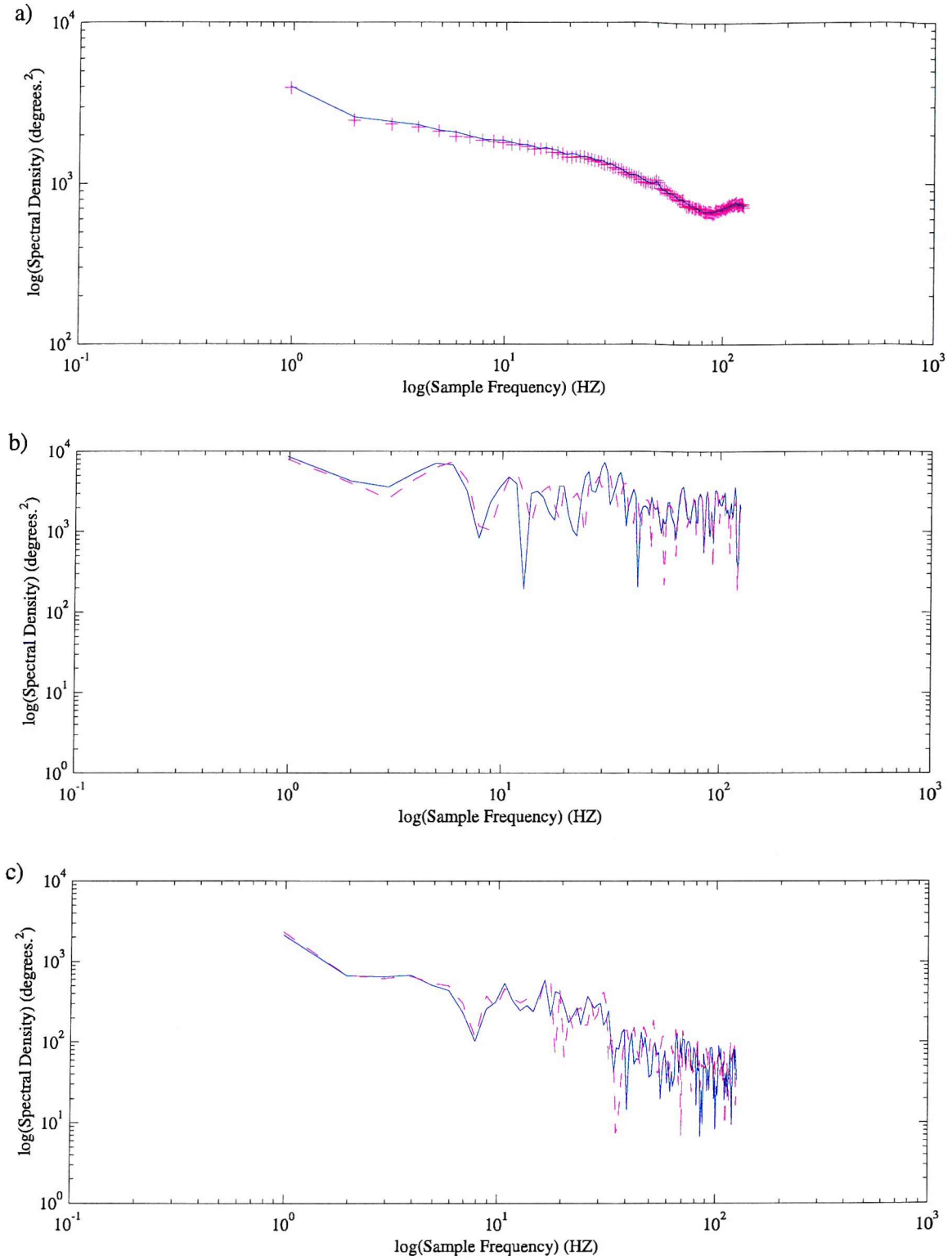

Figure 7.6 Spectral comparisons made with wave slope data experiencing photodiode drop-out included or removed. Data taken from run 2 on 15th April 1996. a) Total wave slope spectra made over the duration of the run without (solid) and with (crossed) drop-out, b) total wave slope spectra over 256 points without (solid) and with (dotted) drop-out and c) control total wave slope spectra over 256 points with all values (solid) and with some slope values replaced (dotted).

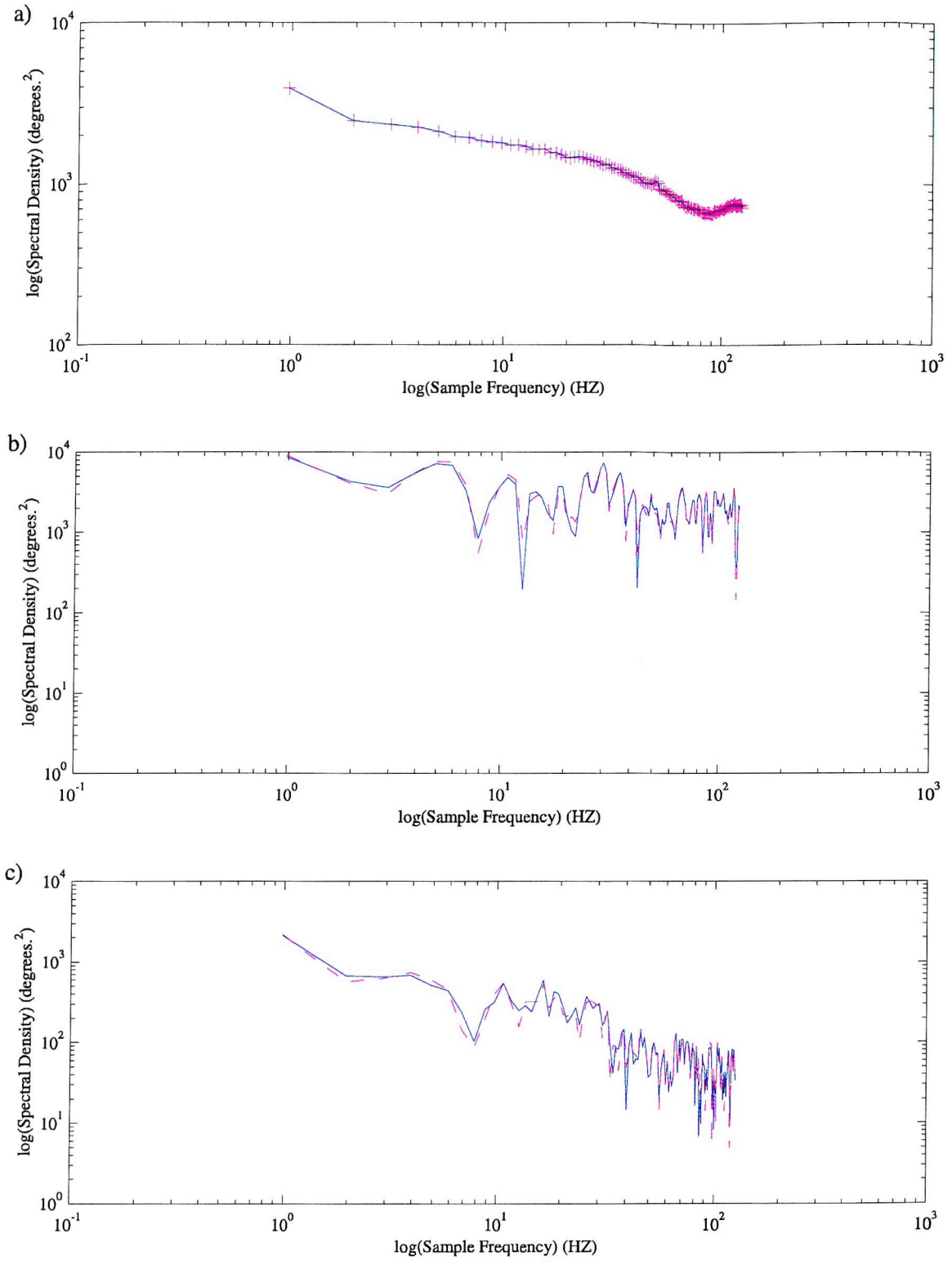

Figure 7.7 Spectral comparisons made with wave slope data experiencing photodiode drop-out included or replaced with adjacent values not experiencing drop-out. Data taken from run 2 on 15th April 1996. a) Total wave slope spectra made over the duration of the run with drop-out replaced (solid) and included (crossed), b) total wave slope spectra over 256 points with drop-out replaced (solid) and included (dotted) and c) control total wave slope spectra over 256 points with all values (solid) and with some slope values replaced (dotted).

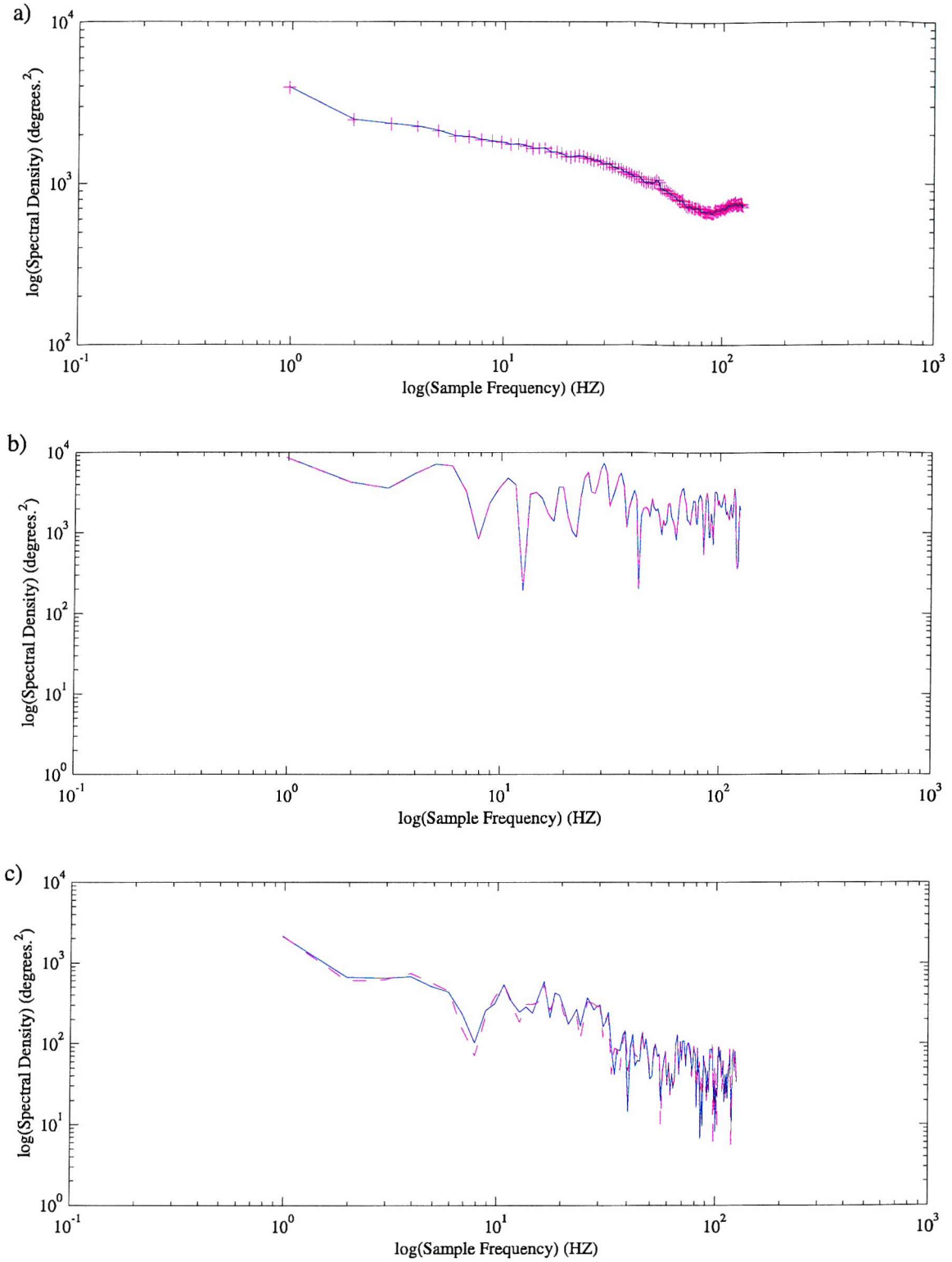

Figure 7.8 Spectral comparisons made with wave slope data experiencing photodiode drop-out included or replaced with the mean of adjacent values not experiencing drop-out. Data taken from run 2 on 15th April 1996. a) Total wave slope spectra made over the duration of the run with drop-out replaced (solid) and included (crossed), b) total wave slope spectra over 256 points with drop-out replaced (solid) and included (dotted) and c) control total wave slope spectra over 256 points with all values (solid) and with some slope values replaced (dotted).

the wave slope values experiencing photodiode drop-out do not have a significant affect on the mean spectrum calculated over the run and their replacement prior to such an analysis would have no advantage. However, the effect of drop-out on an individual spectrum needed to be determined as they were to be used in the spectrographic analysis of the wave slope data.

The greatest change, if any, in an individual wave slope spectrum due to photodiode drop-out will be expected to occur over a region of the data set containing the greatest number of wave slope values that have been determined from photodiode ratios experiencing drop-out. Such an area was found in each run and was used to produce two sections of data each with a length the same as the Fourier transform size of 256 points. The first section of data contained all the original values. The second had all the wave slope values generated from photodiode ratio experiencing drop-out replaced using the methods outlined above. The spectra with wave slope values experiencing drop-out were either removed, replaced with adjacent values, or replaced with the mean of adjacent values are graphed together with corresponding spectrum from the original data set in figures 7.6 (b), 7.7 (b) and 7.8 (b) receptively. To aid clarity the errors which were determined using the technique discussed in section 6.3.2 are not plotted. The differences between the spectra of figures 7.6 (b) and 7.7 (b) are of the order of the estimated errors. It is difficult to determine whether the differences in the spectra are as a result of photodiode drop-out or due to the methods of replacing the affected values. Figure 7.8 (b) gives a more encouraging result. Replacing wave slope values experiencing photodiode drop-out with a mean value calculated from adjacent slopes not experiencing photodiode drop-out maintains a level of continuity in the wave slope profile which the other two techniques do not ensure and for this reason the method is preferred. There is no significant difference between the two spectra of figure 7.8 (b) and again we can conclude that the wave slope values experiencing photodiode drop-out do not have a significant effect on spectra calculated in this manner and their replacement would have no advantage.

Any differences between spectra in figures 7.6 (b), 7.7 (b) and 7.8 (b) may be the result of the inclusion of wave slopes generated from photodiodes experiencing drop-out. However, this could also occur from the removal and replacement of these wave slopes. To allow us to examine the effects, if any, of replacing wave slope values without the chance of photodiode drop-out influencing any change a control is used. A region of data which did not contain wave slope values generated from photodiode ratios experiencing drop-out was found for each run. Two sections of data were produced each with a length the same as the Fourier transform size of 256 points. The first section of data contained all the original values. The second section was generated from the data in this region but with wave slope values replaced at the same relative positions as the second section of data used in figures 7.6 (b), 7.7 (b) and 7.8 (b). The resulting spectra are plotted in figures 7.6 (c), 7.7 (c) and 7.8 (c) for wave slope values removed, replaced with an adjacent value or replaced with the mean of adjacent values, respectively. Again errors are

not plotted to aid clarity. The differences between the two spectra in figures 7.6 (c) and 7.7 (c) are of a similar order to those between the two spectra of figures 7.6 (b) and 7.7 (b). It is likely that the method by which the wave slope values experiencing photodiode drop-out had been replaced in these two cases has led to the differences between the spectra. However, comparing figures 7.8 (b) and 7.8 (c) there is a larger difference between the control spectra than the spectra taken in the region experiencing photodiode drop-out. The control region was taken from a section of the TLS record recorded under calm surface conditions. The region experiencing photodiode drop-out was significantly rougher. The replacing of values with the mean of adjacent values may have a greater effect on the spectrum recorded under calmer conditions than under rougher conditions and this may explain the differences between the two spectral plots.

Of the three methods outlined above, the replacing of wave slope values experiencing photodiode drop-out with a mean value calculated from adjacent wave slope values not experiencing photodiode drop-out is the most preferred. However, given the frequency of photodiode drop-out, 2826 data points in 352350 data points for run 2 on 15th April 1996, and as there is little difference between the original and replaced spectra of figures 7.8 (a) and (b) it was decided that for the ensuing data analysis it was not necessary to replace wave slope values experiencing photodiode drop-out.

7.3.3 Discussion

We have satisfied ourselves that the photodiode data have been processed in a manner which now gives a precise measure of the wave slope and that photodiode drop-out does not have a significant effect on the wave slope spectrum calculated either over an entire run or, when compared to the effects of its removal, over a single Fourier transform. We are now in a position to compare slope data with the extensive video record of the sea surface conditions encountered by the slopemeter during the CSTAR campaign. Such a comparison will enable us to determine whether, or not, the TLS is capable of giving an accurate measure of different sea surface roughness scales and will provide a direct visualisation of the slope changes that can be detected by the instrument.

7.4 Comparison of the TLS Wave Slope Record with Video

Video records of runs 2 and 3 recorded on the 15th April 1996 exhibited a wide range of roughness changes on a nearly smooth background sea surface. The difference in intensity between the nearly smooth ambient surface and the rougher areas of the sea surface, together with the rapid change between these two regimes, allowed different features within the video to be easily identified for comparison with the TLS record. Corresponding roughness changes within the wave

slope data should be identifiable if the TLS is truly capable of measuring the sea surface wave profile.

7.4.1 Run 2 on the 15th April 1996

Run 2 on the 15th April 1996 commenced at 11.00 hours and finished at 11.42 hours. The time stamp associated with the wave slope record is taken as the reference time and is expressed in decimal hours. To aid the clarity of the figures presented and discussions on results the run time in seconds is also given. The run time commences at the start of the run. The mean wind speed and direction with respect to magnetic north during the run were 0.7 ms^{-1} and -86° respectively. The current velocity was 0.02 ms^{-1} and parallel to the Dutch coast. The TLS was towed parallel to the sand waves from B to C in figure 7.1. The catamaran's general heading as recorded by GPS data was -160°.

The video camera was used to film the sea surface within the vicinity of the bows of the catamaran. The time on the video camera can be set to the nearest minute and was displayed together with the correct date in the lower right hand corner of each frame. The TLS record provided the initial time stamp from which the video clock was set at the beginning of each run. The video record was reviewed using a video player which gave the tape position in seconds from the start of the tape. It was possible, using the video player, to determine the time within the video record to the nearest second. This was done by identifying a position within the tape at which a minute increment occurred. However, as the video record can only be set to the nearest minute it can only be assumed to be absolutely accurate to within a minute of the TLS record.

In an attempt to compare the TLS and video records spectrographic analysis was applied to the TLS wave slope data set. Figure 7.9 contains an along track spectrogram taken over run 2 on the 15th April 1996. A FFT length of 256 data points was used. This is the standard FFT length for the spectral analyses presented in this chapter unless otherwise stated. The spectral intensity ranges in colour from dark greens at high spectral intensities to dark reds at low spectral intensities. Therefore, the dark greens which are most notable at low frequencies were attributed to an increase in wave slope and dark reds which are most common at high frequencies, to a decrease in wave slope.

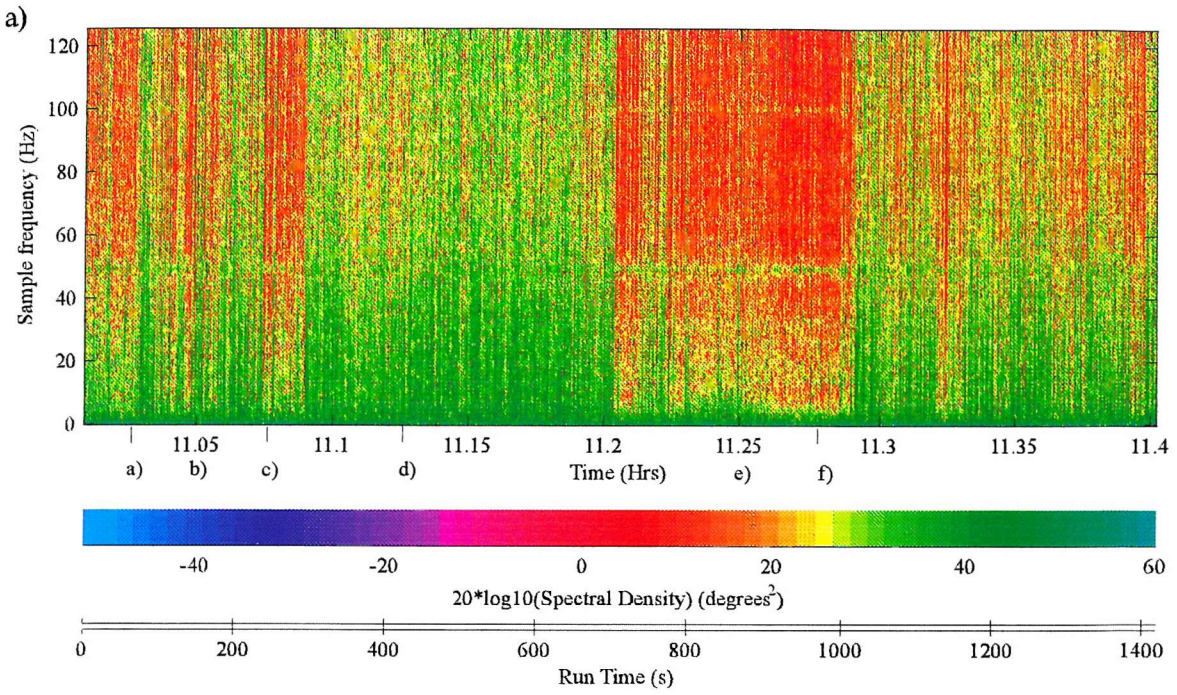

Figure 7.9 Along track wave slope spectrogram of run 2 on the 15th April 1996

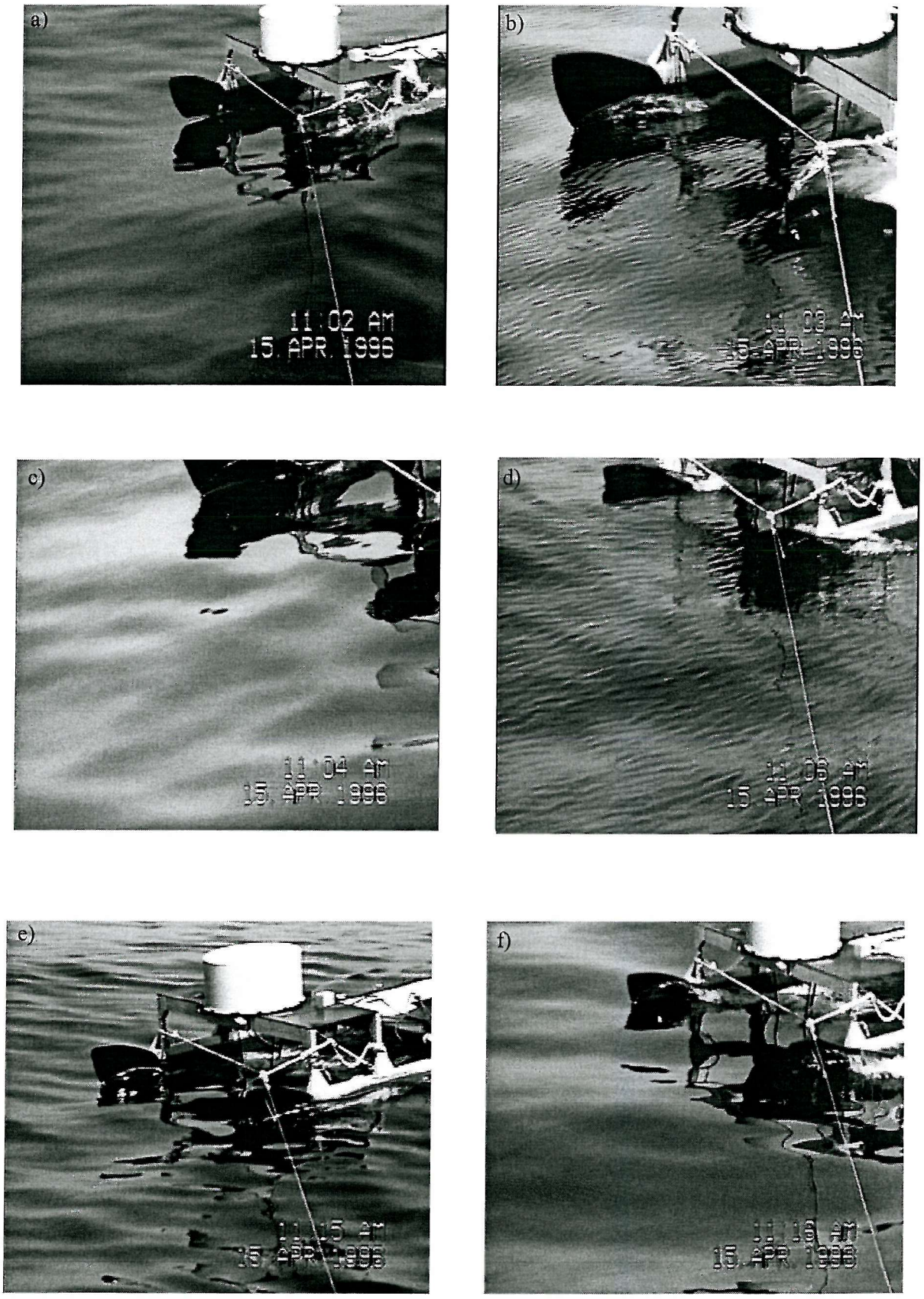

Figure 7.10 Video stills taken at a) 11.03, b) 11.045, c) 11.08, d)11.115, e)11.25 and f) 11.275 hours from run 2 on 15th April 1996

From the spectrogram, increased spectral densities can be seen between 11.05 and 11.08 hours, 11.10 and 11.2 hours and 11.3 and 11.4 hours. Lower spectral intensities are evident at times outside these. Video stills showing different roughness scales were identified at 11.03, 11.045, 11.08, 11.115, 11.25 and 11.275 hours and are presented in figure 7.10. The time in hours and minutes is given in each still. Minutes were converted to a fraction of an hour to allow comparison with the spectrogram. To aid this comparison the time at which the images were taken is marked on the spectrogram and is accompanied with the corresponding letter of the video still. The stills of figure 7.10 (a), (c) and (f) which were taken at 11.03, 11.08 and 11.275 hours respectively, show significantly less roughness than at other times, agreeing with the times of reduced spectral intensity identified from the spectrogram of figure 7.9. From the video the residue of a swell could be seen but there were no short gravity, or gravity-capillary, waves evident during the smooth surface conditions. From the stills of figure 7.10 (b), (d) and (e) an increase in roughness is apparent. In the stills of figure 7.10 (b) and (d) the increase in roughness is seen to occur at gravity-capillary wave scales. In figure 7.10 (e) there are no gravity-capillary waves present, the increase in roughness occurring at short gravity wavelengths.

It is clear from the above comparison that a lower spectral intensity within the spectrogram corresponds to lower wave slopes leading to an observed decrease in the sea surface roughness within the video record. Similarly, a higher spectral intensity corresponds to larger wave slopes leading to an increase in the sea surface roughness evident within the video footage. This explains why in regions of greater surface roughness a range of colours for a given time in the spectrogram can be seen. Although, in periods of lower sea surface roughness the higher frequencies are dominated by a red colour as the noise in the TLS system begins to influence the record. Having found general agreement between the video record and the TLS wave slope data we proceed with the aims of this section and extend our comparison to time scales below a minute-by-minute account.

Two horizontal bands at 50 Hz and 100 Hz can be seen in the spectrogram of figure 7.9. It is believed that the 50Hz line is a signal generated by the transmission of the IMU data producing a signal in the electronics used to determine the spot position. The 100Hz signal is a harmonic of this. It is believed that the signals were present in the Loch Linnhe data but due to system noise remained undetected. The signals can be removed with the suitable application of a notch filter.

It was decided to analyse a section of data from 11.035 to 11.115 hours having a duration of nearly 4 minutes. The review of the video record between and about these times had revealed a variety of roughness changes occurring at different frequency scales including gravity, short gravity and gravity-capillary waves. The intensity of these roughness scales varied to a level that was just discernible over the speckle of the video. Correspondingly, the spectrogram of total wave

slope over this section of data exhibited a range of variations in spectral density. Figures 7.11-7.18 present the results of this detailed analysis. A synopsis of the main results of the comparison of the TLS wave slope record and the video record between 11.035 and 11.115 hours is given in table 7.1 together with time stamps, relevant figures and comments.

The video tape was reviewed from 11.038 hours (11:20:20 GMT) to 11.116 hours (11:07:00 GMT). A written log of all discernible roughness changes together with an associated time stamp to the nearest second was made. To aid the comparison of the video record with the total wave slope spectrogram, the written notes were used to assign subjective roughness values to the time stamp taken from the video. Surfaces exhibiting increased roughness were assigned a value of one and smooth surfaces a value of zero. Faint roughness changes were assigned a value of a half. This allowed a crude plot of the different intensities of sea surface roughness seen within the video record to be made against the corresponding time stamp.

Figure 7.11 (a) contains a spectrogram of the total wave slope on which the roughness levels observed in the video record have been superimposed. If we assume that the time stamps in the two records agree exactly we find little, or no, agreement between the two data sets. This is not surprising as the error in the initial time stamp of the video record relative to the initial time stamp of the TLS record has been estimated to be ± 1 minute. Much better agreement between the two records is found if the time stamp of the video record is incremented by 0.0157 hours (56.7 s) as shown in figure 7.11 (b). Now the bands of increased spectral intensity coincide with observed increases in sea surface roughness evident from the video record. Similarly, lower spectral intensities coincide with smoother areas of sea surface roughness apparent in the video. In this way, the TLS record has been used to determine a more precise time for the video record. To provide clarity in the rest of this section, the video time will be shifted by 0.0157 hours to ensure agreement between the time stamps of the video and TLS records unless otherwise stated.

To aid our analysis of the TLS wave slope record, video stills capturing interesting surface features, roughness conditions and boundaries between regions of varying roughness for this section of data are displayed in figure 7.12. Each still has been given a letter which is marked at the corresponding time on the spectrogram of figure 7.11 (b).

The first four narrow peaks in the subjective roughness value determined from the video record correspond to the passage of a set of 1-2m waves each leading to a sudden increases in the spectral intensity of the spectrogram at the corresponding time. Three of these gravity waves are captured in the video stills of figures 7.12 (a), (b) and (c) which were taken at 11.0546, 11.055 and 11.0567 hours respectively. It should be possible to identify these waves from the corresponding section of wave slope data which is plotted in figure 7.13 (a). A total wave slope profile has been used in this

case as it is easier to identify low frequency changes in wave slope. Low frequency wave profiles can be seen in the data at 11.0545, 11.055 and 11.0566 hours. These variations in wave slope can be enhanced by the application of a 30 point averaging filter to the wave slope profile. The filter reduces the high frequency detail allowing low frequency variations to be identified more readily. The period of these variations which is some 10° is of the order of 2s. The corresponding vessel speed was approximately 1.5 ms^{-1}. The low frequency variations can be attributed to the passage of gravity waves. This is an important result; not only do we have agreement between the times of the video and TLS records at which these changes in wave slope occur but also between the causes of these changes.

After the final gravity wave, the TLS intercepted a patch of gravity-capillary waves. These are captured within the video still of figure 7.12 (d). The duration of the patch within the video record and the duration of the corresponding increase in spectral intensity is some 5s. Agreement within a few seconds between the video and TLS records indicates the how abrupt the boundaries between rough and calm surfaces are as we would expect the TLS to be more sensitive to variations in wave slope and hence surface roughness than the video camera. The region was short lived and the TLS soon moved into a calmer region captured within the video still of figure 7.12 (e) at 11.0594 hours. A few seconds later at 11.06 hours the TLS intercepts a train of gravity waves evident in the still of figure 7.12 (f) and led to the bow of the catamaran being partially submerged. The gravity waves pass by to leave another period of calmer waters as seen in the top half of figure 7.12 (g). These increases and decreases in the roughness evident within the four stills correspond with equivalent changes within the spectrogram.

A second patch of gravity-capillary waves pervade the surface between 11.062 and 11.074 hours having a duration of 46s and led to a corresponding increase in the spectral intensity of the spectrogram over this period. These waves can be seen in the bottom half of figures 7.12 (g) and (h) as the TLS moves into this region. The variability in the intensity of these waves is apparent when the stills of figures 7.12 (i) and (j) are compared. The region ends abruptly which is evident from the spectrogram and from figure 7.10 (k) in which a few gravity-capillary waves can be seen in the middle of the left hand side of the still. A calmer surface is apparent in figure 7.12 (l).

We now investigate this boundary in more detail. Figure 7.14 (a) contains a profile of the along track wave slope recorded over some 18s. There is a greater number of large high frequency negative slopes in the rougher section of data as compared to the calmer section. These do not always coincide with occurrences of photodiode drop-out which are plotted in figure 7.14 (b). The cause of these interesting slope values is not clear at this stage. Screen splash scattering the incident laser light has been suggested as a possible source but was not evident following the inspection of the screen at the end of the run. Wave slopes at the short gravity-capillary, capillary

wave scales may be a cause. Waves converging to form a sharp peak will lead to both positive and negative slopes. Breaking waves forming in a preferred direction will lead to a pre-dominance of large slopes of a given sign. As well as these large negative slopes, it is also apparent from the profile that the calmer region of data exhibits a set of gravity waves.

Spectral analysis of the profile might help to indicate the wavelengths at which the increase in wave slope, and therefore sea surface roughness within the video record, was occurring. To determine any change, spectra from the rougher and the smoother surfaces must be compared. Such surfaces may extend over a number of spectral lengths and to get a representative view a number of spectra should be averaged. Care must be taken when averaging spectra. Averaging over too small a number of spectra will not give a representative cross section of data from which to estimate the error in the spectrum. Too many will lead to sudden and short term changes dominating the spectrum. The last effect is illustrated in figure 7.14 (c) and (d).

The mean spectra in figure 7.14 (c) have been calculated from the along track wave slope data between 11.0735 and 11.0745 hours for the top curve (A) and between 11.0745 and 11.0755 hours for the bottom curve (B). There is a significant difference between the two spectra. As expected the spectral intensity of the rougher surface is greater than the spectral intensity of the smoother surface. Figure 7.14 (d) contains two mean spectra calculated from the along track slope data between 11.072 and 11.0745 hours for the top curve (C) and between 11.0745 and 11.077 hours for the bottom curve (D). Although the spectral intensity of the smoother surface is less than that of the rougher surface, as expected, the difference can not be considered significant. The associated errors in these plots were calculated from the scatter, or the standard deviation, of the individual spectra about their respective mean values. This method is more appropriate for determining any significant change in the average spectrum when comparing different regions of the sea surface, rather than propagating errors through from the wave slope profile which would give a measure of the effect of instrumentational error in the spectrum. Although within the significant levels, both plots show the two spectra overlapping at low frequencies due to the presence of a gravity waves on the calmer surface.

The most significant difference between the two spectra of figure 7.14 (c) occurs between 8 and 20 Hz and is therefore not induced by the high frequency spikes exhibiting large negative slope values. The corresponding true wavenumbers can be estimated from the relationship;

$$\omega_e = \omega - k u \cos\theta \qquad 7.1$$

which was given in chapter 5 and where ω_e is the wave frequency of encounter and ω is the true wave frequency which is related to k, the true wavenumber, through the gravity-capillary

dispersion relation. The vessel speed, u, had a mean value of 1.75 ms^{-1} at the time. The direction of wave propagation relative to the heading of the TLS, θ, was estimated to be -96° from the video still in figure 7.12 (j). For these values the sample frequencies of 8 and 20 Hz correspond approximately to wavelengths of 0.06 and 0.02 m respectively. This is of the order of the wavelength of the waves in the video still which were estimated to be 0.1 ±0.05 m. The wavelength is estimated from the video by counting the number of wave crests between the bows of the catamaran in a given video still. As distance between the bows is known the mean wavelength can be ascertained from the number of crests present. The associated error which is large arises from video flicker, imprecise focus and varying levels of surface illumination within the still.

The smooth surface remains until 11.09 hours. However, this is punctuated with gravity, short gravity and faint gravity capillary waves which are evident in the video record and appear as increases in spectral intensity within the spectrogram. The still of figure 7.12 (m) captures the passage of a gravity wave which causes the bows of the catamaran to become partially submerged. The effect of another gravity wave can be seen in figure 7.12 (n) this time resulting in the bow of the catamaran being lifted from the water. A set of faint gravity-capillary waves can be seen towards the middle of the left hand side and the lower left hand side of figures 7.12 (n) and (o) respectively. A profile of the along track wave slope is given in figure 7.15 (a). A gravity wave occurring at 11.076 hours and corresponding to the one recorded in the still of figure 7.12 (m) can be seen more clearly in the total wave slope profile of figure 7.15 (b). There is an increase in the high frequency waves after 11.078 hours. Low frequency wave slope variations can be seen in the along track profile which correspond to the troughs and crests of larger waves. Spectral plots taken between 11.078 and 11.079 hours for curve (A) and 11.079 and 11.08 hours for curve (B) are given in figure 7.15 (d). It is apparent from this plot that curve (A) was taken from a rougher surface than curve (B). The most significant difference in the two spectra occurs above 12 Hz. For an average vessel speed of 1.6 ms^{-1} and a wave direction of -96° estimated from the faint waves in figure 7.10 (n), this sample frequency corresponds to a wavelength of 0.03 m. Although it is difficult to estimate the exact wavelength of the waves in the video still they are certainly of the centimetre order.

The still of figure 7.12 (p) captures both gravity-capillary waves evident in the lower left hand corner of the frame and the passage of a gravity wave. Figure 7.12 (q) shows a calmer surface, although when compared to the still in figure 7.12 (e) it is evident that there has been an increase in short gravity waves explaining the corresponding increase in the spectral intensity of the spectrogram. Another extended patch of gravity-capillary waves is intercepted by the TLS at 11.09 hours and is captured in the still of figure 7.10 (r). The transition is also evident in the wave profile of figure 7.16 (a). This is evident from the increase in larger slopes. The claim is supported

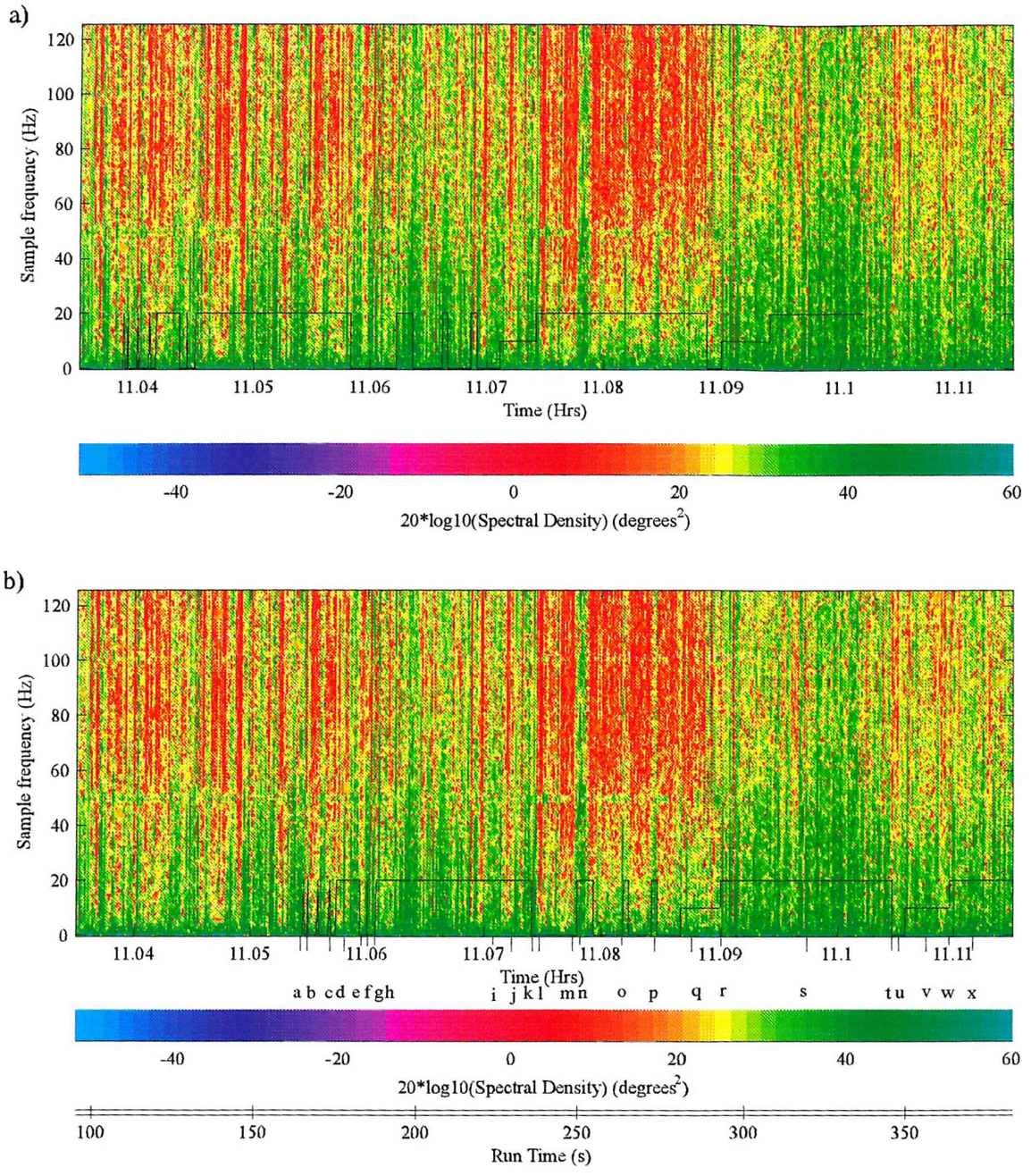

Figure 7.11 Along track wave slope spectrogram between 11.035 and 11.115 hours on 15th April 1996 and superimposed video roughness level a) without offset and b) with offset.

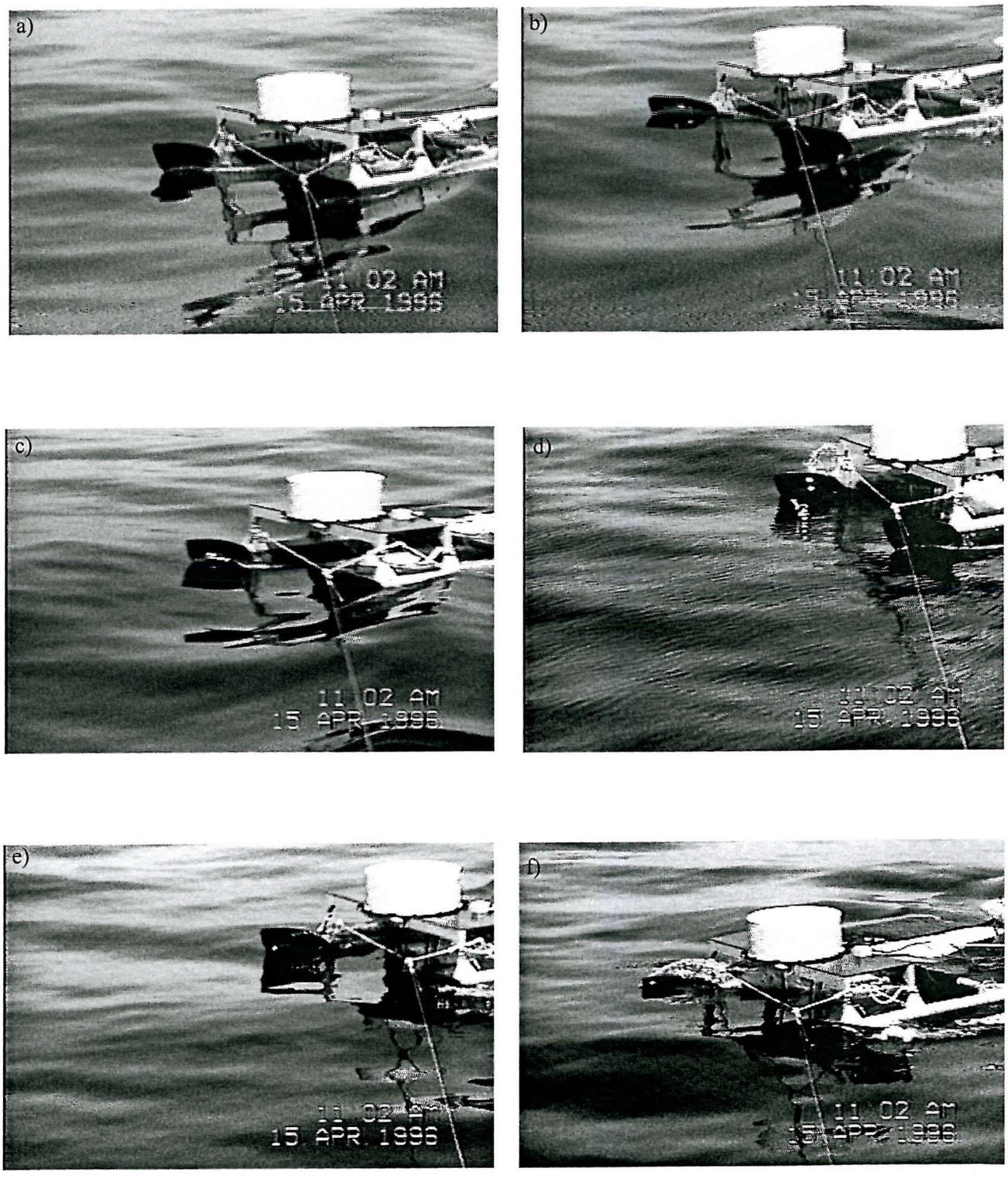

Figure 7.12 Video stills taken at a) 11.0546, b) 11.055, c) 11.0566, d) 11.058, e) 11.0594 and f) 11.06 hours from run 2 on the 15th April 1996

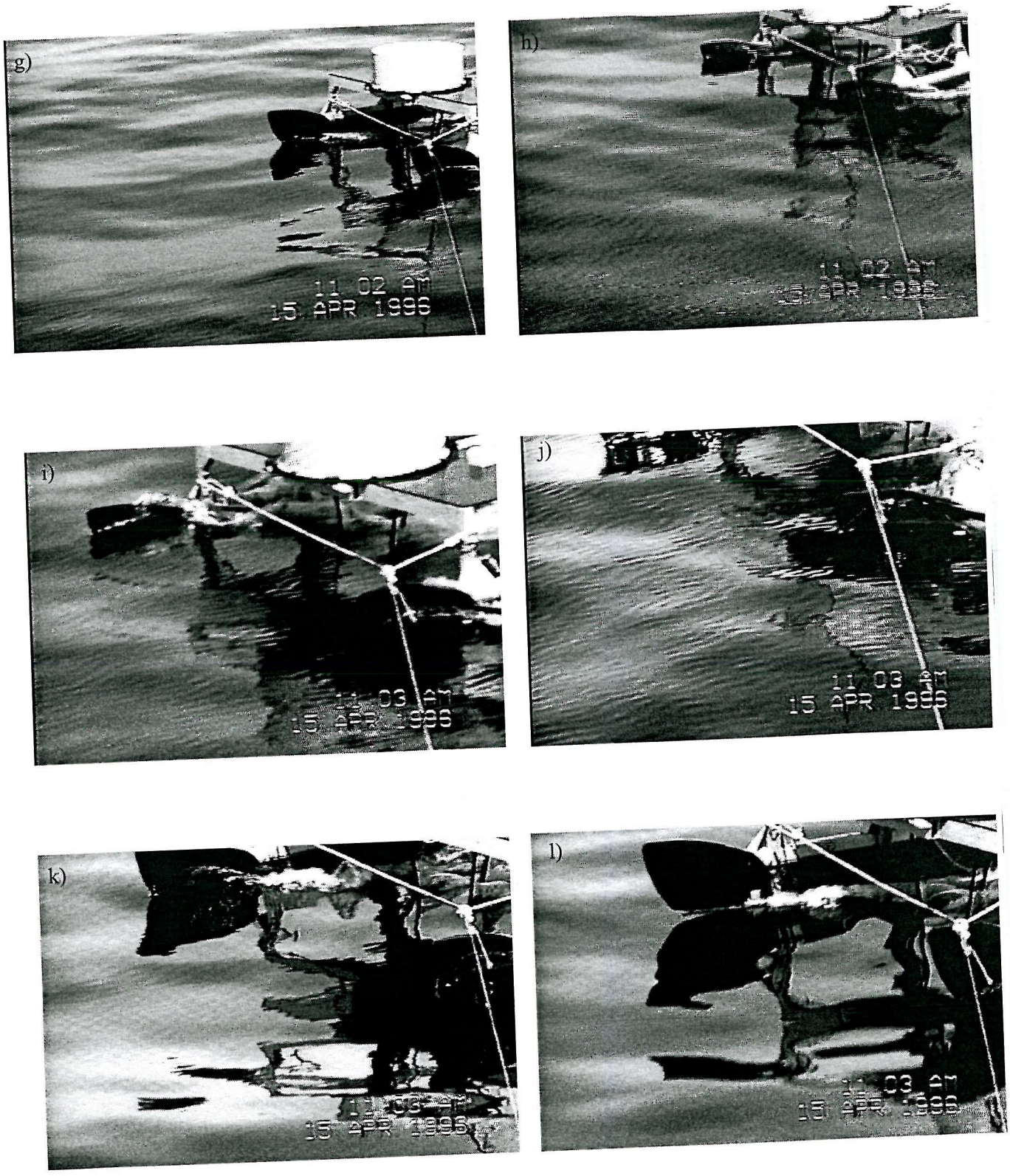

Figure 7.12 (continued) Video stills taken at g) 11.061, h) 11.0614, i) 11.071, j) 11.0725, k) 11.074 and l) 11.0742 hours from run 2 on the 15th April 1996

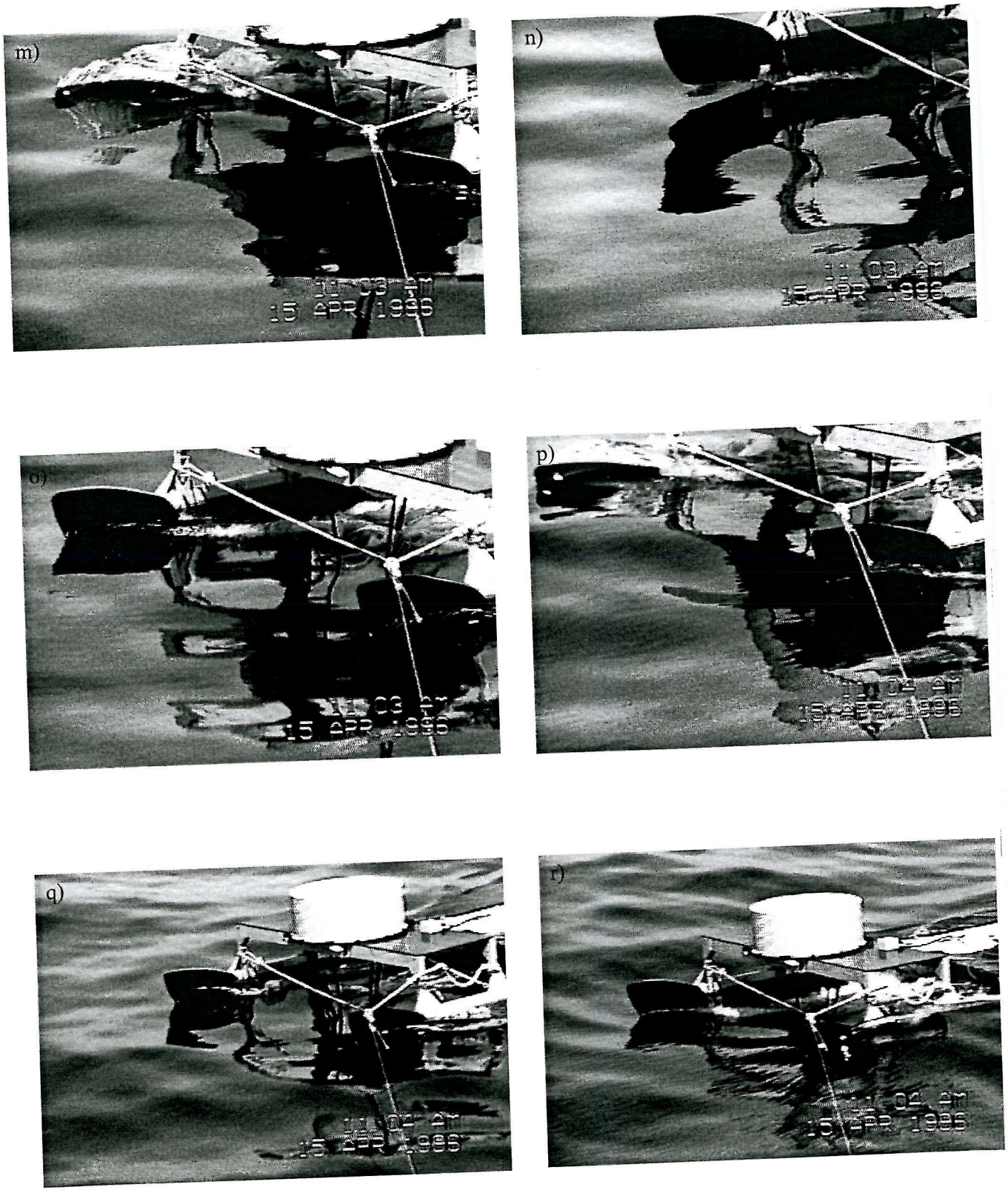

Figure 7.12 (continued) Video stills taken at m) 11.076, n) 11.0775, o) 11.082, p) 11.085, q) 11.088 and r) 11.09 hours from run 2 on the 15th April 1996

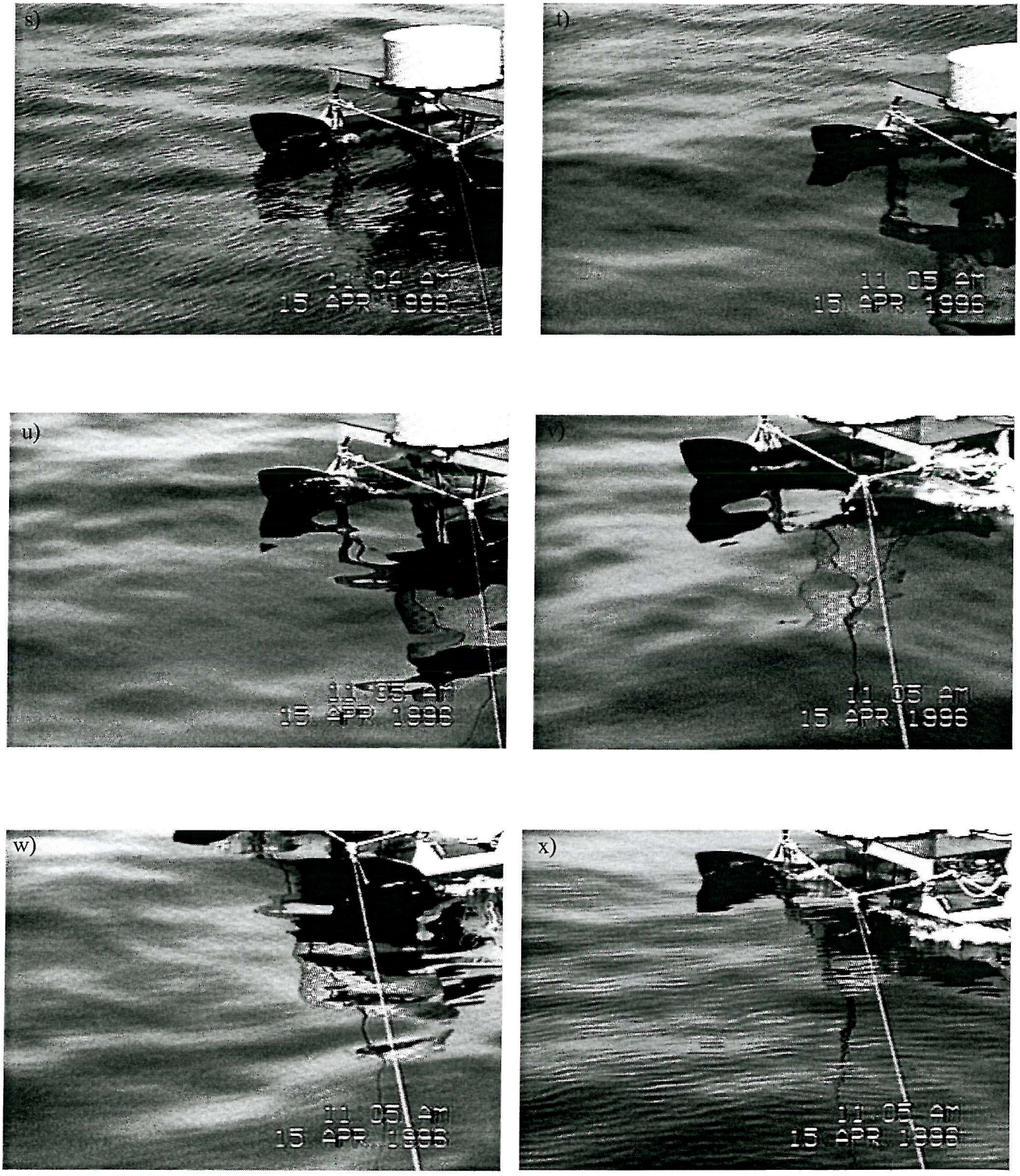

Figure 7.12 (continued) Video stills taken at s) 11.0975, t) 11.1047, u) 11.105, v) 11.1075, w) 11.1097 and x) 11.112 hours from run 2 on the 15th April 1996

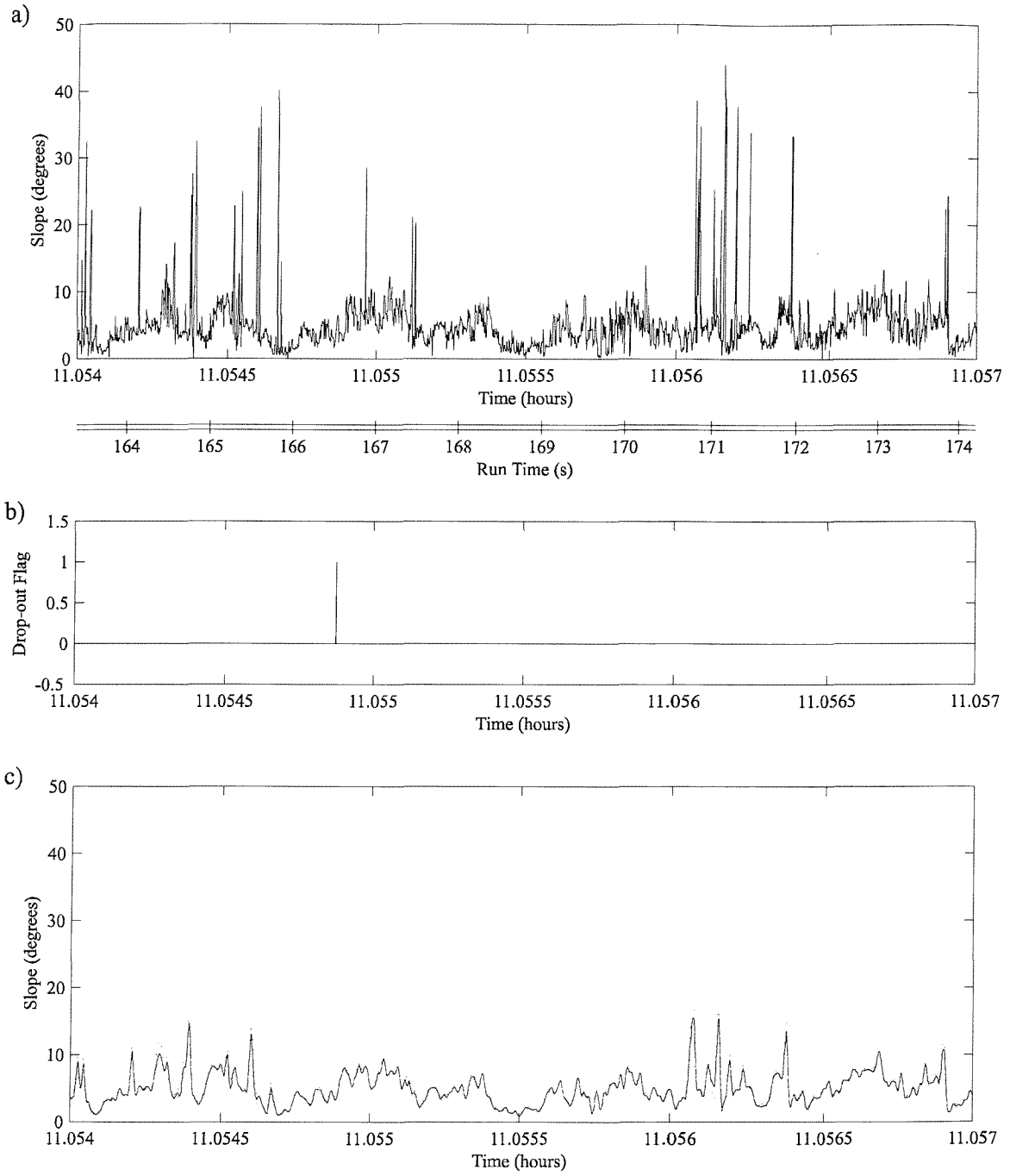

Figure 7.13 Plots of a) along track wave slope profile, b) photodiode drop-out flag and c) 30 point averaged along track wave slope profile (solid curve) with upper (red dotted curve) and lower (green dotted curve) error. Data taken from run 2 on the 15th April 1996.

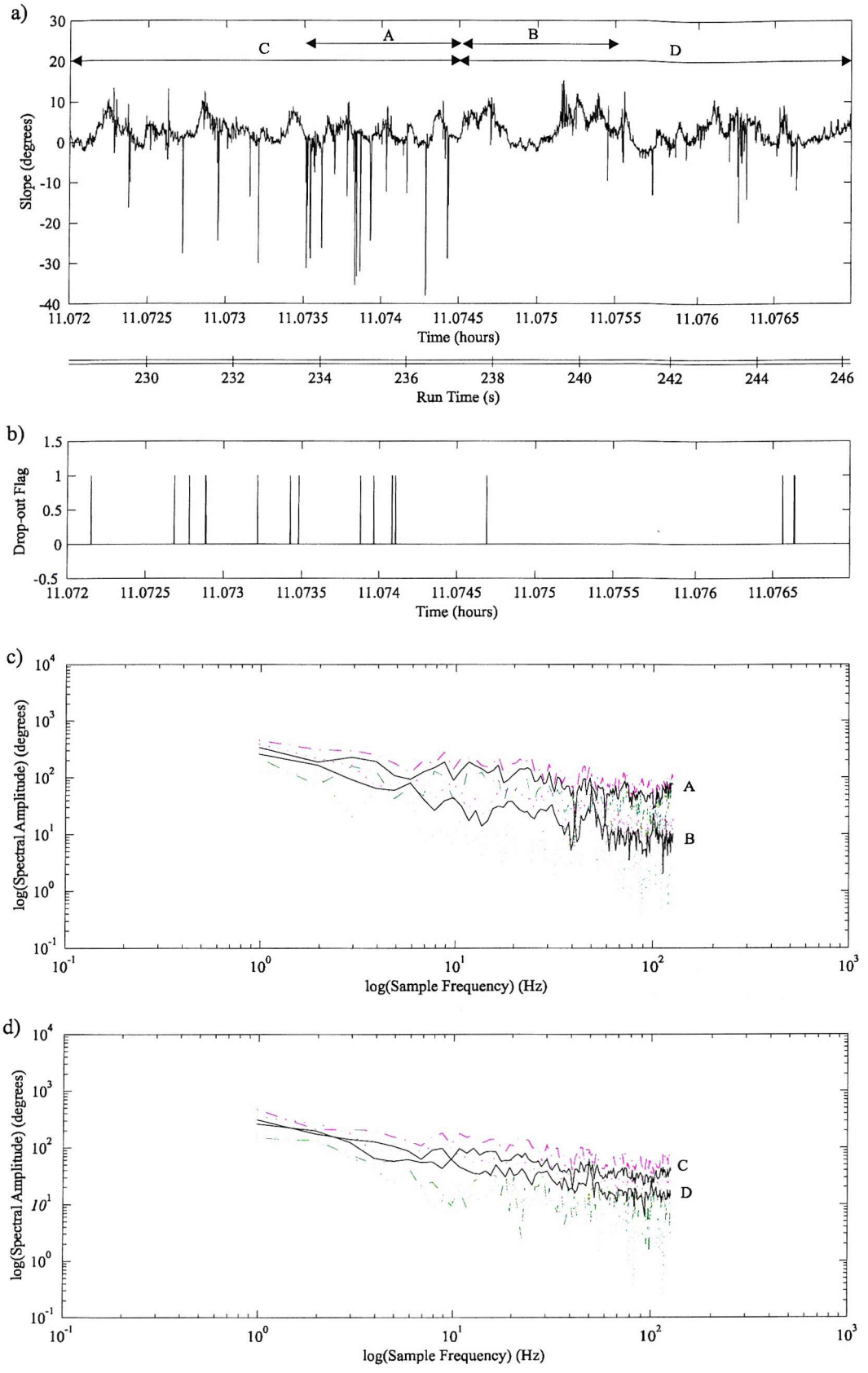

Figure 7.14 Plots of a) along track wave slope profile, b) photodiode drop-out flag, c) along track wave slope spectra between 11.0735 and 11.0745 hours (solid curve A) with upper (red dash) and lower (green dash) errors and between 11.0745 and 11.0755 hours (solid curve B) with upper (dotted red) and lower (dotted green) errors and d) along track wave slope spectra between 11.072 and 11.0745 hours (solid curve C) with upper (red dash) and lower (green dash) errors and between 11.0745 and 11.077 hours (solid curve D) with upper (dotted red) and lower (dotted green) errors. Data taken from run 2 on the 15th April 1996.

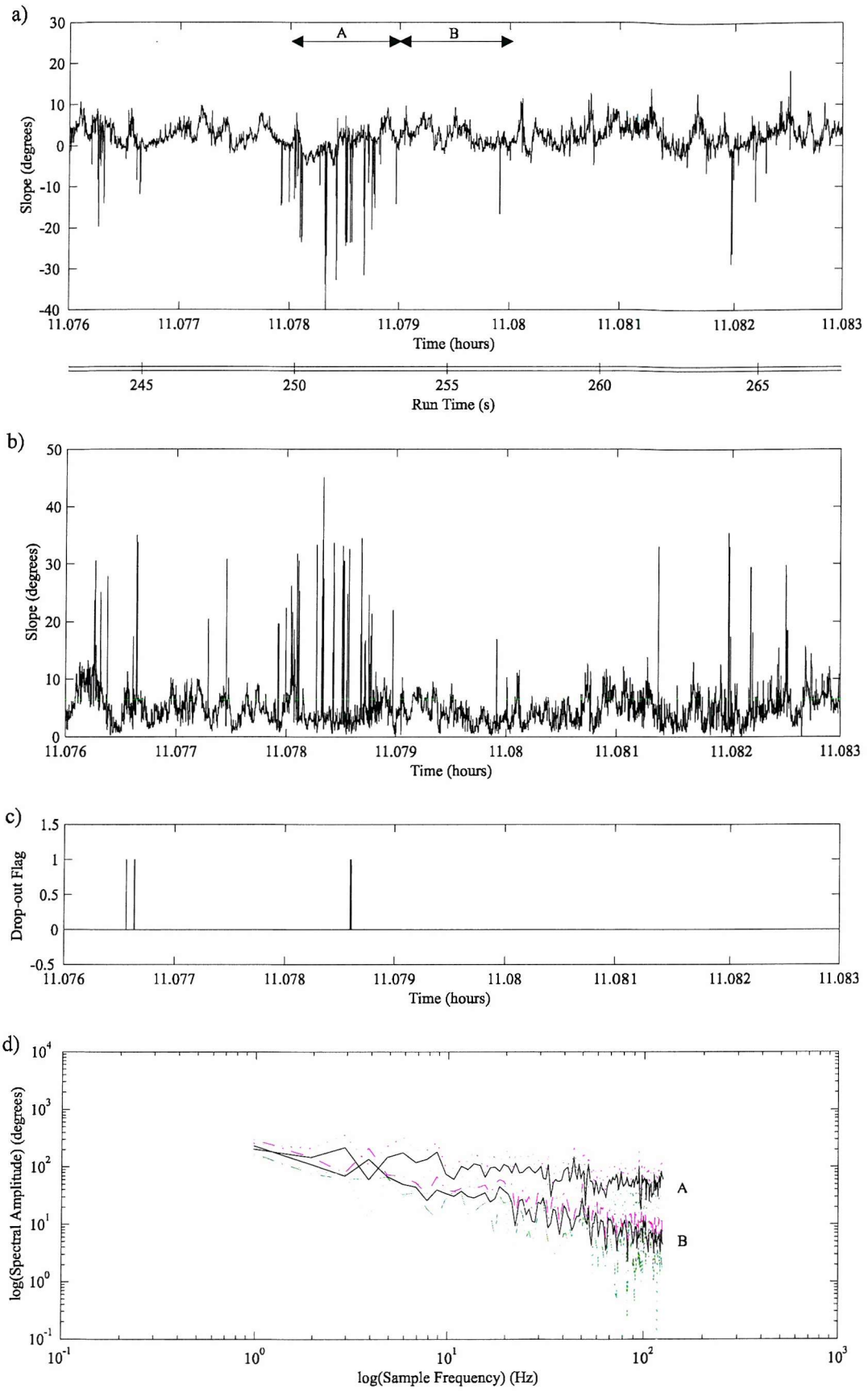

Figure 7.15 Plots of a) along track wave slope profile, b) total wave slope profile, c) photodiode drop-out flag and d) along track wave slope spectra between 11.078 to 11.079 hours (solid curve A) with upper (dotted red) and lower (dotted green) errors and between 11.079 to 11.08 hours (solid curve B) with upper (dashed red) and lower (dashed green) errors. Data taken from run 2 on the 15th April 1996.

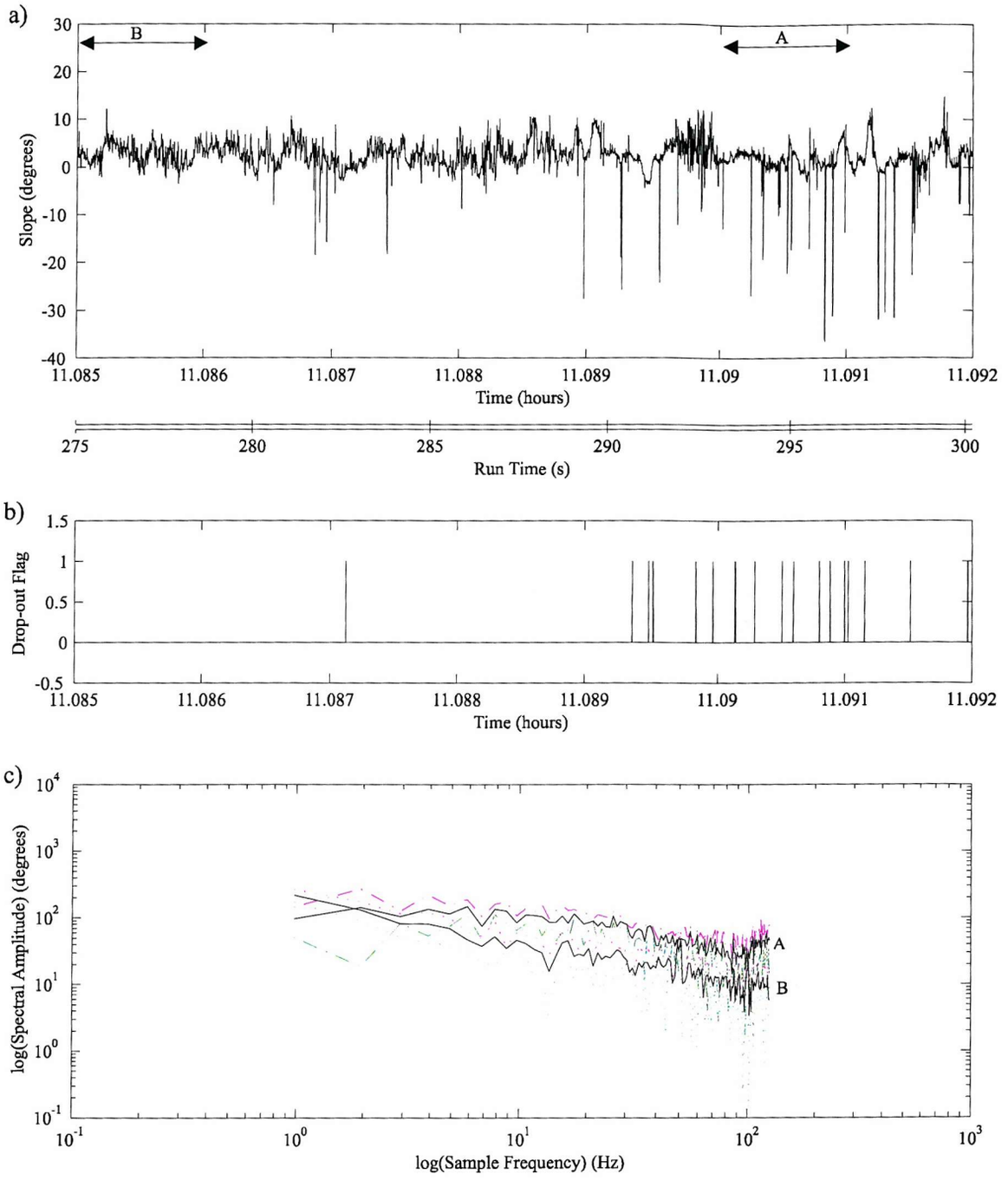

Figure 7.16 Plots of a) along track wave slope profile, b) photodiode drop-out flag and c) along track wave slope spectra between 11.085 to 11.086 hours (solid curve B) with upper (dotted red) and lower (dotted green) errors and between 11.09 to 11.091 hours (solid curve A) with upper (dashed red) and lower (dashed green) errors. Data taken from run 2 on the 15th April 1996.

Time (GMT Hours)	Figure	Comments
11.0546	7.12 a), 7.13 a)	Gravity wave
11.055	7.12 b), 7.13 b)	Gravity wave
11.0558	7.13 c)	Gravity, gravity-capillary waves
11.0566	7.12 c)	Gravity wave
11.058	7.12 d)	Gravity-capillary waves
11.0594	7.12 e)	Calm surface
11.0597	7.12 f)	Gravity wave
11.061	7.12 g)	Start of gravity-capillary waves
11.0614	7.12 h)	Start of gravity-capillary waves
11.071	7.12 i)	Gravity-capillary waves
11.0725	7.12 j)	Gravity-capillary waves
11.074	7.12 k), 7.14	End of gravity-capillary waves λ=0.1±0.05m
11.0742	7.12 l)	Calm surface
11.076	7.12 m), 7.15 a)	Gravity wave
11.0775	7.12 n), 7.15	Gravity-capillary wave. Faint λ=0.03-0.015m
11.082	7.12 o), 7.15 a)	Gravity-capillary waves
11.085	7.12 p)	Gravity and faint gravity-capillary waves
11.086-11.089	7.12 q)	Short gravity waves
11.09	7.12 r) 7.16	Start of gravity-capillary waves
11.0975	7.12 s)	Gravity-capillary waves
11.095	7.12 t)	End of gravity-capillary waves
11.1015	7.12 u)	Calm surface.
11.1075	7.12 v)	Gravity wave
11.1085	7.12 w)	Start of gravity-capillary waves
11.112	7.12 x)	Gravity-capillary waves

Table 7.1 Synopsis of comparison between video and TLS record together with comments, time stamps and relevant figures were λ is wavelength.

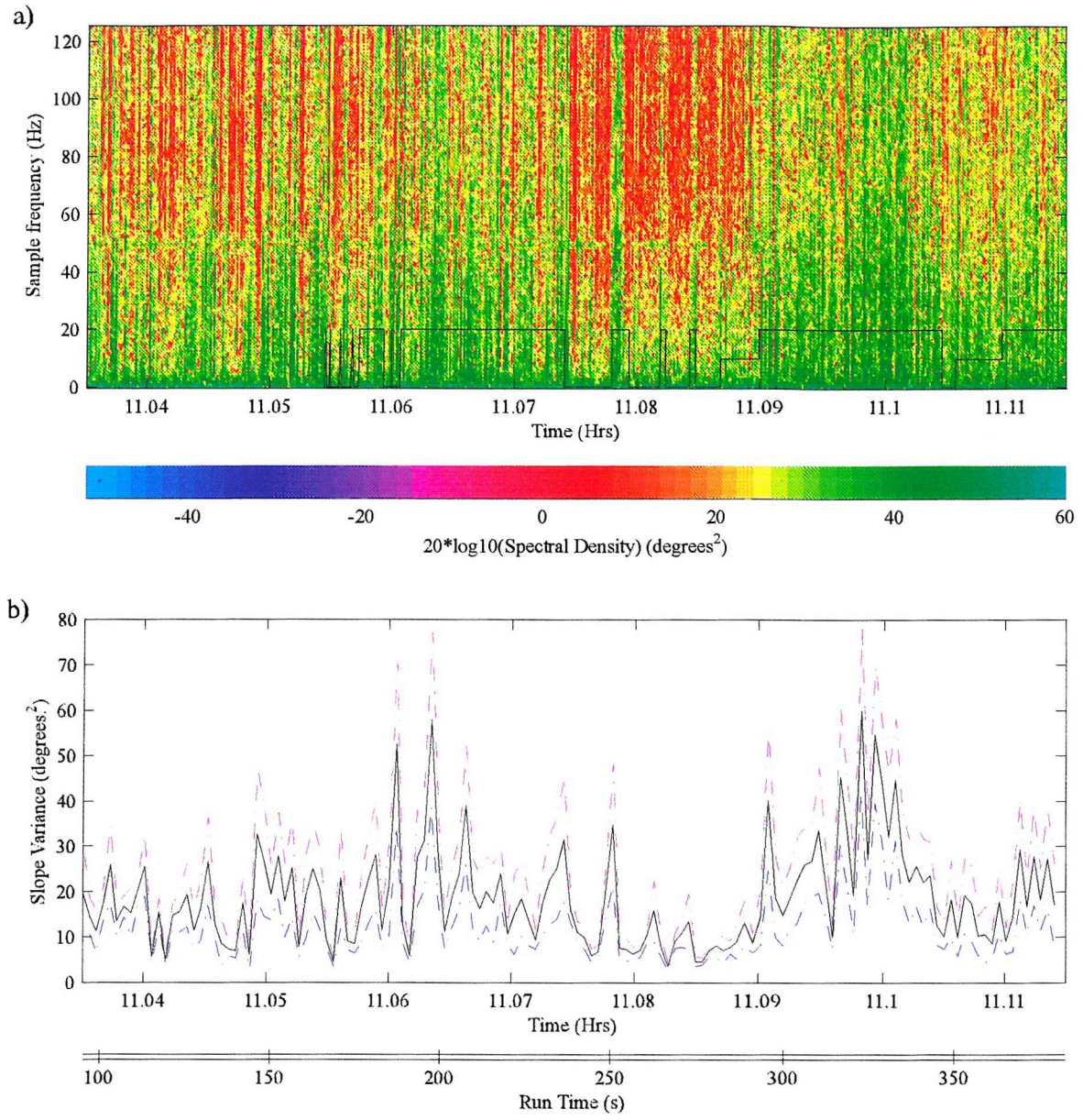

Figure 7.17 a) Along track wave slope spectrogram and superimposed video roughness level between 11.035 and 11.115 hours on 15th April 1996 and b) along track wave slope variance (solid curve) and associated errors (dotted curve) for the same period.

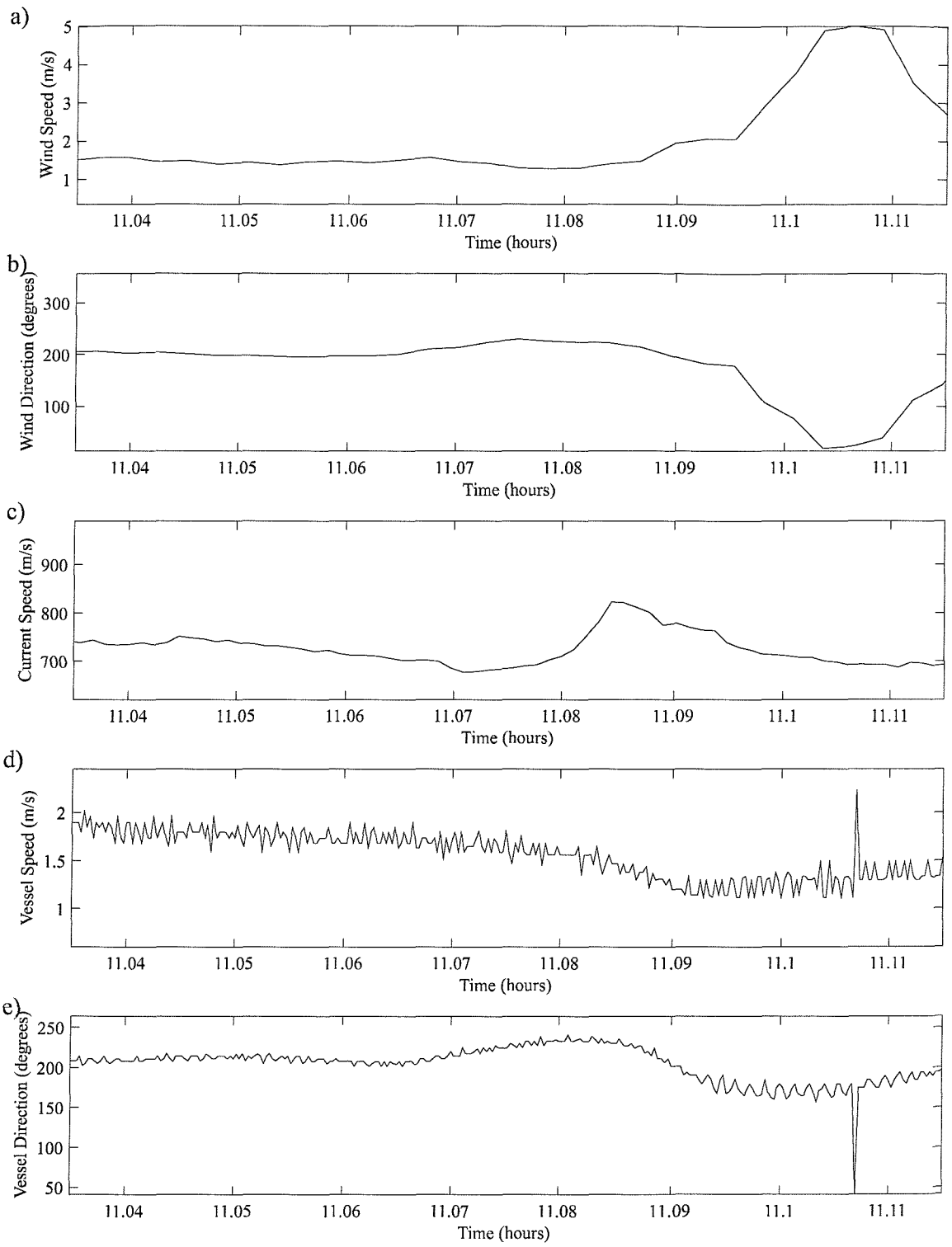

Figure 7.18 Plots of wind speed and direction, vessel speed and direction and sea surface current speed. Data taken from run 2 on the 15th April 1996.

by the comparison of spectra taken between 11.085 and 11.086 hours for curve (B) and 11.09 and 11.091 hours for curve (A) and plotted in figure 7.16 (c). Again, the most significant change between these two spectra occurs above 7.5 Hz. For an average vessel speed of 1.25ms^{-1} and estimating the wave direction relative to the catamaran to be -94°, this sample frequency corresponds to a wavelength of 0.06 m. From the still the wavelength of these gravity - capillary waves was estimated to be 0.1 ±0.05m. This region of gravity-capillary waves evident in the still of figure 7.12 (s) continues for approximately 52s. The still of figure 7.12 (t) captures the end of the region of high frequency waves which gives way to a calmer surface in the lower half of the figure. The calmer surface is evident in the video still of figure 7.12 (u) taken at 11.105 hours. Gravity waves and short gravity waves dominate the region until 11.1085 hours. This explains the higher spectral intensities in the spectrogram. A gravity wave was captured in the video still of figure 7.12 (v) which was taken at 11.107 hours. The gravity-capillary waves return at 11.1085 hours and can be seen in the video stills of figures 7.12 (w) and (x).

Given the relatively abrupt changes in the sea surface roughness apparent from both the video and TLS records, especially at the shorter gravity and gravity-capillary wave scales, it is likely that these changes were occurring as a result of the modulation of the sea surface wave profile. Possible causes of this modulation were;

- a variable surface current resulting from tidal flow over a varying bottom topography
- a variable wind velocity.

Figure 7.17 (a) contains an along track wave slope spectrogram from 11.035 to 11.115 hours on which is superimposed the offset subjective roughness level taken from the video record. Figure 7.17 (b) contains an along track wave slope variance plot and associated error for the same period. The variance was calculated over 512 points. The changes in variance are significant and correspond to the observed changes in the spectrogram and video records. The variance plot is easier to compare with the plots of wave speed and direction, vessel speed and direction and current speed which are given in figure 7.18 for the same period. From the comparison of the figure 7.17 and figure 7.18, variations in wind velocity and current speed do not seem to account for the variations in wave slope detected by the TLS, or the observed sea surface roughness changes apparent in the video record. It is likely that the observed variations in the sea surface roughness at the gravity-capillary wave scale were due to small variations in the relative wind speed over the sea surface. Such variations were not detected by the anemometer, the signal of which tended to be dominated by the forward motion of the tow vessel.

7.4.2 Run 3 on 15th April 1996

Run 3 on 15th April 1996 exhibits similar surface conditions to run 2. The run commenced at 11.81 hours and finished at 12.54 hours, lasting for some 43 minutes. The mean wind speed and direction were 1.35ms^{-1} and 13.5° respectively. The current velocity was 0.05ms^{-1}. The background surface was slightly rougher than run 2 due to an increase in the number of short gravity waves. However, the residue of a swell and patches of gravity-capillary waves similar to those seen in run 2 could be identified within the video. The mean heading of the TLS was 200°.

A basic comparison between the video and TLS record was possible. The along track wave slope spectrogram is given figure 7.19 (a). Increased spectral density which is indicative of increased surface roughness can be seen between 11.8 and 11.9 hours and 12.05 and 12.43 hours. Decreased spectral intensity, indicative of a decrease in surface roughness, are apparent outside these times. A selection of stills taken from the video record during different surface conditions are given in figures 7.19 (b), (c) and (d). Rougher surfaces attributed to the presence of high frequency waves are seen at 12.12 in the still of figure 7.19 (c). Smoother surfaces are apparent at 11.93 and 12.52 hours in figures 7.19 (b) and d) respectively. Waves generated by the tow vessel can be seen in the lower part of figure 7.19 (d).

A non-continuous video record pervented an accurate timing correction and an increase in the number of short gravity waves relative to run 2 made it difficult to identify individual waves within the video record of run 3 for a more detailed comparison with the TLS record. However, using the spectrogram of figure 7.19 (a) it was possible to identify boundaries between rougher and calmer surfaces similar to those of run 2 within the wave slope record and indeed to identify individual gravity waves. Such a boundary is seen towards the start of the run at 11.88 hours. A wave profile over some 36 s between 11.88 and 11.89 hours is given in figure 7.20 (a). Occasional outlying negative slopes are present in the first half of the plot. The exact origin of these is still unknown. Ignoring such outliers the surface between 11.88 and 11.886 hours can be seen to be rougher than the surface between 11.886 and 11.89 hours. Although, from figure 7.20 (b) there appears to be a large degree of photodiode drop-out it should be remembered that the profile contains some 9000 data points. A spectral comparison between the two types of surface roughness is given in figure 7.20 (c). Curve (A) was calculated from along track wave slope data between 11.88 and 11.881 hours and curve (B) between 11.886 and 11.887 hours. Curve (A) has a significantly greater spectral amplitude above 5 Hz lending support to the assertion that the TLS has intercepted a boundary between rough and smooth surfaces evident in the along track spectrogram.

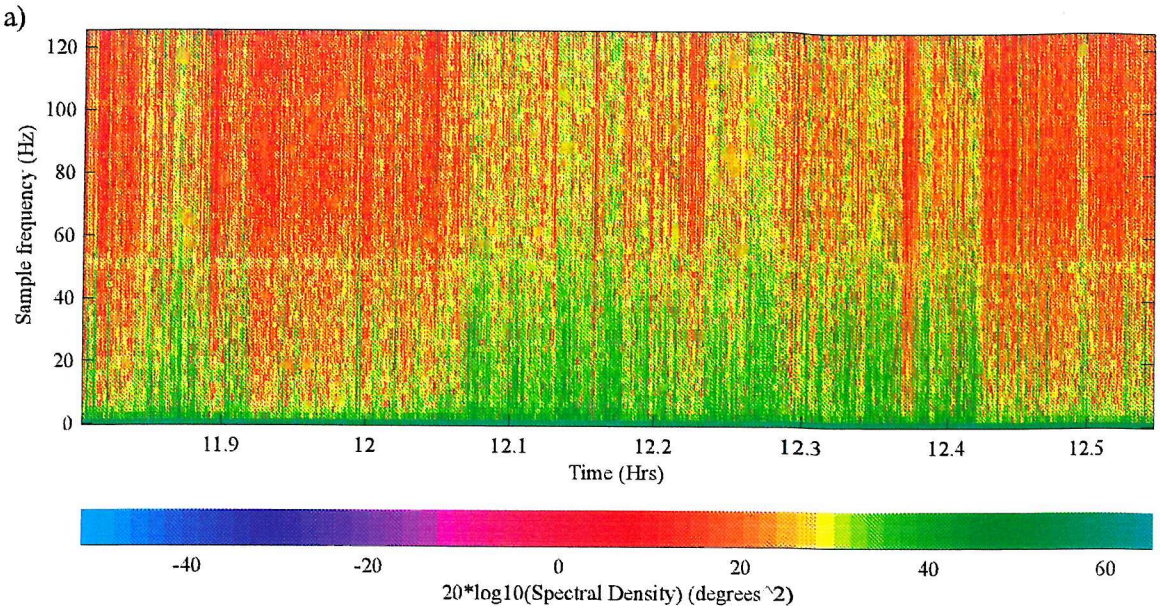

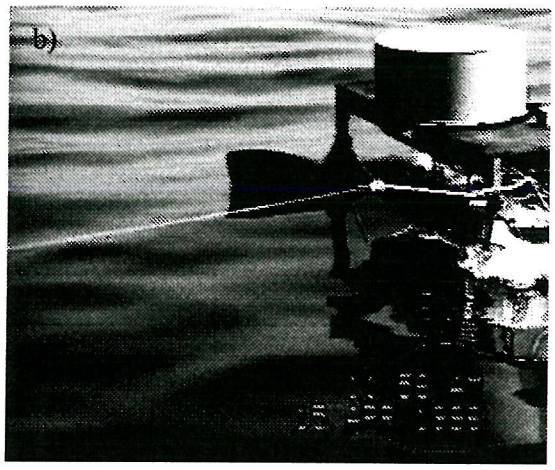

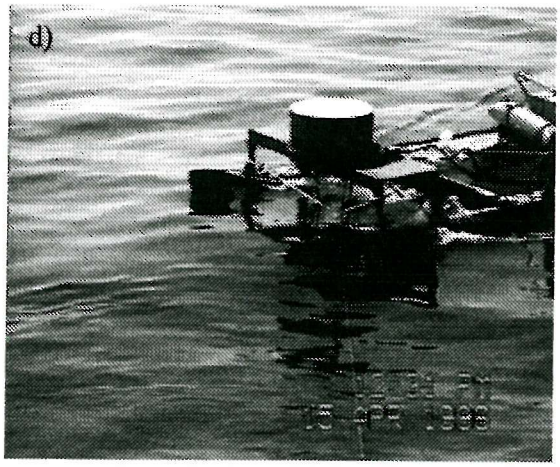

Figure 7.19 a) Along track wave slope spectrogram and video stills taken at b) 11.93 hours, c) 12.12 hours and d) 12.52 hours from run 3 on the 15th April 1996

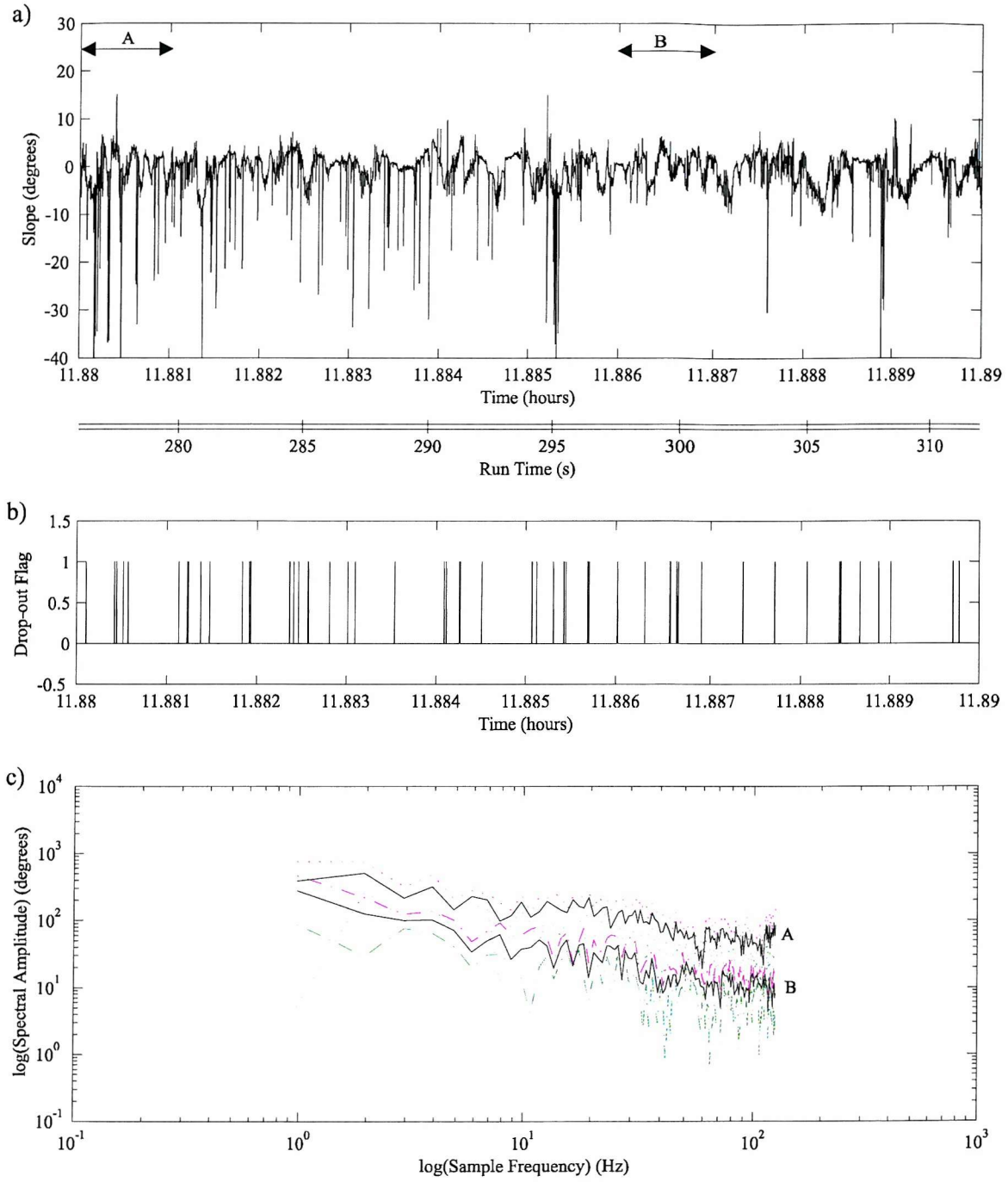

Figure 7.20 Plots of a) along track wave slope profile, b) photodiode drop-out flag and c) along track wave slope spectra between 11.88 to 11.881 hours (solid curve A) with upper (dotted red) and lower (dotted green) errors and between 11.886 to 11.887 hours (solid curve B) with upper (dashed red) and lower (dashed green) errors. Data taken from run 3 on the 15th April 1996.

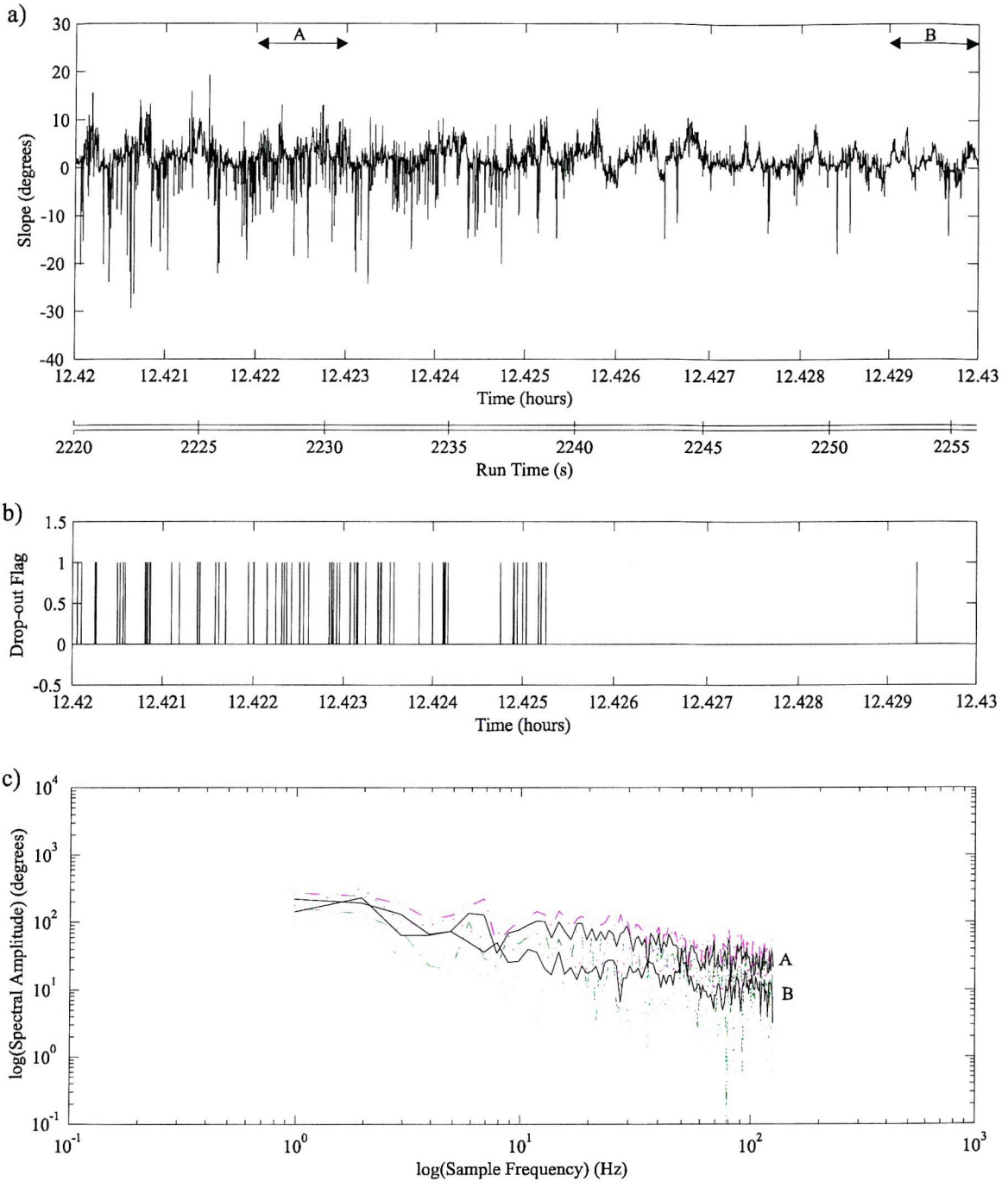

Figure 7.21 Plots of a) along track wave slope profile, b) photodiode drop-out flag and c) along track wave slope spectra between 12.422 to 12.423 hours (solid curve A) with upper (dashed red) and lower (dashed green) errors and between 12.429 to 12.43 hours (solid curve B) with upper (dotted red) and lower (dotted green) errors. Data taken from run 3 on the 15th April 1996.

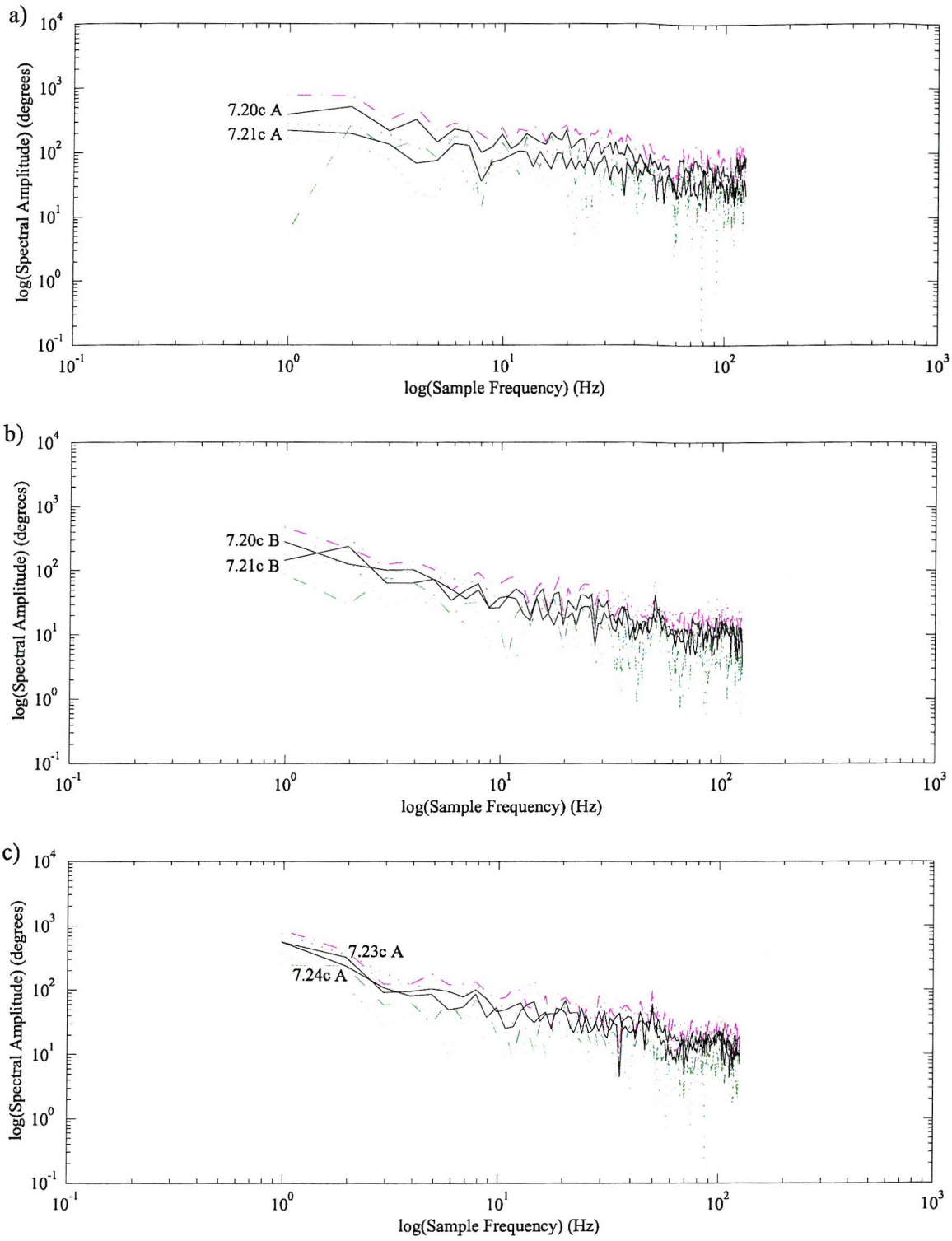

Figure 7.22 Plots of along track wave slope spectra (solid) between a) 11.88 and 11.881 hours (errors dashed) and 12.422 and 12.423 hours (errors dotted), b) 11.886 and 11.887 hours (errors dashed) and 12.429 and 12.43 hours (errors dotted) and c) 11.953 and 11.954 hours (errors dashed) and 12.0445 and 12.0455 hours (errors dotted). Upper errors in red and lower errors in green. Data taken from run 3 on the 15th April 1996.

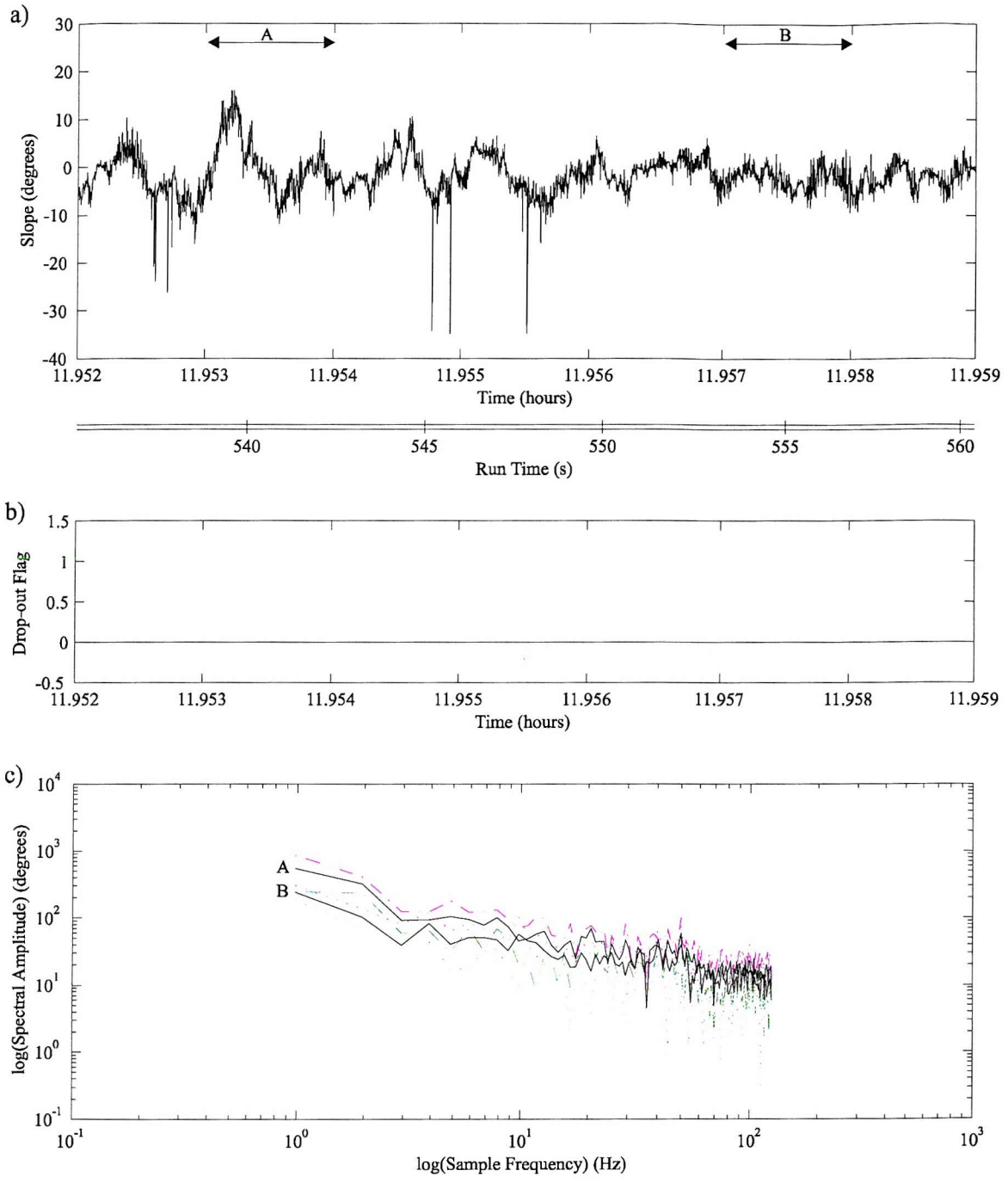

Figure 7.23 Plots of a) along track wave slope profile, b) photodiode drop-out flag and c) along track wave slope spectra between 11.953 to 11.954 hours (solid curve A) with upper (dashed red) and lower (dashed green) errors and between 11.957 to 11.958 hours (solid curve B) with upper (dotted red) and lower (dotted green) errors. Data taken from run 3 on the 15th April 1996.

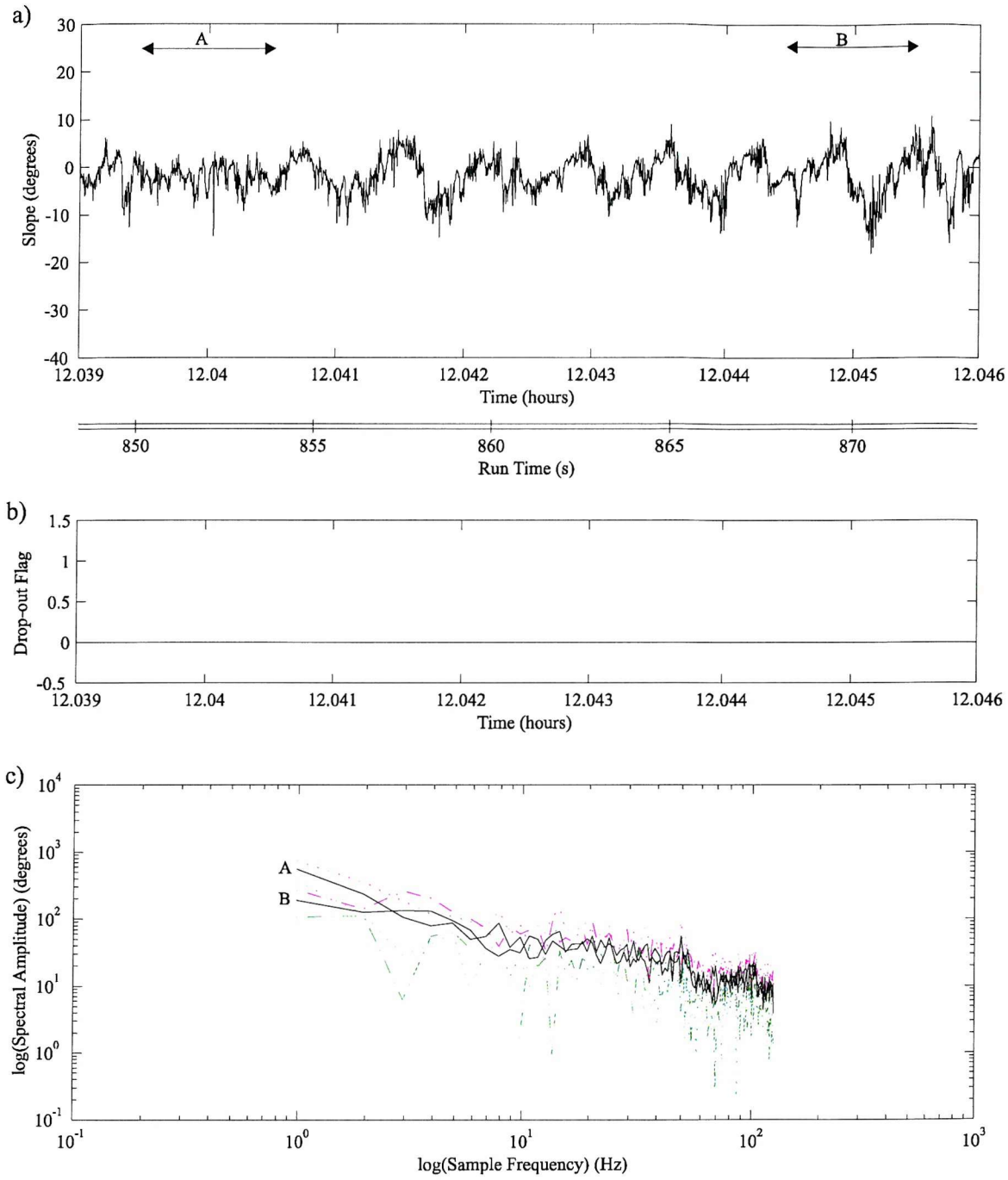

Figure 7.24 Plots of a) along track wave slope profile, b) photodiode drop-out flag and c) along track wave slope spectra between 12.0445 to 12.0455 hours (solid curve A) with upper (dotted red) and lower (dotted green) errors and between 12.0395 to 12.0405 hours (solid curve B) with upper (dashed red) and lower (dashed green) errors. Data taken from run 3 on the 15th April 1996.

Another wave slope profile containing a boundary between rougher and calmer surfaces can be seen in figure 7.21 (a) and was taken towards the end of the run. The two levels of surface roughness are very apparent with the profile between 12.42 and 12.426 hours being visibly rougher than the surface between 12.426 and 12.43 hours. Although the size of the outlying negative slopes is much reduced, the rougher region exhibits a greater degree of photodiode drop-out but these affect only 142 values in 5400 data points. The spectral comparison between these two regions in figure 7.21 (c) confirms these observations. Curve (A) calculated between 12.422 nd 12.423 hours has a greater spectral amplitude than curve (B) calculated between 12.429 and 12.43 hours.

Spectra from the two rougher surfaces above between 11.88 and 11.881 hours and 12.422 and 12.423 hours are compared in the figure 7.22 (a). There is no significant level of difference between the two curves. Similarly the two calmer surfaces between 11.886 and 11.887 hours and 12.429 and 12.43 hours are compared in figure 7.22 (b). Again, there is little difference between the two curves. This is to be expected as roughness levels during the run appeared to the naked eye to have a similar intensity. This confirms that the TLS is capable of giving a precise measure of sea surface wave slopes at different times.

During run 2 a number of gravity waves were identified. Gravity wave trains were also present in the wave slope record from run 3. Such a train is seen in the profile of figure 7.23 (a) were the vessel speed was approximately 1.5 ms^{-1} and the encounter period of the wave was approximately 2.3 s. The variation in wave slope is quite pronounced especially between 11.952 and 11.956 hours. The waves have propagated away to leave a relatively calmer surface between 11.956 and 11.959 hours. Evidence for the presence of gravity waves can also be seen in the spectral plots of figure 7.23 (c). Curve (A), calculated from along track wave slope between 11.953 and 11.954 hours, is significantly greater in spectral amplitude than curve (B), calculated between 11.957 and 11.958 hours, for sample frequencies less than 2 Hz. Another gravity wave train is apparent in figure 7.24 (a). This time the gravity waves with a period of 2.5 s become more pronounced towards the end of the plot. From figure 7.24 (c) the difference between curve (A), calculated between 12.0445 and 12.0455 hours, and curve (B), calculated between 12.0395 and 12.0405 hours, is greatest for sample frequencies less than 2 Hz. The stationarity of the TLS record is once again confirmed from the comparison of the (A) curves from figures 7.23 (c) and 7.24 (c) given in figure 7.22 (c).

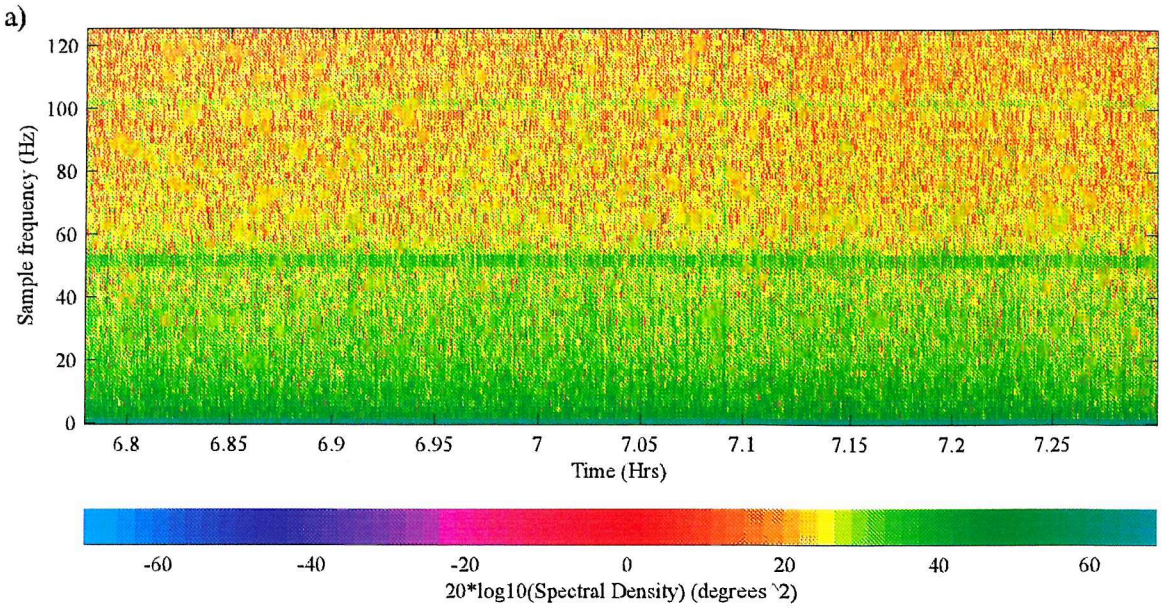

Figure 7.25 a) Along track wave slope spectrogram and b) video still from run 1 on the 16th April 1996

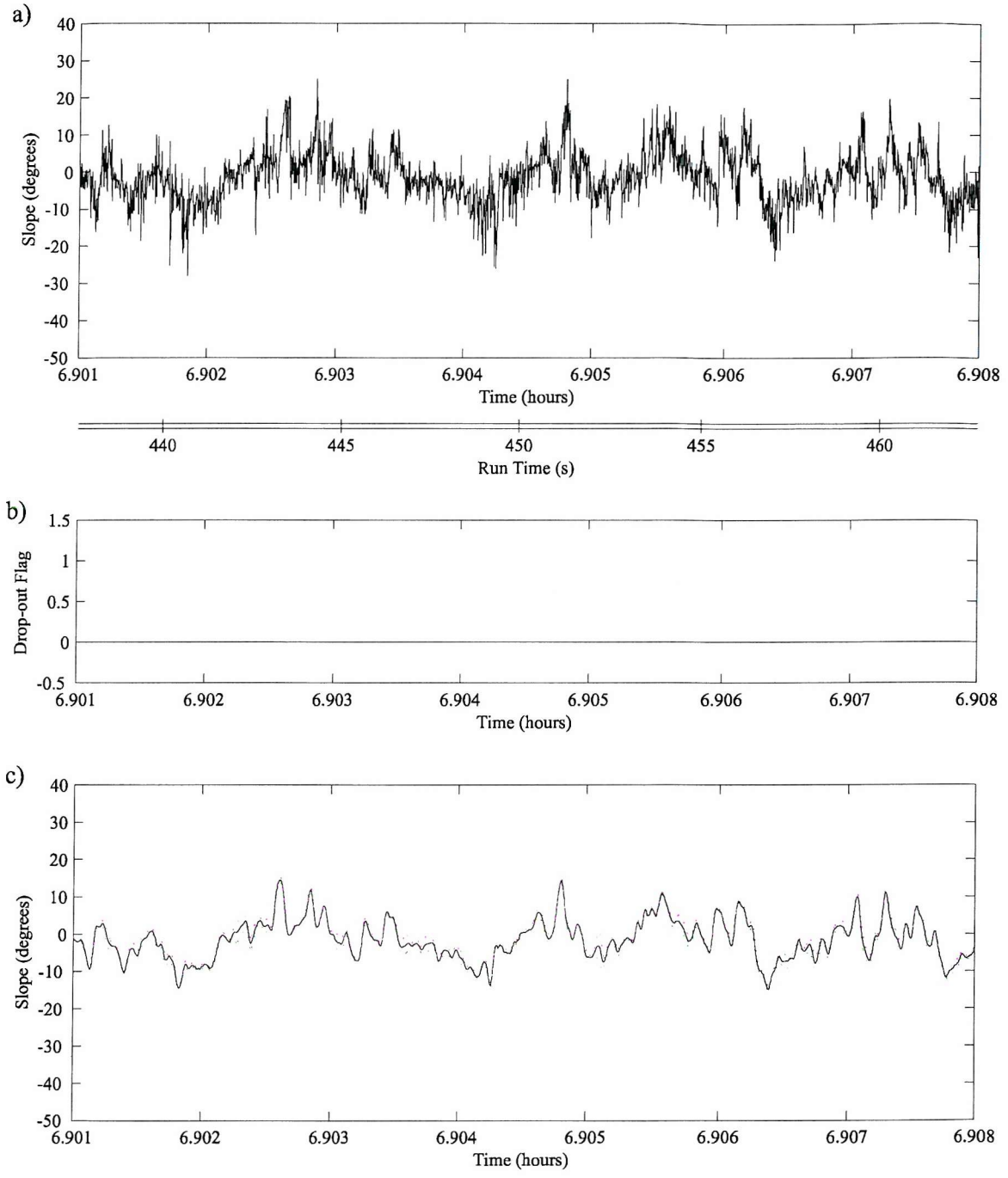

Figure 7.26 Plots of a) along track wave slope profile, b) photodiode drop-out flag and c) 30 point averaged along track wave slope profile (solid curve) with upper (red dotted curve) and lower (green dotted curve) errors. Data taken from run 1 on the 16th April 1996 between 6.901 and 6.908 hours.

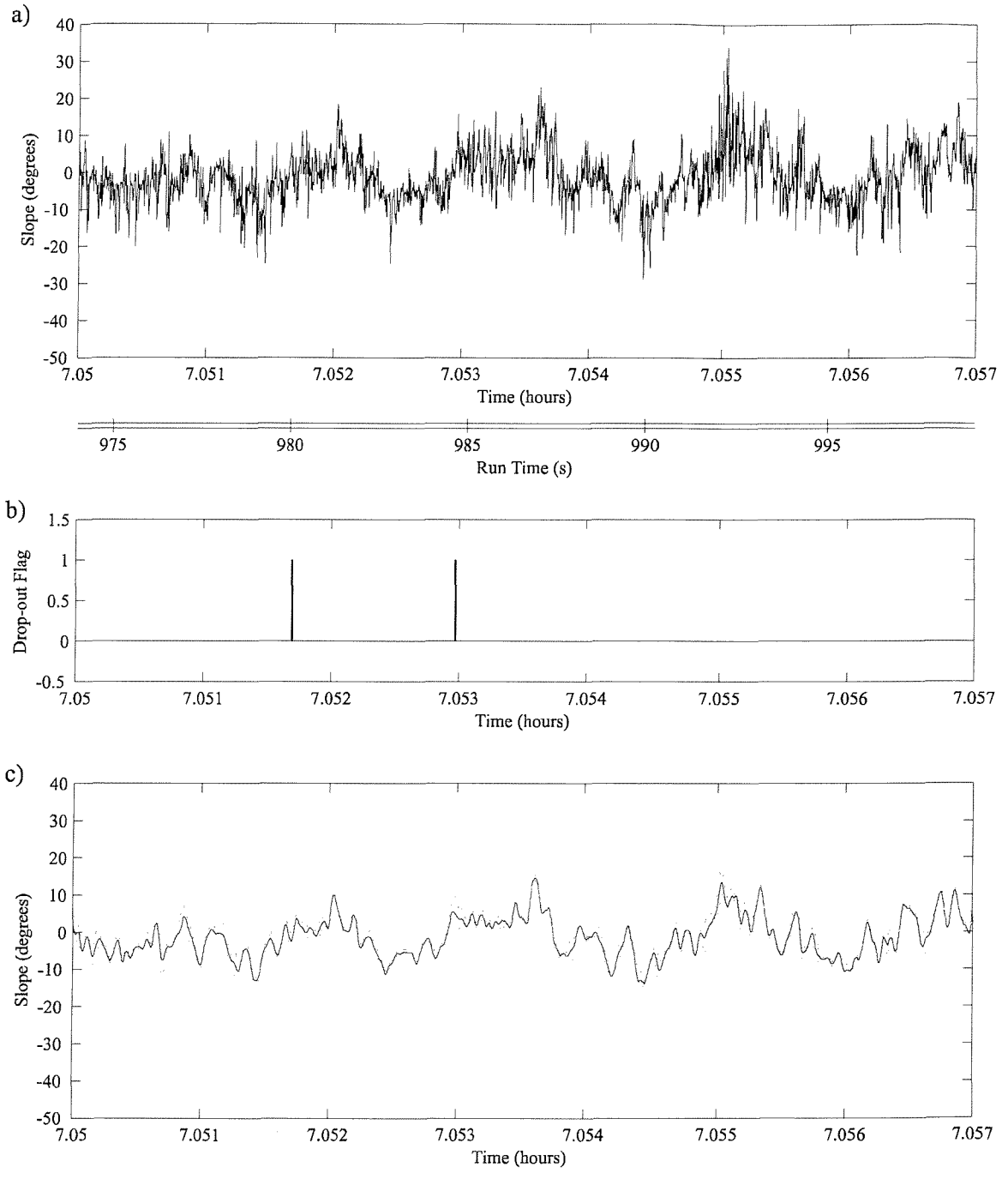

Figure 7.27 Plots of a) along track wave slope profile, b) photodiode drop-out flag and c) 30 point averaged along track wave slope profile (solid curve) with upper (red dotted curve) and lower (green dotted curve) errors. Data taken from run 1 on the 16th April 1996 between 7.05 and 7.057 hours.

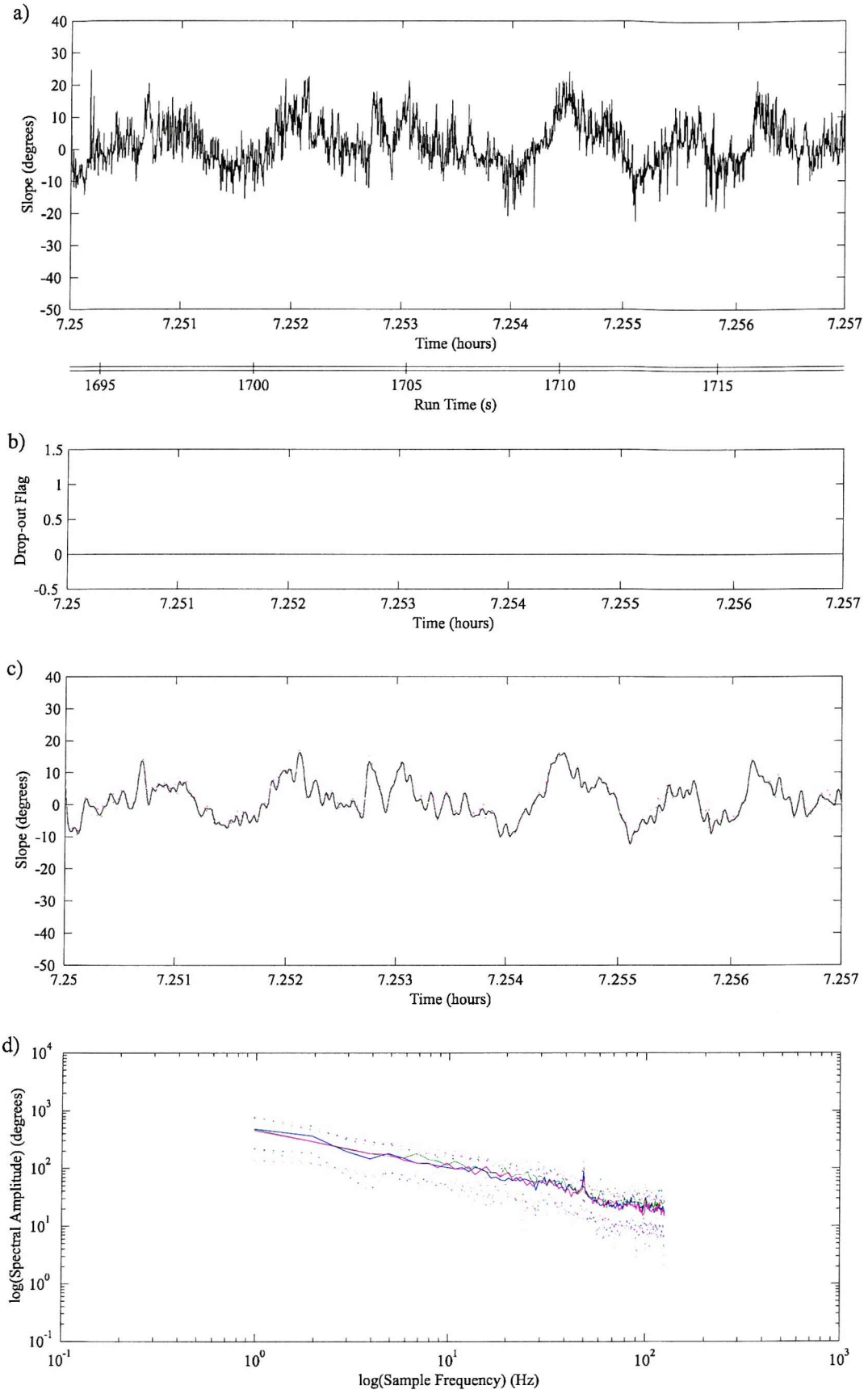

Figure 7.28 Plots of a) along track wave slope profile, b) photodiode drop-out flag, c) 30 point averaged along track wave slope profile (solid curve) between 7.25 and 7.258 hours with upper (red dotted curve) and lower (green dotted curve) errors and d) along track wave slope spectra (solid) taken from run 1 on the 16th April 1996 between 6.901 and 6.908 hours (blue), 7.05 and 7.058 hours (red) and 7.25 and 7.258 hours (green).

7.4.3 Run 1 on 16th April 1996

The first run on 16th April 1996 was recorded under rougher sea surface conditions than the previous two runs studied in this chapter. The mean wind speed was 4.85ms^{-1}. The video record revealed that the surface roughness remained at what appeared to be a constant level throughout the duration of the run which was some 30 minutes. This is supported by the along track spectrogram of the run given in figure 7.25 (a) which appears uniform in time. An example of thevideo footage from the run is given in figure 7.25 (b). It proved near impossible to identify individual waves within the video record, a result of the level of surface roughness and the speed of the waves. However, gravity wave trains could be identified within the TLS wave slope record. Plots of along track wave slope each over a 25s period are given in figures 7.26 (a), 7.27 (a) and 7.28 (a). The profiles were taken from the beginning, middle and end of the run respectively. The application of a 30 point averaging filter to each of the plots is given in figure 7.26 (c), 7.27 (c) and 7.28 (c). Such a filter suppresses the high frequency information, allowing the low frequency trends to be identified more easily. From both types of plots it is evident that the wave slopes of the low frequency waves are greater than those of the gravity waves identified in runs 2 and 3 on the 15th April 1996. Using such statistical techniques rather than spectral methods is more appropriate to the analysis of wave slope data from rougher surfaces. The stationarity of the TLS and the limited variation in the general surface condition over the course of the run is evident from figure 7.28 (d) in which spectra from each of these three slope profiles exhibits no significant difference.

7.5 Conclusion

The TLS was deployed in the North Sea as part of the 1996 CSTAR trial. This was the first deployment of the TLS in the open ocean and followed a comprehensive refit of the instrument. During the trial extensive video records of the surface being observed by the TLS were made. A comparison of the two records has been made to determine whether, or not, the TLS is capable of giving an accurate measure of different sea surface roughness scales and has provided a direct visualisation of waves that can be detected by the instrument. General agreement was found between the video and TLS record for three runs made during the trial. A more detailed comparison using spectrograms and video stills was made over a 4 minute section of data taken from run 2 on 15th April 1996. Strong agreement between the wave scales leading to the observed roughness changes, the times at which these changes occurred and their duration was found in both records. Indeed, the TLS record was used to give a more precise value for the time at which the video record had commenced.

The TLS was shown to be capable of detecting gravity waves present in a variety of sea surface conditions. Such wave profiles were enhanced by the application of filters such as a 30 point averaging filter which reduced the high frequency information to leave the low frequency variations. Boundaries between increased and decreased sea surface roughness' were detected by the slopemeter and captured on the video footage. These regions of increased roughness which were most prevalent in runs 2 and 3 on 15th April 1996, occurred at the gravity-capillary wave scale and exhibited remarkable uniformity in their shape, distribution and intensity. Boundaries between these rougher regions and the smoother ambient wave field were abrupt. This was not only evident in the spectrograms but also in the wave slope profile. Spectra from both regimes showed significant differences from which the wavelengths at which these roughness changes were occurring could be estimated and were found to be in agreement with wavelengths estimated from the video footage.

The TLS was found to be capable of giving a consistent measure of wave slope. Surfaces exhibiting similar roughness scales but sampled at different locations and times were found to give similar levels of spectral intensity. This result was verified under different surface conditions but most notable was run 1 on 16th April 1996 for which the video record of the sea surface wave profile revealed a near stationary and homogeneous sea surface. This was confirmed by the spectrogram taken from the TLS record of the run remained uniform in time. Spectra calculated from data taken at the beginning, middle and end of the run showed no significant differences. This chapter has confirmed that the TLS is capable of making a precise measure of the sea surface wave profile in varying short scale wavelength ranges at different locations, times and sea states.

Chapter 8

Conclusions and Future Work

8.1 Discussion and Conclusions

The motivation for the design and continued deployment of the Towed Laser Slopemeter comes from a need to gain a precise measurement of the sea surface wave profile at the short wave scale range of one metre to a few centimetres. The need for such in-situ measurements arises from a desire to gain a greater understanding of the mechanisms leading to the backscatter of electromagnetic radiation from the sea surface and the interactions between ocean processes and the sea surface at these wave scales. It is hoped that from such an understanding that data sets from satellite-borne synthetic aperture radar systems will provide, on a truly global scale, frequent quantitative monitoring of a variety of ocean processes which have a bearing on man's activities at sea. The research presented within this thesis has been concerned with the physical interpretation of data from the Towed Laser Slopemeter. The objectives of the work were:

- To assess the effect of the Doppler shift on the recorded wavenumber spectrum induced by towing slope measuring instruments.
- To meet the first objective, it became necessary to develop a numerical model for the simulation of the ocean surface over the length scale range measured by the Towed Laser Slopemeter.
- To assess the performance of the Slopemeter in relatively sheltered conditions by identifying the components in the data record, distinguishing between system noise, signals relating to the sea surface wave slope and other surface features.
- To determine whether the slopemeter can be considered to give a reliable measure of sea surface roughness variability encountered in the open sea.

To meet the first objective a numerical model to simulate observations of the sea surface as made by the TLS was implemented and this formed the second objective. The effect of towing the slopemeter on the observed wavenumber spectrum needed to be investigated. The model used a fast Fourier transform of a two dimensional amplitude spectrum to give a surface realisation. The phase component of the model was incremented in time to provide a temporally varying sea surface. An instantaneous transect of the wave field could be used to provide a wavenumber spectrum and a time series of single point measurements to give a frequency spectrum. As the TLS samples the surface along a non-instantaneous transect the number of calculations in the FFT could be reduced whilst still providing a set of wave height, and wave slope, values that varied in time and location along the transect. Reducing the number of calculations in the FFT reduced the run-time of the model. On transformation the values of wave slope, and wave height, gathered in this manner, would provide wavenumber spectra as observed by the TLS.

The model is adequate enough to meet the first objective. However, if a set of wave slopes, or wave height, values over a given area for a number of different times were required then an alternative method for reducing the run-time would be required. The use of a logarithmic representation of the wavenumber spectrum has been suggested as a method by which the size of the initial power spectrum, and hence the number of calculations needed to give a surface realisation over a given wavenumber range, may be reduced. In addition, the analysis of the simulated data sets generated by this new model was only concerned with interpreting the effect of towing the slopemeter on the observed power spectrum. This required amplitude rather than phase information. The phase component was assumed to be random, an assumption adequate for our model, but clearly not the true case. A more precise phase representation would be required if the relationships between waves of differing wavelength were to be modelled more precisely.

The new numerical model was used to achieve the first objective. Relationships were developed to explain the effect of vessel speed and wave direction relative to the direction of travel on the observed wavenumber and the corresponding wavenumber spectrum. It was found that differences between the true and observed wavenumbers, and hence the difference between the true and observed wavenumber spectra, were greatest at low vehicle velocities and large angles of wave direction relative to the direction of travel. It was not possible to tow the TLS at speeds greater than $2ms^{-1}$ as this would have led to an undersampling of the sea surface reducing the wavenumber resolution and presented a greater potential for damaging the instrument. However, maintaining a constant tow speed and deploying the instrument into the main wave direction would limit differences between the observed and true wavenumber spectra.

Methods for gaining a true wavenumber spectrum from the observed wavenumber spectrum were proposed by Cartwright (1963) and Hughes (1978) and were assessed for their suitability to the case of the TLS using simulated data sets provided by the new numerical model. Neither was found to be appropriate. Cartwright's method which was developed for a similar problem arising from the measurement of longer wavelength waves, required a second measurement of the sea surface wave profile. Hughes' method which required assumptions on the vessel speed, wave direction and the forms of the dispersion relation and true wavenumber spectrum proved to be imprecise and difficult to implement. A new approach which avoided the assumptions required by the previous two methods was proposed. It was hoped that a wave height spectrum could be obtained such as the wave slope spectrum. Both spectra would be subject to the spectral distortions introduced by sampling from a moving vehicle. These distortions will be the same for both types of spectra. The Fourier transform of wave slope is equivalent to the product of the wavenumber and the Fourier transformation of the wave height. This continues to be true for the distorted spectra assuming they do not suffer from aliasing or spectral folding. This allows approximate reconstruction of the measured slope and height spectra as a function of wavenumber. However, due to system noise, credible values of wave height could not be obtained from the TLS so the proposed technique could not be fully investigated.

It was hoped that spectra calculated from the TLS wave height and wave slope records could be combined as described above to provide a true wavenumber spectrum. However, this was not possible as precision in the values of wave height were reduced by the noise in the TLS system and as the wave slope tended to zero. Although differences between the observed and true wavenumber spectra were shown to exist, the spectra obtained from the TLS measurements of the sea surface wave slope during the first deployment of the instrument in Loch Linnhe in September 1994 exhibited a shape in agreement with proposed forms. Indeed, the power index of the spectrum was found to be 0.477 ± 0.006 which is similar to the value proposed by Phillips (1985).

The completion of the third objective continued with the assessment of the signals in the TLS data record obtained during the Loch Linnhe trial. It was concluded from an examination of the wave profile, the near Gaussian distribution of the components of wave slope and the shape of the power spectrum that the TLS was indeed measuring the sea surface wave slope. However, it was apparent that at high frequencies this signal had been contaminated by noise. After an analysis of a number of signal-to-noise ratio files it was concluded that this noise which was white in origin, had emanated from the electronic components of the instrument. Low frequency variations in the noise were attributed to variations in the power of the laser beam. The analysis prompted a comprehensive review of the TLS. Individual sources of noise were identified and replaced. The laser was repaired and interference filters which had led to undesirable photodiode responses were removed. Following this refit the TLS exhibited a marked reduction in system noise.

Attempts were made to reconcile the direction of maximum wave slope with the prevailing wind direction. This required a physical interpretation of what is meant by the direction of the maximum wave slope. The results proved inconclusive. It was concluded that the Loch conditions, notably its narrowness and high sides, and the distance between the TLS and the wind measurements together with the frequency of these measurements had hindered the analysis. To further the conclusion that the TLS had indeed measured the wave slope, spectrograms and spectral analyses were used to identify decreases in surface roughness. The decreases in surface roughness that had occurred as a result of the presence of surfactant material on the Lochs surface led to a corresponding decrease in the magnitude of the wave slope and hence the spectral intensity. The times at which these features occurred within the TLS record corresponded with the times at which the surfactant material had been observed to be present on the waters surface. This gave the first conclusive measurement of the effects of an ocean process on the short scale sea surface roughness measured by the TLS.

Following the refit of the TLS and the addition of a variety of support instrumentation the TLS was deployed for the first time in the open ocean, some 30km from the Dutch coast, during a CSTAR campaign in April 1996. An extensive video record of the sea surface sampled by the TLS was made during the trial. A number of sea states were recorded by the instrument. From the video two runs on the 15th April 1996 exhibited a range of interesting roughness levels on a calmer ambient wave field. Both general and more detailed comparisons of the video and the slope records were made. The times at which these features occurred within each record agreed strongly. Indeed, the TLS was able to provide a more precise initial start time for the video record.

From an interpretation of the results of the analysis of the TLS wave slope record using spectrograms, wave slope profiles, spectral analysis, variance plots and filtered wave slope profiles it was concluded that:

- Changes in wave slope corresponding to gravity waves were present.
- The record was sensitive to variations in short gravity and gravity-capillary waves.
- Sharp boundaries between surfaces of differing roughness scales were evident.
- Differences between spectra taken from surfaces exhibiting different roughness scales were used to provide an estimate of the wavelength at which these changes had occurred.
- The TLS record exhibited stationary and homogenous wave profiles when the sea surface condition was stationary and homogeneous.
- Although a number of runs exhibited intermittent photodiode drop-out this was shown not to compromise the ensuing analysis.

To measure such features requires that the instrument is sensitive to changes in sea surface wave slope and is capable of giving a precise measurement.

From the work conducted in the last two chapters the TLS has proven to be a useful tool for making precise in-situ measurements of the sea surface wave slope. Recent deployments of such devices included the use of wire probes deployed on a wave buoy (Stolte (1994)) and a scanning laser slopemeter (Martinsen and Bock (1992)). A case for the continued deployment of the TLS can be made from a comparison of these instruments with respect to the TLS. Stolte's device has a limited frequency resolution of 8Hz which is less than that of the TLS and is a result of the interference of the probes with the surrounding water surface. In an effort to avoid introducing Doppler shifts into the measurement of short scale waves advected by the orbital motion of long wavelength waves passing a stationary instrument the wire probes are deployed on a buoy. This is free to follow the longer wavelength waves. However, it is likely that this motion will result in Doppler shifts at other wavelengths. Although the TLS record suffers from Doppler shifting its motion is more predicable and allows a greater control in the location of the instrument. The movement of the TLS ensures that it does not perturb the wave field it is observing.

The advantage of the TLS over other slopemeters is that it can provide a measure of the wave slope without the need to assume a constant wave height or provide an independent measure of wave height at a different location. This gives a more precise value for the wave slope. Martisen's and Bock's slopemeter also uses a two screen strategy to provide a measure of wave slope independent of wave height. The advantage of this system is that it scans the surface avoiding the problem of introducing Doppler shifts into the observed spectrum when it is towed. Bock and Frew (1993) used this scanning slopemeter to investigated the effect of surfactants on the sea surface wave profile. However, it was used to provide single point measurements along a transect rather than a surface scan.

From the conclusions resulting from the work conducted in this thesis and the discussions above there is still a strong case for the continued deployment of the TLS to study the effects of ocean processes on the short scale sea surface wave profile. This leads us into a discussion on possible areas for future work.

8.2 Future Work

Future work with the TLS should be concerned with investigating the effects of a number of ocean processes on the short scale sea surface wave field. The CSTAR data set provided by the TLS in April 1996 should be analysed in depth together with corresponding wind and surface current data

with a view to determining, or otherwise, the effect of bathymetry-influenced tidal flows on the sea surface wave slope. Statistical techniques such as variance plots and filtered wave slope profiles may be more appropriate than spectral techniques for such an analysis. If evidence for the observation of such features within the data set is strong then the process of validating, or otherwise, current models of such interactions can begin and this should start with providing values for parameters needed in such models.

The DRA are continuing with their investigations of the effects of internal waves on the sea surface wave profile with another deployment of the TLS in Loch Linnhe during February 1997. They have also proposed tank experiments in which the TLS is to be deployed at a fixed location together with a suitable radar system. This will allow TLS and radar data sets to be compared under a range of controlled surface conditions. The main result of such tank measurements would be to influence trials involving more specific comparisons between radar and TLS data sets in the open ocean.

The experience gained during the research conducted using the Towed Laser Slopemeter for this thesis has directly influenced the proposed design of a new scanning slopemeter instrument. The new instrument referred to as the Digital Laser Slopemeter, or DSM, has been proposed by Crossingham and Ramsden (1997a, 1997b) to solve some of the short comings of the TLS that have been identified during theoretical work, the analysis of wave slope data and from deploying the instrument at sea. A brief outline of the influences in the proposed design of the DSM follows. A more detailed overview of the instrument is given in appendix C.

- The single point measurement of wave slope along a transect described by the TLS prevented a true estimate of the wave slope wavenumber power spectrum being calculated from the data set. This was apparent from theoretical work conducted in chapter 5. A scanning unit capable of providing two orthogonal line scans of the surface at each sample time enabling the true wave slope wavenumber power spectrum to be calculated.

- Non-linearities in the screen properties of the TLS instrument resulted in a lengthy processing time needed to provide spot positions, and therefore wave slopes, from the photodiode voltages. This led to the photodiode ratios forming part of the telemetry data. Combining the scanning strategy with the optical detection system of the TLS was prevented by limitations in the telemetry bandwidth. Instead, it was proposed that the screens of the TLS were replaced by open fibre grids enabling the spot positions to be gained in real-time and without the need for instrument calibration.

- The construction of the open fibre grids was influenced by the choice of laser. A new laser system was proposed following the difficulties encountered with the Helium-Cadmium laser used with the TLS system. A solid state laser was procured to eliminate fluctuations in laser power, to reduce the bulkiness of the device and to decrease the possibility of accidental damage.

- In an effort to substantially limit the possibility of electronic noise occurring within the DSM instrument a digital electronics design was proposed. It was evident from the work conducted in chapter 6 that the noise within the TLS instrument had arisen from the necessary conversion of analogue signals to digital signals by the system electronics.

- The Digital Slopemeter is to be mounted on the bow of a research vessel. This avoids the need to crane a catamaran in and out of the water at the beginning and end of each day of trials. and the need for tow ropes reducing the fatigue to the crew. The question of safety in deploying someone into the water to clean the aperture of the optical detection system and to ready the systems on-board the catamaran is eliminated.

- Techniques developed to identify changes in sea surface roughness from the TLS wave slope data are to be incorporated in the real-time display of the wave slope data recorded by the DSM instrument.

Appendix A

The Fast Fourier Transform

The fast Fourier transform was developed by Cooley and Tukey (1963) as a technique for reducing the number of arithmetic operations associated with the computation of discrete signals using the then conventional discrete Fourier transform (DFT). The following section describes how the FFT works.

Consider the discrete one dimensional Fourier transform;

$$X(n) = \sum_{m=0}^{N-1} x_0(m) e^{-i2\pi nm/N} \tag{A.1}$$

where, M is the matrix size, x_0 is the studied observable dependant upon m and X is the Fourier component of x dependant on n, the Fourier component of m.

Let $W = e^{-i2\pi/M}$

Expanding (A.1) for M=4 then;

$$\begin{aligned} X(0) &= x_0(0)W^0 + x_0(1)W^0 + x_0(2)W^0 + x_0(3)W^0 \\ X(1) &= x_0(0)W^0 + x_0(1)W^1 + x_0(2)W^2 + x_0(3)W^3 \\ X(2) &= x_0(0)W^0 + x_0(1)W^2 + x_0(2)W^4 + x_0(3)W^6 \\ X(3) &= x_0(0)W^0 + x_0(1)W^3 + x_0(2)W^6 + x_0(3)W^9 \end{aligned} \tag{A.2}$$

or as a matrix formalisation:

$$\begin{bmatrix} X(0) \\ X(1) \\ X(2) \\ X(3) \end{bmatrix} = \begin{bmatrix} W^0 & W^0 & W^0 & W^0 \\ W^0 & W^1 & W^2 & W^3 \\ W^0 & W^2 & W^4 & W^6 \\ W^0 & W^3 & W^6 & W^9 \end{bmatrix} \begin{bmatrix} x_0(0) \\ x_0(1) \\ x_0(2) \\ x_0(3) \end{bmatrix} \tag{A.3}$$

To generate *X(n)* then M^2 multiplications and *M(M-1)* additions are required. Restricting *M* to a power of two then (A.3) can be written as;

$$\begin{bmatrix} X(0) \\ X(1) \\ X(2) \\ X(3) \end{bmatrix} = \begin{bmatrix} 1 & 1 & 1 & 1 \\ 1 & W^1 & W^2 & W^3 \\ 1 & W^2 & W^0 & W^2 \\ 1 & W^3 & W^2 & W^1 \end{bmatrix} \begin{bmatrix} x_0(0) \\ x_0(1) \\ x_0(2) \\ x_0(3) \end{bmatrix} \tag{A.4}$$

having made use of the relationship that;

$$\begin{aligned} W^{nm} = W^6 &= \exp\left[\left(\frac{-i2\pi}{4}\right)(6)\right] = \exp(-i3\pi) \\ &= \exp(-i\pi) = \exp\left[\left(\frac{-i2\pi}{4}\right)(2)\right] = W^2 = W^{rem(nm/N)} \end{aligned} \tag{A.5}$$

where *rem(nm/N)* is the remainder upon division of *mn* by *M*.

The next step is to factorise the matrix;

$$\begin{bmatrix} X(0) \\ X(2) \\ X(1) \\ X(3) \end{bmatrix} = \begin{bmatrix} 1 & W^0 & 0 & 0 \\ 1 & W^2 & 0 & 0 \\ 0 & 0 & 1 & W^1 \\ 0 & 0 & 1 & W^3 \end{bmatrix} \begin{bmatrix} 1 & 0 & W^0 & 0 \\ 0 & 1 & 0 & W^0 \\ 1 & 0 & W^2 & 0 \\ 0 & 1 & 0 & W^2 \end{bmatrix} \begin{bmatrix} x_0(0) \\ x_0(1) \\ x_0(2) \\ x_0(3) \end{bmatrix} \tag{A.6}$$

which can be written as two matrices;

$$\begin{bmatrix} x_1(0) \\ x_1(1) \\ x_1(2) \\ x_1(3) \end{bmatrix} = \begin{bmatrix} 1 & 0 & W^0 & 0 \\ 0 & 1 & 0 & W^0 \\ 1 & 0 & W^2 & 0 \\ 0 & 1 & 0 & W^2 \end{bmatrix} \begin{bmatrix} x_0(0) \\ x_0(1) \\ x_0(2) \\ x_0(3) \end{bmatrix} \tag{A.7}$$

and

$$\begin{bmatrix} X(0) \\ X(2) \\ X(1) \\ X(3) \end{bmatrix} = \begin{bmatrix} 1 & W^0 & 0 & 0 \\ 1 & W^2 & 0 & 0 \\ 0 & 0 & 1 & W^1 \\ 0 & 0 & 1 & W^3 \end{bmatrix} \begin{bmatrix} x_1(0) \\ x_1(1) \\ x_1(2) \\ x_1(3) \end{bmatrix} \tag{A.8}$$

From equation A.7 $x_1(0)$ is computed by one addition and one multiplication;

$$x_1(0) = x_0(0) + W^0 x_0(0) \tag{A.9}$$

as is $x_1(1)$. However as $W^0 = -W^2$, then only one addition is required to compute $x_1(2)$;

$$\begin{aligned} x_1(2) &= x_0(0) + W^2 x_0(2) \\ &= x_0(0) - W^0 x_0(2) \end{aligned} \tag{A.10}$$

similarly $x_1(3)$ is calculated with one addition. There is an equivalent reduction in the number of computations required to determine $X(n)$. This relationship between pairs of numbers, referred to dual node pairs can be generalised to:

$$\begin{aligned} x_l(m) &= x_{l-1}(m) + W^p x_{l-1}(m + N/2^l) \\ x_l(m + N/2^l) &= x_{l-1}(m) - W^p x_{l-1}(m + N/2^l) \end{aligned} \tag{A.11}$$

As each dual pair is only used in one set of equations, computations can be stored within the original memory space. This greatly reduces storage requirements, by returning values computed to the original array.

The FFT, where $M = 2^\gamma$ is a procedure for factorising an M by M matrix into γ (M x M) matrices such that each factored matrix minimises the number of multiplications, to $M\gamma/2$, and additions, to $M\gamma$. Assuming that the computation time is proportional to the number of multiplications performed as Nussbauer (1981) does, then the approximate ratio of DFT to FFT computing time required is given by:

$$\frac{N^2}{N\gamma/2} = \frac{2N}{\gamma} \tag{A.12}$$

For M =1024 this is a reduction in processing time of 200 to 1.

W^p is determined by first writing the index m in binary form with γ bits, then scaling the binary number γ-1 bits to the right before finally reversing the order of bits to determine the corresponding index p.

Appendix B

A Synopsis of Trial Log Books

During the both the Loch Linnhe and CSTAR trials a written record of interesting surface features and meteorologic and oceanographic conditions was made. The start and stop times of each run and comments made during these times taken form the log books is given below.

B.1 Loch Linnhe 5th-17th September 1994

Date (DD:MM:YY)	Start time (hh:mm) GMT	Stop time (hh:mm) GMT	Comments
05.09.94	14:00	14:14	Very wind.
05.09.94	14:20	14:41	Continued measurement of last runs wake. Slick 14:24.
05.09.94	15:15	15:37	Very rough. Detector splash. Crossed wake 15:22.
05.09.94	17:10	17:28	Crossed wake 17:20.
08.09.94	09:54	10:10	Windy. Crossed wake 10:03. Wind and tide incident at 10°.
08.09.94	11:00	11:13	Windy and wet. Crossed wake 11:06. Detector splash.
08.09.94	12:04	12:18	Windy and wet.
08.09.94	13:30	13:46	Crossed wake 13:40.
08.09.94	14:37	14:54	Crossed wake 14:46. Wave amplitude 30 cm.
08.09.94	15:48	16:01	Mild wind. Rain. Crossed wake 15:51.
09.09.94	13:53	14:25	Mild wind, raining. Crossed wake 10:31.
09.09.94	10:26	10:28	Drizzle. Crossed wake 11:30.
09.09.94	11:26	11:40	Calm surface. Crossed wake 12:38. Smooth patch 12:37.
09.09.94	12:30	12:45	Heavy rain. Crossed wake 13:32.
09.09.94	13:30	13:46	Rain increased during run. No wind. Calm sea. Foam on surface 14:25.
12.09.94	11:25	11:35	NE wind. Sea state 2-3.
12.09.94	12:26	12:40	Run delayed due to vicinity of fishing vessel.
12.09.94	13:40	14:02	Wind dropped calm surface. Smooth patch 13:41,13:43. Drizzle 13:56.
12.09.94	14:35	14:59	
12.09.94	15:33	15:56	No rain, mild wind sometimes gusty. Calm sea.
12.09.94	16:46	17:08	Calm sea, no rain, sun.
14.09.94	12:06	12:23	Sea state 2. Little wind, overcast. No rain.
14.09.94	13:09	13:27	Very windy. Very disturbed sea.

14.09.94	13:54	14:13	
14.09.94	14:52	15:13	Windy. Sea state 3.
14.09.94	16:05	16:31	
14.09.94	17:21	18:10	Low wind. Low high frequency wave structure. Heading into wind. Foam on surface 17:43, 17:49.
16.09.94	13:01	13:27	Going into waves. Calm surface little wind.
16.09.94	13:29	13:44	
16.09.94	14:32	14:41	
16.09.94	15:24	15:42	Detector crabbing. Light wind. Mildly disturbed surface.
16.09.94	16:41	17:04	Low wind. No rain.
16.09.94	17:37	17:55	Crabbing. Wood chippings on surface 17:38.
17.09.94	12:46	13:10	Low wind, calm sea, no rain, dry screen.
17.09.94	13:36	13:47	Very calm surface with some small structure.
17.09.94	14:23	14:43	Smooth patch 14:31. Crabbing.
17.09.94	15:24	15:43	Wake crossed 15:32.
17.09.94	16:38	16:57	Smooth patches 16:44, 16:52, 16:57.
17.09.94	17:41	17:56	

B.2 CSTAR 14th - 17th April 1996

Date (DD:MM: YY)	Start time (hh:mm) GMT	Stop time (hh:mm) GMT	Comments
14.04.96	11:07	11:27	Crabbing. Swell waves
15.04.96	08:59	09:04	Rudder problem encountered.
15.04.96	10:59	11:24	Surface roughness changes due to sand waves apparent
15.04.96	11:48	12:33	Surface roughness changes due to sand waves apparent Right angled turns.
16.04.96	06:48	07:51	Roughness changes not as visible as previous day. Screen splash. Swell waves
16.04.96	08:07	08:39	Surface roughness changes due to sand waves apparent. Screen splash. Swell.
16.04.96	09:02	09:52	Surface roughness changes due to sand waves apparent 180° turn.
16.04.96	10:06	10:36	Surface roughness changes due to sand waves apparent. Screen splash. 7 to 8m waves.
16.04.96	11:02	11:27	Smooth surface some effects due to sand waves. 180° turn.
16.04.96	11:40	12:25	Some effects due to sand waves. Increasing swell. Screen splash.
16.04.96	12:35	13:29	Surface roughness changes due to sand waves apparent. 180° turn.
17.04.96	08:34	09:54	180° turn. Changes in bottom profile. Outside test area.
17.04.96	10:07	11:18	Visible vessel wakes. Changes in bottom topography observed
17.04.96	11:26	12:10	180° turn. Changes in bottom profile. Swell.
17.04.96	12:36	13:56	Roughness changes. Changes in bottom profile. Visible wake

Appendix C

An Overview of the Digital Laser Slopemeter

A new instrument to measure the sea surface wave slope has been proposed. Its design has been influenced by the experience gained in using the Towed Laser Slopemeter for the research described in this thesis. The new instrument referred to as the Digital Slopemeter, or DSM, has been proposed by Crossingham and Ramsden (1997a, 1997b) to solve some of the short comings of the TLS that have been identified during theoretical work, the analysis of wave slope data and from deploying the instrument at sea. A brief overview of the Digital Slopemeter is given in this appendix.

To avoid the surrounding structure of the instrument disturbing the surface under investigation the instrument is moved across the wave field. This led to the Doppler shift in the observed wave slope power spectrum calculated from the data recorded by the TLS. The difficulty in determining a precise form for the true wavenumber spectrum lead the Southampton team to propose a second instrument capable of resolving this. A technique was required which would give an instantaneous measure of the sea surface wave slope whilst towing the instrument to avoid interference from the surrounding structure. Rather than measuring wave slope at each position, its was proposed by Crossingham and Ramsden (1997b) to scan the surface rapidly with a laser beam in order to gain an instantaneous measure of sea surface slope along two orthogonal lines. A line scan reduces system requirements imposed by scanning over a given area. A sketch of the scanning system is given in figure C1.

The scanner consists of a small mirror mounted on a rotating shaft which is driven by an electric motor. The laser beam falls on the mirror and is reflected onto a collimating lens. By rotating the mirror rapidly, the beam is scanned over the entire face of the lens. The beam is refracted by the

collimating lens in such a manner as to produce a column of parallel light. This shaft of laser light falls on a mirror assembly. Half the laser light falls on a mirror angled at 45° to the horizontal and vertical planes. This ensures that light is reflected into the vertical plane. The remaining laser light falls on a mirror angled at 45° to the lens which deflects it through 90° but still keeps it with in the horizontal plane. This light then falls on a second mirror also angled at 45° to the horizontal and vertical planes deflecting the light into the vertical plane. Using such a mirror assembly ensures that two orthogonal lines of laser light can be scanned onto the sea surface. Relative to the time scales at which the waves of interest evolve, the line scans provided by the DSM can be considered to be near instantaneous. These provide a set of wave slope measurements along each line which when Fourier-transformed will give a true estimate of the wave slope wavenumber power spectrum. Two orthogonal line scans ensure that information on the directional properties of the spectrum can be determined.

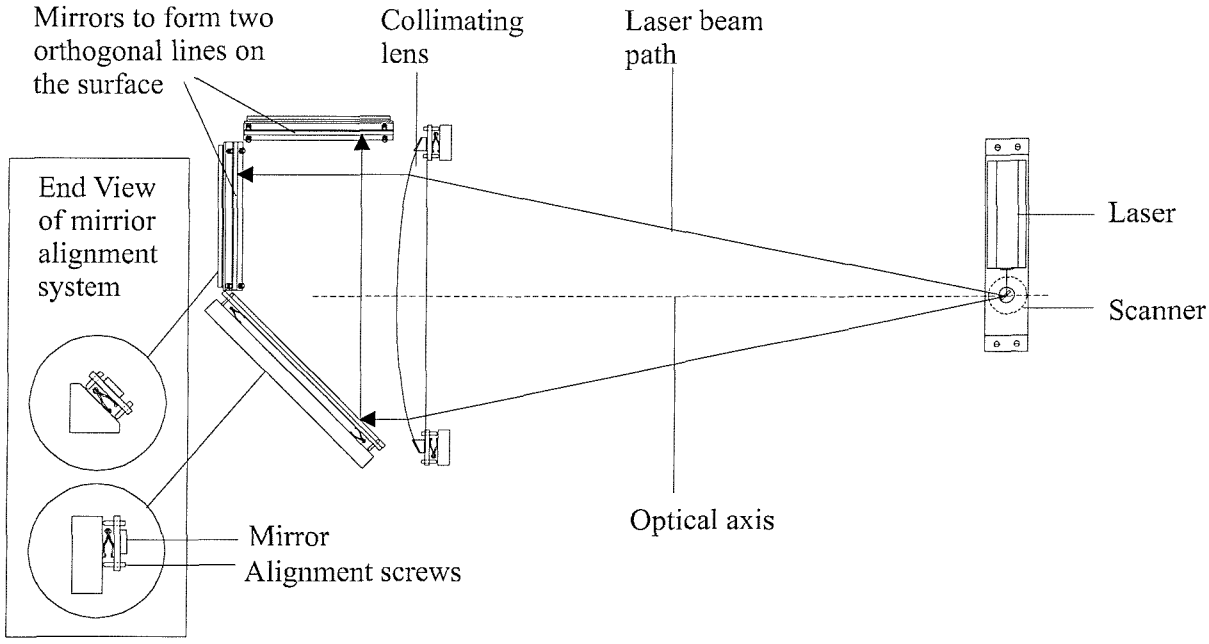

Figure CI Proposed scanning unit for the Digital Slopemeter

Instead of a single point of laser light at the sea surface we now have a set of points describing two perpendicular lines. The same approach for determining the wave slope from a single point measurement can be used. The combination of this scanning unit with the optical detection system of the TLS instrument was investigated. Six photodiode ratios are used to determine a single spot position. The spot position cannot be calculated in real-time and must be processed after a trial. This led to the photodiode ratios forming part of the telemetry data. The telemetry bandwidth is not large enough to permit more than six photodiode ratios to be transmitted in each sample

period. As the new instrument generates more than one spot position in each sample period it is not practical to combine the TLS optical detection system with this proposed scanning strategy. This led Crossingham and Ramsden (1997a) to propose a new optical detection assembly to be used in conjunction with the new scanning system to reduce the amount of data needed to be processed. The instrument is referred to as the Digital Slopemeter, or DSM, as it evaluates the wave slope digitally as opposed to the TLS which made an analogue measure of the sea surface wave slope.

Like the TLS, the new optical detection system consists of two parallel detection planes. Instead of using a continuous sheet of plastic wavelength shifting wave guide material, each detection plane consists of an open fibre grid. A sketch of the fibre grid is given in figure C2. From this figure, each grid is made from two rows of fibres. Each row is orientated at 90° to the other. The fibres are made from a similar material to the screens of the TLS. For a minimum slope range of ±30° and a minimum resolution of 1° the top fibre grid covers an area of 0.87 m by 0.87 m. At one end of each of the fibres is placed a photodiode. Photodiode arrays each containing sixteen photodiodes spaced at 1.6 mm are used. With a fibre spacing of 1.6mm there are 544 fibres in each row. The laser spot size is 2mm. The laser beam refracted by the sea surface wave slope will impinge on both grids, illuminating two or more fibres in each orthogonal row.

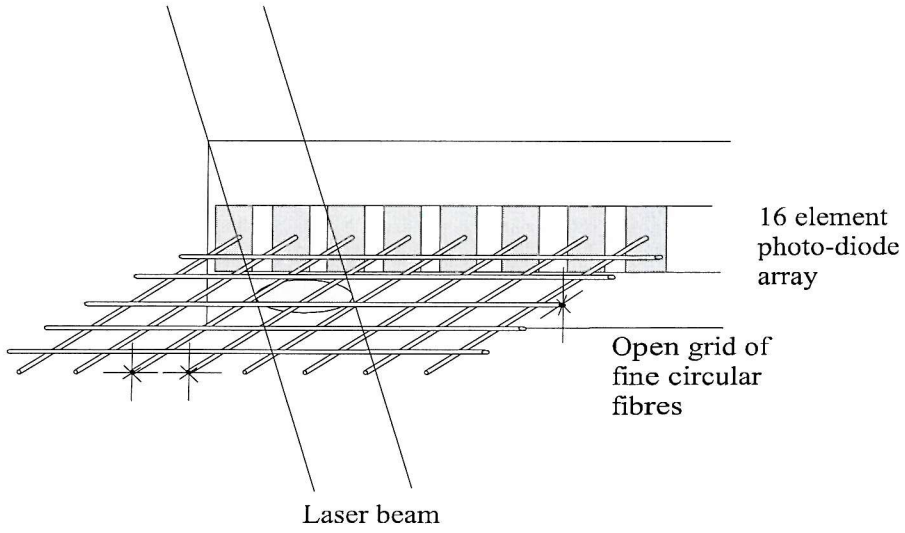

Figure C2 A sketch of a single detection plane comprising of a plastic wavelength shifting open fibre grid.

The refracted beam, produced at each point in the scan, falls on the optical detection system and the corresponding wave slope at the point of refraction may be evaluated. The advantage of using an open fibre grid instead of a continuous plastic screen for each detection plane in the optical detection system is that the spot position can be determined without the need for calibration. This allows the real-time processing and display of the wave-slope data. Maintaining two detection

planes permits the calculation of wave slope without the need to measure, or assume a constant wave height.

The TLS used a Helium-cadmium laser source emitting light at blue wavelengths. A greater percentage of light is scattered at these wavelengths. To ensure that the top screen of the TLS instrument was illuminated, the laser had to provide a powerful spot intensity and this led to the device being relatively large. The source was not only bulky but easily damaged and prone to fluctuations in power output, an inherent feature of this type of gas laser. An alternative would have been to use a solid state diode laser. These can provide a similar but stable power output. They are less easily damaged and much smaller. Prior to the design of the TLS instrument diode lasers could only produce light at red wavelengths. Plastic wavelength shifting wave-guides were not sensitive to this wavelength range. Liquid dyes which absorb and emit light at red wavelengths are available but could not be incorporated into the design due to obvious practical reasons.

A small, stable, but rugged laser source would be an advantage to the proposed design of the new scanning unit. Thin glass tubes filled with liquid dyes, to provide fibres for detection planes of the optical detection system of the DSM instrument, were investigated but their construction proved difficult. Fortunately, a solid state diode laser emitting light at blue wavelengths had recently been developed. A plastic wavelength-shifting fibre sensitive to the output from this new laser was identified and both were included in the proposed design of the Digital Slopemeter.

The noise in the TLS instrument which was apparent from the analysis of the data from the Loch Linnhe trial was attributed to the power converters on the printed circuit boards and the cross-talk between the ADC and the sample and hold circuit. These electronic systems were required to convert analogue voltages from the photodiodes to digital signals required if they were to provide an input to the VME. The TLS instrument measures a light intensity within the detector planes and this is processed to give spot position. By using a fibre grid, the new detector is only required to determine whether, or not, a fibre has been illuminated. As only two states exist the output from the fibres can be considered to be digital. The light content within each fibre is measured using a photodiode.

A comparator is used to compare the output from each photodiode with a reference voltage. The photodiode voltage output from a fibre illuminated by the laser will be greater than the reference voltage and this produces an output signal from the comparator of unity. A fibre which has not been illuminated by the laser produces a photodiode voltage output which is less than the reference voltage and this produces an output signal from the comparator of zero. These digital signals provide an input to an EPROM microchip which is used to determine the address and therefore the position of the illuminated fibres. Using two orthogonal rows of fibres to describe an

open fibre grid, the spot position within each detection plane can be determined. When the spot position within each of the two detection planes is combined, the wave-slope can be calculated using equation 3.7. This technique greatly simplifies the electronics and eliminates the need for analogue to digital conversion, greatly reducing the chance for noise to occur in the new detector. The name Digital Slopemeter refers to the fact that the new system evaluates the wave slope digitally as opposed to the TLS which makes an analogue measure of the sea surface.

Difficulties in deploying the TLS instrument, associated with the use of a catamaran, had been experienced in the Loch Linnhe and CSTAR campaigns:

- At the beginning, and end, of each day of deployment the TLS had to be craned in, and out, of the water so that it could be left on a stable platform overnight. This increased the potential of damaging the instrument.

- Before a scientific run could commence, tow ropes would have to be attached, telemetry and optical cables connected and batteries connected to the on-board electronics. This required that someone was put on-board the catamaran. In addition the same person would have to be deployed into the water to clean the aperture of the optical detection system. Both actions were at a risk to personnel safety.

- The continuous manning of tow ropes and optical and telemetry cables was tiring. The possibility of towing ropes becoming wrapped around the propeller shaft of the tow vessel was ever present.

To limit these deployment difficulties it was decided to abandon the catamaran and instead mount the Digital Slopemeter on the bow of the research vessel. Cabling could then be passed directly to the cabin, housing the personnel computers used in the data logging and other support equipment, without the need for it to enter the water. In addition an on-board power source would supply current directly to the DSM instrument eliminating the need for batteries. The research vessel also offers greater stability than the catamaran reducing the pitch, roll and yaw motions that are recorded using the IMU.

It has been proposed that the DSM instrument is to be deployed on a *ducking stool* type assembly (Crossingham (1998)). A sketch of this bow mounted assembly is given figure C3. The *ducking stool* is operated using a hydraulic lift. The detector and scanning unit can be kept above the water line whilst the research vessel is under way to the trial site. Once at the trial area, the scanning unit and optical detector are deployed into position ready for the gathering of scientific data. The aperture to the optical detection system can be cleaned without the need to deploy somebody into

the water by using the hydraulic lift to tilt the instrument onto the deck. The distance between the leading edge of the bow and the area of water surface scanned by the laser is such that the research vessel does not interfere with the wave slopes being measured. The *ducking stool* will be hydraulically damped enabling the Digital Slopemeter to ride large waves reducing stress and therefore the risk of damage to the surrounding structure.

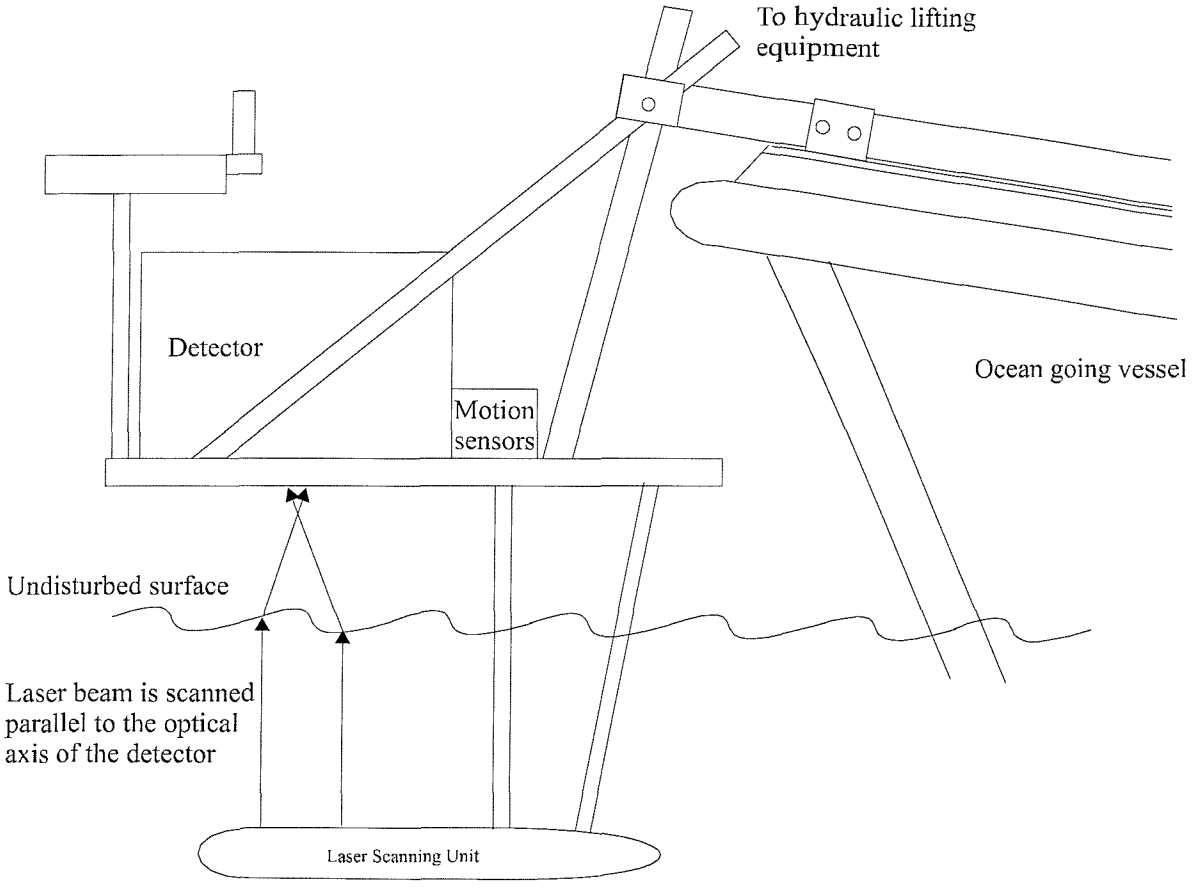

Figure C.3 A sketch of the proposed Digital Slopemeter bow mounted assembly

As a result of the Loch Linnhe trials a number of support instrumentation were included on the tow vessel and the catamaran. These proved useful in the subsequent analysis of the data from the CSTAR trial. It is proposed that such instrumentation will be deployed together with the Digital Slopemeter. These include a weather station, featuring an anemometer, a DGPS antenna and an echo sounder. The instruments will be mounted on the DSM to simplify deployment and to ensure localised measurements. A sketch of the proposed integrated system set-up is given in figure C4.

The simplification of the optical detection system and processing electronics permits the real-time display of wave slope data. Spectrograms, variance plots and power spectra have been used extensively in the analysis of TLS data sets to identify, and investigate, sea surface roughness changes recorded in the wave slope data. These analysis tools will be used in a front end computer

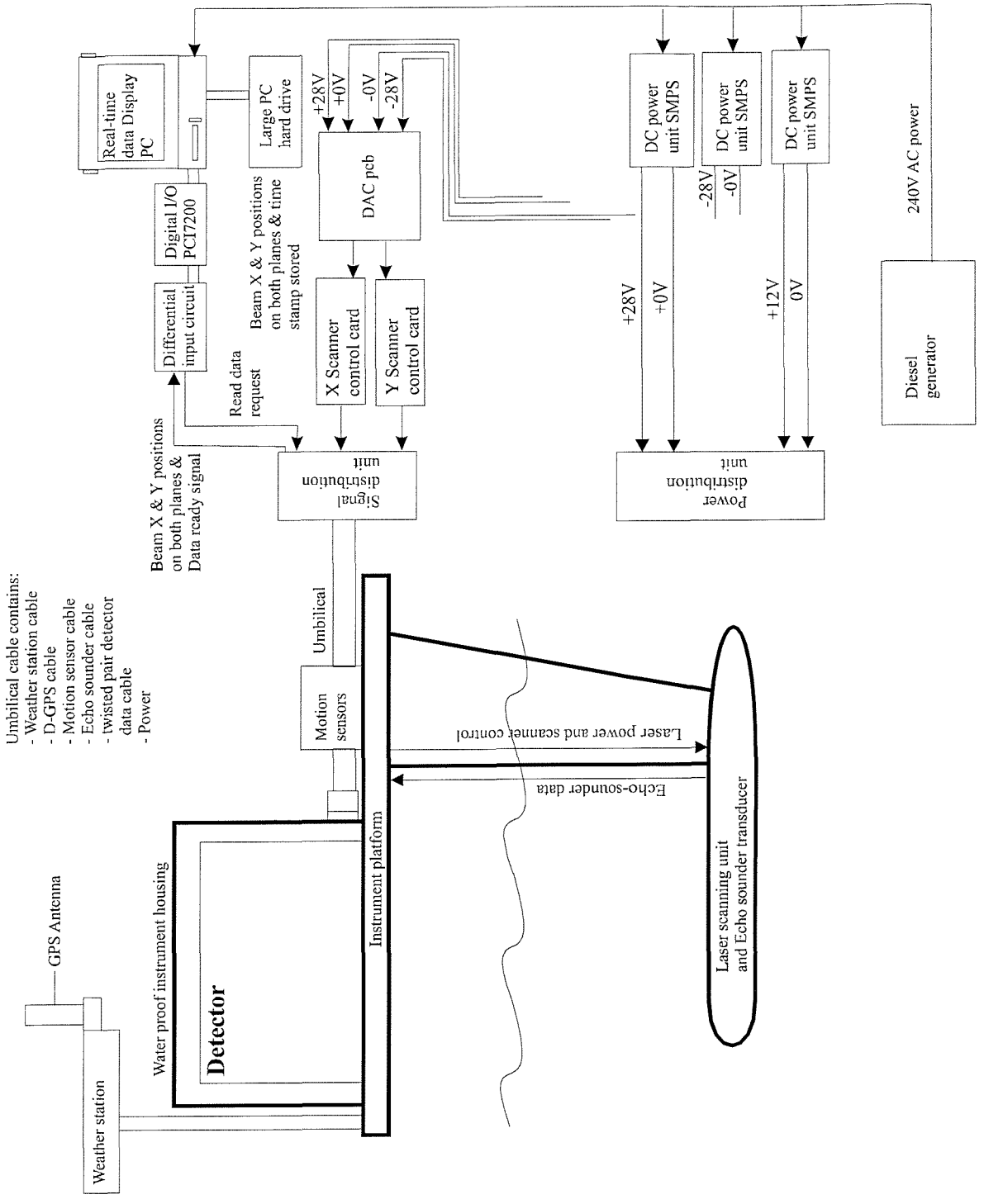

Figure C4 A sketch of the fully integrated Digital Slopemeter instrument.

package to examine the wave slope in real-time. The wave slope data can be visualised together with the data from the weather station and echo sounder a feature which was not possible with the Towed Laser Slopemeter system. Interesting regions of sea surface roughness can be identified and returned to permitting further investigation.

The bow mounted assembly has been designed to fit the bow of the *Wilventure*. The *Wilventure* is a 12m Nelson Class commercial launch based at the Empress Dock in Southampton. The *Wilventure* has been used extensively during deployments of the Towed Laser Slopemeter within Solent waters. From such campaigns it was evident that Solent waters contain a wide verity of interesting ocean processes responsible for changes to the sea surface roughness. A recent proposal has been accepted by the Natural Environment Research Council (NERC) to develop the Digital Slopemeter.

The experience gained from the research conducted with the Towed Laser Slopemeter presented in this thesis has directly influenced the development of all aspects of the design of a new Digital Slopemeter instrument. It is envisaged that the Digital Slopemeter will provide a precise measure of wave slope and an undistorted measurement of the directional wave slope wavenumber spectrum. Such precise measurements will be required if mechanisms that lead to the changes in the sea surface roughness induced by a variety of ocean phenomena are to be fully understood.

References

Alpers, W., and Hasselmann, K., "The two-frequency microwave technique for measuring ocean wave spectra from an airplane or satellite", *Boundary Layer Meteorol.*, Vol. *13*, pp 215-230, 1978.

Alpers, W., and Hennings, I., "A theory of the imaging mechanism of underwater bottom topography by real and synthetic aperture radar", *Jnl. Geophys. Res.,* Vol. 89, pp 10529-10546, 1984.

Alpers, W. R., Ross, D. B., Rufenach, C. L., "On the detectability of ocean surface waves by real and synthetic aperture radar", *Jnl. Geophys. Res.,* Vol. 86, No. C7, pp 6481-6498, 1981.

Apel, J.R., and Gonzela, F.I., "Nonlinear features of internal waves off Baja California as observed by SEASAT imaging radar", *Jnl. Geophys. Res.,* Vol. 88, pp4459-4466, 1983.

Banner, M. L., Jones, I. S. F. and Trinder, J. C., "Wavenumber spectra of short gravity waves", *J. Fluid Mech.*, Vol. 198, pp 321-344, 1989.

Boch, E. J. and Frew, N. M., "Static and dynamic responce of natural multicomponent oceanic surface films to compression and dilation; laboratory and field observations", *Jnl. Geophys. Res.* Vol. 98, No. C8, pp 14,599-14,617, 1993.

Brigham, E. O., "The Fast Fourier Transform and its Applications", (Prentice-Hall, Inc., Englewood Cliffs, N. J.), 1988.

Caponi, E. A., Crawford, D. R., Yuen, H. C. and Saffman, P.G., "Modulation of radar backscatter from the ocean by a variable surface cuurent", *J. Geophys. Res.*, Vol. 93, No. C10, pp 12,249-12,263, 1988.

Cartwright, D. E., "The use of directional spectra in studying the output of a wave recorder on a moving ship", *N.A.S. Ocean Wave Spectra* (Prentice-Hall, Inc., Englewood Cliffs, N. J.), pp 203-218, 1963.

Charnock, H., "Wind stress on a water surface", *Q. J. R. Meteorol. Soc.*, Vol. 81, pp 639-640, 1955.

Cooley, J. W. and Tukey, J. W., "An algorithm for the machine calculation of complex Fourier series", *Math. of Comput.*, Vol. 19, No. 90, pp 297-301, 1965.

Cote, L. J., Davis, O. J., Marks, W., McCough, R. J., Mehr, E., Pierson, W. J., Ropek, J. F., Stephenson, G. and Vetter R. C., "The directional spectrum of a wind generated sea as determined from data obtained by the Stereo Wave Observation Project", *Meteorol. Papers, New York University, College of Engineering*, Vol. 2, No. 6, 1960.

Cox, C. and Munk, W., "Statistics of the sea surface derived from sun glitter", *Jnl. Mar. Res.*, Vol. 13, No. 2, pp 198-227, 1954.

Cox, C. S., "Measurement of slopes of high frequency wind waves". *Jnl. Mar. Res.*, Vol. 16, pp 199-225, 1958.

Crossingham, G. J., and Ramsden, D., "First quarterly report on progess in the digital slopemeter development", Internal Document Southampton University, 1997a

Crossingham, G. J., and Ramsden, D., "Second quarterly report on progess in the digital slopemeter development", Internal Document Southampton University, 1997b

Crossingham, G. J., Ph.D Thesis, *to be submitted*, 1998

Evans, D. D. and Shemdin, O. H., "An investigation of the modulation of capillary and short gravity waves in the open ocean", Jnl. Geophys. Res., Vol. 85, No. C9, pp 5019-5024, 1980.

Fung, A. K. and Chen, M. F., "Numerical simulation of scattering from simple and composite rough surfaces", *J. Opt. Soc. Am.*, Vol. A2, pp 2274-2284, 1985.

Gibson, G. E., "Loch Linnhe 1994: Trial plan", DRA/CIS(CSC2)/4/36/4/TP1/2.2, DRA Farnborough, 1994.

Hennings, I., Stolte, S., and Ziemer, F., "Experimental method to measure surface signature generation by sea bottom undulations", *IEEE Journal of Oceanic Engineering* Vol. 19. pp 10-22, 1994.

Holliday, D., St.-Cyr, G., and Woods, N. E., "A radar ocean imaging model for small to moderate incidence angles", *Int. J. Remote. Sens.*, Vol 7, pp 1809-1834, 1986

Hsiao, S. V., and Shemdin, O. M., "Measurements of wind velocity and pressure with a wave follower during MARSDEN", *J. Geophys. Res.*, Vol. 88, No. C6, pp 9844-9849, 1983.

Hulburt, E. O., "The polarization of light at sea"., *J. Optic. Soc. Am.*, Vol. 24, pp 35-42, 1934.

Hughes, B. A., Grant, H. L. and Chappell, R. W., "A fast responce surface slopemeter and measured wind-wave moments", *Deep-Sea Res.*, Vol. 24, pp 1,211-1,223, 1977.

Hughes, B. A. and Grant, H. L., "The effect of internal waves on surface wind waves I: Experimental measurements", *Jnl. Geophys. Res.*, Vol. 83, pp 443-454, 1978.

Hughes, B. A., "The effect of internal waves on surface wind waves 2. Theoretical analysis", *Jnl Geophys. Res.*, Vol. 83, No. C1, pp 455-465, 1978.

Jähne, B. and Waas. S., "Optical measuring technique for small scale water surface waves", *SPIE Proceeding: Advanced Optical Instrumentation for the Remote Sensing of Earth's Surface From Space*, Vol. 1129, pp 147-, 1989

Jähne, B., Waas, S. and Klinhe, J., "A critical theoretical review of optical techniques for ocean wave measurements", *SPIE proceedings: Optics Air-Sea Interface*, Vol. 1749, pp 204-215, 1992.

Keller, W. C., and Gotwols, B. L., "Two dimensional optical measurement of slope", *Applied Optics*, Vol. 22, No. 22 pp 3476-3478, 1983.

Keller, W.C., and Wright, J. W., "Microwave scattering and the straining of wind-generated waves", *Radio Science*, Vol. 10, pp 139-147, 1975.

Kinsman, B., "Wind Waves", (Prentice-Hall, Inc., Englewood Cliffs, N. J.), 1965.

Lange, P. A., Jähne, B., Tschiersch, J. and IImberger, I., "Comparison between an amplitude-measuring wire and a slope-measuring laser water wave gauge", *Rev. Sci. Instrum.*, Vol. 53, No. 5, pp 651-655, 1982.

Lee, C. G-Y., Willoughby, B.J., Ghataure, H. S., Ramsden, D., and Robinson, I. S., *" A Towed Laser Slopemter"*, Sixth International Conference: Electronic Engineering in Oceanography, IEE, 148-152, 1994

Lee, C. G-Y., "The Design of a towed Laser Slopemeter system for the measurement of short scale sea waves", Ph.D Thesis, University of Southampton, Southampton, U.K., 1995.

Lee, P. H. Y., Barter, J. D., Beach, K. L., Hindman, C. L., Lake, B. M., Rungaldier, H., Schatzman, J. C., Shelton, J. C.,Wagner, R. N., Williams, A. B., Yee, R. and Yuen, H. C., "Recent advances in ocean surface characterisation by a scanning laser slope gauge", *SPIE Proceedings: Optics Air-sea Interface.*, 1749, pp 234-244, 1992.

Liu, H-T., Katsaros, K. B. and Weissman, M. A., "Dynamic response of thin-wire wave gauges", *Jnl. Geophys. Res.*, Vol 87. No. C8, pp 5686-5698, 1982.

Lobemeier, P., "A wire probe for measuring high frequency sea waves", *J. Phys E: Sci. Instrum.*, Vol. 14, pp 1,407-1,410, 1981.

Longuet-Higgins, M. S., Cartwright, D. E., and Smith, N. D., "Observations of the directional spectrum of sea wave using the motions of a floating buoy", *Ocean Wave Spectra*, (Prentice-Hall Inc., EngleWood Cliffs, N. J.), pp 111-136, 1963.

Longuet-Higgins, M.S., "The effect of non-linearities on statistical distributions in the theory of sea waves", *Deep Sea Res.*, Vol. 11, pp 459-480, 1964.

Longuet-Higgins, M.S., and Stewart, R. W., "Radiation stresses in water waves, a physical discussion with applications", *Deep Sea Res.*, Vol. 11, pp 529-562, 1964.

Lyzenga, D. R., "Interaction of short surface and electromagnetic waves with ocean fronts"J. Geophys. Res., Vol. 96, No. C6, pp 10,756-10,772, 1991.

Martinsen, R. J. and Bock, E. J., "Optical measurments of ripples using a scanning laser slope gauge. Part I: Instrumentation and preliminary results", *SPIE Proceedings: Optics Air-sea interface*, 1749, pp 258-269, 1992.

Nussbaumer, H. J., "Fast Fourier Transform and Convolution Algorithms", (Springler-Verlag, New York), 1982.

Oligvy, J. A., "Computer simulation of acoustic wave scattering from rough surfaces", *J. Phys. D: Appl. Phys.*, Vol. 21, pp 260-277, 1988.

Paniker, N. N., "A review of techniques for directional wave spectra", *Int. Symp. Ocean Wave Measurement and Spectral Anal.*, No. 3391, 1975.

Palm, C. S., Anderson, R. C. and Reece, A. M., "Laser probe for measuring 2-D wave slope spectra of ocean capillary waves", *Applied Optics,* Vol. 16, No. 4, pp 1,074-1,081, 1977.

Phillips, D. L., "A technique for the numerical solution of certain integral equations of the first kind", *J. Ass. Comput. Mach.*, Vol. 9, pp 84-87, 1962.

Phillips, O. M., "The Dynamics of the Upper Ocean", (Cambridge University Press, Cambridge), 1958.

Phillips, O. M., "Spectral and statistical properties of the equilibrium range in wind generated gravity waves", *J. Fluid Mech.*, Vol. 156, pp 505-531 , 1985.

Pierson, W. J., and Moskowitz, L., "A proposed spectral form for fully developed wind seas based on the similarity theory of S. A. Kitaigorodskii", *J. Geophys. Res.*, Vol 69, No 24, pp5181-5190, 1964.

Plant, W. J., "A relationship between wind stress and wave slope", *J. Geophys. Res.*, Vol 87, No. C9, pp 10,735-10,749, 1986.

Plant, W. J. and Wright, J. W., "Growth and equilibrium of short gravity waves in a wind-wave tank", *J. Fluid Mech.*, Vol 82, pp 767-793, 1977.

Press, W. H., Flannery, B. P., Teukolsky, S. A., and Vetterling, W.T., "Nummerical recipies in C", (Cambridge University Press, Cambridge), 1988

Prettyman, C. E. and Cermak, M. D., "Time variation of the rough ocean surface and its effect on an incident laser beam". *IEEE Trans. Geosci.* Vol. GE-7, No. 4, pp 235-243, 1969.

Robinson, I. S., "Satellite Oceanography", (Ellis Horwood Ltd., England) 1991.

St. Denis, M. and Pierson, W. J., "On motion of ships in confused seas", *Trans. S.N.A.M.E.*, Vol. LX1, pp 332-357, 1953.

Scott, J. C., "An optical probe for measuring water wave slopes", *J. Phys. E: Sci. Instrum.*, Vol. 7, pp 747-749, 1974.

Scott, J. C., "Oil on troubled waters. A bibliograhpy on the effects of surface active films on surface wave motions", (mult-science Pub. Co), 1979.

Scott, J. C., "Oil on troubled waters-part II. A bibliograhpic update on the effects of surface active films on surface wave motions", (mult-science Pub. Co), 1979.

Shemdin, O. H., Tran, H. M. and Wu, S. C., "Directional measurement of short ocean waves with stereophotography", *Jnl. Geophys. Res.*, Vol. 93, No. C11, pp 13,891-13,901, 1988.

Shemdin, O. H. and Hwang, P. A., "Comparison of measured and predicted sea surface spectra of short waves", *Jnl. Geophys. Res.*, Vol. 93, No. C11, pp 13,883-13,890, 1988.

Shuchman, R.A., Lyzenga D. R., and Meadows, G. A., "Synthetic aperture radar imaging of ocean-bottom topography via tidal-current interactions: theory and observations", *Int. J. Rem. Sens.*, Vol. 6, pp 1,179-1,200, 1985.

Stilwell, D., "Directional energy spectra of the sea from photographs", *Jnl. Geophys. Res.*, Vol. 74, pp 1,974-1,986, 1969.

Stolte, S., "Short wave measurements by a fixed tower based and drifting buoy system", *IEEE J. Oce. Eng.*, Vol. 19, No. 1, pp 10-22, 1994

Sturm, G. V. and Sorrell, F. Y., "Optical wave measurement and experimental comparison with conventional wave height probes", *Applied Optics*, Vol. 12, No. 8, pp 1,928-1,933, 1973.

Taylor, V. J. knight, T. A. M. and Perry, J. R., "Loch Linnhe 1994: Towed Laser Slopemeter analysis report", DRA/CIS(CIS2)/CR95012/1.0, DRA Farnborough, 1995.

Taylor, V. J., "Towed Laser Slopemeter full preliminary data analysis report",

DRA/CIS/CIS2/WP96012/1.0, DRA Farnborough, 1996.

Taylor, V. J., "C-Star experiment: Browse file and data quality assessment", DRA/CIS/CIS2/WP97353, DRA Farnborough, 1997.

Tober, G., Anderson, R. C. and Shemdin, O. H., "Laser instrument for detecting water ripple slopes", *Applied Optics*, Vol. 12, No. 4, pp 788-794, 1973.

Trulsen, G. N., Dysthe, K. B., and Trulsen J., " Evolution of a gravity wave spectrum through a current gradient", *J. Geophys. Res.*, Vol 95, No. C10, pp 22, 141-22,151, 1990.

Tucker, M. J., "A wave recorder for use in ships", *Nature*, Vol. 170, No. 4320, pp 657-659, 1952.

Tucker, M. J., "A shipborne wave recorder" *Trans. Instn. Naval Arch.*, Vol. 98, No. 3, pp 236-246, 1956.

Twoney, S., "On the numerical solution of Fredholm integral equations of the first kind by the inversion of the linear system produced by quadrature", *J. Ass. Comput. Mach.*, Vol 10 pp 97-101, 1963

Venn, J.F., and D'Olier, B., "Preliminary observations for a model of sand bank dynamics" North Sea Dynamics (Springer-Verlag, New York), pp 472-485, 1983.

Vogelzang, J., "Mapping submarine sand waves with multiband imaging radar. 1. Model development and sensitivity analysis", *Jnl. Geophys. Res.*, Vol 102, No C1, pp 1163-1181, 1997.

Watson, G., "Internal waves in the strait of Gibraltar: A study using radar imagery" (Ph.D. Thesis, University of Southampton, U.K.), 1988.

Wensink, G.J. et al, "Coastal sediment transport assessment using SAR imagery (CSTAR) annual report" *EC Contract Number MAS3-CT95-0035,* 1997

Wilmhurst, T. H., "Signal recovery from noise in electronic instrumentation", 2nd Edition, Adam Higner, 1990.

Wright, J. W. and Keller, W. C., "Doppler spectra in microwave scattering from wind waves", *Phys. Fluids*, Vol 14, pp 466-474, 1971.